A population synthesis model for young stars and their discs

Alice Somigliana

München 2024

A population synthesis model for young stars and their discs

Alice Somigliana

Dissertation
der Fakultät für Physik
der Ludwig-Maximilians-Universität
München

vorgelegt von
Alice Somigliana
aus Mailand, Italien

München, den 22. Oktober 2024

Erstgutachter: Prof. Dr. Barbara Ercolano
Zweitgutachter: Prof. Dr. Leonardo Testi
Tag der mündlichen Prüfung: 9. Dezember 2024

"L'incanto sarà godersi un po' la strada..."

Cesare Cremonini

This work was carried out at the European Southern Observatory (ESO) in Garching bei München under the supervisor of Professor Leonardo Testi. The committee members for the doctoral defense were Professors Katia Parodi, Barbara Ercolano, Leonardo Testi, and Paola Caselli.

Contents

List of Figures

List of Tables

Abstract

Protoplanetary discs are structures of gas and dust orbiting young stars, that form as a consequence of angular momentum conservation during the star formation process. They act as a mass reservoir, storing and delivering the material that feeds the protostar and supports its accretion; furthermore, they provide the location and building blocks to form planetary systems. The main driver of the disc evolution is accretion onto the protostar. While it is well understood that this happens as a consequence of the loss of angular momentum by the disc material, the mechanism at its root is still a topic of debate. The traditional picture, prescribing a turbulent viscosity to redistribute angular momentum, is challenged by the observational evidence of low levels of turbulence; the alternative scenario of magnetic disc winds, which extract material (and angular momentum with it), provides a viable solution. Assessing the relative contribution of viscosity and winds in driving protoplanetary disc accretion is a timely question, and the main focus of this work.

The ideal ground to test evolutionary models is offered by the use of large amounts of data. The increasing availability of measured disc properties - such as the mass, accretion rate, and radius - has driven the development of numerical simulations to treat entire disc populations. This approach, called population synthesis, allows to interpret the results of surveys of star-forming regions in terms of physical processes and evolutionary parameters.

In this thesis, I have explored the impact of the angular transport mechanism on observables of populations of protoplanetary discs, with the goal of looking for novel evolutionary proxies. To this end, I have developed and released to the community the population synthesis tool `Diskpop`. I have investigated the time evolution of the observed disc mass-stellar mass and accretion rate-stellar mass correlations, finding a model-dependent behaviour; an assessment of the observability of this result highlighted the need for larger samples to be able to recover the predicted difference. In particular, completing the existing surveys - especially for the more evolved populations - would allow to use the time evolution of the slopes as a probe of the accretion mechanism. I have then investigated the possibility of using the distribution of disc lifetimes, defined as the ratio between the disc mass and accretion rate, as an observational diagnostic for disc evolution. With `Diskpop` simulations, I have found that the time evolution of the width of the distribution is different enough to be observable, under the assumption of reliable disc mass measurements, even after convolving with the observational uncertainties. The upcoming gas-estimated disc masses from ongoing observational programs will improve the constraints on disc lifetimes, allowing to fully exploit these theoretical predictions.

This thesis lays the foundation to the systematic interpretation of disc observables with population synthesis. The proposed diagnostics will play a crucial role in constraining the disc evolution process, as larger amounts of data become available; moreover, the possibility to build on `Diskpop` will allow to test the impact of further physical mechanisms beyond the accretion model, refining our understanding of the star and planet formation process and bridging the current gap with the earlier evolutionary stages.

Zusammenfassung

Protoplanetare Scheiben sind Strukturen aus Gas und Staub, die junge Sterne umkreisen und sich als Folge der Drehimpulserhaltung während des Sternentstehungsprozesses bilden. Sie dienen als Massenreservoir, welches das Material speichert und abgibt, das den Protostern ernährt und seine Akkretion unterstützt; außerdem sind sie der Ort, an dem sich Planetensysteme bilden, und liefern die dafür nötigen Bausteine. Der Hauptantrieb für die Entwicklung der Scheibe ist die Akkretion auf den Protostern. Es ist zwar bekannt, dass dies als Folge des Drehimpulsverlusts des Scheibenmaterials geschieht, aber der zugrunde liegende Mechanismus ist immer noch umstritten. Das traditionelle Bild, das eine turbulente Viskosität für die Umverteilung des Drehimpulses vorschreibt, wird durch die Beobachtung geringer Turbulenzen in Frage gestellt; das alternative Szenario von magnetischen Scheibenwinden, die Material (und damit Drehimpuls) abziehen, bietet eine praktikable Lösung. Die Beurteilung des relativen Beitrags von Viskosität und Winden bei der Akkretion protoplanetarer Scheiben ist eine aktuelle Frage, die im Mittelpunkt dieser Arbeit steht.

Die Verwendung großer Datenmengen ist eine ideale Grundlage für die Prüfung von Evolutionsmodellen. Die zunehmende Verfügbarkeit von gemessenen Scheibeneigenschaften - wie Masse, Akkretionsrate und Radius - hat die Entwicklung numerischer Simulationen zur Behandlung ganzer Scheibenpopulationen vorangetrieben. Dieser Ansatz, der als Populationssynthese bezeichnet wird, ermöglicht es, die Ergebnisse von Durchmusterungen sternbildender Regionen im Hinblick auf physikalische Prozesse und Entwicklungsparameter zu interpretieren.

In dieser Arbeit habe ich die Auswirkungen des Winkeltransportmechanismus auf die Beobachtungsdaten von Populationen protoplanetarer Scheiben untersucht, mit dem Ziel, nach neuen evolutionären Proxies zu suchen. Zu diesem Zweck habe ich das Populationssynthesetool `Diskpop` entwickelt und der Gemeinschaft zur Verfügung gestellt. Ich habe die zeitliche Entwicklung der beobachteten Korrelationen zwischen Scheibenmasse und stellarer Masse sowie zwischen Akkretionsrate und stellarer Masse untersucht und dabei ein modellabhängiges Verhalten festgestellt; eine Bewertung der Beobachtbarkeit dieses Ergebnisses hat gezeigt, dass größere Stichproben erforderlich sind, um die vorhergesagte Differenz zu ermitteln. Insbesondere die Vervollständigung der bestehenden Durchmusterungen - vor allem für die weiter entwickelten Populationen - würde es ermöglichen, die zeitliche Entwicklung der Steigungen als Sonde für den Akkretionsmechanismus zu nutzen. Ich habe dann die Möglichkeit untersucht, die Verteilung der Scheibenlebensdauer, definiert als das Verhältnis zwischen Scheibenmasse und Akkretionsrate, als Beobachtungsdiagnose für die Scheibenentwicklung zu verwenden. Mit `Diskpop`-Simulationen habe ich herausgefunden, dass die zeitliche Entwicklung der Breite der Verteilung unterschiedlich genug ist, um unter der Annahme zuverlässiger Messungen der Scheibenmasse beobachtbar zu sein, selbst nach Faltung mit den Unsicherheiten der Beobachtung. Die bald verfügbaren, anhand von Gaseigenschaften abgeschätzten Scheibenmassen aus laufenden Beobachtungsprogrammen werden eine bessere Einschränkung der Scheibenlebensdauer ermöglichen, so dass diese

theoretischen Vorhersagen voll genutzt werden können.

Diese Arbeit legt den Grundstein für die systematische Interpretation von Scheibenbeobachtungen mittels Populationssynthese. Die vorgeschlagene Diagnostik wird eine entscheidende Rolle bei der Eingrenzung des Scheibenentwicklungsprozesses spielen, sobald größere Datenmengen zur Verfügung stehen. Darüber hinaus wird die Möglichkeit, auf `Diskpop` aufzubauen, es erlauben, die Auswirkungen weiterer physikalischer Mechanismen jenseits des Akkretionsmodells zu testen, unser Verständnis des Stern- und Planetenentstehungsprozesses zu verfeinern und die derzeitige Lücke zu früheren Entwicklungsstadien zu schließen.

1

Introduction

1.1 Star and planet formation

The process of star and planet formation begins in molecular clouds (Shu et al., 1987), where dense, rotating conglomerates of molecular gas - commonly referred to as 'pre-stellar cores' - undergo gravitational collapse (Terebey et al., 1984); each collapsing core gives birth to one, or possibly more, protostars embedded in their parental cloud. While the initial rotation of the cores is rather modest on their typical scales ($E_{\rm rot}/|E_{\rm grav}| \sim 0.02$, according to the observational estimates of Goodman et al. 1993), the rapid collapse magnifies the initial rotational velocity, and the angular momentum is in fact non-negligible at smaller scales. Angular momentum conservation prescribes the rotating material, a mixture of gas and solid particles, to arrange itself in a disc-like shape surrounding the newborn protostar, while the outskirts of the original core form the so-called 'envelope' that slowly accretes onto the disc-star system - leading the protostar to its main accretion phase. When accretion is over, the protostar reaches a thermodynamic state compatible with hydrogen burning, therefore becoming a main sequence star; for this reason, the previous evolutionary stages are referred to as pre-main sequence.

Depending on the relative extent of the disc and envelope, Young Stellar Objects (hereafter YSOs) in the pre-main sequence phase are empirically divided in classes based on the slope of the infrared excess of their spectral energy distribution (see Section 1.2), ranging from 0 to III, sketched in Figure 1.1. For the sake of simplicity, let us consider that each collapsing core gives birth to one protostar. Class 0 (middle top image in Figure 1.1) corresponds to the very beginning of the star formation process, where the protostar has just formed and is surrounded by a thick envelope (Andre et al., 2000): these objects are too embedded to be observed at optical wavelengths, however it is possible to detect the disc at millimetric wavelengths (Tobin et al., 2013). This is the earliest stage where

we can observe signs of accretion onto the protostar: the material gets accreted both directly from the infalling envelope and through the accretion disc, that has formed due to the conservation of angular momentum of the whole cloud. The redistribution of angular momentum is accompanied by strong bipolar jets and outflows, that eject a small part of the accreted material perpendicularly to the disc and contribute to the removal of angular momentum from the infalling material. Through this process, YSOs reach the Class I phase (top right image in Figure 1.1): at this point, the envelope is still a prominent feature but its optical depth is decreased. When the envelope is mostly dissipated, its contribution to the YSO emission is negligible and it can be observed at optical wavelengths, which leads the object to enter the Class II phase (bottom right image in Figure 1.1) . Class IIs are commonly referred to as 'protoplanetary discs', due to the ease of observation of the disc itself that is not obscured by the envelope anymore. The disc, composed of a mixture of gas and dust, evolves under the influence of viscosity and/or magnetohydrodynamics (MHD) winds: this evolution results in a redistribution, or loss, of angular momentum that causes accretion onto the central protostar. Furthermore, the solid component of the disc forms the planetary embryos that eventually lead to the formation of planetary cores. While the dispersal of the disc does not directly coincide with the beginning of the main sequence phase, it leaves the protostar directly observable and marks the end of the accretion process; from there on, the protostar evolves towards the main sequence at fixed mass. Another popular observational classification of YSOs is based on the accretion properties, determined by optical spectroscopy: protostars are divided in classical-(C) or weak-(W) T Tauri stars (TTs), mostly based on the intensity of the Hα emission line. CTTs are actively accreting gas from the disc and correspond to Class IIs, while WTTs are non-accreting objects, therefore mostly associated with Class III.

The main physical interest of proto*planetary* discs is indeed that they are the cradles of planets. Not only do they make the perfect environment for protoplanets to grow - they also provide the ingredients to both form the planetary core, through the accretion of the solid, dusty component, and to assemble their atmospheres out of the gaseous counterpart. Nowadays, we can count on an extraordinary amount of data on exoplanets: the several different observational methods that we observe them with provide us with information on their dynamics, their composition and their suitability to host life. Since the birth of exoplanetary studies, dating back to 1995 with the groundbreaking discovery of the first exoplanet around a main sequence star by Mayor & Queloz (1995), the field has seen an unprecedented growth with now more than 5700 confirmed exoplanets[1]; most of these planets are remarkably different from those in our Solar System, showing a striking variety of masses, densities, radii and eccentricities. These observations even uncovered entirely new classes of planets, that are not present at all around our Sun (like hot Jupiters, super Earths and mini Neptunes). These differences seem to suggest that our planetary system may not be so typical after all; this realisation revolutionised the early planet formation theories, that originally strove to reproduce the architecture of the Solar System.

[1]The exact number of confirmed exoplanets at the time of printing this thesis is 5780. For an up-to-date count, see the NASA Exoplanet Archive: https://exoplanetarchive.ipac.caltech.edu.

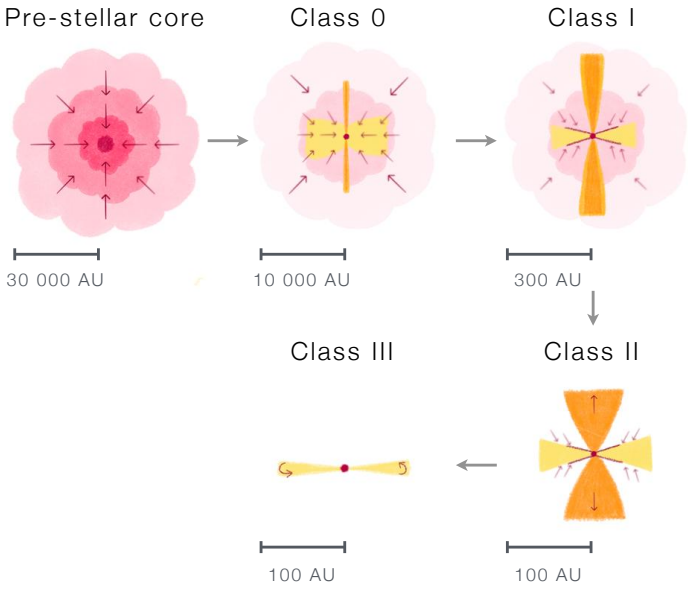

Figure 1.1: Classification of Young Stellar Objects (YSOs) based on the extent of the disc and the surrounding envelope. Adapted from M. Persson.

According to the currently most accredited theories (cfr. Section 1.5.3), the typical timescale of planet formation is of the order of a few Myr (Pollack et al. 1996; see the recent reviews of Johansen & Lambrechts 2017; Ormel 2017; Liu & Ji 2020). This time frame is roughly the same as protoplanetary disc lifetimes (cfr. Section 1.4.2), which deeply links the disc evolution with the formation of planets within them. A key ingredient for planet formation is the nature and availability of the building blocks of planets themselves, often referred to as planetesimals, within the disc. The disc secular and chemical evolution, together with the driving mechanisms and duration of disc dispersal and the interaction with the surrounding environment, all contribute to shape the planet-forming regions; hence, a deep understanding of the physics of protoplanetary discs is an essential step to advance our knowledge of planet formation theories.

This thesis aims at understanding the impact of the accretion mechanism on disc populations, as well as looking for diagnostic criteria to discriminate between the different theoretical scenario. I will particularly focus on the statistics of the global disc properties and the correlations between them and the mass of the central protostar. In the following, I introduce the context in which this work fits - from the formation mechanism of protoplanetary discs (Section 1.2), to the available observational probes (Sections 1.3 and 1.4) and the theoretical models that describe disc evolution (Section 1.5). Finally, in Section 1.6 I discuss the role of this thesis within the field and describe the content of the following Chapters.

1.2 The origin of protoplanetary discs

Protoplanetary discs originate during the star formation process and store the excess angular momentum, which is not dissipated during the collapse phase of the pre-stellar core. The Solar System is a good example to have a grasp of the orders of magnitude involved: if we consider the angular momentum of the Sun $J_\odot$, we can write it as

$$J_\odot = kM_\odot {R_\odot}^2 \Omega, \tag{1.1}$$

where k is a constant of order unity and Ω the angular velocity of the Sun. Since the (equatorial) rotational period of the Sun is ~ 25 days, we obtain $J_\odot \simeq 3 \times 10^{49} k \,\mathrm{cm^2\,g\,s^{-1}}$. On the other hand, the angular momentum of a point mass M_p orbiting the Sun is given by

$$J_p = M_p \sqrt{G M_\odot a_p}, \tag{1.2}$$

where a_p is the orbital major semi-axis; for Jupiter, this gives $J_{\mathrm{Jup}} \simeq 2 \times 10^{50} \,\mathrm{cm^2\,g\,s^{-1}}$. This simple exercise shows that the angular momentum of Jupiter alone is one order of magnitude more than that of the Sun, implying that the majority of the total angular momentum of the Solar System is in the planets rather than the Sun itself. Furthermore, the angular momentum in the Solar System is several orders of magnitude less than in molecular cloud cores: their typical specific angular momentum ranges between 10^{21} and $10^{24} \,\mathrm{cm^2\,s^{-1}}$ (depending on the sizes - see Myers & Benson 1983; Goldsmith & Arquilla 1985; Heyer 1988; Goodman et al. 1993), corresponding to $J_{\mathrm{core}} = 9 \times 10^{53} \,\mathrm{cm^2\,g\,s^{-1}}$ for a core of $1\,\mathrm{M_\odot}$. While it is true that the Sun rotates slower than young stars, the difference in velocity is of two orders of magnitude at most (Herbst et al., 2007), as the maximum speed is regulated by the breakup velocity, and it cannot account for the missing angular momentum. This means that the high angular momentum of the pre-solar young core must have moved somewhere during the collapsing phase, as collapse itself cannot dissipate it: the most accredited hypothesis is that the angular momentum is stored in thin, rotationally supported structures, which are protoplanetary discs. The exact mechanism through which angular momentum is transported within the disc and leads to accretion onto the central protostar is still debated and a very hot topic in protoplanetary disc physics, and the main focus of this thesis.

Besides the theoretical argument supporting their existence, we have been routinely observing protoplanetary discs since decades. The current variety of instruments and tracers allows to probe different properties and evolutionary stages, and is the apex of the effort to characterise discs that started with the simple detection - based on the analysis of the Spectral Energy Distribution (SED). Protoplanetary discs are made of a gaseous and solid component: the former accounts for approximately 99% of the total mass, while

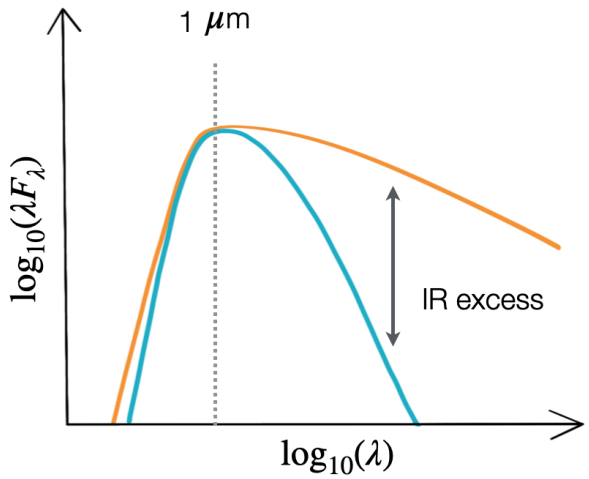

Figure 1.2: Schematic of a protoplanetary disc SED. The light blue line shows the protostellar photosphere, while the orange line represents the total emission including the dust thermal emission. The total disc emission shows an excess both at wavelengths longer (IR) and shorter (UV) than $\sim 1\,\mu$m. Adapted from Armitage (2007).

dust (predominantly silicates grains) makes up the small ($\sim 1\%$) remainder. Despite its almost negligible contribution to the mass, dust plays a crucial role in setting the disc opacity: because it intercepts and absorbs the radiation coming from the central star, dust heats up from ~ 10 K (in the outskirts) to ~ 1000 K (at some fraction of AU from the central star) and consequently has a thermal emission ranging from the near infrared (NIR) to the sub-millimetre. This emission, summed to that of the central protostar, is easily observed in the disc SED: compared to a 'discless' star, the dust component in the disc contributes to the SED at wavelengths from the near infrared on, resulting in an excess emission commonly referred to as IR excess (see Figure 1.2). Furthermore, the surrounding envelope also contributes to the IR excess by reprocessing the radiation coming from the central protostar. This characteristic signature makes an ideal proxy for the presence of a disc/envelope: the classic parameter used to distinguish YSOs in the classes mentioned above is the slope of the SED in the near-mid infrared window ($2.2 - 20\,\mu$m - Lada 1987; Lada & Wilking 1984; Greene et al. 1994),

$$\alpha_{\rm IR} = \frac{{\rm d}\log(\lambda F_\lambda)}{{\rm d}\log(\lambda)}. \tag{1.3}$$

The value of $\alpha_{\rm IR}$ depends on the relative importance of the disc and envelope with respect to the protostar - in particular, it decreases as accretion proceeds and the infalling material gets accreted onto the protostar. Protoplanetary discs, corresponding to Class II YSOs, have $-1.6 < \alpha_{\rm IR} < -0.3$.

Together with the IR excess, Class II objects also exhibit an ultraviolet (UV) excess. This emission is due to the infall in the innermost region of the disc. The accreting material follows the stellar magnetic field lines and travels at almost free-fall velocity; when it impacts the stellar surface, it shocks and heats up - typically to temperatures of $\sim 10^4$ K, which means that the material becomes ionised. Its thermal emission then falls in the UV wavelengths and shows strong recombination lines, the most important of which is the Hα line, a powerful tracer of accretion (see Section 1.3.3).

1.3 Observed disc properties

The observational characterisation of protoplanetary discs has tremendously improved since the early studies aiming at detecting discs from their SEDs. Nowadays, we can count on statistical studies in several star-forming regions (SFRs) that give us insights on the disc lifetimes; we have estimates of disc masses, accretion rates, and radii; we probe winds and measure turbulence. In this Section, I summarise the observational methods employed to determine the disc properties that are relevant for this thesis and discuss their caveats.

1.3.1 Class II objects statistics

Class II YSOs, originally inferred from the IR excess in their SED (as discussed in in Section 1.2), were soon targeted by millimetric observations performed with the first generation of interferometers. Historically, the geometrical configuration of protoplanetary discs was proposed by Beckwith et al. (1990); they observed emission from small particles around pre-main sequence stars, which was not compatible with the assumption of a spherical distribution as the inferred column density would have resulted in a prohibitive optical extinction. The proposed solution was then a thin, disc-like geometry - later confirmed with the first millimetre observations of protoplanetary discs (e.g., Sargent & Beckwith 1987), as well as high resolution optical images of the Hubble Space Telescope (HST) in the Orion Nebula (O'Dell et al., 1993).

Since then, discs have been the focus of an increasing amount of surveys with several different instruments. The very first of these surveys, aiming at detecting the presence of protoplanetary discs in young SFRs, were performed with the Spitzer Space Telescope in the near- and far-IR (Evans et al., 2009; Dunham et al., 2014, 2015); the sensitivity was enough to identify the disc-produced IR excess for targets distant up to ~ 1 kpc, giving a comprehensive and *at the time* complete view of the disc populations in the nearby, mapped SFRs. Since then however, the advent of Gaia (Gaia Collaboration et al., 2016) has unveiled additional members in several of the targeted SFRs, like Lupus (Manara et al., 2018; Galli et al., 2020; Luhman, 2020), Vela (Beccari et al., 2018), Serpens (Herczeg et al., 2019), NGC2264 (Venuti et al., 2019a), χ^1 Fornacis (Galli et al., 2021), Upper Sco (Luhman & Esplin, 2020), Ophiuchus (Esplin & Luhman, 2020) and Corona Australis (Esplin & Luhman, 2022).

The aforementioned surveys detected a large number of discs, opening the floor for statistical studies. The sole SED analysis gives information on the occurrence of discs in a given SFRs and its evolution in time, as well as the impact of the environmental factors; I discuss this more in detail in Section 1.4.2. However, to learn more about the physics of discs themselves and their accretion and dissipation process, the integrated disc properties - such as the disc mass and accretion rate - are needed. Measuring these quantities requires imaging and stellar spectroscopic surveys, in practice performed with the Atacama Large Millimeter Array (ALMA) and X-Shooter (mounted on the Very Large Telescope, VLT) thanks to their high sensitivity and wide spectral coverage, respectively. In the last decade, the advent of these instruments has revolutionised the field, paving the way for direct tests of disc evolution theories and unveiling a plethora of details in the discs morphology otherwise unimaginable.

1.3.2 Disc masses

The mass content is arguably among the key properties of protoplanetary discs, as it informs on the availability of material to both accrete the protostar and form planets. The total amount of material is in principle given by the sum of the gaseous and solid component; however, their abundance ratio - of the order of 100 to 1, as mentioned above - is such that, effectively, the disc mass is roughly given by the gas content. Despite being the most abundant ingredient, measuring the amount of gas in discs is far from being an easy task. As the dust emission is on the contrary significantly easier to observe, it has been common practice to infer the total disc mass from dust observations, assuming the standard 1% dust to gas ratio; nonetheless, dust-inferred disc masses are not free from (sometimes strong) assumptions. In the following, I describe the main methods used to estimate protoplanetary disc masses, and discuss their caveats and limitations together with the current results.

Gas masses

Despite its abundance, detecting the gaseous component of protoplanetary discs is an exceptional observational challenge and constitutes one of the biggest outstanding questions in the field (Miotello et al., 2023). The main species contributing to the gaseous budget of discs is neutral hydrogen, H_2, which has an extremely faint emission at the typical disc gas temperatures (around 20-30 K) because of the details of its molecular physics, in particular the absence of an electric dipole moment (Field et al., 1966). The only region where it could be observable is closer to the central star, where the temperature reaches $T > 100$ K; however, the emission coming from that region is insensitive to the bulk of the disc mass (Thi et al., 2001; Pascucci et al., 2006; Carmona et al., 2008; Bitner et al., 2008; Bary et al., 2008; Pascucci et al., 2013).

For these reasons, the gas content of discs has been historically determined from the emission of brighter (although less abundant) molecular species. A very promising can-

didate is hydrogen deuteride, HD: its chemistry is similar to that of H_2, as it does not freeze-out onto dust grains at low temperature (as instead CO and its isotopologues do), and also shields itself from the photodissociating UV photons (although at a reduced efficiency, see Wolcott-Green et al. 2011); however, its dipole moment allows the emission at 20-30 K to be significantly higher than that of H_2. The fundamental rotational transition of HD is at 112 μm and was covered by the PACS (Photodetector Array Camera and Spectrometer) instrument on the Herschel Space Observatory: three discs have been observed with this facility, namely TW Hya (Bergin et al., 2013), DM Tau, and GM Aur (McClure et al., 2016). Despite the promising results, the end of the Herschel mission and the lack of other operating or planned facilities covering the required wavelength range makes it currently unfeasible to use HD as a gas mass tracer.

Another alternative is carbon monoxide (CO) and its isotopologues. CO is widely employed as the second most abundant molecule (after H_2) and because of its stability and relatively simple interstellar chemistry, as well as detectability at sub-millimetre wavelengths. The main issue in inferring gas masses from CO observations lies in the uncertainty in the C/H ratio in discs: actually, comparing the HD- and CO-determined masses of TW Hya showed that the latter can be up to two orders of magnitude smaller than the first, even including isotope-selective processes and CO freeze-out (Bergin et al., 2013; Favre et al., 2013; Cleeves et al., 2015; Trapman et al., 2017; Calahan et al., 2021). Despite this uncertainty, CO isotopologues are the most widely used gas mass tracers and have been observed in many SFRs such as Chameleon I (Pascucci et al., 2016), Lupus (Ansdell et al., 2016), Orion Nebula Cluster (Eisner et al., 2016), Ophiuchus (Cieza et al., 2019), Taurus (Long et al., 2018), Corona Australis (Cazzoletti et al., 2019), σ-Orionis (Ansdell et al., 2017), λ-Orionis (Ansdell et al., 2020), and Upper Sco (Barenfeld et al., 2016). These surveys have unveiled a fainter-than-expected CO emission; they were however carried out with short integration times. CO observations have also been used to obtain dynamical disc mass constraints: Veronesi et al. (2021) determined the rotation curve of Elias 2-27 and inferred the disc mass comparing it with the theoretical expectation (see also Lodato et al. 2023; Veronesi et al. 2024.

In the last couple of years, Trapman et al. (2022) have proposed a novel approach that combines N_2H^+ and $C^{18}O$ to reduce the uncertainty on the CO-inferred masses. The method was validated against the three discs observed in HD, showing that the $N_2H^+/C^{18}O$ line scales with the disc's CO/H_2 ratio as inferred from thermo-chemical models. The main uncertainty of this novel approach, also employed by Anderson et al. (2022), is the cosmic ionisation rate.

Dust masses

When it comes to the dusty component of protoplanetary discs, two main properties are of great interest: the total amount of solids, which informs on the available material to form planets, and the particle sizes, that determines their aerodynamic behaviour (see Section

1.5.3) - which in turn determines their interaction with each other and with the gaseous component. As mentioned above, the dust grains in protoplanetary discs emit in the IR and sub-millimetre: the millimetric flux is especially easy to observe with interferometers such as ALMA and is known fairly accurately. However, translating the dust millimetric emission into dust content is far from trivial. Assuming an appropriate 'average' (i) disc temperature $\bar{T}_{\rm d}$ and (ii) dust opacity $\bar{\kappa}$, as well as (iii) optically thin emission, the millimetric flux F_ν and the disc dust mass $M_{\rm dust}$ are linked as

$$F_\nu = \frac{B_\nu(\bar{T}_{\rm d})\bar{\kappa}}{d^2} M_{\rm dust}, \tag{1.4}$$

where $B_\nu(\bar{T}_{\rm d})$ is the Planck spectrum at the dust temperature and $\bar{\kappa}$, the opacity, is a pure material property and in principle dependent on the wavelength (hence the average value). This flux-to-mass conversion was originally proposed by Hildebrand (1983) (see also Beckwith et al. 1986, 1990); despite the three strong assumptions required for it to hold, it has been extensively used in the literature since then and still is nowadays. An important caveat to keep in mind is that, while it might seem like a good *relative* measure of mass, it also depends on the temperature, size and grain properties of the disc - which can differ from one source to another. Furthermore, the high-resolution ALMA images of several discs in different SFRs have highlighted ubiquitous optically thick substructures in bright discs (see e.g. Andrews et al. 2018a; Huang et al. 2018; Long et al. 2018): this might imply that a non-negligible fraction of the dust emission is coming from an optically thick region, invalidating the optically thin assumption and leading to an underestimate of the solid content in discs. Finally, the opacity $\bar{\kappa}$ also poses difficulties as it depends on the dust grains composition and growth (see Testi et al. 2014 for a review, Tazzari et al. 2021).

Notwithstanding these caveats, we now have access to inferred dust masses for a vast number of discs in several SFRs, like Taurus (Andrews et al., 2013), Lupus (Ansdell et al., 2016), Upper Sco (Barenfeld et al., 2016), Chameleon I (Pascucci et al., 2016), σ Orionis (Ansdell et al., 2018), ρ-Ophiuchus (Williams et al., 2019; Cieza et al., 2019), Corona Australis (Cazzoletti et al., 2019) and even some Perseus Class 0/I sources (Tychoniec et al., 2018). The dust content in discs appears to be, on average, decreasing with time - as expected from accretion theories (cfr. Section 1.5); however, Testi et al. (2022) have pointed out an apparent increase around 2-3 Myr before the expected decrease, possibly hinting at a replenishment of small grains due to secondary dust production (Turrini et al., 2019; Bernabò et al., 2022).

1.3.3 Accretion rates

The main signature of ongoing accretion of material onto young stars shows in their spectra, as a strong excess continuum in the UV area together with the wealth of strong emission lines at all wavelengths. These lines are mostly hydrogen series lines, such as Balmer

(Hα, Hβ, ...), Paschen (e.g. Paβ) or Brackett (e.g. Brγ), but also helium and calcium lines. They originate in the region where the material effectively accretes the star, which is commonly thought to happen via magnetospheric accretion (Hartmann et al., 2016). In this model, the gaseous, ionised material of the inner disc is channelled by the interaction with the stellar magnetic field to fall onto the protostar; while travelling towards the star, the material gets accelerated and almost reaches free-fall velocity, giving rise to the broad emission lines observed in the protostellar spectrum. When the gas eventually hits the stellar surface, its kinetic energy is dissipated creating a hot spot, responsible for the UV emission. Under this mechanism, the gravitational potential energy released is converted into accretion luminosity $L_{\rm acc}$ as

$$L_{\rm acc} = \frac{GM_\star \dot{M}}{R_\star}\left(1 - \frac{R_\star}{R_m}\right), \tag{1.5}$$

where R_m is the radius at which the disc is truncated by the magnetic field. With the assumption of $R_m = 5R_\star$ (Gullbring et al., 1998), the accretion rate onto the star is given by

$$\dot{M} = \frac{L_{\rm acc} R_\star}{0.8 G M_\star}. \tag{1.6}$$

Together with the stellar mass and radius, the main quantity to measure to know the accretion rate based on Equation (1.6) is the accretion luminosity $L_{\rm acc}$. Accretion luminosities were originally directly measured from the excess Balmer continuum emission and the Balmer jump (Bertout, 1989; Basri & Bertout, 1989; Valenti et al., 1993; Gullbring et al., 1998, 2000) and the veiling of the photospheric emission (Basri & Batalha, 1990; Hartigan et al., 1991, 1995). In these works, the accretion continuum is measured over some wavelength range and then converted into a total accretion luminosity applying a bolometric correction, which can be obtained by (i) shock models (Calvet & Gullbring, 1998; Ingleby et al., 2013), (ii) plane-parallel hydrogen slab models (Bertout, 1989; Basri & Bertout, 1989; Valenti et al., 1993) or (iii) assuming $\sim 10^4$ K black-body emission (Mendigutía et al., 2011).

Measuring the excess UV emission can be difficult, if not impossible, for sources that are heavily extincted - for example because they are embedded in their envelope. This motivated the use of emission lines as secondary accretion rate measurement: in this approach, the luminosity or shape of a given line is converted into an accretion luminosity based on the correlation between the two, inferred from stars where both are measured (Muzerolle et al., 1998; Natta et al., 2004; Mohanty et al., 2005; Dahm, 2008; Herczeg & Hillenbrand, 2008; Alcalá et al., 2017; Manara et al., 2017a). However, this does not solve the problem for very early objects such as Class 0/I: the even higher extinction and veiling of these sources prevents the UV to be observable and forces to rely on the IR emission,

which is the result of the contribution of the disc, the stellar photosphere, the outflows and jets and the envelope - making it complicated to disentangle the several components. There is an ongoing effort trying to characterise the accretion properties of young YSOs, following the pioneering work of Fiorellino et al. (2023).

Recently, the use of broadband, flux-calibrated optical spectra from X-Shooter has allowed to measure simultaneously the accretion continuum flux, the photospheric temperature and flux, extinction, and many emission lines (Rigliaco et al., 2012; Ingleby et al., 2013; Manara et al., 2014; Fairlamb et al., 2015; Alcalá et al., 2017; Rugel et al., 2018; Schneider et al., 2020), significantly reducing the observational uncertainties. However, there are some intrinsic uncertainties that cannot be further reduced, such as the one stemming from the intrinsic variability of accretion (Stauffer et al., 2014) whose magnitude, typically of the order of $\lesssim 0.5$ dex, can reach peaks as high as ~ 1.5 dex (Claes et al., 2022).

1.3.4 Disc radii

Protoplanetary discs are continuous structures, giving the definition of 'radius' a certain degree of arbitrariness. The commonly adopted definition of disc size is the radius enclosing a certain percentage of the disc mass; however, as discussed in Section 1.3.2, the observed property is not the surface density (that would directly link to the mass) but rather the surface brightness, which is linked to the flux instead. Therefore, a more observationally motivated definition of disc size relies on the construction of a cumulative intensity profile (Tripathi et al., 2017),

$$f_\nu(R) = 2\pi \int_0^R I_\nu(R') R' \, dR', \tag{1.7}$$

where we can assign an effective radius $R_{\rm eff}$ that encloses a certain fraction x of the total flux; by definition, $f_\nu(R_{\rm eff}) = xF_\nu$ with $x \in [0, 1]$. The main advantage of this definition is that it does not depend on the chosen surface density profile: any choice that faithfully reproduces the observed emission will lead to the same $R_{\rm eff}$. Furthermore, the value of x is technically arbitrary; common choices usually span in the interval $x \in [0.5, 0.9]$, where $x = 0.5$ would correspond to a 'half-light' radius and $x = 0.68$ to the 'standard deviation' in the approximation of a Gaussian surface brightness profile (used for example by Tripathi et al. 2017 and Andrews et al. 2018b).

Like the case of disc masses, the gaseous and solid component of the disc may have a different spatial distribution and therefore result in different inferred radii (depending on the coupling between the two components - see Section 1.5.3 for details). When dust grains are small and well coupled to the gas, the dust distribution is expected to resemble that of the gas; on the other hand, larger, drifting grains migrate faster towards the central star, resulting in smaller dust radii with respect to the gaseous counterpart. So

far, measurements of both the gas and dust radii are only available for ~ 40 sources in the Lupus SFR (Sanchis et al., 2021) and show a median gas over dust 68% disc radius of 2.5. This result is a factor 2 lower than the theoretical prediction of radial drift (Toci et al., 2021), highlighting the role of (potentially unresolved) substructures.

The dust disc size, measured from the extent of the millimetric thermal continuum emission, has been inferred for discs in Ophiucus (Cox et al., 2017; Cieza et al., 2019), Lupus (Ansdell et al., 2016; Tazzari et al., 2017; Andrews et al., 2018b; Hendler et al., 2020) and Taurus (Long et al., 2019; Kurtovic et al., 2021). However, it is important to keep in mind that the emission of compact dust grains is linked to their opacity, which in turn depends on their size: the opacity is maximum for grains of $\sim 10^{-2}$ cm and shows a steep decrease for smaller sizes. Rosotti et al. (2019b) have shown how an x smaller than 0.95 would trace the 'opacity radius' rather than the flux radius, cautioning the physical interpretation of the results, especially in the context of probing viscous spreading as a proxy for viscous evolution (see Section 1.5.1). On the other hand, as the observations required to infer gas disc radii are more expensive, fewer measurements are available (Barenfeld et al., 2017; Ansdell et al., 2018; Huang et al., 2018; Trapman et al., 2020).

1.3.5 Disc winds

The observed decrease in number of Class II sources across SFRs of different ages (cfr. Section 1.4.2) indicates that discs are eventually dispersed, on timescales of the order of $\sim$ Myr. The most accredited theory prescribes this dispersal to be driven by outflowing gas, launched from the disc surface and opening at wide angles from the disc itself. This characteristic distinguishes what is commonly referred to as 'disc wind' from jets, a common mass ejection mechanism which instead sees collimated, fast ($\geq 100\,\mathrm{km\,s^{-1}}$) outflowing gas (see, e.g., Frank et al. 2014). Jets, together with large scale bipolar outflows, have historically dominated the discussion of mass ejection from young stars; the recent use of new wind diagnostics has opened the floor for the systematic search and detection of disc winds (see Pascucci et al. 2023 for a review). As winds can be originated by several different physical mechanisms, their characteristics and relevant diagnostic may vary depending on their source. The two ejection processes most relevant for this thesis are photoevaporative and magneto-hydrodynamic (MHD) winds.

The main difference between photoevaporative and MHD winds is that the former are purely thermal winds and therefore have no impact on the angular momentum distribution. Photoevaporative winds, arising from the heating of the gaseous component of protoplanetary discs, are thought to gain importance towards the final evolutionary stages and eventually disperse the disc (Alexander et al., 2014). They are expected to launch from approximately the gravitational radius $\sim r_g = GM_\star/c_\mathrm{s}$ (see Section 1.5.3) and to have velocities of the order of $\leq 10\,\mathrm{km\,s^{-1}}$ (Hollenbach et al., 1994; Liffman, 2003; Clarke & Alexander, 2016). MHD winds, on the other hand, can be launched from a range of radii and can have higher initial velocities (Blandford & Payne, 1982; Lesur, 2021).

Observationally probing disc winds is key to characterise their driving mechanism, together with the efficiency of mass loss and angular momentum extraction. The direct detection of winds has so far been limited to a few cases (Ballabio et al., 2020a; Bjerkeli et al., 2016; Tabone et al., 2020; Booth et al., 2021; Valegård et al., 2022), while optical emission lines, like the [NeII] 12.81 μm and [OI] 6300 Å forbidden lines of neon and oxygen (e.g. Alexander 2008; Pascucci et al. 2011; Natta et al. 2014; Simon et al. 2016). These lines show a complex spectral profile, often blueshifted with respect to the stellar velocity, indicating a motion towards the observer; the redshifted emission, corresponding to the receding outflow, is instead obscured by the disc dust (Font et al., 2004; Gorti & Hollenbach, 2008; Pascucci & Sterzik, 2009). The optical lines are often decomposed into one or multiple Gaussian components; high-velocity components (HVCs) $\geq 30\,\mathrm{km\,s^{-1}}$ are associated to fast jets (Nisini et al., 2018), while low-velocity components (LVCs) are instead attributed to slower winds (Hamann, 1994; Hartigan et al., 1995). LVCs can be further decomposed into broad components, with FWHM $\geq 40\,\mathrm{km\,s^{-1}}$, and narrower components (Rigliaco et al., 2013; Simon et al., 2016; Fang et al., 2018; Banzatti et al., 2019). Assuming Keplerian broadening, broad components are believed to trace winds originating in the innermost regions of the disc (within 0.5 au), corresponding to MHD winds (Simon et al., 2016); on the other hand, narrow components stem from outflows at larger radii and are consistent with both MHD (Banzatti et al., 2019) and photoevaporative winds (Ercolano & Owen, 2010; Weber et al., 2020; Ballabio et al., 2020b). The observed line profiles are compared with synthetic observations of theoretical models; Picogna et al. (2019) and Weber et al. (2020) reproduced the narrow component in observed emission lines, modelling the spectral profile and fluxes in an XEUV photoevaporation model (Owen et al., 2010).

1.4 Probing the physics of discs: observational constraints

The observational techniques described in the previous Section have provided invaluable insights on the disc properties. In this Section, I discuss the main constraints that observations have put on the discs physics, both from single sources and from the statistical perspective using entire disc populations.

1.4.1 Constraints from single discs

Measurements of turbulence

The traditional picture of protoplanetary disc accretion prescribes the presence of an effective viscosity, redistributing angular momentum within the disc, that leads to the infall of some material onto the central protostar and carries some other material outwards to conserve the total angular momentum (see Section 1.5.1 for a detailed description). In this scenario, viscosity is the macroscopic manifestation of turbulence: the magneto-rotational instability (MRI, Balbus & Hawley 1991) is the prevalent explanation in most astrophys-

ical contexts, however protoplanetary discs are cold (tens of K) and are therefore weakly ionised, and have weak magnetic fields (Vlemmings et al., 2019; Harrison et al., 2021), making them a hostile environment for MRI to be effective enough to lead to the level of turbulence required to explain accretion.

As I discuss in Section 1.5.1, the popular prescription of Shakura & Sunyaev (1973) parameterises the efficiency of angular momentum transport from turbulence with the α_{SS} parameter. The physical origin of turbulence is still an open question, although several hydrodynamical processes could generate it in addition to the MRI - like the gravitational instability (Kratter & Lodato, 2016) or the vertical shear instability (Nelson et al., 2013) (see Lesur et al. 2023 for a review); in the past few years however several empirical constraints on the value of α_{SS} became available. For a review of the direct and indirect measurements of turbulence in discs, see Rosotti (2023); the main result from the significant efforts to constrain α_{SS} is that most tracers exclude discs to be highly turbulent ($\alpha_{SS} \sim 10^{-2}$), at least in general (although some isolated cases where turbulence is high do exist, like DM Tau and IM Lup, Flaherty et al. 2020, 2024). Furthermore, while the strong evidence of direct measurement is only available for a handful of sources, the population-level constraints only provide upper limits, questioning whether discs are turbulent at all. However, even if accretion was driven by other mechanisms (such as MHD winds, see Section 1.5.2), the efforts towards characterising turbulence in discs would still be meaningful for the many processes that are impacted by it, such as the locations of the water snow lines and the accretion of dust onto planetesimals.

1.4.2 Surveys of entire star-forming regions

The targeted observations of specific sources allow to reach an incredible level of detail, that also ensures the possibility to build models dedicated to reproducing the observed features. A classic example of this process is the Smoothed Particle Hydrodynamics (SPH) simulation of Dipierro et al. (2015), which reproduced the morphology of the dust in HL Tau (ALMA Partnership et al., 2015) in striking detail by including in the simulated disc three embedded planets of masses between 0.2 and 0.55 Jovian masses.

However, such detailed observations come at a cost - in terms of both observing time and possibility of generalisations. The aforementioned observation of HL Tau required 4.5 hours of ALMA Band 6, and the locations and masses of the embedded planets determined from simulations are only applicable to the specific source they were inferred from. The success in explaining the morphology of an object does not necessarily mean that the same physics would work as well for another source, let alone the exact values of the parameters themselves; going back to the HL Tau example, substructures in other discs *might not* be explainable in terms of embedded planets, and even if they were, their properties would likely be different - requiring to apply the same methodology again for every new sources put to test. Furthermore, we can observe structures only in the largest and brightest discs, while the majority of the discs in a SFR are more compact and fainter, which does not

allow to perform such a detailed comparison.

While they may look underwhelming, the more common, small and faint discs hold a great potential to understand the physics of accretion discs - not each of them alone but considered together as a population. The integrated disc properties such as disc mass, accretion rate, and disc radius do not require such extensive observations; moreover, their distribution, correlations and time evolution are signatures of the underlying physics and obtaining them for a large number of sources allows to perform statistical studies to test evolutionary models.

In this Section, I discuss the main constraints obtained from the observation of large samples of discs across several SFRs. When discussing large amount of data, that aim at leading to results of statistical significance, it is important to address the issue of completeness. The surveys of protoplanetary discs are impacted by the fact that a large fraction of the disc-bearing stars are co-located with molecular clouds; this is particularly true for Upper Sco, whose latest discovered members (Luhman, 2020) are however targeted by ongoing ALMA programs. Nonetheless, the degree of completeness for protoplanetary disc populations is usually around $80-90\%$, which is enough to ensure robust derived statistical properties.

The disc and accretion fraction

Accretion theories predict both the disc mass and the accretion rate to be decreasing functions of time (see Section 1.5); it is indeed easy to imagine that discs will eventually disperse and stop accreting once all of their material is used up, either because accreted onto the central protostar or used as planet formation ingredients. The standard proxies of the presence of protoplanetary discs suggest a simple way to probe disc dispersal on the population level: by measuring the occurrence of disc-bearing (showing IR excess due to the thermal dust emission, hinting at the presence of a disc) or accreting (showing UV excess caused by the shocking material accreting the protostar) objects in a given SFR, and comparing them across multiple regions of different ages, we can have an estimate of the duration of the disc dispersal and infer the typical disc lifetimes.

The work of Hernández et al. (2007) on disc fractions highlighted a clear decay in the occurrence of Class II objects across progressively older SFRs, eventually reaching zero at 10-20 Myr (left panel of Figure 1.3). Assuming an exponential decrease with time, the e-folding time is $\sim$ 2-3 Myr at 3-12 μm. Ribas et al. (2014) performed a similar analysis on a larger sample, investigating not only the evolution of the disc fraction with age but also its dependency on the wavelength: they found longer depletion times at longer wavelengths, compatible with inside-out disc clearing (predicted by e.g. internal photoevaporation, see Section 1.5.3). The literature generally agrees on disc lifetimes shorter than $\sim$ 10 Myr (Haisch et al., 2001; Hernández et al., 2007, 2008; Mamajek, 2009; Williams & Cieza, 2011; Murphy et al., 2013; Ribas et al., 2014). The fraction of accreting objects in evolving SFRs is also found to decrease with time (Fedele et al. 2010, right panel of Figure 1.3):

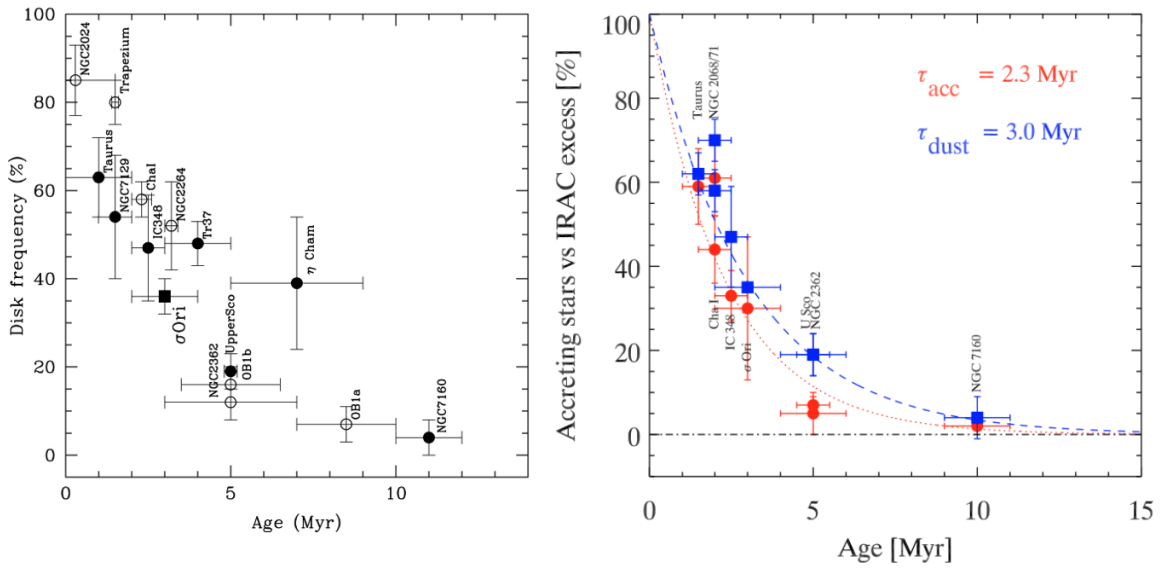

Figure 1.3: Disc and accretion fraction (left and right panel respectively) as a function of age across several star-forming regions. Plots from Hernández et al. (2007) (left) and Fedele et al. (2010) (right).

assuming an exponential decay, the e-folding time is 2.3 Myr. The results on disc and accretion fractions are ubiquitous across several SFRs; any theory looking to explain disc evolution ought to account for disc dispersal on the observed timescales, with the addition of external mechanisms if necessary (see Section 1.5.3).

Correlation between disc and stellar properties

Intuitively, it makes sense to think that the disc properties would depend on those of the central protostar. Several surveys of entire SFRs have focused on measuring disc-integrated properties and looking for correlations between them and the stellar mass; this is the case of the dust-inferred disc mass, the accretion rate, and (marginally) the disc radius.

The disc mass inferred from the sub-mm continuum emission of the dust component $M_{\rm dust}$ shows a power-law correlation with the stellar mass $M_\star$, $M_{\rm dust} \propto {M_\star}^{\lambda_{\rm m}}$ (Ansdell et al., 2016; Barenfeld et al., 2016; Pascucci et al., 2016; Testi et al., 2016; Ansdell et al., 2017; Sanchis et al., 2020; Testi et al., 2022). Comparing the best-fitting parameters of the correlation over SFRs of different ages (Ansdell et al., 2017), one can see the normalisation decreasing in time: this is a consequence of the accretion of dust onto the star, that eventually decreases the total solid mass available - however certain regions appear not to behave the same way, see Cazzoletti et al. 2019; Williams et al. 2019. The slope[2] of the correlation, instead, appears to be increasing with age, implying a steepening of the

[2]Throughout this work, I often use 'slope' as a synonym of 'exponent' for power-law correlations, referring to the expression of the correlations as a line in the logarithmic plane.

correlations for older disc populations.

In a similar way to the dust-inferred disc mass, the accretion rate $\dot{M}$ was also shown to correlate as a power-law with the stellar mass over a number of SFRs, $\dot{M} \propto {M_\star}^{\lambda_{\rm acc}}$ (Muzerolle et al., 2003; Natta et al., 2004; Mohanty et al., 2005; Dullemond et al., 2006; Natta et al., 2006; Herczeg & Hillenbrand, 2008; Rigliaco et al., 2011; Manara et al., 2012; Alcalá et al., 2014, 2017; Kalari et al., 2015; Manara et al., 2016a, 2017b, 2020; Testi et al., 2022). Several authors agree on a roughly constant slope in time, of the order of $\approx 1.8 \pm 0.2$.

The correlation between the disc radius and the stellar mass instead is less well constrained. The extent of the millimetric thermal continuum emission has been measured in the Ophiucus (Cox et al., 2017; Cieza et al., 2019), Lupus (Ansdell et al., 2016; Tazzari et al., 2017; Andrews et al., 2018b; Hendler et al., 2020) and Taurus (Long et al., 2019; Kurtovic et al., 2021) SFRs; Andrews et al. (2018b) found evidence of a correlation between the dust disc radius and the stellar mass with slope ~ 0.6. For what concerns gas radii, less data are currently available due to the difficulties in observing gas emission; the ongoing ALMA Large Programs AGE-PRO and DECO, targeting specifically the molecular lines in a large sample of discs, will provide a statistically significant sample and help shed light on the matter.

The establishment and evolution of the disc properties-stellar mass correlations in different evolutionary scenarios is one of the main focuses of this thesis. In Chapter 3 and 5, I show my results on the impact of the accretion model on the evolution of the correlations and discuss the possibility to use them as a proxy for secular disc evolution.

The numerical side: population synthesis

The large amount of data on disc masses, accretion rates, and radii available thanks to the surveys mentioned above has revived the interest in understanding the fundamental mechanisms underlying disc evolution. The ideal way to test theoretical models is running simulations of entire disc populations through the so-called population synthesis approach, the numerical counterpart to observational surveys; dealing with a synthetic population of objects allows to assess the impact of different evolutionary models and physical mechanisms on discs from a statistical perspective, giving virtually infinite freedom to customise the experiment.

Evolving several objects at once necessarily requires simplified evolutionary models to contain the numerical cost of the simulation. Protoplanetary discs are usually modelled in one dimension, which does not retain information on the vertical structure; however informative, especially for the chemical composition of discs, the vertical dimension is not essential for population synthesis models aiming at reproducing the integrated disc properties. Furthermore, for the scope of this type of studies, a simplified description applied to a large number of objects is more efficient than a detailed modelling limited to a handful of sources.

Because of the relatively recent availability of the large amount of data required to perform proper comparisons (with ALMA starting operations only in the last decade), disc population synthesis is still in its infancy. The pioneering work of Lodato et al. (2017) was the first in the field to explicitly mention 'population synthesis' for protoplanetary disc (some type of disc population synthesis was however employed in exoplanetary science, see below) - although the early photoevaporation studies (e.g. Alexander & Armitage 2009; Owen et al. 2011) effectively employed the same method, despite the fewer available observational diagnostics available at the time. Lodato et al. (2017) explored the evolution of disc populations in the disc mass - accretion rate plane in the viscous framework; since then, synthetic populations have gained increasing popularity and have been used to look for signatures of a variety of physical processes, such as the evolutionary diagnostics in the viscous and external photoevaporation framework (Rosotti et al., 2017), the impact of internal photoevaporation on the disc mass-accretion rate correlation (Somigliana et al., 2020), the impact of MHD wind-driven accretion on disc observables (Tabone et al., 2022b), the interplay between dust evolution and internal photoevaporation (Sellek et al., 2020a), the dust radial drift (Zagaria et al., 2021a,b; Appelgren et al., 2023), the dust sizes in different evolutionary regimes (Zagaria et al., 2022b), the millimetric size-luminosity relation (Zormpas et al., 2022), and the impact of substructures on dust properties (Delussu et al., 2024).

Population synthesis is often employed also in exoplanetary science, since the first work of Ida & Lin (2004). The main goal of such models is to reproduce the observed diversity of exoplanets, assuming it to be the result of different initial conditions - in turn determined by their birthplace, protoplanetary discs, linking discs and planets with a global model of planetary formation. The thousands of detected exoplanets triggered the development of the population synthesis method; both the statistics of planet properties (such as their distances from the host star, mass, and radius) and the correlations with the stellar properties can be compared with the model predictions to test the global consequences of individual physical descriptions (for example orbital migration, Masset & Casoli 2010). Improvements to the original Ida & Lin model included numerically solving the disc evolution equation (Mordasini et al., 2009a,b), considering the disc structure (Fouchet et al., 2012), the solid accretion rate (Fortier et al., 2013), type I migration (Dittkrist et al., 2014), the planet's thermodynamic evolution subsequent to formation (Mordasini et al., 2012), atmospheric escape (Jin et al., 2014) and the concurrent formation of multiple interacting protoplanets (Alibert et al., 2013).

1.5 Protoplanetary disc evolution

The formation, evolution, and dispersal of protoplanetary discs - as much as other accretion discs, such as those around active galactic nuclei and stellar remnants - is directly linked to angular momentum conservation and therefore transport. Despite its fundamental importance, the mechanism through which angular momentum it effectively redistributed within,

or removed from, the disc is still being actively debated. The two main competing transport theories that have been proposed are turbulence and magneto-hydrodynamic (MHD) winds. The former has been traditionally preferred in disc evolution models thanks to the simple parameterisation by Shakura & Sunyaev (1973); however in the recent years disc winds, originally proposed by Blandford & Payne (1982), have regained popularity as a way to transport angular momentum - thanks to both MHD simulations (see e.g. Lesur et al. 2014; Bai 2017) and the analytical work of Tabone et al. (2022a), that provided a simple mathematical treatment quite similar to the 'viscous α' prescription of the turbulent scenario. The last decade has seen an increasing interest in discriminating between accretion models: the question on the driving mechanism of disc evolution is the main focus of this thesis, explored from the theoretical and numerical perspective in Chapter 3, 4, and 5. In this Section, I describe the turbulent and MHD wind-driven accretion from the theoretical point of view and present their predictions for disc evolution.

1.5.1 The viscous model

The traditional picture of accretion in protoplanetary discs invokes the presence of turbulence, acting like a macroscopic viscosity that redistributes angular momentum within the disc (Pringle, 1981). The origin, physical nature, and effective magnitude of turbulence is debated, as I discussed in Section 1.4.1; for now, let us assume that turbulence does exist (for example due to the magneto-rotational instability, MRI, Balbus & Hawley 1991; Balbus 2011). The transfer of angular momentum is kicked off by the presence of a viscous torque, which can be written as

$$g(R) = -2\pi R^3 \nu \Sigma \Omega^{'}, \tag{1.8}$$

where ν is the kinematic viscosity and $\Omega^{'}$ the radial derivative of the Keplerian angular velocity Ω, in a cylindrical coordinates system centred in the protostar. The requirement to have a non-zero torque therefore translates to having a non-ideal fluid (i.e., to have a non-zero viscosity, $\nu \neq 0$) and a radially dependent angular velocity ($\Omega^{'} \neq 0$).

Describing protoplanetary discs as non-ideal fluids, one can derive their geometric configuration and evolution equations from the basic fluid equations, continuity and Navier-Stokes, under three main assumptions:

1. thin disc, $H/R \ll 1$, where H is the vertical extent of the disc. This assumption allows to neglect vertical variations of the disc quantities; typical values of H/R are of the order of ~ 0.1.

2. $M_{\rm d} \ll M_{\star}$, implying that the disc does not contribute to its gravity (no self-gravitating disc). This is usually true for Class II objects and allows to consider Keplerian discs.

3. axisymmetric disc, which allows to neglect dependencies on the azimuthal coordinate.

Projecting the Navier-Stokes equation in the three cylindrical coordinates, and further assuming an isothermal fluid ($P = \rho {c_\mathrm{s}}^2$), one obtains (i) the disc density profile from the vertical direction, (ii) the form of the angular velocity v_ϕ from the radial component, and (iii) the surface density evolution equation from the azimuthal component.

Vertical component: the density profile

The projection of the Navier-Stoker equation in the vertical direction, under the assumptions above, reduces to the balance between the pressure and gravitational potential. This leads to a differential equation that can be solved as

$$\rho = \rho_0 \exp\left(-\frac{z^2}{2H^2}\right), \quad \text{where} \quad H^2 = \frac{{c_\mathrm{s}}^2 R^3}{GM_\star} = \frac{{c_\mathrm{s}}^2}{\Omega^2}; \tag{1.9}$$

the density profile is a Gaussian, centred in ρ_0 with a width H. Furthermore, from the Keplerian definition of Ω follows that the thin disc approximation, $H/R \ll 1$, implies $v_\phi \gg c_\mathrm{s}$ - corresponding to supersonic rotation of the disc.

Radial component: the angular velocity

The radial projection of the Navier-Stokes equation gives the definition of the azimuthal velocity,

$$v_\phi = \sqrt{\frac{\partial \Phi}{\partial R} R}; \tag{1.10}$$

note that this expression is valid for any gravitational potential. If Φ is the Keplerian potential $\Phi = -GM/R$, then $v_\phi = \sqrt{GM/R}$ is the Keplerian velocity (to first order, neglecting pressure gradients), as expected.

Azimuthal component: the surface density evolution

The azimuthal component of the Navier-Stokes equation gives the form of the radial velocity; plugging it into the continuity equation, it yields

$$\frac{\partial \Sigma}{\partial t} = \frac{3}{R}\frac{\partial}{\partial R}\left(R^{1/2}\frac{\partial}{\partial R}(\nu \Sigma R^{1/2})\right). \tag{1.11}$$

Equation (1.11) is a non-linear (as potentially $\nu = \nu(\Sigma)$) diffusion equation (as potentially $\nu = \nu(\Sigma)$) that describes the time evolution of the gas surface density in protoplanetary discs under the influence of the viscosity ν. Depending on the functional form of ν, it may be solved analytically or require a numerical implementation.

The physical meaning of viscosity

The main underlying assumption of the viscous model is viscosity itself: rather than a standard collisional viscosity, which would lead to evolution longer than the age of the universe, it is assumed to have a turbulent origin - which is supported by the high Reynolds number of protoplanetary discs, $\sim 10^{11}$, that means it is prone to become turbulent. Shakura & Sunyaev (1973) parameterised the ignorance on the turbulent processes with the famous α parameter, so that the kinematic viscosity ν reads $\nu = \alpha c_s H$. The exact value of α, together with the fairness of assuming turbulence to be the driver of accretion, is still debated (see Rosotti 2023 for a review). In the paragraph below, I describe the most popular analytic solution to Equation 1.11, which assumes viscosity to be a power-law of radius, by Lynden-Bell & Pringle (1974).

Self-similar solution

Lynden-Bell & Pringle (1974) solved Equation (1.11) under the assumption of a power-law scaling of viscosity with radius, $\nu = \nu_c (R/R_c)^\gamma$, where R_c is a characteristic radius. The self-similar solution reads

$$\Sigma(R,t) = \frac{M_0}{2\pi {R_c}^2}(2-\gamma)\left(\frac{R}{R_c}\right)^{-\gamma} T^{-\eta} \exp\left(-\frac{(R/R_c)^{2-\gamma}}{T}\right), \tag{1.12}$$

where $\eta = (5/2-\gamma)(2-\gamma)$ and T is defined as

$$T = 1 + \frac{t}{t_\nu} \quad \text{and} \quad t_\nu = \frac{{R_c}^2}{3(2-\gamma)^2 \nu_c}; \tag{1.13}$$

t_ν is the timescale after which a viscously evolving disc can be considered evolved.

Figure 1.4 shows the time evolution of the surface density Σ as a function of the radius in a disc undergoing self-similar evolution. The most interesting features of the solution are (i) the decreasing normalisation of the surface density, as the disc mass gets accreted onto the protostar, and (ii) the growing radius. This latter behaviour is a consequence of the conservation of angular momentum within the disc: as part of the material loses angular momentum and drifts inwards, some other portion of material gains angular momentum instead and moves to further radii, increasing the radial extent of the disc.

The two main integrated quantities, the disc mass and accretion rate, can be derived from Equation (1.12). Integrating the surface density, the disc mass reads

$$M(t) = M_0 T^{1-\eta}; \tag{1.14}$$

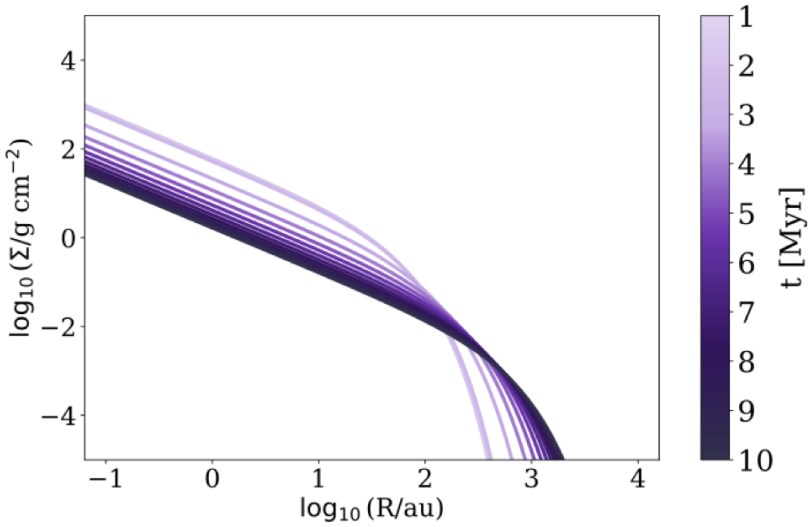

Figure 1.4: Surface density Σ as a function of the radius R at different ages, following the self-similar solution by Lynden-Bell & Pringle (1974) with $\gamma = 1$. The disc is undergoing viscous spreading, expanding with time as expected from the conservation of angular momentum. Plot from Somigliana et al. (2024).

in the standard assumption $\gamma < 2$ (required to find the self-similar solution), $1-\eta$ is larger than 0 and therefore the disc mass decreases with time - in agreement with the prediction of an accreting disc. The accretion rate, defined as the mass that is lost per unit time, is obtained deriving Equation (1.14) and reads

$$\dot{M} = (\eta - 1)\frac{M_0}{t_\nu} T^{-\eta}. \tag{1.15}$$

Like the disc mass, the accretion rate decreases with time, slowing the accretion process down as the disc evolves.

The disc mass - accretion rate plane is of particular interest in protoplanetary discs and has seen a significant attention from the community in the past decade, in particular towards the isochrones in this plane. 'Isochrones' refers to the curves described in a given plane by a population of objects of the same age; in the context of protoplanetary disc, isochrones in the disc mass - accretion rate plane have proven to be an evolutionary proxy. In the viscous framework, for $t \gg t_\nu$ said isochrones read (Lodato et al., 2017)

$$\dot{M} = \frac{M_\mathrm{d}}{2(2-\gamma)t}\left[1 - \left(\frac{M_\mathrm{d}}{M_0}\right)^{2(2-\gamma)}\right] \tag{1.16}$$

and are represented by the black lines in Figure 1.5. The location of a single disc on the

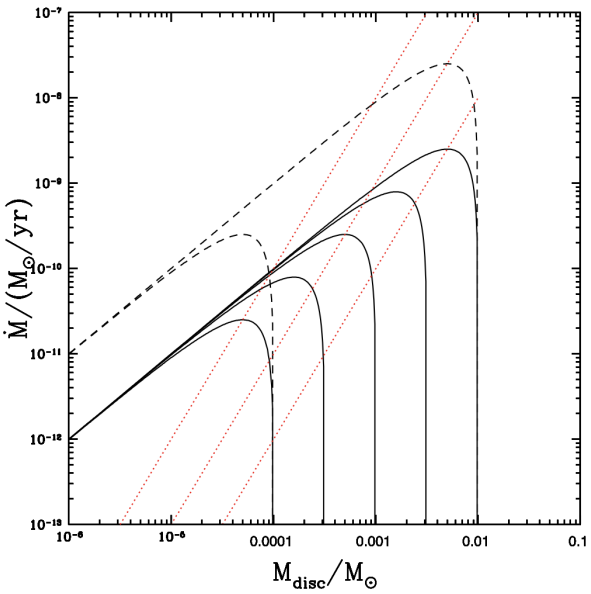

Figure 1.5: Isochrones in the disc mass - accretion rate plane at 0.1 (dashed black lines) and 1 (solid black lines) Myr, for different initial disc masses. The red dashed lines show the evolutionary track of a disc with $M_0 = 10^{-2}\,M_\odot$ and viscous timescale $t_\nu = 10^6$, 10^5 and 10^4 from right to left. Plot from Lodato et al. (2017).

isochrone depends on the relative value of t and t_ν: in particular, it will reach the linear part of the curve when $t \gg t_\nu$, corresponding to when the disc can be considered evolved.

Isochrones are a powerful tool to study disc evolution, as they 'only' require measuring two integrated quantities, mostly available for a large sample of objects (although affected by uncertainties - see Section 1.3.2 and 1.3.3). They should not be confused with the evolutionary tracks, in red in Figure 1.5, which trace the evolution on the plane of a single disc throughout its lifetime instead.

1.5.2 MHD wind-driven accretion

An alternative theory to explain protoplanetary disc accretion prescribes net vertical magnetic fields, anchored in the discs themselves, to launch winds (usually referred to as MHD winds) that carry angular momentum away. This mechanism, originally proposed by Blandford & Payne (1982), *removes* angular momentum from the disc instead of transporting it (as is the case for viscosity); this leads to a fundamental difference in the disc evolution, as there is no wind counterpart to the viscous spreading predicted in the turbulent scenario. MHD winds have been gaining increasing popularity in the past few years, after the challenges posed to the viscous paradigm by the evidence of turbulence levels too low to sustain the observed accretion (at least at large radii, see Pinte et al. 2016; Flaherty et al. 2018).

Parameterizing disc winds

From the mathematical point of view, a wind is locally described by the rate at which it removes mass ($\dot{\Sigma}_w$) and angular momentum. The latter is commonly characterised through the dimensionless parameter (Blandford & Payne, 1982)

$$\lambda = \frac{L}{R\Omega(R)}; \tag{1.17}$$

as L is the specific angular momentum in the wind, λ is the ratio of the extracted to Keplerian specific angular momentum. For a wind to extract angular momentum, λ must be > 1. The conservation of mass and angular momentum yields to the master equation under MHD evolution,

$$\frac{\partial \Sigma}{\partial t} = \frac{2}{R}\frac{\partial}{\partial R}[(\lambda - 1)R^2\dot{\Sigma}_w] - \dot{\Sigma}_w. \tag{1.18}$$

The solution of Equation (1.18) requires a parameterisation for both $\dot{\Sigma}_w$ and λ. While the viscous equation effectively has a traditional standardised approach in the Shakura & Sunyaev (1973) α parameterisation, the wind counterpart is fairly recent; until a couple of years back, there was no common ground despite several different parameterisations, based on the results of MHD simulations, were available (Suzuki et al., 2010; Armitage et al., 2013; Bai, 2016; Chambers, 2019). In this context, Tabone et al. (2022a) have developed a simple approach that significantly popularised the wind paradigm: effectively an equivalent to the α prescription, this parameterisation introduces an $\alpha_{\rm DW}$ which allows to write the mass loss rate $\dot{\Sigma}_w$ as

$$\dot{\Sigma}_w = \frac{3\alpha_{\rm DW}{c_{\rm s}}^2}{4(\lambda - 1)\Omega R^2}\Sigma; \tag{1.19}$$

the normalisation of $\dot{\Sigma}_w$ is such that, for a given surface density, the accretion rate would be the same as in the viscous case. $\alpha_{\rm DW}$ is the efficiency of the wind in removing angular momentum, and it is closely related to the magnetisation of the material in the disc (Lesur, 2021; Lebreuilly et al., 2024). With this approach, the master equation (1.18) reads

$$\frac{\partial \Sigma}{\partial t} = \frac{3}{2R}\frac{\partial}{\partial R}\left(\frac{\alpha_{\rm DW}\Sigma{c_{\rm s}}^2}{\Omega}\right) - \frac{3\alpha_{\rm DW}\Sigma{c_{\rm s}}^2}{4(\lambda - 1)\Omega R^2}. \tag{1.20}$$

The two terms on the right hand side of Equation (1.20) represent wind-driven accretion, which corresponds to an advection term, and wind-driven mass loss respectively. In the

general case where both viscosity and winds contribute to the disc evolution, Equations (1.11) and (1.20) can be combined as

$$\frac{\partial \Sigma}{\partial t} = \frac{3}{R}\frac{\partial}{\partial R}\left[\frac{1}{\Omega R}\frac{\partial}{\partial R}(R^2 \alpha_{\rm SS} \Sigma {c_{\rm s}}^2)\right] + \frac{3}{2R}\frac{\partial}{\partial R}\left(\frac{\alpha_{\rm DW}\Sigma {c_{\rm s}}^2}{\Omega}\right) - \frac{3\alpha_{\rm DW}\Sigma {c_{\rm s}}^2}{4(\lambda-1)\Omega R^2}, \tag{1.21}$$

where the first term on the right hand side is the viscous contribution, and the viscosity ν is expressed with the Shakura & Sunyaev (1973) prescription (from here on, α is labelled $\alpha_{\rm SS}$ to avoid confusion with $\alpha_{\rm DW}$).

Self-similar solutions

The power of the approach of Tabone et al. (2022a) is the ability to write a simple analytical equation, that is readily implemented in numerical integration and also allows for analytical solutions. The availability and shape of the solutions to Equation (1.21) depends on the values and functional form of the accretion parameters $\alpha_{\rm SS}$, $\alpha_{\rm DW}$ and λ; out of the available analytical solutions, we focus on two classes - the so-called hybrid and pure wind solutions, which differ for the time dependence of $\alpha_{\rm DW}$, both proposed by Tabone et al. (2022a).

The general self-similar solution reads

$$\Sigma(R,t) = \Sigma_{\rm c}(t)\left(\frac{R}{R_{\rm c}(t)}\right)^{-1+\xi} e^{-R/R_{\rm c}}, \tag{1.22}$$

where $R_{\rm c}(t)$ is the characteristic disc radius at time t and $\Sigma_{\rm c}(t)$, the surface density at radius $R_{\rm c}$, is a function of time only; moreover, ξ is the mass ejection index,

$$\xi = \frac{1}{4}(\psi+1)\left[\sqrt{1+\frac{4\psi}{(\lambda-1)(\psi+1)^2}}-1\right], \tag{1.23}$$

which quantifies the local mass loss to accretion rate; $\psi = \alpha_{\rm DW}/\alpha_{\rm SS}$ represents the relative strength of winds and viscosity. The shape of $R_{\rm c}(t)$ and $\Sigma_{\rm c}(t)$ differs depending on whether $\alpha_{\rm DW}$ is constant in time (hybrid solution) or not (pure wind solution).

In the first case, when $\alpha_{\rm DW} \neq \alpha_{\rm DW}(t)$, the solution leads to

$$M(t) = M_0\left(1+\frac{t}{(1+\psi)t_{\rm acc,0}}\right)^{-\frac{1}{2}(\psi+2\xi+1)}, \tag{1.24}$$

$$\dot{M} = \frac{\psi + 1 + 2\xi}{\psi + 1} \frac{M_0}{2t_{\rm acc,0}(1 + f_{\rm M,0})} \left(1 + \frac{t}{(1+\psi)t_{\rm acc,0}}\right)^{-\frac{1}{2}(\psi+4\xi+3)} ; \tag{1.25}$$

in Equations (1.24) and (1.25), $t_{\rm acc,0}$ is the MHD equivalent of the viscous timescale t_ν and $f_{\rm M,0} = (R_{\rm c}(0)/R_{in})^\xi - 1$ is the dimensionless mass ejection-to-accretion ratio (with R_{in} initial disc radius). Consequently, one can write the isochrones in the disc mass - accretion rate plane as

$$\dot{M}(t) = \frac{\psi + 1 + 2\xi}{2(1 + f_{\rm M,0})t} M(t) \left[1 - \left(\frac{M(t)}{M_0}\right)^{\frac{2}{\psi+1+2\xi}}\right] \left(\frac{M(t)}{M_0}\right)^{\frac{2\xi}{\psi+1+2\xi}} . \tag{1.26}$$

The pure wind solution, instead, result from the assumption of a varying $\alpha_{\rm DW}$ with time: assuming $\alpha_{\rm DW} \propto \Sigma_{\rm c}(t)^{-\omega}$, one finds

$$M(t) = M_0 \left(1 - \frac{\omega}{2t_{\rm acc,0}} t\right)^{1/\omega} , \tag{1.27}$$

$$\dot{M}(t) = \frac{M_0}{2t_{\rm acc,0}(1 + f_{\rm M,0})} \left(1 - \frac{\omega}{2t_{\rm acc,0}} t\right)^{-1+1/\omega} ; \tag{1.28}$$

the isochrones then read

$$\dot{M}(t) = \frac{1}{\omega(1 + f_{\rm M,0})t} M(t) \left[\left(\frac{M(t)}{M_0}\right)^{-\omega} - 1\right] . \tag{1.29}$$

1.5.3 Additional physics: internal mechanisms

While viscosity and/or MHD winds *drive* accretion in protoplanetary discs, there are several other mechanisms that can impact the accretion processes and the overall secular evolution of discs. Among the main ones are internal and external photoevaporation, infall from an external envelope and planet formation, as well as the dust evolution processes that shape the solid content of the disc. In this paragraph and the following one, I describe these processes separating them in 'internal' and 'external'.

Internal photoevaporation

Internal photoevaporation is the ionisation of the upper, less dense layers of protoplanetary discs due to the radiation emitted from the central protostar. While the bulk of the emission

is made up by optical photons, which are not energetic enough to dissociate the gaseous molecules that constitute the disc, the protostar also emits a non-negligible amount of higher-energy radiation - such as Far Ultra Violet (FUV, $6\,\mathrm{eV} < h\nu < 13.6\,\mathrm{eV}$), Extreme Ultra Violet (EUV, $13.6\,\mathrm{eV} < h\nu < 100\,\mathrm{eV}$) and X-rays ($h\nu > 100\,\mathrm{eV}$), which are capable of dissociating H_2 molecules and hydrogen atoms. This radiation can heat the gas up to $100 - 1000$ K; at these temperatures, much higher than the average 20 K attained at the disc midplane, the gravitational radius

$$R_\mathrm{g} = \frac{GM_\star}{{c_\mathrm{s}}^2}, \tag{1.30}$$

the radius beyond which the thermal energy of the particle exceeds its gravitational energy, can fall within the radial extent of the disc, and the material can therefore become unbound from the star (Shu et al., 1993; Hollenbach et al., 1994; Font et al., 2004; Alexander et al., 2014; Clarke & Alexander, 2016; Sellek et al., 2021). Recent hydrodynamical models including EUV, FUV and X-ray photoevaporation suggest that FUV photons determine the base height from where the winds are launched, while EUV and X-ray photons contribute to their acceleration (Wang & Goodman, 2017; Nakatani et al., 2018; Komaki et al., 2021).

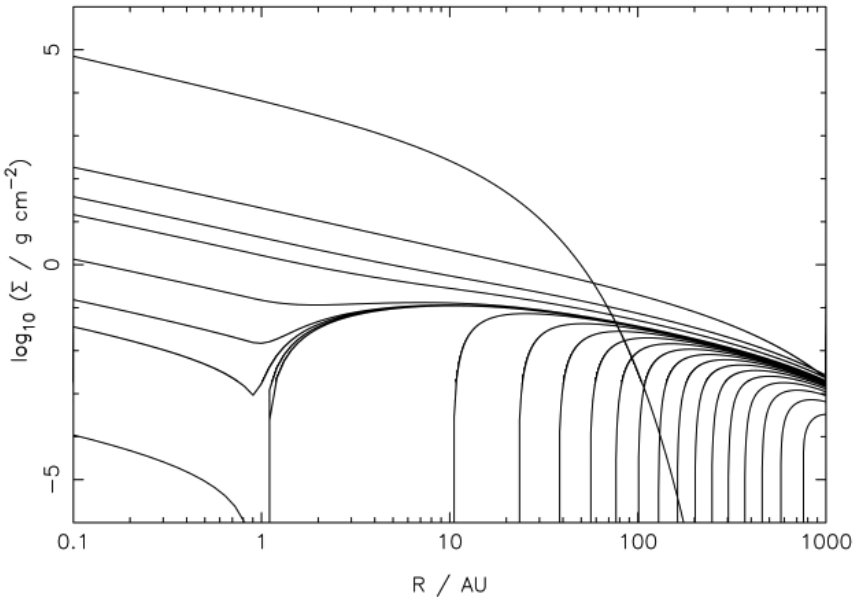

Figure 1.6: Evolution of the gas surface density in a viscous model with internal photoevaporation. Snapshots at $t = 0, 2, 4, 5.9, 6.0, 6.01, 6.02, ..., 6.18$ Myr. From Alexander et al. (2006b).

Qualitatively, photoevaporative models combined with viscous evolution prescribe a two-timescale behaviour. Internal photoevaporation starts to have an impact on the disc once its accretion rate drops below the threshold represented by the photoevaporative

mass loss rate, which typically happens on timescales of $\sim$ Myr. At that point, accretion is rapidly shut down and the mass loss causes the opening of a gap at the gravitational radius (Clarke et al., 2001), dividing the disc in inner and outer disc (see Figure 1.6). The inner disc has a smaller radius, which implies that it also has a shorter viscous timescale, of the order of 10^5 yr. After that time, the inner disc is dispersed and the outer disc is slowly evaporated.

The two-timescale behaviour was proposed by Clarke et al. (2001) to explain the observed frequency of transition to standard discs (Luhman et al., 2010). Furthermore, as it provides a way of removing discs from the inside-out (Ercolano et al., 2011), internal photoevaporation has historically been invoked as a dispersal mechanism in the purely viscous framework, which would otherwise produce virtually eternal, sparse discs (Hartmann et al., 1998). Still, the mass loss rate drops outside the gravitational radius, making the dispersal of the outer disc long enough (of the order of 10 Myr) to be observable: as a consequence, population-level surveys should show several 'relic discs' in the act of dispersing the outer part, which are however not observed (Ercolano et al., 2021).

The secular evolution equation of viscous discs undergoing internal photoevaporation reads

$$\frac{\partial \Sigma}{\partial t} = \frac{3}{R}\frac{\partial}{\partial R}\left(R^{1/2}\frac{\partial}{\partial R}(\nu \Sigma R^{1/2})\right) - \dot{\Sigma}_{\rm photo}; \tag{1.31}$$

the exact form of the mass loss term $\dot{\Sigma}_{\rm photo}$ depends on the specific photoevaporative model considered (see Alexander et al. 2014 for a review).

Dust evolution and planet formation

Over 99% of the total mass budget of protoplanetary disc is in the gaseous form. The remaining 1% of solid material is little with respect to the total, and is often neglected in secular disc evolution models: indeed, the physical and mathematical description of discs presented so far is based on the gas content. Depending on the grain properties, dust can be either coupled to the gas (and therefore follows its dynamics) or undergo specific evolutionary processes, as well as evolving through grain growth and fragmentation. Together with representing the most directly observable component of protoplanetary discs, dust also constitutes the building blocks of planets: ongoing planet formation in turn leaves an imprint on the disc, both in terms of dynamical structures and observational signatures.

Dust grains are mostly characterised by the dimensionless parameter St, the Stokes number, which describes their coupling with the gaseous component. The general definition of St is the timescale on which a dust grain couples with the gas, in units of the local dynamical timescale $t_{dyn} \propto \Omega^{-1}$; hence, a small Stokes number corresponds to a tight coupling, where dust and gas evolve coherently. For the majority of protoplanetary discs,

dust grains are smaller than the mean free path of the gas molecules; in this regime (called the Epstein regime), St can be written as

$$\mathrm{St} \propto \frac{\rho_0 a}{\Sigma} \exp\left(\frac{z^2}{2{H_g}^2}\right), \tag{1.32}$$

where a is the radius of a dust particle, ρ_0 is the volume density of a *single* dust particle, Σ is the local vertically integrated gas density, H_g is the height of the gaseous disc, and z is the vertical coordinate. Equation (1.32) shows that the Stokes number increases, and therefore the coupling decreases, for (i) larger grains ($\mathrm{St} \propto a$), (ii) higher vertical locations in the disc ($\mathrm{St} \propto \exp(z^2)$), (iii) denser dust grains ($\mathrm{St} \propto \rho_0$), and (iv) less dense gaseous component ($\mathrm{St} \propto \Sigma^{-1}$). Moreover, St is a function of the radius through Σ; the coupling with the gas of a same dust grain then depends on its radial location, so that the size of a marginally coupled particle (usually called 'pebble') at 1 au will be of the order of centimetres or larger, while at 100 au sub-millimetre grains are already in this aerodynamical regime.

The degree of coupling between the dust particles and the gas component determines the dust dynamics both in the vertical and azimuthal direction. While grains with small Stokes number simply follow the dynamics of the gas (see Section 1.5.1) and large, decoupled grains behave as a separate fluid, marginally coupled grains tend to vertically settle towards the midplane; the height of the dusty disc H_d can be expressed as

$$H_d = H_g \sqrt{\frac{\alpha}{\alpha + \mathrm{St}}} \tag{1.33}$$

(Dubrulle et al., 1995), where α is the Shakura & Sunyaev (1973) turbulent parameter and H_g is the height of the gaseous disc, so that $H_d < H_g$. Furthermore, pebbles are subject to a drag in the azimuthal direction, generated by the difference in orbital velocity with the gaseous component. In a typical disc, where the gas density and temperature decrease with the radius, the radial pressure gradient is negative and the hence the gas rotates at sub-Keplerian velocity. This causes a headwind to act on the pebbles (which rotate at Keplerian velocity instead), that has the effect of removing angular momentum and causing them to drift inwards.

Radial drift poses a significant challenge for planet formation, which requires the pebbles to grow into planetesimals. If the radial drift timescale is shorter than the growth timescale, dust growth is halted by the so-called radial drift barrier (Adachi et al., 1976; Weidenschilling, 1977; Takeuchi & Lin, 2002; Brauer et al., 2008; Pinte & Laibe, 2014). Alongside radial drift, turbulent collisions can also prevent pebbles from growing - depending on the velocities at which the grains collide with each other, they can either stick together (sticky collisions) or have a disruptive interaction that breaks them apart. The

threshold velocity that corresponds to the turbulent fragmentation limit is however debated, from ~ 1 m/s for silicates (Güttler et al., 2010) to ~ 10 m/s (Gundlach & Blum, 2015) or even $30 - 80$ m/s (Yamamoto et al., 2014) for icy grains. The traditional approach to model dust evolution is that of Birnstiel et al. (2012), which divides the total dust component in two populations with different representative size and takes both the radial drift and turbulent fragmentation limit into account.

While the radial drift problem might be mitigated by the presence of dust traps, pressure (i.e. density) maxima that have the net effect of accumulating gas at the radial location in the disc where they form, the formation of planetesimals via direct growth is unlikely (Pinilla et al., 2012). The currently most accredited theory for planetesimals formation is the collapse of dusty dense filaments promoted by the gravitational (Longarini et al., 2023b,a) or streaming instability (Johansen et al., 2007; Youdin & Johansen, 2007; Carrera et al., 2015; Yang et al., 2017), which in turn can be triggered by the dust back reaction on radial drift. Once planetesimals are formed, the two competing theories for planet formation prescribe the assembly of the planetary core via accretion of either planetesimals themselves or pebbles (see the reviews by Johansen & Lambrechts 2017; Ormel 2017; Liu & Ji 2020). The biggest impact of protoplanets on evolving discs is arguably substructures. High-resolution observations of discs, both with ALMA in the millimetre continuum and VLT in the scattered light, have identified a plethora of features ranging from gaps, to bright rings, to arcs and spirals (see e.g. Andrews et al. 2018a, and Andrews 2020; Benisty et al. 2023 for a review); despite not being the only one, ongoing planet formation is the favoured explanation for the evidence of substructures in Class II discs (Dong et al., 2015; Zhang et al., 2015; Teague et al., 2018; Bae et al., 2023).

1.5.4 Additional physics: environmental effects

The classical picture of star formation described in Section 1.1 assumes axisymmetric, spherical, and isolated accretion from molecular clouds to protoplanetary discs. In general, this is a legitimate assumption when focusing on the intrinsic physics driving disc evolution, the scope of this thesis; however, it is important to point out that (i) accretion at all stages of the star formation process is likely non-axisymmetric, which results in the presence of infalling material through the so-called streamers, and (ii) depending on the nature of the surrounding environment, the resulting protoplanetary discs may be quite far from being isolated, which leads to the phenomenon known as external photoevaporation.

Infall

Contrary to the standard assumption of the star formation model, both simulations (Bate et al., 2003; Smith et al., 2011; Mignon-Risse et al., 2021) and observation (Benson & Myers, 1989; Myers et al., 1991; Bacmann et al., 2000; Stutz et al., 2009; Tobin et al., 2012; Spezzano et al., 2017; Pineda et al., 2019) have suggested pre- and proto-stellar cores to have a non-axisymmetric nature. Ongoing accretion from the surrounding envelope

causes the formation of narrow, elongated shapes outside the YSO that is usually referred to as 'streamer'. Streamers are defined as velocity-coherent structures with an infalling motion that transfers material onto the central object; they are observed as asymmetries in the protostellar envelopes with lengths ranging from 500 au (Garufi et al., 2022) to even 10 000 au (Pineda et al., 2020). They have mostly been detected around Class 0 and I objects (Chou et al., 2016; Valdivia-Mena et al., 2022; Kido et al., 2023; Aso et al., 2023), but more recently also around Class IIs (Ginski et al., 2021; Garufi et al., 2022; Gupta et al., 2023; Harada et al., 2023); they appear as elongated structures in the line intensity profile of several molecules, but also in the dust continuum (see Cacciapuoti et al. 2024).

Infall through streamers can have a significant impact on the accreted sources. It might (i) trigger gravitational instability (Kuffmeier et al., 2018; Speedie et al., 2024), (ii) lead to the formation of spirals and rings in the gaseous component of the disc (Hennebelle et al., 2017; Kuznetsova et al., 2022), (iii) cause accretion outbursts (Bae et al., 2014), (iv) rejuvenate the disc - due to the addition of material coming from outside the original molecular cloud (Kuffmeier et al., 2023), (iv) create warps - if the angular momentum of the infalling material is different than that of the disc (Kuffmeier et al., 2021), (v) significantly contribute to the disc mass budget (Gupta et al., 2023), (vi) affect the disc chemical structure (Garufi et al., 2022).

The origin and frequency of streamers is still a matter of debate. Numerical simulations suggest that they might be generated by turbulence, either within the core itself (Walch et al., 2010; Seifried et al., 2013; Hennebelle et al., 2020) or coming from the outside (Kuffmeier et al., 2017, 2023; Heigl et al., 2024); the new observational programs (Valdivia-Mena et al., 2024) and methods (Gupta et al., 2023) specifically designed to systematically look for streamers will give valuable insights on their characteristics and occurrence.

External photoevaporation

The process of external photoevaporation is fundamentally similar to that of internal photoevaporation. Both mechanisms involve the depletion of the disc through thermal winds, originating by the heating of the gaseous component by photons, but contrary to internal photoevaporation (where the source of radiation is the protostar at the centre of the disc) external photoevaporation is driven by an external OB star. OB stars quickly ionise the disc material due to their high FUV and EUV luminosities; moreover, as their region of influence is in the outskirts of the disc and therefore less gravitationally bound, external photoevaporation results in a very rapid outside-in depletion (Johnstone et al., 1998).

Star formation typically takes place in clusters or associations where OB stars are present (Miller & Scalo, 1979), which makes external photoevaporation - at least in principle - a frequent phenomenon. However, externally photoevaporating discs have not been extensively observed until recently; this is mostly because high-mass SFRs are less numerous, and farther away, than low-mass SFRs and the available surveys have so far prioritised closer regions (see Section 1.4.2). Historically, discs undergoing external photoevaporation

were first detected in Orion with the Hubble Space Telescope (HST) (O'Dell et al., 1993; Johnstone et al., 1998): these sources, also known as 'proplyds', show a characteristic cometary shape with tails pointing away from the ionising source (O'Dell et al., 1993; O'Dell & Wen, 1994; McCaughrean & O'Dell, 1996; Ricci et al., 2008) as the thermal wind depletes the disc. The mass loss rate induced by external photoevaporation is estimated to be between 10^{-6} and $10^{-8}\,M_{\odot}/\,yr$ (for proplyds within 0.3 pc from the OB star θ^1 Ori C in Orion; see Henney & Arthur 1998; Henney & O'Dell 1999; Henney et al. 2002), higher than - or at most comparable to - the typical values of stellar accretion rates (Manara et al., 2012) and mass loss due to internal photoevaporation (Owen et al., 2010).

When discs are exposed to the ionising radiation of an OB star, the evolution of their masses (Mann et al., 2014; Ansdell et al., 2017; van Terwisga & Hacar, 2023), radii (Eisner et al., 2018), and lifetimes (Guarcello et al., 2016; Winter et al., 2018; Concha-Ramírez et al., 2019; Sellek et al., 2020b; Winter et al., 2020) is significantly impacted by external photoevaporation. In the recent years, the community has been striving to better characterise proplyds and develop external photoevaporation theories and numerical implementations. From the observational side, alongside the early HST observations, proplyds have been observed with ALMA (Ballering et al., 2023; van Terwisga & Hacar, 2023) and MUSE (Aru et al., 2024); on the other hand, the development of the FRIEDv2 grid by Haworth et al. (2023) has allowed to run simulations of protoplanetary discs undergoing external photoevaporation (see e.g. Anania et al. in prep, Coleman et al. 2024; Ndugu et al. 2024).

1.6 Structure and role of this thesis

The goal of this thesis is to study protoplanetary disc evolution with a combination of analytical calculations and numerical simulations performed with the population synthesis approach. To this end, I have developed and released the Python code `Diskpop` that I describe in detail in Chapter 2. This work tackles three fundamental questions:

1. **What is the impact of viscous evolution on a set of power-law initial correlations between the disc properties and the stellar mass?** In Chapter 3 I show how the correlations can either steepen, flatten, or remain constant in time depending on the values of the initial parameters. I discuss the evolutionary implications and interpret these results in light of the findings of the surveys of entire star-forming regions;

2. **Can we find a new diagnostic for the accretion models?** In Chapter 4 I propose the width of the disc lifetimes distribution as a proxy for disc evolution. I show how its time evolution is model-dependent and allows to discriminate between the viscous and the wind-driven scenario, and discuss the observational requirements to fully exploit these predictions;

3. **Is the evolution of the disc properties-stellar mass correlations tracing**

the secular disc evolution mechanism? In Chapter 5 I analyse the impact of the accretion model on the time evolution of the disc properties-stellar mass correlations, finding that with the current sample sizes the dominant effect is disc dispersal;

Finally, in Chapter 6 I present the conclusions of this thesis and discuss the next big questions that the protoplanetary disc community is moving towards.

2

Methods: `Diskpop`

As outlined in the Introduction, in this thesis I explore turbulent and wind-driven angular momentum transport in protoplanetary discs with a population synthesis approach. While this method has been gaining increasing interest from the community in the past few years - especially as a consequence of the availability of surveys of entire SFRs probed by ALMA and X-Shooter, cfr. Section 1.4.2 -, until recently there was no freely available, common software to perform this kind of studies.

A significant portion of this thesis has been the development and release (Somigliana et al. 2024, Chapter 5) of the Python population synthesis code `Diskpop`, specifically devised to carry out population synthesis models of protoplanetary discs, evolved either via viscosity or MHD winds. In this Chapter, I describe the features and algorithms of `Diskpop`, from the initial conditions (Section 2.1) to the numerical implementation of the solver (Section 2.4), the treatment of disc dispersal (Section 2.3) and the output and analysis of the results.

2.1 Initial conditions

The first step in any numerical simulation is the choice of initial conditions, and population synthesis simulations are no exception. Alongside with the number of objects in the population, the initial conditions include a distribution of (i) stellar masses, (ii) disc masses, (iii) disc radii, and (iv) accretion rates. These four quantities are however not independent on one another; in particular, the disc radius and the accretion rate are linked via the viscous/accretion timescale (depending on the evolutionary model considered, although the dependence is the same, see Equations 1.13). Therefore, one needs to set three out of four parameters per YSO to generate a synthetic population.

Besides the intrinsic physical relation between the disc radius and the accretion rate, one can also consider additional correlations between the initial parameters. As discussed in Section 1.4.2, surveys of several star-forming regions point in the direction of power-law correlations between the disc parameters and the stellar mass; while the early population synthesis did not implement such correlations for simplicity and rather linearly spanned the parameters space (see e.g. Lodato et al. 2017; Somigliana et al. 2020), the physically motivated choice would be to take the correlations into account. `Diskpop` allows to determine the disc parameters based on the value of the stellar mass, through the workflow described in the following paragraphs.

2.1.1 Stellar masses

`Diskpop` simulations begin by determining a distribution of stellar masses, following a given Initial Mass Function (IMF). The IMF (divided by the total number of extracted points) is a probability density function (PDF): writing it as $\xi(m)\mathrm{d}m$, it represents the probability for a star to have an initial mass in the interval $(m, m+\mathrm{d}m)$. From the numerical point of view, the implementation inverts the corresponding cumulative distribution function, defined as the integral of the PDF, to determine initial stellar masses from random numbers between 0 and 1.

The standard `Diskpop` simulation follows Kroupa (2001), which expresses the IMF as a multiple-part power-law:

$$\xi(m) \propto m^{-\alpha_i}, \qquad \begin{cases} \alpha_0 = 0.3 \pm 0.7, & 0.01 \leq m/\,\mathrm{M}_\odot \leq 0.08 \\ \alpha_1 = 1.3 \pm 0.5, & 0.08 \leq m/\,\mathrm{M}_\odot \leq 0.5 \\ \alpha_2 = 2.3 \pm 0.3, & 0.5 \leq m/\,\mathrm{M}_\odot \leq 1 \\ \alpha_3 = 2.3 \pm 0.7, & 1 \leq m/\,\mathrm{M}_\odot. \end{cases} \tag{2.1}$$

Once the distribution of stellar masses is determined, `Diskpop` proceeds to assemble a YSO for each star. The main parameters needed at this stage are the disc mass and the accretion rate onto the central star (or, equivalently, the disc radius).

2.1.2 Disc masses

As discussed in Section 1.4.2, there is observational evidence of a power-law correlation between the disc mass and the stellar mass. `Diskpop` assumes this correlation to hold as initial condition and determines the mean values of the disc masses as

$$< M_\mathrm{d}(0) >= M_{\mathrm{d},\odot}(0) \left(\frac{M_\star}{\mathrm{M}_\odot}\right)^{\lambda_{\mathrm{m},0}}, \tag{2.2}$$

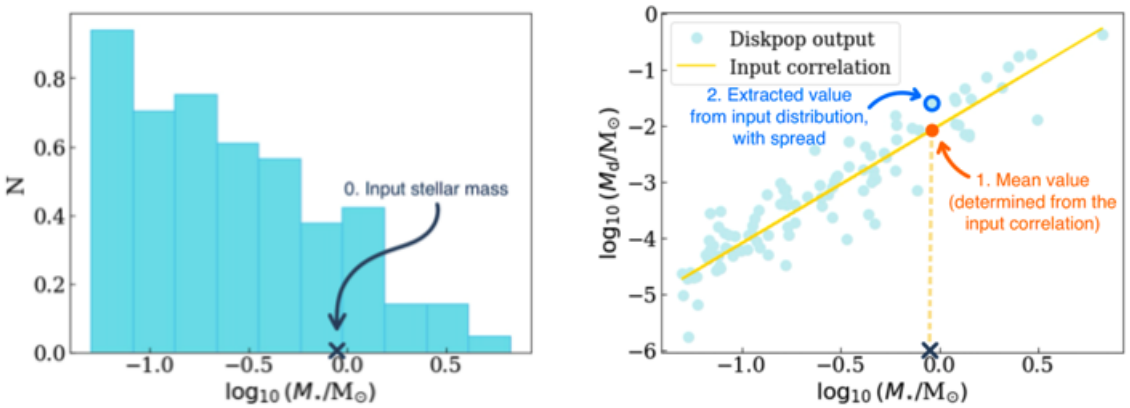

Figure 2.1: Sketch illustrating the workflow to associate a disc mass to a star. The left panel shows the initial stellar mass distribution, while the right panel shows the initial correlation between the disc mass and the stellar mass. Following a specific YSO with $M_\star \sim 1\,\mathrm{M}_\odot$, the sketch shows the derivation of its mean disc mass (using the $M_\mathrm{d} - M_\star$ correlation) to the extraction of the final value. Figure from the Diskpop documentation.

where $M_{\mathrm{d},\odot}(0)$ is the normalisation at one solar mass and $\lambda_{\mathrm{m},0}$ is the *initial* slope of the disc mass - stellar mass correlation; as the correlations can evolve and change their slope during the secular evolution of the discs (see Chapter 3 for a detailed study), the initial slope is not necessarily the one observed at present time. Once the mean value is determined, the actual disc mass is then extracted from a chosen distribution (typically log-normal) with a given spread, both determined by the user. Figure 2.1 shows the steps to determine the disc mass of a YSO from the drawing of its stellar mass.

2.1.3 Accretion rates

Alongside with the disc mass, the accretion rate also shows evidence of a power-law correlation with the stellar mass (see Section 1.4.2); hence, the method to determine the mean initial accretion rates is equivalent as what shown above, using the relation

$$< \dot{M}(0) >= \dot{M}_\odot(0) \left(\frac{M_\star}{\mathrm{M}_\odot} \right)^{\lambda_{\mathrm{acc},0}}, \tag{2.3}$$

where $\lambda_{\mathrm{acc},0}$ is the initial slope of the accretion rate - stellar mass correlation and $\dot{M}_\odot(0)$ is the initial accretion rate for a solar type star, that can be expressed as

$$\dot{M}_\odot(0) = M_{\mathrm{d},\odot}(0) \sqrt{\frac{G\,\mathrm{M}_\odot}{R_{\mathrm{d},\odot}}} \frac{3}{2} \alpha_{\mathrm{SS}} \left(\frac{H}{R}\Big|_{R=R_{\mathrm{d},\odot}} \right)^2; \tag{2.4}$$

Equation (2.4) links the normalisation of the initial accretion rate $\dot{M}_{\odot}(0)$ and radius $R_{\mathrm{d},\odot}$, so that once the disc mass is determined, it is equivalent to either find the radius through the accretion rate or the other way around.

2.1.4 Evolutionary parameters

Once the population of YSOs is assembled, they can be evolved following the general protoplanetary disc evolution equation including the desired physical processes. At this stage, more parameters (described below) come into play. Unless otherwise specified, these are global parameters, whose value is set for the whole population.

- Viscous evolution: α_{SS}, quantifying the turbulence strength; γ, describing the radial dependence of viscosity (see Section 1.5.1);
- MHD wind-driven evolution: α_{DW}, quantifying the wind strength; λ, magnetic lever arm; ω, describing the time dependence of α_{DW} (see Section 1.5.2);
- Internal photoevaporation: $\dot{M}_{\mathrm{wind}}$, photoevaporative mass loss rate, determined from the observed correlation with the stellar mass, with the same methodology as the disc mass and the accretion rate (see Section 1.5.3),

$$< \dot{M}_{\mathrm{wind}}(0) >= \dot{M}_{\mathrm{wind},\odot}(0) \left(\frac{M_{\star}}{\mathrm{M}_{\odot}} \right)^{\lambda_{\phi}}, \tag{2.5}$$

  where $\dot{M}_{\mathrm{wind},\odot}(0)$ is the normalisation at one solar mass and λ_{ϕ} is the slope;
- External photoevaporation: FUV flux experienced by each disc in unit of G_0, out of the available values from the FRIEDv2 grid (Haworth et al. 2023, see Section 1.5.4).

2.2 Numerical evolution

The synthetic population of discs, consisting of N star-disc objects, is then ready to evolve. From the numerical point of view, this means solving the partial differential equations regulating the gas (and dust) dynamics of the disc. The exact form of the disc evolution equation depends on the included physical effects; in the following, I describe the most general case which includes all of the available possibilities.

Combining all of the information in Section 1.5, the general disc evolution equation reads

$$\frac{\partial \Sigma}{\partial t} = \frac{3}{R}\frac{\partial}{\partial R}\left[\frac{1}{\Omega R}\frac{\partial}{\partial R}(R^2 \alpha_{\mathrm{SS}} \Sigma {c_{\mathrm{s}}}^2)\right] + \frac{3}{2R}\frac{\partial}{\partial R}\left(\frac{\alpha_{\mathrm{DW}} \Sigma {c_{\mathrm{s}}}^2}{\Omega}\right) - \frac{3\alpha_{\mathrm{DW}} \Sigma {c_{\mathrm{s}}}^2}{4(\lambda - 1)\Omega R^2} - \dot{\Sigma}_{\mathrm{photoev}}; \tag{2.6}$$

it describes the time evolution of the gas surface density of a disc undergoing (i) viscous accretion, (ii) wind-driven advection, (iii) wind-driven mass loss, (iv) photoevaporative mass loss (due to either internal or external photoevaporation). Equation (2.6) is a non-linear partial differential equation (PDE) of the second order. While it does admit analytical solutions for some specific parameters choices, the most general solution requires its numerical integration.

2.2.1 Solution of partial differential equations

The standard method for the numerical solution of differential equations relies on the discretisation of the variables. Assuming the problem to depend on time t and space x, the discretisation reads

$$\begin{aligned} x &\rightarrow x_i \in \{x_1, ..., x_{N_x}\} \\ t &\rightarrow t_n \in \{t_1, ..., t_{N_t}\}. \end{aligned} \tag{2.7}$$

Equation (2.7) represent the continuous space and time with a set of discrete points, usually referred to as 'grid' or 'mesh'; PDEs are then solved on these grid points. Along with the coordinates, also functions $q(x,t)$ are replaced by their discrete counterparts: the function q, evaluated at the grid point x_i in space and t_n in time, is written as

$$q(x_i, t_n) := q_i^n. \tag{2.8}$$

Note that, in the notation (2.8), n is not a power law index but rather the time index.

To obtain the solution for a differential equation, we need to discretise the derivatives by evaluating them on the grid. The mathematical definition of derivative,

$$\frac{\partial q}{\partial x} = \lim_{\Delta_x \to 0} \frac{q(x + \Delta x) - q(x)}{\Delta x}, \tag{2.9}$$

involves a limit on the timestep Δx that cannot be evaluated numerically, as it would require an infinite amount of grid points. The usual approximation for a derivative is then

$$\left.\frac{\partial q}{\partial x}\right|_{i+1/2} = \frac{q_{i+1} - q_i}{x_{i+1} - x_i} + \mathcal{O}(\Delta x^2), \tag{2.10}$$

which provides an expression evaluated in between the grid points i and $i+1$, referred to

as $i+1/2$[1]. Partial differential equations involve derivatives with respect to more than one variable: for example, considering the general diffusion equation $\partial_t q - D\partial_x^2 q = 0$, we can discretise it as

$$\frac{q_i^{n+1} - q_i^n}{t_{n+1} - t_n} - D\frac{2}{x_{i+1} - x_{i-1}}\left(\frac{q_{i+1}^{n+1/2} - q_i^{n+1/2}}{x_{i+1} - x_i} - \frac{q_i^{n+1/2} - q_{i-1}^{n+1/2}}{x_i - x_{i-1}}\right) = 0. \tag{2.11}$$

The first term of Equation (2.11) is the time derivative of q, evaluated at the ith point on the spacial grid and the $(n+1/2)$th point on the time grid; the second term instead is the second derivative in space, evaluated at the same grid points.

In order to employ the numerical solution algorithms for differential equations to conservation equations, we must make sure to formulate the solution in a numerically flux conserving form. In this approach, instead of only considering grid points, we sample the spacial grid with *cells*: the grid points represent the centres of the cells, while their interfaces are defined as

$$x_{i+1/2} = \frac{1}{2}(x_i + x_{i+1}), \tag{2.12}$$

with $i + 1/2$ denoting a point between the centre of cell i and $i + 1$. A grid of N cells will have $N - 1$ interfaces, plus two boundaries corresponding to the left side of cell x_1 and the right side of cell x_N, defined as $x_{1/2} = (x_2 - x_1)/2$ and $x_{N+1/2} = (x_N - x_{N-1})/2$. Assuming the problem to be a 3D flow of material through a pipe of cross-sectional surface S, the cells will have a volume $V = \Delta x \cdot S$ (assuming constant spacing Δx). The quantity $Q_i^n = q_i^n V$ in the ith cell then can only vary as a consequence of moving it to one of the neighbouring cells (which would cause a decrease) or because something was moved from the neighbouring cells to the ith cell (which would instead imply an increase). Denoting the flux at the cell border $f_{i+1/2}$, we have

$$\frac{\mathcal{Q}_i^{n+1} - \mathcal{Q}_i^n}{\Delta t} = (f_{i-1/2}^{n+1/2} - f_{i+1/2}^{n+1/2}) \cdot S, \tag{2.13}$$

assuming the material to flow from the cell i to $i+1$ (in the other way around, $f_{i-1/2}^{n+1/2}$ and $f_{i+1/2}^{n+1/2}$ would have the opposite sign). Substituting $\mathcal{Q}_i^n = q_i^n V$ and $V = S \cdot \Delta x$, Equation (2.13) becomes

[1]Some algorithms require the derivative to be evaluated specifically at a grid point, which is achieved substituting q_i to q_{i-1}.

$$\frac{q_i^{n+1} - q_i^n}{\Delta t} = \frac{f_{i-1/2}^{n+1/2} - f_{i+1/2}^{n+1/2}}{\Delta x}; \tag{2.14}$$

with a non-constant grid spacing (such as a power law, employed in `Diskpop`) and written in explicit form, Equation (2.14) becomes

$$q_i^{n+1} = q_i^n + \frac{\Delta t}{x_{i+1/2} - x_{i-1/2}}(f_{i-1/2}^{n+1/2} - f_{i+1/2}^{n+1/2}); \tag{2.15}$$

algorithms using this type of flux-conserving schemes are called Finite Volume Methods. The shape of the fluxes $f_{i\pm1/2}^{n+1/2}$ depend on the specific algorithm used.

2.2.2 Donor cell scheme

`Diskpop` implements the flux conserving algorithm, for example to solve the advection equation, following the donor cell scheme. This type of implementation is crucial when the velocity u at which q is flowing on the spatial grid is not constant (note that, if it was, the equation would have an analytic solution). In this case, the flux f is defined as the product of q and the velocity, evaluated at the cell interfaces:

$$f_{i+1/2}^{n+1/2} = \tilde{q}_{i+1/2}^{n+1/2} u_{i+1/2}, \tag{2.16}$$

where $\tilde{q}_{i+1/2}^{n+1/2}$ is some estimate of the average value of q at the interface. In the donor cell scheme, illustrated in Figure 2.2, $\tilde{q}_{i+1/2}^{n+1/2}$ is defined as

$$\tilde{q}_{i+1/2}^{n+1/2} = \begin{cases} q_i^n & \text{for } u_{i+1/2} > 0 \\ q_{i+1}^n & \text{for } u_{i+1/2} < 0; \end{cases} \tag{2.17}$$

the average q at the interface is given by the value at the centre of the previous cell, where the definition of 'previous' is based on the sign of the velocity at the interface. Therefore, the flux at the interface is defined as

$$f_{i+1/2}^{n+1/2} = \begin{cases} u_{i+1/2} q_i^n & \text{for } u_{i+1/2} > 0 \\ u_{i+1/2} q_{i+1}^n & \text{for } u_{i+1/2} < 0. \end{cases} \tag{2.18}$$

At the end of each timestep, q has covered a distance $u_{i+1/2}\Delta t$, where Δt is determined requiring stability of the algorithm (cfr. Section 2.2.4); each cell is then filled with a step function (central panel of Figure 2.2), which is then averaged to find the new value at

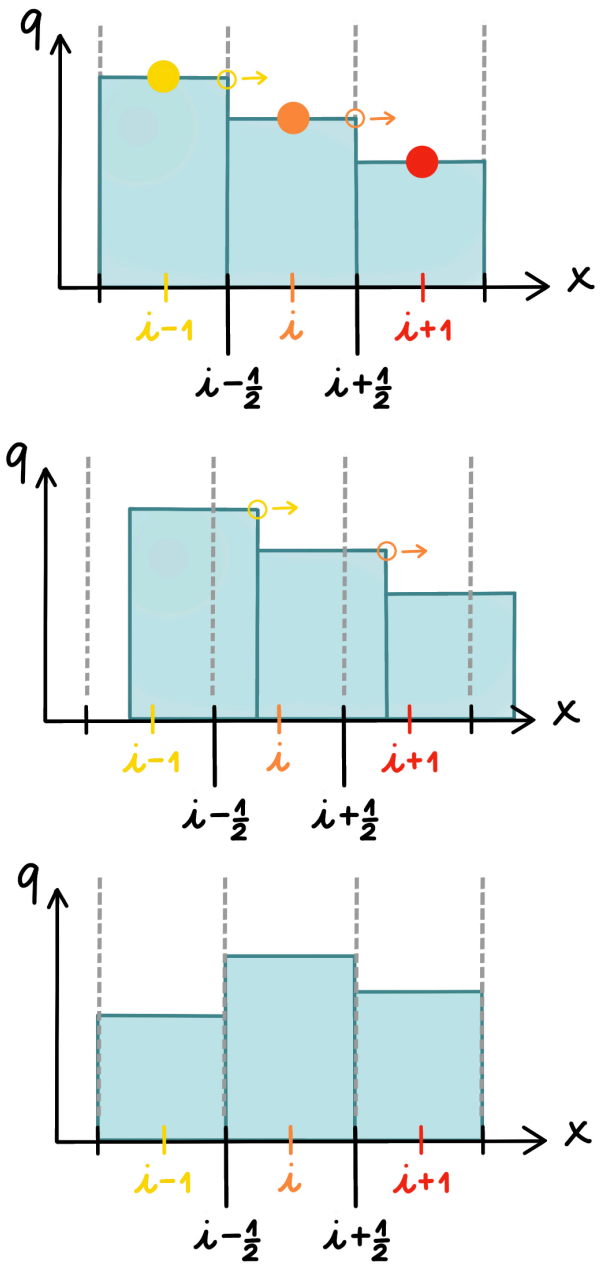

Figure 2.2: Sketch illustrating the donor cell scheme. The full dots represent the values of q^n evaluated in the centre of the cells $i-1$ (yellow), i (orange) and $i+1$ (red), while the empty circles show the locations of the velocities evaluated at $i-1/2$ (yellow) and $i+1/2$ (orange). The top panel shows the nth timestep; the middle panel shows the intermediate state, when the quantity q is flowing from cell i to $i+1$; the bottom panel shows the $(n+1)$th timestep, where advection is completed and the values of q^{n+1} are obtained as the average of each cell.

the $(n+1)$th time step. The donor cell scheme is an application of the upstream/upwind differencing method, which evaluates the derivative at a given point using information coming from the 'upstream' direction of the flow, i.e. opposite to the sign of the velocity.

2.2.3 Operator splitting

`Diskpop` solves the master equation using operator splitting, meaning that each contribution to the master equation is integrated separately and then combined with the others to obtain the full solution. Equation (2.6) constitutes of four components, five further separating the contribution of internal and external photoevaporation $\dot{\Sigma}_{\rm photoev}$, which are solved as follows.

Viscous accretion

The viscous contribution to the master equation,

$$\frac{\partial \Sigma}{\partial t} = \frac{3}{R}\frac{\partial}{\partial R}\left[\frac{1}{\Omega R}\frac{\partial}{\partial R}(R^2 \alpha_{\rm SS} \Sigma {c_{\rm s}}^2)\right], \tag{2.19}$$

has the form of a diffusion equation. The general equation for the diffusion of a quantity q reads $\partial_t q - D\partial_x^2 q = 0$: the time derivative of q is proportional to its second spatial derivative, through the diffusion coefficient D. The diffusive behaviour of Equation (2.19) is more readily noticeable with the change of variables $X = 2R^{1/2}$, $S = 2\Sigma X/3$,

$$\frac{\partial S}{\partial t} = 12\frac{\nu}{X^2}\frac{\partial^2 S}{\partial X^2}; \tag{2.20}$$

the diffusion coefficient is then $D = 12\nu/X$. `Diskpop` solves the viscous contribution with a first-order explicit finite-volume update. We assume a temperature profile $T \propto R^{-1/2}$, $\gamma = 1$, and $H/R = 1/30$ at 1 au. The viscous solver is based on the code published by Booth et al. (2017).

MHD-driven accretion

The second term to the right hand side (RHS) in Equation (2.6),

$$\frac{\partial \Sigma}{\partial t} = \frac{3}{2R}\frac{\partial}{\partial R}\left(\frac{\alpha_{\rm DW}\Sigma {c_{\rm s}}^2}{\Omega}\right), \tag{2.21}$$

is the accretion due to MHD winds, and is effectively an advection term. The general advection equation for a quantity q with velocity v has the form $\partial_t q(x,t) + v\partial_x q(x,t) = 0$;

comparing to Equation (2.21), we see how the advected quantity is $R\Sigma$ and the velocity $v_{\rm DW} = (3\alpha_{\rm DW} H c_{\rm s})/2R$. We solve this equation with an explicit upwind algorithm.

MHD-driven mass loss

The third term to the RHS of Equation (2.6),

$$\frac{\partial \Sigma}{\partial t} = \frac{3\alpha_{\rm DW}\Sigma {c_{\rm s}}^2}{4(\lambda-1)\Omega R^2}, \tag{2.22}$$

is the mass loss induced by disc winds, which is simply integrated in time multiplying by the time step as it does not include any partial derivative.

Internal and external photoevaporation

Finally, the explicit form of the generic $\dot{\Sigma}_{\rm photo}$ term depends on which photoevaporative model is being considered. From the numerical point of view, the impact of both internal and external photoevaporation is a mass loss term, which is integrated multiplying by the time step. `Diskpop` features the implementation of internal photoevaporation following the model of Owen et al. (2012): the prescription depends both on the radius and on the presence of a gap, with a switch in the photoevaporative rate after the gap opening. External photoevaporation instead is based on the FRIEDv2 grid by Haworth et al. (2023), where the mass loss rate is obtained at each radial position with a bi-linear interpolation. The further outside-in depletion of material follows the prescription of Sellek et al. (2020b).

2.2.4 Stability and boundary conditions

`Diskpop` solves the master equation on a radial grid of 10^3 points with power-law spacing and exponent 1/2, extending from 3×10^{-3} au to 10^4 au. The operator split algorithm requires each piece of Equation (2.6) to be solved on the same time step before putting them all together to form the global solution. The time step for each physical process is computed following the Courant-Friedrichs-Lewy (CFL) condition,

$$\Delta t = C \min(\Delta x / v), \tag{2.23}$$

which ensures that within one time step Δt, material moving at velocity v does not flow further than one grid spacing Δx. C, the Courant number, is a positive constant smaller than 1 where $C = 1$ corresponds to the maximum allowed timestep that keeps the algorithm stable. We set zero-gradient boundary conditions, where the value of the 0th and Nth cells are set to those of the 1st and $(N-1)$th cell.

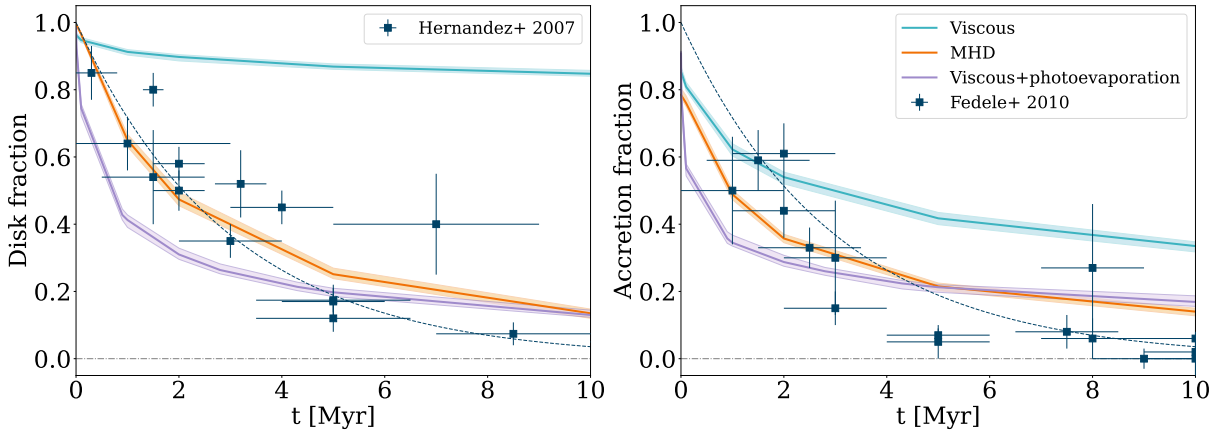

Figure 2.3: Disc and accretion fraction (left and right panel respectively) for a viscous (blue), MHD wind-driven (orange), and viscous+internal photoevaporation (lilac) model compared to the observational data by Hernández et al. (2007) and Fedele et al. (2010). From Somigliana et al. (2024).

2.3 Disc dispersal

The observational evidence of decreasing disc and accretion fraction in time hints at some disc dispersal mechanism happening across disc populations (see Section 1.4.2). From the numerical point of view, there are two reasons that can lead to the disc to be considered dispersed:

1. the disc mass drops below a detectability threshold. This is implemented as a disc mass threshold, that flags YSOs as their mass drops below it;

2. when internal photoevaporation is at play, the photoevaporative gap (see Section 1.5.3) becomes larger than the disc itself.

In both cases, if the condition is met, the disc is marked as dispersed and the YSO moves from Class II to Class III, i.e. the central star only. Figure 2.3 shows the disc and accretion fraction (left and right panel respectively) for a same disc population, evolved with `Diskpop`, following either the viscous (blue), MHD wind-driven (orange), or viscous+internal photoevaporation (lilac) model. The numerical evolution is compared to the observational datasets from Hernández et al. (2007) and Fedele et al. (2010). The disc fraction at all ages is determined by the number of Class II objects over the total YSOs, while the accretion fraction is computed in post-processing as the fraction of *accreting* Class IIs, where 'accreting' is defined as having an accretion rate over a chosen threshold (usually of the order of $10^{-11} - 10^{-12}\,M_\odot/yr$).

2.4 Output and analysis

The output of Diskpop is a .hdf5 file that contains the properties of both star and disc (as long as the disc itself is not dispersed) for every YSO in the population, at every timestep requested by the user. .hdf5, short for Hierarchical Data Format version 5, is a directory-like format that supports heterogeneous and complex data; the storing mechanism is similar to a computer folder, where the directories correspond to 'groups' and the files to 'datasets' in HDF5. HDF5 files are engineered to store large amount of data and are therefore easy to *slice*; moreover, they are a heterogeneous format, meaning that they can contain datasets of different types. Figure 2.4 shows a sketch of the HDF5 format.

Figure 2.4: Sketch of the structure of a .hdf5 file. In the analogy with a computer folder, a 'group' corresponds to a directory and 'datasets' correspond to the files within the directories. 'Metadata' provide details on the object they refer to, such the hierarchical structure of groups, the content of datasets, or the origin of the content.

3

On the time evolution of the $M_{\rm d} - M_\star$ and $\dot{M} - M_\star$ correlations for protoplanetary discs: the viscous timescale increases with stellar mass

Published as
Somigliana et al., 2022, MNRAS, Volume 514, n. 4, pp. 5927-5940

Full authors list:
Alice Somigliana; Claudia Toci; Giovanni Rosotti; Giuseppe Lodato; Marco Tazzari; Carlo F. Manara; Leonardo Testi; Federico Lepri.

Large surveys of star-forming regions have unveiled power-law correlations between the stellar mass and the disc parameters, such as the disc mass $M_{\rm d} \propto {M_\star}^{\lambda_{\rm m}}$ and the accretion rate $\dot{M} \propto {M_\star}^{\lambda_{\rm acc}}$. The observed slopes appear to be increasing with time, but the reason behind the establishment of these correlations and their subsequent evolution is still uncertain. We conduct a theoretical analysis of the impact of viscous evolution on power-law initial conditions for a population of protoplanetary discs. We find that, for evolved populations, viscous evolution enforces the two correlations to have the same slope, $\lambda_{\rm m} = \lambda_{\rm acc}$, and that this limit is uniquely determined by the initial slopes $\lambda_{\rm m,0}$ and $\lambda_{\rm acc,0}$. We recover the increasing trend claimed from the observations when the difference in the initial values, $\delta_0 = \lambda_{\rm m,0} - \lambda_{\rm acc,0}$, is larger than 1/2; moreover, we find that this increasing trend is a consequence of a positive correlation between the viscous timescale and the stellar mass. We also present the results of disc population synthesis numerical simulations, that allow us to introduce a spread and analyse the effect of sampling, which show a good agreement with our analytical predictions. Finally, we perform a preliminary comparison of our numerical results with observational data, which allows us to constrain the parameter space of the initial conditions to $\lambda_{\rm m,0} \in [1.2, 2.1]$, $\lambda_{\rm acc,0} \in [0.7, 1.5]$.

3.1 Introduction

Protoplanetary discs are the cradle of planets. Their evolution and dispersal strongly impact the outcome of planet formation; they especially affect the extent and availability of planetesimals, the building blocks of planets (Morbidelli et al., 2012; Mordasini et al., 2015).

Discs also serve as a mass reservoir for the central accreting protostar. For accretion to take place, material stored in the disc needs to lose most of its angular momentum. The trigger to this process is conventionally identified as a macroscopic viscosity; the pioneering work of Lynden-Bell & Pringle (1974), based on the α prescription of Shakura & Sunyaev (1973), set the ground for numerous following studies treating accretion as a redistribution of angular momentum within the disc. Despite being by far the most widely used, viscosity is not the only accretion theory; several studies have suggested MHD winds as promising candidates to explain protoplanetary disc accretion (Lesur et al., 2014; Bai, 2017; Béthune et al., 2017; Lesur, 2021; Tabone et al., 2022a,b). In this scenario, angular momentum is *removed* instead of being redistributed, leading to significant differences in the evolutionary predictions.

Thanks to the great technological development of the last decades, and in particular to the advent of facilities like the Atacama Large Millimeter Array (ALMA), observational data allow to test evolutionary models. Extended data sets collecting information on a large number of young stellar objects provide the ideal ground to test theoretical predictions; the observational focus is therefore on surveys of entire star-forming regions. A number of such surveys have been already carried out (for example, Barenfeld et al. 2016, Pascucci et al. 2016, Ansdell et al. 2016, Testi et al. 2016, Alcalá et al. 2017, Manara et al. 2017b, Ansdell et al. 2017, Cieza et al. 2019, Williams et al. 2019, Sanchis et al. 2020, Testi et al. 2022, Manara et al. 2020), unveiling interesting features and patterns, such as power-law correlations between the properties of discs and their host stars.

Two crucial steps are required to test evolutionary models: first, performing numerical simulations of the different prescriptions; second, a comparison of these numerical results with data. Identifying key predictions for each model allows to distinguish between different scenarios. The viscous case shows a characteristic behaviour, known as viscous spreading: as part of the disc mass loses angular momentum and drifts inwards, accreting the protostar, another portion of the disc gains the same amount of angular momentum instead, expanding towards larger radii. Therefore, the radial extent of the disc increases with time, despite the ongoing accretion. This prediction does not apply to the MHD winds scenario (Trapman et al., 2020); its removal of angular momentum causes disc radii to decrease as evolution proceeds. Whether the available data in the Lupus star-forming region agree with the viscous spreading predictions has been debated in the literature (Sanchis et al. 2020, Toci et al. 2021, Trapman et al. 2020). Unfortunately, detecting viscous spreading using dust radius as a tracer is non-trivial: Rosotti et al. (2019a) showed that

this method requires significantly deep observations, targeting a fraction as high as 95% of the total flux.

The disc mass - accretion rate correlation provides another diagnostic criterion. In the purely viscous case, where the self-similar solution (Lynden-Bell & Pringle, 1974) holds, such a correlation naturally stems from the analytical prescriptions for $M_{\rm d}$ and $\dot{M}$; in particular, it is expected to have slope of ~ 1 (Hartmann et al., 1998; Mulders et al., 2017; Lodato et al., 2017; Rosotti et al., 2017) and a spread decreasing in time (Lodato et al., 2017), as the age of the population reaches and then outgrows the viscous timescale. The analysis of the first data from Lupus and Chameleon (Manara et al., 2016b) showed a possible agreement with this prediction. However, Tabone et al. (2022b) showed that an MHD disc winds model could be tuned to reproduce the $M_{\rm d} - \dot{M}$ correlation equally well, both in slope and spread - making it more challenging to distinguish between these two models solely using this relation. Moreover, there are some behaviours that cannot be fully explained by any of the two scenarios alone: an example is the Upper Scorpius star-forming region (Manara et al., 2020), where the observational data show a large scatter in the $M_{\rm d} - \dot{M}$ relation (see also Testi et al. 2022). Additional mechanisms have been invoked to explain these inconsistencies, such as internal and external photoevaporation (Rosotti et al., 2017; Sellek et al., 2020b; Somigliana et al., 2020) and dust evolution (Sellek et al., 2020a); however, understanding the right combination of processes to retrieve the observed spread is non-trivial.

These similar behaviours, and the difficulties in observing the key prediction of viscous spreading, may sound discouraging. However, surveys also provide additional information - namely, the correlation between stellar and disc parameters. Many independent works (Muzerolle et al., 2003; Mohanty et al., 2005; Natta et al., 2006; Herczeg & Hillenbrand, 2008; Alcalá et al., 2014; Kalari et al., 2015; Manara et al., 2017b) have found a correlation between the disc accretion rate $\dot{M}$ and the stellar mass $M_\star$, with a slope of $\sim 1.8 \pm 0.2$; on the other hand, the disc mass versus stellar mass correlation appears to steepen with time (Ansdell et al. 2017). Some attempts to explain both the $\dot{M} - M_\star$ correlation (Alexander & Armitage, 2006; Dullemond et al., 2006; Clarke & Pringle, 2006; Ercolano et al., 2014) and the $M_{\rm d} - M_\star$ correlation (Pascucci et al., 2016; Pinilla et al., 2020) have been made; nonetheless, it is sill not clear whether these correlations are determined by the initial conditions, or rather established later on in the disc lifetime as a consequence of the evolutionary processes. Whether the time evolution of these correlations can be understood in the context of viscously evolving disc populations has not been investigated so far.

The numerical counterpart of star-forming regions surveys is population syntheses, i.e., generating and evolving synthetic populations of discs through numerical methods. Performing population syntheses is particularly useful to test evolutionary models, as well as the impact of different physical effects on the diagnostic quantities of interest (such as disc masses and radii). Population syntheses have been carried out already, investigating different aspects of evolution and dispersal of protoplanetary discs (Lodato et al., 2017;

Somigliana et al., 2020; Sellek et al., 2020a,b); however, none of them included both a proper Monte Carlo drawing of the involved parameters and the correlations between disc and stellar properties. The usual assumptions were a fixed stellar mass and a linear span of the parameter space, which make a good first approximation but lack the spread and statistics that really make population syntheses a powerful tool. In this paper, we employ a new and soon to be released Python code, `Diskpop`, which performs a coherent population synthesis of protoplanetary discs and sets the basis for future developments taking into account more and more physical effects acting on discs.

In this work, we aim to study the dependency of disc properties on the stellar mass $M_\star$, discussing its implications from the evolutionary point of view. These observed correlations are most likely linked to both evolution and initial conditions, and our goal is to disentangle between the two. We investigate the case where the correlations are already present as initial conditions. With this first paper we focus on setting up the framework for population syntheses: we limit our case study to purely viscous discs, but the natural progression is to include more evolutionary predictions to compare (and hopefully distinguish) between each other. The structure of the paper is as follows: in Section 3.2 we report and discuss state of the art of the observational evidences on disc masses, accretion rates and radii; in Section 3.3 we present our analytical considerations on the effects of viscous evolution on power-law initial correlations between the disc parameters and the stellar mass; in Section 3.4 we discuss our population synthesis model, including both the implementation in `Diskpop` and the numerical results; we compare out results with observational data and discuss their implications in Section 3.5 and finally, we draw the conclusions of this work in Section 3.6.

3.2 Summary of observational evidence

3.2.1 Disc mass

Numerous surveys of star-forming regions, where disc masses were determined observing the sub-mm continuum emission of the dust component (Ansdell et al., 2016; Barenfeld et al., 2016; Pascucci et al., 2016; Testi et al., 2016; Ansdell et al., 2017; Sanchis et al., 2020; Testi et al., 2022), have highlighted a power-law correlation between the disc mass $M_{\rm dust}$ (of the *dusty* component) and the stellar mass $M_\star$. This relationship can be parameterised as linear in the logarithmic plane,

$$\log_{10}\left(\frac{M_{\rm dust}}{M_\oplus}\right) = \lambda_{\rm m,obs}\log_{10}\left(\frac{M_*}{M_\odot}\right) + q_{\rm obs} + \varepsilon_{\rm obs}, \tag{3.1}$$

with slope $\lambda_{\rm m,obs}$ and intercept $q_{\rm obs}$[1]. $\varepsilon_{\rm obs}$ is a gaussian random variable with mean 0, representing the scatter of the correlation.

[1]Our notation slightly differs from the ones previously used by Pascucci et al. (2016) and Ansdell et al.

The values of the parameters $\lambda_{\rm m,obs}$ and $q_{\rm obs}$ can be determined from observations by fitting the correlation between $M_{\rm dust}$ and $M_\star$. Ansdell et al. (2017) and Testi et al. (2022) (hereafter A17 and T22 respectively) performed this fit for different star-forming regions; the results are shown in Table 3.1 (same as Table 4 in A17 and Table H.1 in T22), where $\Delta_{\rm obs}$ represents the intrinsic dispersion (namely, the standard deviation of the distribution of $\varepsilon_{\rm obs}$).

Region	Age [Myr]	$\lambda_{\rm m,obs}$	$q_{\rm obs}$	$\Delta_{\rm obs}$
Taurus	1-2	1.7 ± 0.2	1.2 ± 0.1	0.7 ± 0.1
Lupus	1-3	1.8 ± 0.4	1.2 ± 0.2	0.9 ± 0.1
Cha I	2-3	1.8 ± 0.3	1.0 ± 0.1	0.8 ± 0.1
σ Orionis	3-5	2.0 ± 0.4	1.0 ± 0.2	0.6 ± 0.1
Upper Sco	5-11	2.4 ± 0.4	0.8 ± 0.2	0.7 ± 0.1

Region	Median age [Myr]	$\lambda_{\rm m,obs}$	$q_{\rm obs}$	$\Delta_{\rm obs}$
Corona	0.6	1.3 ± 0.5	0.4 ± 0.4	1.1 ± 0.7
Taurus	0.9	1.5 ± 0.2	1.1 ± 0.1	0.8 ± 0.3
L1668	1	1.5 ± 0.2	1.0 ± 0.1	0.8 ± 0.3
Lupus	2	1.7 ± 0.3	1.4 ± 0.2	0.7 ± 0.3
Cha I	2.8	1.6 ± 0.3	1.1 ± 0.2	0.7 ± 0.4
Upper Sco	4.3	2.2 ± 0.3	0.8 ± 0.2	0.7 ± 0.3

Table 3.1: Fitted values of $\lambda_{\rm m,obs}$, $q_{\rm obs}$ and $\Delta_{\rm obs}$ (see paragraph 3.2.1 for details) for different star-forming regions as performed by A17 (top table) and T22 (bottom table).

Table 3.1 shows that the mean value of $q_{\rm obs}$ tends to get lower and lower with time. This behaviour, which is more visible in the top panel, is an intrinsic characteristic of the standard viscous scenario: as discs get older, part of their mass is lost due to the ongoing accretion of the central protostar, which eventually depletes the disc. However, it is worth pointing out that some star-forming regions appear not to follow this trend (Cazzoletti et al., 2019; Williams et al., 2019), and the reason behind that is still unclear.

On the other hand, the mean value of $\lambda_{\rm m,obs}$ appears to be increasing with time, implying a steepening of the correlation between the (dust) disc mass and the stellar mass. Investigating the mathematical origin, physical meaning and expected evolution of such a trend is one of the main goals of this paper, and will be addressed from Section 3.3.

(2017): in the first paper the slope (here $\lambda_{\rm m,obs}$) is α and the intercept (here $q_{\rm obs}$) is β, while the second one uses the opposite convention. Moreover, we named the intrinsic dispersion $\Delta_{\rm obs}$ instead of δ to avoid confusion with another parameter that we define later in our paper.

3.2.2 Disc accretion rate

The main signatures of young stars accreting material from their surrounding disc can be found in their spectra. Gas falling onto the stellar surface along the magnetic field lines (Calvet & Gullbring, 1998) causes an excess emission, paticularly visible in the UV area of the spectrum (and especially in the Balmer continuum, see Gullbring et al. 1998). Characteristic emission line profiles are also typical indicators of accretion. Modelling the Balmer continuum excess in the spectra of young stars, and fitting emission line profiles, provide effective ways of measuring accretion rates.

Numerous surveys focusing on different star-forming regions have targeted accretion rates (Muzerolle et al., 2003; Natta et al., 2004; Mohanty et al., 2005; Dullemond et al., 2006; Herczeg & Hillenbrand, 2008; Rigliaco et al., 2011; Manara et al., 2012; Alcalá et al., 2014, 2017; Kalari et al., 2015; Manara et al., 2016a, 2017b, 2020; Testi et al., 2022). Many of them have found a power-law correlation between the accretion rate and the stellar mass, $\dot{M} \propto {M_\star}^{\lambda_{\rm acc,obs}}$. The best fit value of $\lambda_{\rm acc,obs} \approx 1.8 \pm 0.2$ seems to be roughly constant throughout different regions, suggesting that it could be independent on age (unlike the $M_{\rm d} - M_\star$ correlation, see subsection 3.2.1). On the contrary, Manara et al. (2012) (hereafter M12) do see an increasing trend of $\lambda_{\rm acc,obs}$ with the age of the population, a trend similar to the one claimed by A17 with respect to $\lambda_{\rm m,obs}$. There is, however, a significant difference between this latter work and the others mentioned: M12 analysed a sample of ~ 700 stars in the single star-forming region of the Orion Nebula Cluster, determining the isochronal age of each object in the region independently. On the other hand, A17 and T22 considered different star-forming regions and assumed all of the objects in each of them to be coeval - determining therefore the mean age of each sample. The ages of young stellar objects are usually determined by comparing their position on the Hertzsprung-Russell (H-R) diagram with theoretical isochrones (see Soderblom et al. 2014 for a review): however, this method comes with a series of caveats (Preibisch, 2012). In particular, translating a spread in luminosity into a spread in ages is not straightforward due to a number of factors that can impact the shape of the H-R diagram, such as measurement uncertainties and variation of the accretion processes. Determining a mean age for a whole star-forming region absorbs part of this uncertainty, which is the reason why the approach of M12 is less used. Nonetheless, their results intriguingly show a behaviour of $\lambda_{\rm acc,obs}$ similar to that of $\lambda_{\rm m,obs}$, and therefore represent a case study worth considering. In this work, when comparing to observational data (see subsection 3.5.1), we will consider the fits for $\lambda_{\rm acc,obs}$ obtained from M12 as well as T22. Table 3.2 summarises the fitted values from both works.

As discussed for $\lambda_{\rm m,obs}$, there is in principle no theoretical reason for the correlation of the accretion rate with the stellar mass to steepen or flatten in time. However, if we assume the viscous framework to hold, we do expect the accretion rate to be a decreasing function of time; in particular, Hartmann et al. (1998) showed that the viscous evolution implies $\dot{M} \propto t^{-\eta}$, where $\eta \sim 1.5$.

Age [Myr]	$\lambda_{\rm acc,obs}$
0.8	1.15 ± 2.00
1	1.26 ± 2.02
2	1.61 ± 2.06
5	2.08 ± 2.13
8	2.32 ± 2.16
10	2.43 ± 2.18

Region	Age [Myr]	$\lambda_{\rm acc,obs}$
L1668	1.0	1.8 ± 0.5
Lupus	2.0	1.6 ± 0.3
Cha I	2.8	2.3 ± 0.3
Upper Sco	4.3	1.5 ± 0.8

Table 3.2: Fitted values of the $\dot{M} - M_\star$ slope, $\lambda_{\rm acc,obs}$ (see paragraph 3.2.2 for details), by M12 (left table) and T22 (right table)

3.2.3 Disc radius

Evolutionary models predict disc sizes to vary with time. In particular, radial drift is expected to influence the dust discs size (Weidenschilling, 1977): large dust grains drift inwards, eventually disappearing, while small grains are left behind and follow the motion of the gaseous component. In the viscous framework, gas is subject to the so-called viscous spreading: as a consequence of the conservation of angular momentum, the accretion onto the central star leads to a radial expansion of the disc. Once the large grains are removed, discs are expected to be wide and faint (Rosotti et al., 2019b) and may be challenging to observe. These caveats must be taken into account when discussing disc radii, and in practice may severely limit the ability of observing viscous spreading, even when it does take place (Toci et al., 2021).

The radial size of the dust component in discs is measured by analysing the extent of the millimetric thermal continuum emission. In the Ophiucus (Cox et al., 2017; Cieza et al., 2019), Lupus (Ansdell et al., 2016; Tazzari et al., 2017; Andrews et al., 2018b; Hendler et al., 2020) and Taurus (Long et al., 2019; Kurtovic et al., 2021) star-forming regions, this method has been widely employed. Andrews et al. (2018b) found evidence of a correlation between the dust disc radius and the stellar mass, namely $R_{\rm d} \propto {M_\star}^{0.6}$; recent works (Andrews et al., 2018b; Sanchis et al., 2021) have also found a correlation between the disc radius and the disc dust mass, which could be used to derive additional correlations with the stellar mass. However, as measuring radii requires to spatially resolve the discs, the sample of objects with measured $R_{\rm d}$ is smaller than that with measured $M_{\rm d}$; moreover, both those measurements carry significant uncertainties due to optically thick emission. This makes it not convenient to prefer this relation to $R_{\rm d} - M_\star$.

Using gas tracers, such as the rotational line emission of the ^{12}CO molecule, one can also measure the gas disc size ($\rm R_{CO}$). As these observations are very time consuming, less data are available for the gaseous component (Barenfeld et al., 2016; Ansdell et al., 2018; Sanchis et al., 2021). In their work, Ansdell et al. (2018) did not see any correlation between the gas disc size and the stellar masses in Lupus, but their sample is biased towards the highest-masses discs around the highest-masses stars. At the present time, there is no

strong evidence of a correlation between the disc gas size and the stellar mass; however, if a correlation exists, it is probably positive (see Appendix 3.7.1).

3.3 Analytical considerations

In the previous subsection, we have analysed the observational evidence for correlations between the the stellar mass and the three major disc properties - mass, accretion rate, and radius. We have presented the possibility, discussed by previous works, to describe these correlations (with the possible exception of $R_{\rm d} - M_\star$) with power-laws. In this section, we conduct a theoretical analysis of these correlations and their evolution in the purely viscous framework: we aim at determining the initial conditions needed to recover the observational findings.

We start with two assumptions:

1. Self-similar discs: we assume that all discs in the population only evolve under the effect of the viscosity ν. ν can be modelled as a power-law of the disc radius, $\nu = \nu_c \left(\frac{R}{R_c}\right)^\gamma$, where $\nu_c = \nu(R = R_c)$ and R_c is the exponential cutoff radius. The value of ν is prescribed following Shakura & Sunyaev (1973) as $\nu = \alpha c_s H$ (where α is a dimensionless parameter, c_s is the sound speed, H the height of the disc). This implies that the self-similar solution by Lynden-Bell & Pringle (1974) describes the evolution of the gas component in protoplanetary discs,

$$\Sigma(R,t) = \frac{M_{\rm d}(0)}{2\pi {R_c}^2}(2-\gamma)\left(\frac{R}{R_c}\right)^{-\gamma} T^{-\eta} \exp\left(-\frac{(R/R_c)^{2-\gamma}}{T}\right), \tag{3.2}$$

   where $\eta = (5/2-\gamma)/(2-\gamma)$, $T = 1 + t/t_\nu$ and t_ν is the viscous timescale, defined as $t_\nu = {R_c}^2/(3\nu_c)$, on which viscous processes leading to evolution of discs take place.

2. Power-law initial conditions: we assume power-law correlations with the stellar mass as *initial conditions* for $M_{\rm d}$, $\dot{M}$ and R_c. The value of the slopes can vary as evolution takes place, and we will refer to the evolved values as $\lambda_{\rm m}$, $\lambda_{\rm acc}$ and ζ. The initial correlations are set as follows:

$$\begin{cases} M_{\rm d}(0) \propto {M_\star}^{\lambda_{\rm m,0}} \\ \dot{M}(0) \propto {M_\star}^{\lambda_{\rm acc,0}} \\ R_c(0) \propto {M_\star}^{\zeta_0}. \end{cases} \tag{3.3}$$

The self-similar solution provides analytical expressions for both the disc mass and accretion rate:

$$M_{\rm d}(t) = M_{\rm d,0}\left(1 + \frac{t}{t_\nu}\right)^{1-\eta}, \tag{3.4}$$

$$\dot{M}(t) = (\eta - 1)\frac{M_{\rm d,0}}{t_\nu}\left(1 + \frac{t}{t_\nu}\right)^{-\eta}. \tag{3.5}$$

Note that, as the ratio $M_{\rm d}/\dot{M}$ has the dimension of a time, by choosing the initial $M_{\rm d}$ and $\dot{M}$ we completely specify their time evolution. Depending on the age of the disc with respect to its viscous timescale, set by the radius of the disc itself, discs can be considered young ($t \ll t_\nu$) or evolved ($t \gg t_\nu$). In these two limits, it is possible to simplify equations (3.4) and (3.5). We divide the following discussion based on these two evolutionary scenarios, as they lead to different results and theoretical expectations (subsections 3.3.1 and 3.3.2).

Equations (3.4) and (3.5) make clear that the time evolution of the slopes depends on how t_ν scales with stellar mass. Because at $t = 0$ the initial accretion rate can be written as $\dot{M}_0 \propto M_{\rm d,0}/t_\nu$, a scaling of t_ν is already implicitly assumed given a choice of $\lambda_{\rm m,0}$ and $\lambda_{\rm acc,0}$. We can see from the definition of the viscous timescale that the dependence on stellar mass is contained in any of the three parameters α, c_s, or H. In this paper, we assume α to be a constant across all stellar masses; moreover, we also consider it as constant in radius and time, and fix its value to 10^{-3}. However, note that the assumption that α does not depend on stellar mass does not affect our general results on the evolution of the slopes (see the end of subsection 3.3.2), since this depends only on the scaling of viscous timescale with stellar mass. On the other hand, this assumption does affect how aspect ratio H/R and disc radius scale with stellar mass. Regarding the aspect ratio, this quantity can be defined as

$$\frac{H}{R} = \frac{c_s}{v_k},$$

where v_k is the keplerian velocity. Assuming a radial temperature profile $T \propto R^{-1/2}$, then $c_s \propto R^{-1/4}$ so that H/R will scale as $R^{1/4}$. Note that this implies $\gamma = 1$, which will be the case from now on. We can parameterise the dependency on $M_\star$ as a power-law with exponent β:

$$\frac{H}{R} = \frac{H}{R}\Big|_{R=R_0}\left(\frac{R}{R_0}\right)^{1/4}\left(\frac{M_\star}{M_\odot}\right)^{\beta}. \tag{3.6}$$

In this work, we have considered three possible values for β which correspond to different physical situations:

- H/R does not depend on the stellar mass, which implies $\beta = 0$;
- c_s does not depend on the stellar mass, implying $\beta = -1/2$;
- $T \propto {M_\star}^{0.15}$ (derived by radiative transfer models - see Sinclair et al. 2020), which implies $\beta = -0.425$. Physically, this means that, while radiative transfer predicts that discs around lower mass stars should be colder due to their lower luminosity, this is a sub-dominant effect in setting the scale-height: the weaker gravity of these stars drives most of the change in scale-height.

Of these three possibilities, the third one is the more realistic; nonetheless, the resulting value of β is very close to $-1/2$ - meaning that we can approximate it to the second case, which makes mathematical calculations more straightforward. On the other hand, despite not being realistic, the first scenario is usually assumed for the sake of simplicity; for this reason, we decided to include it in this work. In conclusion, we considered β to be either equal to 0 or 1/2.

3.3.1 Young populations: $t \ll t_\nu$

If the age of the population is much smaller than its viscous timescale, no evolution has taken place yet. This means that we are still observing the initial condition, and that the parameters λ_m, λ_acc and ζ coincide with $\lambda_{\mathrm{m},0}$, $\lambda_{\mathrm{acc},0}$ and ζ_0. However, in the viscous scenario these parameters are always linked to one another; for young discs, Equation (3.5) can be written as $\dot{M}(0) \approx M_\mathrm{d}(0)/t_\nu$. In our notation, M_d represents the *total* disc mass, which is given by 99% gas mass and 1% dust mass; since the observed power-law correlation (Equation 3.1) refers to the *dust* mass, we need to translate M_dust to M_d dividing by the dust-to-gas ratio ε, which is assumed to be constant in time and $M_\star$. The initial, theoretical disc mass can therefore be written as

$$M_\mathrm{d}(0) = K_1 \left(\frac{M_\star}{M_\odot}\right)^{\lambda_{\mathrm{m},0}}, \tag{3.7}$$

where the normalisation constant K_1 is given by $10^q M_\oplus/\varepsilon$. Taking into account the dependence of the aspect ratio of the disc H/R on the stellar mass through Equation (3.6), and using a generic value for β, we can write the initial accretion rate in the self-similar scenario as

$$\dot{M}(0) = K_2 \left(\frac{M_\star}{M_\odot}\right)^{\lambda_{\mathrm{m},0}+2\beta+1/2-\zeta_0}, \tag{3.8}$$

defining the normalisation constant K_2 as

$$K_2 = \frac{10^q M_\oplus}{\varepsilon}\sqrt{\frac{GM_\odot}{R_{c,\odot}}}\frac{3}{2}\alpha\left(\frac{H}{R}\Big|_{R=R_{c,\odot}}\right)^2, \tag{3.9}$$

where $R_{c,\odot}$ is the value of the cut-off radius R_c for a solar-type star. The only free parameter in Equation (3.8) is the stellar mass $M_\star$: all of the other parameters ($\lambda_{\rm m,0}$, ζ_0, $R_{c,\odot}$, β) can be determined by comparing this expression to the observational data. In particular, since $\dot{M} \propto {M_\star}^{\lambda_{\rm acc,0}}$, assuming that we can determine the values of $\lambda_{\rm m,0}$ and $\lambda_{\rm acc,0}$ from observations and that α is known we could constrain the value of ζ_0,

$$\zeta_0 \equiv \lambda_{\rm m,0} + 2\beta + \frac{1}{2} - \lambda_{\rm acc,0}. \tag{3.10}$$

On the other hand, $R_{c,\odot}$ can be set imposing the normalisation constant K_2 to equal the typical value for the accretion rate of a solar-type star. Based on the observation of Manara et al. (2017b), $\log_{10}(\dot{M}/M_\odot {\rm yr}^{-1}) = -8.44$, which leads to $R_{c,\odot} = 1.6 \times 10^{14}$ cm ≈ 10 au (assuming $\alpha = 10^{-3}$, as stated above). This is a reasonable initial disc radius; various recent papers have also assumed radii of the same order of magnitude (Rosotti et al., 2019a,b; Trapman et al., 2019; Toci et al., 2021).

3.3.2 Evolved populations: $t \gg t_\nu$

If the age of the population is larger than its viscous timescale, discs can be considered evolved. In principle, at this stage the initial conditions are not observed anymore - meaning that we expect to see an evolution of both the slopes and spreads of the correlations. In particular, if $t \gg t_\nu$, the self-similar accretion rate reduces to

$$\dot{M}(t) = \frac{1}{2}\frac{M_{\rm d}(t)}{t}; \tag{3.11}$$

as t does not depend on the stellar mass, we can see that Equation (3.11) implies that the dependency on $M_\star$ in evolved discs is the same for $\dot{M}$ and $M_{\rm d}$. Moreover, the distributions of the two quantities $M_{\rm d}$ and $\dot{M}$ are expected to resemble each other more and more as evolution takes place and the condition given in Equation (3.11) is reached: this means that, eventually, we expect both the slope and the spread of the two correlations to reach the same value.

Slopes

As we did in the young populations scenario, expressing $M_{\rm d}(t)$ through the first assumption in Equation (3.3) and using the definition of t_ν leads to

$$M_{\rm d}(t) = K_3 \left(\frac{M_\star}{M_\odot}\right)^{\lambda_{\rm m,0}+\zeta_0/2-\beta-1/4} t^{-1/2}, \tag{3.12}$$

where K_3 is a normalisation constant that does not depend on the stellar mass or the age, defined by

$$K_3 = M_{\rm d,\odot} \left(\frac{{R_{c,\odot}}^3}{GM_\odot}\right)^{1/4} \frac{1}{\sqrt{3\alpha}} \left(\frac{H}{R}\Big|_{R=R_{c,\odot}}\right)^{-1};$$

$M_{\rm d,\odot}$ represents the initial disc mass for a solar-type star. Denoting the evolved slopes, at $t \gg t_\nu$, as $\lambda_{\rm m}$ and $\lambda_{\rm acc}$, this implies that

$$\lambda_{\rm m} \equiv \lambda_{\rm acc} = \lambda_{\rm m,0} + \frac{\zeta_0}{2} - \beta - \frac{1}{4}. \tag{3.13}$$

There are two ways in which Equation (3.13) can be satisfied:

- $\lambda_{\rm m,0} = \lambda_{\rm acc,0}$: if the two slopes start from the same value, they do not evolve with time;
- $\lambda_{\rm m,0} \neq \lambda_{\rm acc,0}$: if the initial values of the two slopes are different, an evolution of their values must take place due to accretion processes.

In the first scenario, as we do not expect any evolution with time of the two slopes, we can use the initial condition (see Equation 3.10) to determine the value of ζ_0, finding $\zeta_0 = 2\beta + 1/2$. As expected, substituting this value of ζ_0 in Equation (3.13) leads to $\lambda_{\rm m} = \lambda_{\rm acc} = \lambda_{\rm m,0}$. This implies that observing the same slope for the two correlations $M_{\rm d} - M_\star$ and $\dot{M} - M_\star$ is not enough to claim anything on the age of the population. It could either be evolved, in which case we are observing a direct consequence of viscous evolution, or it could be young, and we would be observing the initial condition. This endorses what we suggested earlier, that observed correlations can be due either to the initial conditions or the evolution - or, most likely, a combination of the two. It would be possible to disentangle between the two possibilities if additional information was provided, for example

- observations at earlier ages (to try and see a change in the slopes with time);
- measurements of disc radii R_c, which is in principle observable (although with some caveats - see Toci et al. 2021) to determine the viscous timescale and give an estimate of the evolutionary stage of the population. Note that there is a degeneracy in the determination of the viscous timescale, as it depends on α, R_c and $H/R\big|_{R=R_c}$;

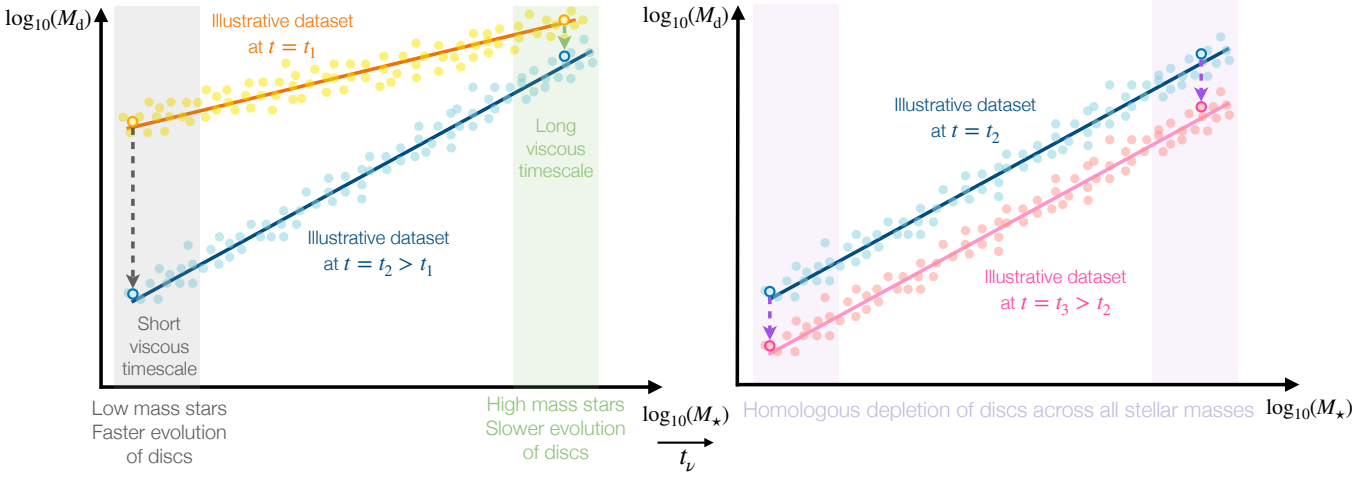

Figure 3.1: Illustrative sketch to show how steepening slopes are a consequence of a positive correlation between viscous timescales and stellar masses. The dots represent artificial datasets with their linear fits displayed as solid lines. The left panel shows an early evolutionary stage, where $t_\nu \propto {M_\star}^{\delta_0}$ with $\delta_0 > 0$: as discs around more massive stars have a longer viscous timescale, in the time interval $\Delta_t = t_2 - t_1$ their mass is less depleted than that of discs around less massive stars, which in turn have a short viscous timescale. This implies that, after Δ_t, the correlation between $M_{\rm d}$ and $M_\star$ is steeper. On the other hand, the right panel represents a later evolutionary stage, where δ has reached the limit value of 0. In that case, the viscous timescale does not depend on the stellar mass anymore and this implies a homologous depletion of discs around stars of all masses. The same argument applies for $\dot{M}$.

- the $\dot{M} - M_{\rm d}$ correlation: a large spread implies that the population cannot be considered evolved yet (Lodato et al., 2017).

The other possibility is that the two initial values of the slopes are different. If that is the case, we can define the difference between the initial values as $\delta_0 = \lambda_{\rm m,0} - \lambda_{\rm acc,0}$. This means that the initial condition for ζ_0 (Equation 3.10) is given by $\zeta_0 = 1/2 + 2\beta + \delta_0$, which can be used in Equation (3.13) to give

$$\lambda_{\rm m} = \lambda_{\rm acc} = \frac{3\lambda_{\rm m,0} - \lambda_{\rm acc,0}}{2}. \tag{3.14}$$

Note that Equation (3.14) is not symmetric in $\lambda_{\rm m,0}$ and $\lambda_{\rm acc,0}$, meaning that the impact of the initial condition for the $M_{\rm d} - M_\star$ correlation is more long-lived that that for $\dot{M} - M_\star$. Whether $\lambda_{\rm m,0}$ and $\lambda_{\rm acc,0}$ grow steeper or shallower with time, towards the limit value determined by Equation (3.14), depends on the sign of δ_0:

- A steepening of the correlation, $\lambda_{\rm m} > \lambda_{\rm m,0}$, is achieved if $\lambda_{\rm m,0} > \lambda_{\rm acc,0}$ ($\delta_0 > 0$); this

condition also implies $\lambda_{\rm acc} > \lambda_{\rm acc,0}$;

- On the other hand, a flattening of the correlation, $\lambda_{\rm m} < \lambda_{\rm m,0}$, is obtained if $\lambda_{\rm m,0} < \lambda_{\rm acc,0}$ ($\delta_0 < 0$); as in the previous case, this also implies $\lambda_{\rm acc} < \lambda_{\rm acc,0}$.

In conclusion, there are two possible scenarios: either both slopes increase towards the common value for evolved populations, if $\lambda_{\rm m,0} > \lambda_{\rm acc,0}$, or they both decrease towards it, it $\lambda_{\rm m,0} < \lambda_{\rm acc,0}$. In both cases, the difference between the two slopes $\delta = \lambda_{\rm m} - \lambda_{\rm acc}$ will tend towards zero. This argument stems from purely mathematical considerations, but can be easily understood from the physical point of view. As the initial accretion timescale of the disc can be written as the ratio $M_{\rm d}/\dot{M}$, it will itself show a power-law correlation with the stellar mass. In particular, its slope will be the difference of those of $M_{\rm d} - M_\star$ and $\dot{M} - M_\star$; in our notation, its initial value is δ_0. A positive correlation (i.e., a positive δ_0) means that discs around more massive stars will evolve slower than discs around less massive stars, causing a steepening of the correlations between disc and stellar parameters. The contrary argument applies for a negative δ_0, which leads to flattening correlations. As the evolution proceeds, $\delta = \lambda_{\rm m} - \lambda_{\rm acc} \to 0$, eventually reaching a homologous depletion of discs around more and less massive stars. Figure 3.1 illustrates this concept in form of sketch.

These conclusions on the evolutionary behaviour of $\lambda_{\rm m}$ and $\lambda_{\rm acc}$ only depend on the scaling of the viscous timescale with the stellar mass. This is the reason why our assumption that α does not depend on $M_\star$ does not influence this result. It should be noted, however, that if α did depend on the stellar mass we would find a different relation between $\lambda_{\rm m,0}$, $\lambda_{\rm acc,0}$ and ζ_0, as the viscous timescale is set by α and R_c.

Spread

As we have mentioned before, not only the mean slopes, but also the spreads of the $M_{\rm d} - M_\star$ and $\dot{M} - M_\star$ correlations are expected to reach the same limit value in the viscous scenario. Lodato et al. (2017) have shown that the $\dot{M} - M_{\rm d}$ correlation is expected to tighten in time, leading to a decreasing spread; on the other hand, as the stellar masses hardly change, we expect the $M_{\rm d} - M_\star$ correlation to follow the same behaviour of that of the distribution of disc masses, which we discuss below.

If we assume the initial disc masses and radii to be distributed log-normally, we can show that viscous evolution preserves the log-normal shape of the distributions. Moreover, the spread of the $M_{\rm d}$ distribution at $t \gg t_\nu$ writes (see Appendix 3.7.2 for derivation)

$$\sigma_M^2(t) = \sigma_M^2(0) + (1-\eta)^2 \sigma_{t_\nu}^2(0); \tag{3.15}$$

σ_{t_ν} is the spread of the distribution of viscous timescales, which in our case, given the direct proportionality between the viscous timescale and radius, is very close to that of radii σ_R. Equation (3.15) shows that the dispersion in the distribution of disc masses increases with

disc evolution.

Conversely, we expect the dispersion of the distribution of accretion rates to decrease with time. As the initial accretion rate can be written as $\dot{M} \propto M_{\rm d,0}/t_\nu$, the initial dispersion $\sigma_{\dot{M}}(0)$ is given by $\sigma^2_{\dot{M}}(0) = \sigma^2_M(0) + \sigma^2_{t_\nu}(0)$. At evolved times, instead, we have already noticed that the two distributions will coincide: this means that also $\sigma_{\dot{M}}(t)$ will be given by Equation (3.15). For $\gamma = 1$, $(1-\eta)^2 = 1/4$, meaning that $\sigma_{\dot{M}}(t) > \sigma_{\dot{M}}(0)$.

3.3.3 Summary: implications of the different scenarios

If we assume a power-law dependence of the disc mass $M_{\rm d}$ and accretion rate $\dot{M}$ on the stellar mass $M_\star$ as initial condition for a population of discs, viscous theory predicts four different evolutionary scenarios for the observed correlations at later times:

- young populations ($t \ll t_\nu$): evolution has not taken place yet, therefore the observed slopes $\lambda_{\rm m}$ and $\lambda_{\rm acc}$ are the same as the initial values $\lambda_{\rm m,0}$ and $\lambda_{\rm acc,0}$;
- old populations ($t \gg t_\nu$): evolution has taken place and both slopes have had the time to reach the evolved value, $\lambda_{\rm m} = \lambda_{\rm acc} = (3\lambda_{\rm m,0} - \lambda_{\rm acc,0})/2$. This can take place either via
    1. both slopes already starting at the final value λ, if $\lambda_{\rm m,0} = \lambda_{\rm acc,0}$ (implying $\delta_0 = \lambda_{\rm m,0} - \lambda_{\rm acc,0} = 0$);
    2. a steepening of both slopes towards $\lambda_{\rm m} = \lambda_{\rm acc}$, if $\lambda_{\rm m,0} > \lambda_{\rm acc,0}$ (implying $\delta_0 > 0$);
    3. a flattening of both slopes towards $\lambda_{\rm m} = \lambda_{\rm acc}$, if $\lambda_{\rm m,0} < \lambda_{\rm acc,0}$ (implying $\delta_0 < 0$).

Table 3.3 summarises all of the possible theoretical scenarios, each line representing a set of parameters. The steps to determine a set of values are as follows:

1. first, the initial values of the slopes of the correlations $M_{\rm d} - M_\star$ and $\dot{M} - M_\star$, $\lambda_{\rm m,0}$ and $\lambda_{\rm acc,0}$, are chosen. This determines δ_0, defined as the difference between the two;
2. β, the slope of the correlation $H/R - M_\star$ (Equation 3.6), is chosen;
3. using Equation (3.10), ζ_0 - the slope of the correlation $R_{\rm d} - M_\star$ - is determined.

However, as we discussed above, not all parameters can assume any possible theoretical value while still maintaining physical relevance. In particular, β (the slope of the correlation of H/R with $M_\star$) is unlikely to be zero, and ζ_0 (the initial slope of the correlation between R_c and $M_\star$) is unlikely to be negative. These conditions are visualized in Table 3.3 as cells with a gray background. Note that the assumption of a constant α does influence this argument: the increasing, decreasing and constant behaviour of $\lambda_{\rm m}$ and $\lambda_{\rm acc}$ based on the initial conditions is not affected, but the physical likelihood of the different scenarios is. Some lines in Table 3.3 show the same value of β but different intervals for δ_0; this is

$$\frac{H}{R} \propto M_\star{}^{\beta}, \qquad R_c(0) \propto M_\star{}^{\zeta_0}, \qquad \delta_0 = \lambda_{\mathrm{m},0} - \lambda_{\mathrm{acc},0}$$

$\boldsymbol{\lambda_{\mathrm{m},0} = \lambda_{\mathrm{acc},0} \Rightarrow \delta_0 = 0}$

β	ζ_0
0	$\frac{1}{2}$
$-\frac{1}{2}$	$-\frac{1}{2}$

$\boldsymbol{\lambda_{\mathrm{m},0} > \lambda_{\mathrm{acc},0} \Rightarrow \delta_0 > 0}$

β	δ_0	ζ_0
0	$(0, +\infty)$	$\left[\frac{1}{2}; +\infty\right)$
$-\frac{1}{2}$	$\left(0, \frac{1}{2}\right]$	$(-\infty; 0]$
$-\frac{1}{2}$	$\left[\frac{1}{2}; +\infty\right)$	$[0; +\infty)$

$\boldsymbol{\lambda_{\mathrm{m},0} < \lambda_{\mathrm{acc},0} \Rightarrow \delta_0 < 0}$

β	δ_0	ζ_0
0	$\left(-\infty; -\frac{1}{2}\right]$	$(-\infty; 0]$
0	$\left[-\frac{1}{2}; 0\right)$	$\left[0; \frac{1}{2}\right]$
$-\frac{1}{2}$	$(-\infty; 0)$	$\left(-\infty; -\frac{1}{2}\right]$

Table 3.3: Summary of the different possible theoretical scenarios divided by the relative values of $\lambda_{\mathrm{m},0}$ and $\lambda_{\mathrm{acc},0}$ (see text for details, especially Equation 3.10 and paragraph 3.3.3). The definition of each parameter appearing in the table is reminded in the top grey box. Each line represents a set of parameters. As discussed in the text, we dismiss the cases where $\beta = 0$ (which would imply an aspect ratio independent on $M_\star$) and $\zeta_0 < 0$ (implying disc radii decreasing with $M_\star$): for visual purposes, cells corresponding to these two conditions have a gray background. The only line which does not include any gray cells is the one that is not influenced by any of these restraints, i.e., the most physically reasonable scenario, and is framed in green.

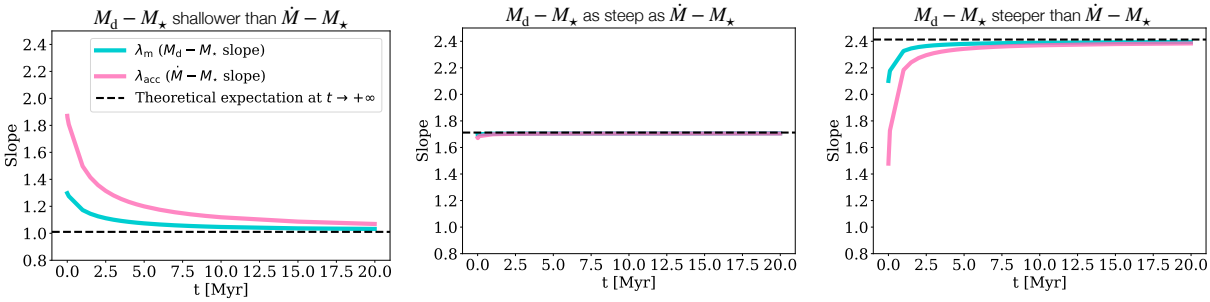

Figure 3.2: Time evolution of the mean values of the slopes of the $M_{\rm d} - M_\star$ and $\dot{M} - M_\star$ correlations, $\lambda_{\rm m}$ and $\lambda_{\rm acc}$ (cyan and pink respectively), as obtained running `Diskpop` and fitting the results using `linmix`. The black dashed line represents the limit value of both slopes for $t \to +\infty$ (see Equation 3.14). Each panel corresponds to a different choice in the initial values $\lambda_{\rm m,0}$ and $\lambda_{\rm acc,0}$. Left panel: $\lambda_{\rm m,0} = 1.3$, $\lambda_{\rm acc,0} = 1.9$, $\delta_0 = \lambda_{\rm m,0} - \lambda_{\rm acc,0} < 0$; middle panel: $\lambda_{\rm m,0} = \lambda_{\rm acc,0} = 1.7$, $\delta_0 = 0$; right panel: $\lambda_{\rm m,0} = 2.1$, $\lambda_{\rm acc,0} = 1.5$, $\delta_0 > 0$. The numerical behaviour follows the theoretical prediction derived in Section 3.3: $\lambda_{\rm m,0} < \lambda_{\rm acc,0}$ (left panel) leads to a flattening trend, $\lambda_{\rm m,0} = \lambda_{\rm acc,0}$ (middle panel) to a constant slope, and $\lambda_{\rm m,0} > \lambda_{\rm acc,0}$ to a steepening trend. Moreover, the theoretical limit value is recovered for every choice of parameters. In every simulation, $H/R\big|_{R=1\text{ au}} = 0.33$ for $M_\star = 1 M_\odot$, $\alpha = 10^{-3}$, $\beta = -0.5$, and both initial conditions $M_{\rm d}(0)$ and $R_c(0)$ follow a log-normal distribution.

because based on the value of δ_0, different possibilities for ζ_0 may arise - in particular, it is meaningful to split the different possibilities if they include a change in the sign of ζ_0. Given that each line in the table represents a set of parameters, lines that contain one or more gray cells turn out to be discarded.

The only line that is not influenced by these restrictions, framed in green, represents the physically meaningful scenario. It is interesting to note that the requirement for both β and ζ_0 to assume reasonable values determines the difference between the initial slopes $\lambda_{\rm m,0}$ and $\lambda_{\rm acc,0}$. Specifically, it prescribes δ_0 to be greater than $1/2$: this implies $\lambda_{\rm m,0} > \lambda_{\rm acc,0}$, making the steepening slopes scenario the most reasonable one. Moreover, as we discussed in the previous paragraph, $\delta_0 > 0$ also implies a positive initial correlation between the accretion timescale and the stellar mass. The observational claim by A17 is intriguingly matching our theoretical consideration; a preliminary comparison with data and a discussion of its implications is performed in subsection 3.5.1.

3.4 Population synthesis

In this Section we discuss the numerical counterpart of the theoretical analysis presented in Section 3.3. In particular, we describe the population synthesis model that we have implemented in `Diskpop`: we briefly present the physical framework, and we show the

numerical results as well as discussing their agreement with the theoretical predictions.

3.4.1 Numerical methods - `Diskpop`

Developing a population synthesis model requires to implement a numerical code to generate and evolve a synthetic population of protoplanetary discs. In this paper, we have used the Python code `Diskpop` that we developed and that we will release soon. In this paragraph, we briefly describe its basic functioning; for a more detailed presentation of it, we refer to the upcoming paper.

`Diskpop` generates an ensemble (which we term *population*) of N discs using the following scheme:

1. determines N stellar masses: this is achieved performing a random draw from an input probability distribution. In `Diskpop`, we use the initial mass function proposed by Kroupa (2001);

2. determines the N mean values of initial disc masses and radii: this is where we account for correlations between stellar and disc parameters. Following the initial correlations listed in Equation (3.3), we choose the values of $\lambda_{\mathrm{m},0}$ and $\lambda_{\mathrm{acc},0}$ and evaluate ζ_0 using Equation (3.10); the initial mean disc mass and radius are then computed, for each of the N stellar masses from step (i), using the prescriptions (3.7) and (3.8). Note that, by doing so, the correlations are intrinsically set to hold only for the mean value of the relevant parameters;

3. draws the N disc masses and radii: for this, the user needs to set two distributions (usually normal or log-normal) and their initial spread in dex (usually between 0.5 and 1.5 dex). After these parameters are determined, the draw is performed using the mean values computed in step (ii).

The other relevant parameters besides $M_\star$, M_d and R are fixed in our model. In particular, the aspect ratio of the disc at 1 au and the α parameter for the Shakura & Sunyaev (1973) prescription are set to be $\frac{H}{R}\Big|_{R=1\text{ au}} = 0.03$ for a 1 $M_\odot$ star and $\alpha = 10^{-3}$. As for the value of α, it is still very much debated how high, or low, it should be or even if it should be constant in time or across the discs in a population at all (Rafikov, 2017); some works have also suggested a dependence of α on the radial position in the disc, namely a lower value in the inner disc with respect to the outer disc (Liu et al., 2018). Nonetheless, assuming a constant value of around 10^{-3} leads to reproducing the observed evolution. A proper study of the α value is out of the scope of this paper.

Once the population is initialized, we want to evolve it using the chosen prescription. In the purely viscous case, which is the focus of this first paper, we can either use the analytical self-similar solution (3.2) or solve the viscous evolution equation,

$$\frac{\partial \Sigma}{\partial t} = \frac{3}{R}\frac{\partial}{\partial R}\left(R^{1/2}\frac{\partial}{\partial R}(\nu \Sigma R^{1/2})\right); \tag{3.16}$$

to do so, `Diskpop` employs the Python code presented in Booth et al. (2017). In this work we have used the numerical approach, but as long as an analytical solution is available there is no difference in the two methods.

The raw numerical solution is an array of values for the gas surface densities Σ at the chosen ages, from which we compute the other quantities of interest: the disc mass is defined as the integral of the surface density from the inner (R_{in}) to the outer (R_{out}) radius,

$$M_{\rm d} = \int_{R_{in}}^{R_{out}} 2\pi r \Sigma \, dr, \tag{3.17}$$

and R as the radius enclosing 68 % of the total disc mass.

3.4.2 Numerical simulations and comparison with theoretical expectations

In this section, we show the results obtained from simulating populations of $N = 100$ protoplanetary discs using `Diskpop`, evolved via numerical solution of Equation (3.16). Following the scheme of Section 3.3, we divide the following discussion on the basis of the evolutionary regime considered. Our aim is to compare population synthesis results with the analytical prescription that we derived in the previous Section.

Young populations: $t \ll t_\nu$

The discussion in section 3.3.1 shows that, if the considered population is much younger than its viscous timescale, we do not expect any significant evolution of the initial conditions. It is worth making a couple of considerations on the order of magnitude of the viscous timescale. For $\gamma = 1$, t_ν scales with the disc radius (as well as α^{-1}, which is fixed in this work though), and given that our initial disc sizes are of the order of 10 au, the typical viscous timescale will be shorter than 1 Myr; this is the case for more than 98% of the discs in the synthetic population. This constraint stems from the need to reproduce the mean observed mass and accretion rate, as discussed in section 3.3.1. Such a short viscous timescale means that young populations would be very challenging to observe. The earliest data available for populations of discs usually correspond to ages around 1 Myr (e.g., Lupus and ρ Ophiucus); if the distribution of t_ν reproduced the viscous timescales of these regions, already the youngest populations would be too old for $t \ll t_\nu$ to hold. For this reason, in the following we only show numerical results for the evolved populations scenario. As mentioned earlier, all of this discussion holds for the particular viscous

timescales that derive from the chosen parameters in our simulations: there is in principle the possibility of obtaining longer viscous timescales (lower α, larger R_c), which would reverse this argument. However, from the observational point of view, this would require larger disc masses or lower accretion rates.

Evolved populations: $t \gg t_\nu$

In the case of evolved populations, which are observed at ages longer than their viscous timescales, we present the numerical results for all of the three scenarios discussed in section 3.3.3. Figure 3.2 shows the mean fitted slopes of the $M_\mathrm{d} - M_\star$ and $\dot{M} - M_\star$ correlations (λ_m and λ_acc respectively) versus the age of the population. As summarised in section 3.3.3, from the theoretical point of view we expect both λ_m and λ_acc to reach the same evolved value, either through a steepening, a flattening or a constant evolution. Each of these three possibilities correspond to a choice of the initial parameters, and is determined by the sign of their difference $\delta_0 = \lambda_{\mathrm{m},0} - \lambda_{\mathrm{acc},0}$. In Figure 3.2 we present our results, where the cyan and pink lines refer to λ_m and λ_acc respectively, obtained in each of these scenarios:

- the left panel corresponds to $\lambda_{\mathrm{m},0} = 1.3, \;\; \lambda_{\mathrm{acc},0} = 1.9 \Rightarrow \delta_0 < 0$, which is expected to produce a flattening of the slopes towards the evolved value;
- the middle panel shows the evolution if $\lambda_{\mathrm{m},0} = \lambda_{\mathrm{acc},0} = 1.7 \Rightarrow \delta_0 = 0$, which corresponds to the theoretical expectation of constant slopes;
- finally, in the right panel we set $\lambda_{\mathrm{m},0} = 2.1, \;\; \lambda_{\mathrm{acc},0} = 1.5 \Rightarrow \delta_0 > 0$, which should lead to an increasing trend of the slopes.

All simulations have the same values of $\alpha = 10^{-3}$, $H/R\big|_{R=1\mathrm{au}} = 0.03$ for $M_\star = 1 M_\odot$, $\beta = -1/2$. The black dashed line shows the theoretical evolved value, computed based on the initial values of the slopes as per Equation (3.14). We can see that all of the three simulations do match our analytical evolutionary predictions: the limit value for evolved populations is recovered, and the flattening, constant and increasing trends are recovered. The middle panel shows a small evolution at very early ages, but it is most likely due to numerical effects and can be neglected. Note that the synthetic populations showed in the plots are evolved up to 20 Myrs; while we do not expect to observe disc-bearing protostars at those very late ages (due to the disc removal processes at play that this work does not include - see Mamajek 2009), we evolved our synthetic populations up to such a long age to make sure no transient affected our results. Moreover, the evolved value is reached at very late ages ($\sim$ 10 Myrs), when we expect processes other than viscous evolution to have taken place.

3.4.3 Numerical simulations introducing a spread

The real power of disc population syntheses is the possibility of introducing a spread in the initial conditions of the population: in this paragraph, we explore the influence of such

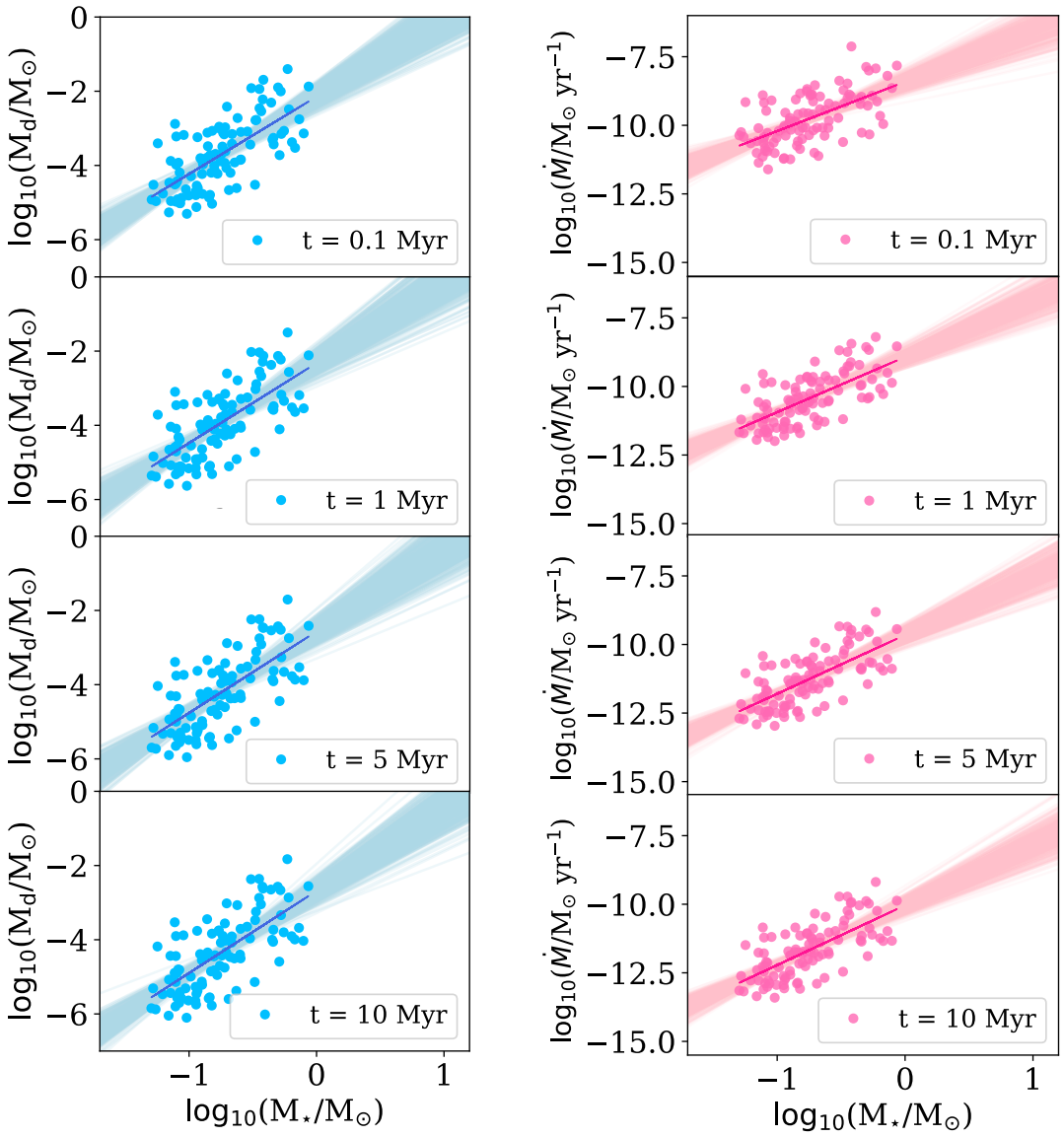

Figure 3.3: $M_{\rm d} - M_\star$ (left panel) and $\dot{M} - M_\star$ (right panel) correlations obtained with `Diskpop` at four consequent time steps from top to bottom, as shown in the legend. The dots represent discs in the population, and the numerical fit is overplotted. These simulations were performed with the same parameters as the right panel of Figure 3.2 ($\delta_0 > 0$), with the addition of a spread in the initial conditions of $\sigma_{M,0} = 0.65$ dex and $\sigma_{R,0} = 0.52$ dex.

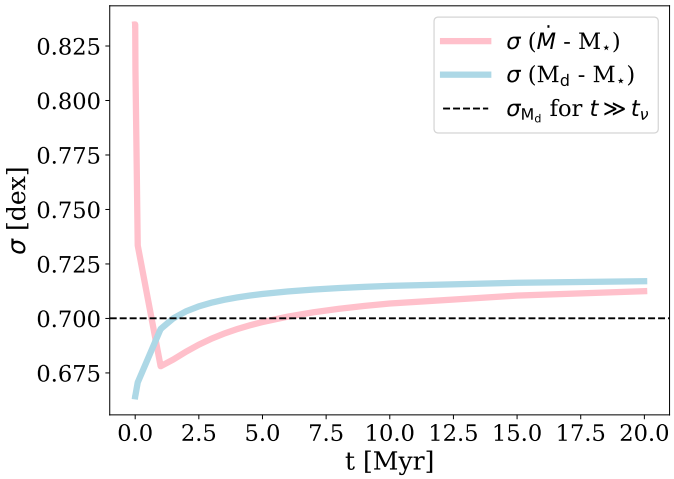

Figure 3.4: Time evolution of the spread of the $M_{\rm d} - M_\star$ (light blue) and $\dot{M} - M_\star$ (pink) correlations. The black dashed line shows the analytical spread of the $M_{\rm d}$ distribution for $t \gg t_\nu$ as per Equation (3.15). Both spreads reach the same value after some Myrs of evolution, in agreement with $M_{\rm d}$ and $\dot{M}$ reaching a unity correlation in the logarithmic plane; this final spread slightly differs from the analytical estimation for evolved populations due to the addition of a spread in the stellar masses.

a spread on our results. Figure 3.3 shows the output of `Diskpop`: the left and right panels display the correlation $M_{\rm d} - M_\star$ and $\dot{M} - M_\star$ respectively, at four subsequent timesteps as per the legend. Each dot represents a disc in the population; the fit was performed using the Python package `linmix`.

We also analysed the time evolution in the spreads of both correlations. The spread is determined as the standard deviation of the vertical distances of every point from the fitted relation. Figure 3.4 shows the results with input values $\sigma_M(0) = 0.65$ dex, $\sigma_R(0) = 0.52$ dex (chosen to be consistent with the observed values in the data sets from A17 and T22, referring to log-normal distributions). The light blue and pink line show the evolution of the dispersion of the $M_{\rm d} - M_\star$ and $\dot{M} - M_\star$ correlations respectively. As we pointed out in paragraph 3.3.2, we expect the spread of the two correlations to reach the same evolved value, represented in the figure by the black dashed line. The numerical limit of 0.71 dex is very close to the theoretical one of 0.7; the slight difference is most likely due to the fact that the numerical dispersion in t_ν also accounts for the dispersion in stellar masses, which is not considered in the analytical calculation.

3.5 Discussion

In Section 3.3, we have performed a theoretical analysis of the viscous evolution of power-law initial conditions. Through it, we have determined three possible physical scenarios

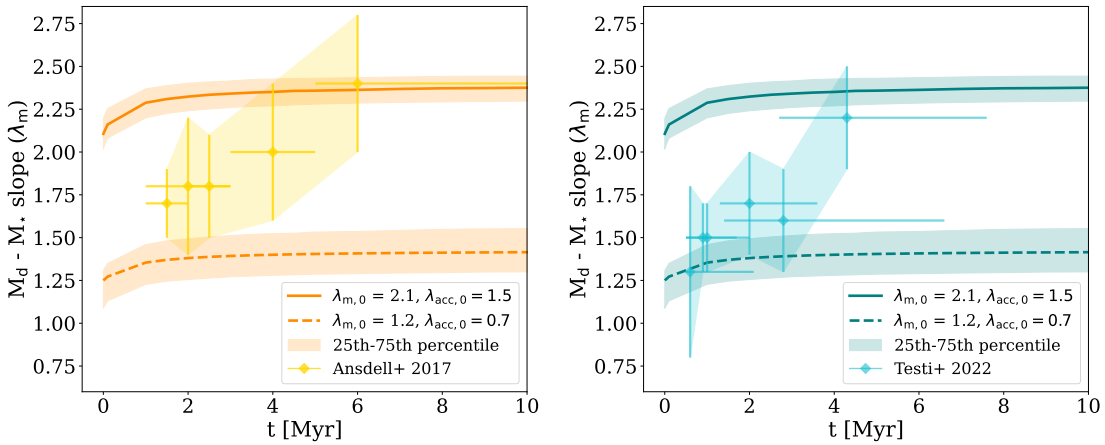

Figure 3.5: Comparison of the numerical results for $\lambda_{\rm m}$ obtained from `Diskpop` with the observational data from A17 (top panel) and T22 (bottom panel). The solid and dashed lines in each panel represent the results of simulations performed with two different sets of parameters, as shown in the legend. The diamonds correspond to the observational mean values, while the vertical and horizontal lines represent the 1σ error bars. The two sets of parameters displayed are able to match (from a qualitative point of view) the youngest and oldest populations, respectively; they represent the limits of the parameter space. Both are chosen to fall in the most physically meaningful scenario, with $\delta > 1/2$. The darker shaded regions around the solid and dashed lines represent the 25th and 75th percentile for the fitted slopes, obtained from 100 different statistical realisations of the same simulation.

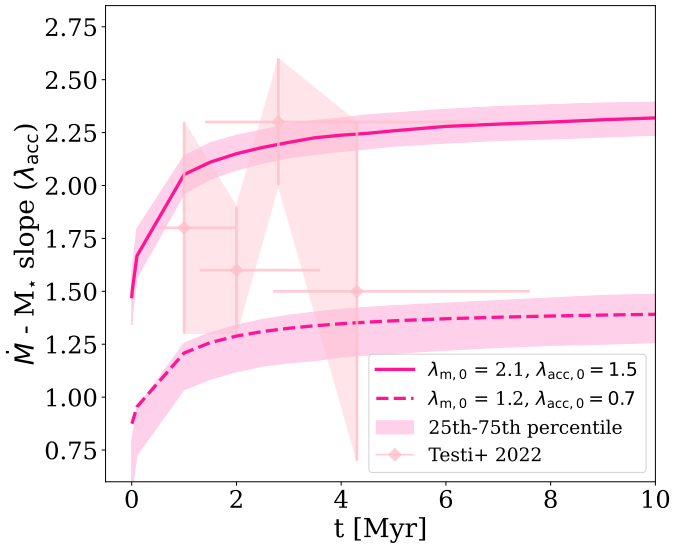

Figure 3.6: Same as Figure 3.5, but referring to $\lambda_{\rm acc}$, showing both the numerical results from `Diskpop` and the observational data from T22. See the caption of Figure 3.5 for detail on annotations.

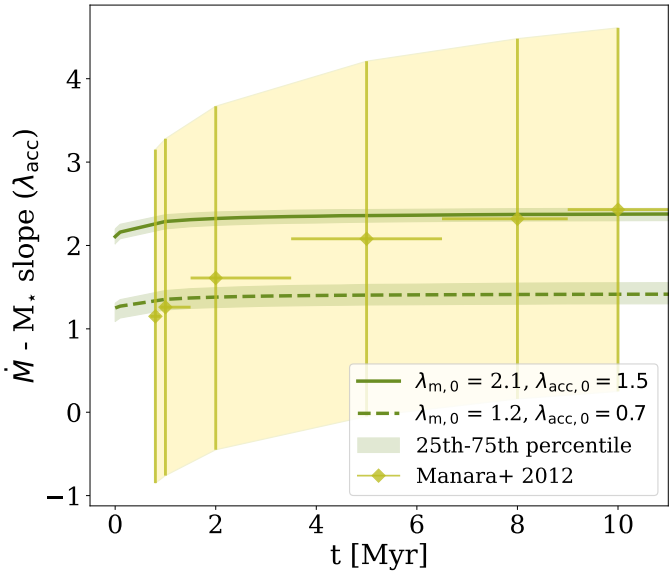

Figure 3.7: Same as Figure 3.6, but compared to the observational data from M12. See the caption of Figure 3.5 for detail on annotations. Note that the horizontal bars in this figure do not represent the errors on the ages, but rather the extent of the age interval that was considered in performing the fit (see text for details).

which differ by the relative values of the initial slopes $\lambda_{m,0}$ and $\lambda_{acc,0}$. We have then analysed the output of our population synthesis code `Diskpop` and compared the evolutionary behaviour with our theoretical expectations (Section 3.4). In this Section, we perform a preliminary comparison with some of the available observational data (section 3.5.1) and discuss the implications of our findings (section 3.5.2).

3.5.1 Preliminary comparison to observational data

After we tested `Diskpop`, recovering the analytical prediction for the viscous evolution of λ_m and λ_{acc}, we performed a preliminary comparison using three sets of observational data (A17, T22, M12).

There are some relevant caveats to these comparisons. First of all, we did not include any observational effects, biases, or sensitivity limitations in our simulations. However, the goal of this comparison is not to fit any data set, nor to perfectly reproduce the observations: our aim is just to have a qualitative idea of the parameter space, and to see whether the general trend shown by observations can (at least in principle) be reproduced from the theoretical point of view.

Figure 3.5, 3.6 and 3.7 show the data comparison for the $M_d - M_\star$ (Figure 3.5) and the $\dot{M} - M_\star$ (Figure 3.6 and 3.7) correlation. The top panel of Figure 3.5 refers to data from A17, the bottom panel of Figure 3.5 and Figure 3.6 from T22, and Figure 3.7 from M12.

Each panel in these figures contains two sets of simulations, represented by the solid and dashed lines respectively, corresponding to two different sets of parameters ($\lambda_{\rm m,0}$ and $\lambda_{\rm acc,0}$, see legend), with a spread of $\sigma_M(0) = 0.65$ dex and $\sigma_R(0) = 0.52$ dex. The darker shaded areas around the solid and dashed lines represent the 25th and 75th percentiles for the fitted slopes, obtained from 100 different statistical realisations of the same simulations. The initial conditions on $\lambda_{\rm m}$ and $\lambda_{\rm acc}$ were chosen to qualitatively match the observed slopes at later and younger ages respectively; the other parameters in the simulations are fixed - in particular, $H/R\big|_{R=1\text{ au}} = 0.33$ for $M_\star = 1 M_\odot$, $\alpha = 10^{-3}$, and $\beta = -0.5$. The mean observational values are represented by diamonds, and the vertical and horizontal lines show their uncertainties. As we already discussed in Section 3.2, there is a key difference between the data by M12 and all of the other observations: M12 focused on a single star-forming region, dividing the protostars based on their isochronal age group, while data from both A17 and T22 instead refer to different star-forming regions, each with its own mean age. For this reason, the horizontal bars in Figure 3.7 do not refer to the errors in age, but rather to the extent of the age intervals considered when performing the fits. Because of these considerable differences from the observational point of view, we divided Figure 3.6 and 3.7.

It is worth recalling that, out of the two diagnostics $M_{\rm d}$ and $\dot{M}$, the second is more readily translated in the observational space. On the other hand, disc mass measurements always refer to *dust* content; given that our simulations only include the gaseous component, all of the observed masses shown here have been multiplied by the dust-to-gas ratio (set to the usual value of 100, see Bohlin et al. 1978). If `Diskpop` included dust evolution, the numerical disc mass $M_{\rm d}$ would be affected - and so would the $M_{\rm d} - M_\star$ correlation and its time evolution; on the other hand, we do not expect a significant influence of the presence of dust on the accretion rate. At this stage, we also assumed spread-less initial conditions for the disc masses and radii. For these reasons, as well as not including any observational effects or biases, the comparison shown in Figures 3.5, 3.6 and 3.7 is qualitative.

Nonetheless, our comparison does suggest some interesting ideas. A17 claimed to have found an increasing trend of $\lambda_{\rm m}$ with the age of the sample, which can also apply to T22 - even if it is not as evident. Furthermore, in T22 the mean value for $\lambda_{\rm acc}$ seems to be increasing as well: the visible exception of the last point (Upper Scorpius) must be treated carefully, as it represents a highly incomplete sample - hence the large error bars (see the original paper for more detail). Due to the method adopted to determine the age of the subgroups in the Orion Nebula Cluster, M12 found significant errors on the fitted slopes; despite not being statistically significant, the mean measured values are increasing, and these data show a general agreement with the steepening trend. The interesting message of Figure 3.5, 3.6 and 3.7 is that the observed increasing trend can be reproduced from the theoretical point of view, as the simulations show. Despite including a spread of around 0.5 dex in both the disc mass and radius, the analytical expectations are well recovered: given the choices of parameters (in particular, $\delta_0 > 1/2$) our simulations show the steepening evolution of both $\lambda_{\rm m}$ and $\lambda_{\rm acc}$. The main result is that, if this is the case, such observed

correlations would be naturally explained in the purely viscous framework by

1. assuming power-law correlations as initial conditions;

2. imposing a positive correlation between the viscous timescale and the stellar mass.

Figure 3.5, 3.6 and 3.7 also show the effect of a spread in the initial conditions on the evolution of the slopes. At $t = 0$, the median slopes (solid and dashed lines for the two initial conditions) and the input values $\lambda_{\mathrm{m},0}$ and $\lambda_{\mathrm{acc},0}$ coincide with a precision of $\sim 10^{-3}$ and $\sim 10^{-2}$ respectively; moreover, the evolutionary path of both λ_{m} and λ_{acc} is not changed. Therefore, including a spread in the initial condition only influences the starting point of the evolution, and does not affect the fundamental results that we have discussed.

As we mentioned above, we chose the parameters in the two different runs of `Diskpop` to qualitatively match the youngest and most evolved values for both $\lambda_{\mathrm{m,obs}}$ and $\lambda_{\mathrm{acc,obs}}$: this identifies a region of the parameter space for $\lambda_{\mathrm{m},0}$ and $\lambda_{\mathrm{acc},0}$, which lead to an evolution that roughly matches the observations (within their 1σ error bars). These two sets of parameters are given by $\lambda_{\mathrm{m},0} = 2.1$, $\lambda_{\mathrm{acc},0} = 1.5$ and $\lambda_{\mathrm{m},0} = 1.2$, $\lambda_{\mathrm{acc},0} = 0.7$; the interval in the parameter space is

$$\lambda_{\mathrm{m},0} \in [1.2, 2.1] \quad \lambda_{\mathrm{acc},0} \in [0.7, 1.5]. \tag{3.18}$$

Figure 3.5, 3.6 and 3.7 unveil another feature worth pointing out. Different values of $\lambda_{\mathrm{m},0}$ and $\lambda_{\mathrm{acc},0}$ can change the starting point of the curves obtained, but cannot change their shape - i.e., the rate of steepening or flattening of the slopes is not influenced by the initial parameters in the purely viscous case. We will discuss this further in the next Section.

3.5.2 Evolution of the slopes

As we discussed above, the key promising aspect worth pointing out is that there is indeed a theoretical scenario which is able to reproduce the observed steepening of the correlations. Furthermore, this case also corresponds to the most likely physical regime - which leads to a positive correlation between the disc radius and the stellar mass. If these analytical requirements are matched, our analysis finds that power-law initial conditions for the correlations λ_{m} and λ_{acc} can only be steepened by viscous evolution. This implies that the observed correlations could be easily explained in terms of initial conditions and viscous evolution, without invoking any additional physical process.

On the other hand, we also found that changing the initial values $\lambda_{\mathrm{m},0}$ and $\lambda_{\mathrm{acc},0}$ raises or lowers the evolution curve, adding only a small modification to the rate at which the exponents of the correlation steepen. Indeed, even if the difference $\delta_0 = \lambda_{\mathrm{m},0} - \lambda_{\mathrm{acc},0}$ does impact the viscous timescales, with these choices of parameters they still remain of

the order of 1 Myr; as the bulk of the evolution in our models happens on comparable timescales, the effect of these changes is minimal.

Initial conditions within the parameters space specified in Equation (3.18), and with $\delta_0 > 1/2$, are able to qualitatively match the observed slopes within 1σ (although note that, as the error bars are large, this is not strongly constraining on any of the three models). However, the youngest and oldest populations seem to be better described by different simulations. This can be explained in two different ways:

1. initial conditions are not the same for every star-forming region. This would mean that different curves must be considered for different regions to match their evolution;

2. viscous evolution alone is not enough to explain the whole extent of star-forming regions.

The second possibility is very much reasonable; a number of physical effects are now thought to affect disc evolution, sooner or later in their lifetime. We can mention in particular MHD winds, which are expected to play a role alongside viscosity (Tabone et al., 2022a), internal and external photoevaporation (Clarke et al., 2001; Alexander et al., 2004; Owen et al., 2012), or dust evolution (Sellek et al., 2020a); these effects are complicated to include in the mathematical analysis, but may be implemented in numerical codes to test whether they do lead to any modifications to the steepening rates of $\lambda_{\rm m}$ and $\lambda_{\rm acc}$. Dust evolution in particular would likely affect the computed disc mass, while it should not have a considerable influence on the accretion rate. This expected behaviour is encouraging, as Figure 3.5 shows that the shape of the time evolution of $\lambda_{\rm acc}$ (right panel) qualitatively matches the observed data way better than that of $\lambda_{\rm m}$ (left and central panels). An ideal candidate to show the signature of more complex evolutionary patterns would be Upper Scorpius, which is notorious for being difficult to explain through classic viscous models (Manara et al., 2020; Trapman et al., 2020) unless adding additional physics, such as dust evolution (Sellek et al., 2020a).

3.6 Conclusions

In this paper, we investigated the correlation between the stellar mass and disc properties, $M_{\rm d} - M_\star$ and $\dot{M} - M_\star$. Assuming power-law correlations as initial conditions ($M_{\rm d}(0) \propto {M_\star}^{\lambda_{\rm m,0}}$, $\dot{M}(0) \propto {M_\star}^{\lambda_{\rm acc,0}}$), as well as viscous evolution, we obtained analytical equations to describe how the exponents of these correlations should evolve with time. Our main findings are the following:

1. In the viscous picture, the two correlations follow the same trend: they both either grow steeper or shallower with time. Given enough time, they tend to the same value, which is determined by the initial slopes or, in other terms, by the scaling of the viscous timescale with the stellar mass. If we further make the plausible assumption

that $H/R \propto {M_\star}^\beta$, with $\beta = -1/2$ (as supported by radiative transfer models), α does not depend on $M_\star$ and $\delta_0 = \lambda_{\mathrm{m},0} - \lambda_{\mathrm{acc},0} > 1/2$, both correlations steepen with time, as tentatively suggested by observations. This is a consequence of viscous time increasing with stellar mass. Moreover, the spread of the two correlations is also bound to evolve to reach the same value, determined by the initial spreads in disc masses and viscous timescales;

2. motivated by this early success, we attempted a comparison of our predictions with the available data. To this end we built a numerical tool, `Diskpop`, to evolve synthetic disc populations and include effects that cannot be tackled in the analytical approach (such as a spread in the initial conditions and the effect of random sampling);

3. with the two sets of initial conditions $\lambda_{\mathrm{m},0} = 1.2, \lambda_{\mathrm{acc},0} = 0.7$ and $\lambda_{\mathrm{m},0} = 2.1, \lambda_{\mathrm{acc},0} = 1.5$ we obtain two limit curves which match either the youngest or the oldest region in the samples (within their error bars). This means that the range $\lambda_{\mathrm{m},0} \in [1.2, 2.1]$, $\lambda_{\mathrm{acc},0} \in [0.7, 1.5]$ as exponents in the initial conditions allows to span the observed parameter space;

4. changing the initial condition can either raise or lower the curve, without significantly modifying its shape: this implies that our model cannot exactly match both the youngest and the oldest populations. This behaviour can imply two consequences: either the initial condition is not the same for every star-forming region, or viscosity alone is not enough to explain the observed long-term evolution (as already discussed in previous works, e.g. Mulders et al. (2017), Manara et al. (2020), Testi et al. (2022)). Of course, these two possibilities can also be valid at the same time. In particular, we expect dust evolution and planet formation, followed by disc-planet interaction, to play a crucial role: affecting the disc mass M_{d}, it will likely change the time evolution of λ_{m}. However, it would probably not affect λ_{acc} - which intriguingly already resembles the observations better.

In our future work we aim at further developing `Diskpop`, increasing its complexity adding relevant physical effects such as MHD winds, photoevaporation and dust evolution; this will allow us to test the influence of these phenomena on the evolution of populations, and to obtain numerical results more suitable for a comparison with observational data.

Acknowledgements

We thank an anonymous referee for their valuable comments that helped us improve the clarity of this paper. We thank Richard Alexander, Barbara Ercolano, Til Birnstiel and Kees Dullemond for the interesting discussions. This work was partly supported by the Italian Ministero dell'Istruzione, Università e Ricerca through the grant Progetti Premiali 2012 – iALMA (CUP C52I13000140001), by the Deutsche Forschungs-gemeinschaft (DFG, German Research Foundation) - Ref no. 325594231 FOR 2634/1 TE 1024/1-1, by the DFG

cluster of excellence Origins (www.origins-cluster.de), and from the European Research Council (ERC) via the ERC Synergy Grant *ECOGAL* (grant 855130). GR acknowledges support from an STFC Ernest Rutherford Fellowship (grant number ST/T003855/1). M.T. has been supported by the UK Science and Technology research Council (STFC) via the consolidated grant ST/S000623/1. G.L., G.R, L.T., C.F.M., and C.T. have been supported by the European Union's Horizon 2020 research and innovation programme under the Marie Sklodowska-Curie grant agreement No. 823823 (RISE DUSTBUSTERS project).

3.7 Appendix

3.7.1 $R_d - M_\star$ correlation

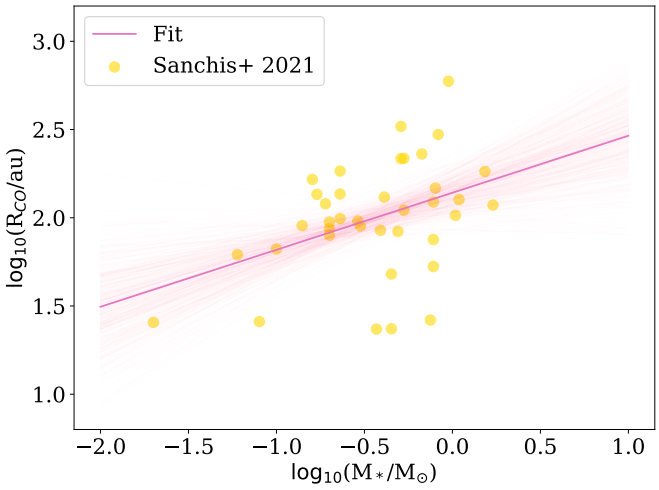

Figure 3.8: Disc radius from CO observations (Sanchis et al., 2021) as a function of the stellar mass in Lupus.

Figure 3.8 shows a plot of the gas (CO) disc radius as a function of the stellar mass using data by Sanchis et al. (2021), fitted using `linmix`. The best-fit parameters[2] are $\alpha = 2.14 \pm 0.08$, $\beta = 0.32 \pm 0.13$, with a spread $\sigma = 0.32 \pm 0.16$ dex. As discussed in paragraph 3.2.3, the correlation is positive but the fit is not particularly strong; the correlation coefficient is $\rho_{XY} = 0.32$, which implies weak correlation.

3.7.2 Evolution of the disc mass distribution in the self-similar scenario

Here, we demonstrate that an initially log-normal distribution of disc masses keeps being log-normal at long times under the assumption of self-similar viscous evolution and estimate

[2]Using the standard convention for linear relations, $y = \alpha + \beta x$.

the relevant distribution parameters.

We start by defining some useful quantities: let $m_0 = \log M_{\rm d,0}$ and $\tau_\nu = \log t_\nu$ be the log of the initial disc mass and viscous time of a specific disc in a population. Now, the initial distributions of disc masses and viscous times are assumed to be log-normal, so that:

$$\frac{\partial N}{\partial m_0} = N_1 \exp[-(m_0 - \bar{m}_0)^2/2\sigma_M^2], \tag{3.19}$$

$$\frac{\partial N}{\partial \tau_\nu} = N_2 \exp[-(\tau_\nu - \bar{\tau}_\nu)^2/2\sigma_{t_\nu}^2], \tag{3.20}$$

where $\bar{m}_0$ and $\bar{\tau}_\nu$ are the average values of the initial disc mass and viscous time (in logarithmic sense), σ_M and σ_{t_ν} are their dispersions, and N_1 and N_2 are normalisation constants. Note that the two log-normal probability distributions are independent, in the $m_0 - \tau_\nu$ space, and their means and variances may depend on the stellar mass. For a self-similar disc in the limit $t \gg t_\nu$, the disc mass at time t is $M_{\rm d}(t) = M_{\rm d,0}(t/t_\nu)^a$, where $a = 1 - \eta$ (see Eq. 3.4). In logarithmic form, this is:

$$m = m_0 + a\tau - a\tau_\nu, \tag{3.21}$$

where $m = \log M_{\rm d}(t)$ and $\tau = \log t$. We can invert Eq. (3.21), obtaining:

$$\tau_{\nu,m} = \frac{m_0}{a} - \frac{m}{a} + \tau, \tag{3.22}$$

so that $\tau_{\nu,m}$ is the viscous time for which a disc with initial mass m_0 evolves into m after a time τ.

The distribution of disc masses at time t can then be obtained by integrating over the distribution of initial disc masses and viscous times, under the condition that Eq. (3.22) is satisfied:

$$\frac{\partial N}{\partial m} = \int\int \frac{\partial N}{\partial m_0}\frac{\partial N}{\partial \tau_\nu}\delta(\tau_\nu - \tau_{\nu,m}){\rm d}\tau_\nu{\rm d}m_0, \tag{3.23}$$

where here δ is the Dirac function. The integral over viscous times can be readily be done, and, after inserting the initial distributions of disc masses and viscous times and using Eq. (3.22), we obtain:

$$\frac{\partial N}{\partial m} = N_1 N_2 \int \exp\left\{ -\frac{(m_0 - \bar{m}_0)^2}{2\sigma_M^2} - \left[\frac{(m_0 - m)}{a} + (\tau - \bar{\tau}_\nu)\right]^2 \frac{1}{2\sigma_{t_\nu}^2} \right\} \mathrm{d}m_0. \tag{3.24}$$

Let us define $\bar{m} = \bar{m}_0 + a\tau - a\bar{\tau}_\nu$, which we will see is the average disc mass at time τ. We also define $\tilde{m} = m - \bar{m}$ and $\tilde{m}_0 = m_0 - \bar{m}_0$. The exponent in Eq. 3.24 can be then rewritten as (neglecting the factor $-1/2$):

$$\mathcal{M} = \frac{\tilde{m}_0^2}{\sigma_M^2} + \left[\frac{\tilde{m}_0}{a} - \frac{\tilde{m}}{a}\right]^2 \frac{1}{\sigma_{t_\nu}^2}. \tag{3.25}$$

We can now easily rewrite the exponent $\mathcal{M}$ in such a way to isolate the dependence on m_0 (that we integrate upon). After some straightforward algebra, we get:

$$\mathcal{M} = \left(A\tilde{m}_0 - \frac{B^2}{A}\tilde{m}\right)^2 + \frac{A^2 - B^2}{A^2/B^2}\tilde{m}^2, \tag{3.26}$$

where

$$B^2 = \frac{1}{a^2\sigma_{t_\nu}^2} \tag{3.27}$$

and

$$A^2 = B^2 + \frac{1}{\sigma_M^2}. \tag{3.28}$$

Now, integrating Eq. (3.24) over $\tilde{m}_0$, the whole first term on the RHS in Eq. (3.26) translates into a normalization constant, leaving us with just a Gaussian distribution for $\tilde{m}$. This means that the disc masses at time t are distributed log-normally, with mean $\bar{m} = \bar{m}_0 + a\tau - a\bar{\tau}_\nu$ and with dispersion

$$\sigma_M(t) = \frac{A^2/B^2}{A^2 - B^2} = \sigma_M^2 + a^2\sigma_{t_\nu}^2. \tag{3.29}$$

4

The time evolution of $M_d/\dot{M}$ in protoplanetary disks as a way to disentangle between viscosity and MHD winds

Published as
Somigliana et al., 2023, ApJL, Volume 954, n. 1, p. L13

Full authors list:
Alice Somigliana; Leonardo Testi; Giovanni Rosotti; Claudia Toci; Giuseppe Lodato; Benoît Tabone; Carlo F. Manara; Marco Tazzari.

As the classic viscous paradigm for protoplanetary disk accretion is challenged by the observational evidence of low turbulence, the alternative scenario of MHD disk winds is being explored as potentially able to reproduce the same observed features traditionally explained with viscosity. Although the two models lead to different disk properties, none of them has been ruled out by observations - mainly due to instrumental limitations. In this work, we present a viable method to distinguish between the viscous and MHD framework based on the different evolution of the distribution in the disk mass ($M_{\rm d}$) - accretion rate ($\dot{M}$) plane of a disk population. With a synergy of analytical calculations and 1D numerical simulations, performed with the population synthesis code `Diskpop`, we find that both mechanisms predict the spread of the observed ratio $M_{\rm d}/\dot{M}$ in a disk population to decrease over time; however, this effect is much less pronounced in MHD-dominated populations as compared to purely viscous populations. Furthermore, we demonstrate that this difference is detectable with the current observational facilities: we show that convolving the intrinsic spread with the observational uncertainties does not affect our result, as the observed spread in the MHD case remains significantly larger than in the viscous scenario. While the most recent data available show a better agreement with the wind model, ongoing and future efforts to obtain direct gas mass measurements with ALMA and ngVLA will cause a reassessment of this comparison in the near future.

4.1 Introduction

The gaseous component of protoplanetary disks has traditionally been described as undergoing viscous accretion (Lynden-Bell & Pringle 1974, Pringle 1981). In recent years, however, a growing observational evidence is challenging this picture, as the low levels of turbulence detected in protoplanetary disks appear incompatible with the observed evolution (Pinte et al. 2016, Flaherty et al. 2018, Rosotti 2023). The best alternative to the classic viscous scenario is currently provided by MHD disk winds, originally proposed by Blandford & Payne (1982). This model has gained increasing popularity in the recent years, as several studies (see Lesur 2021 for a review) have shown it to reproduce the key evolutionary features of protoplanetary disks; moreover, Tabone et al. (2022a) have developed a simple analytical parameterisation, making it a valid alternative to the viscous theory.

A compelling question is which of these mechanism, or which combination of the two, drives angular momentum transport in protoplanetary disks (Manara et al., 2023). Answering this question has proven to be a surprisingly difficult task: even though the two models are in principle well distinguishable through their characteristic theoretical predictions, the observational counterpart is lagging behind (e.g., Rosotti et al. 2019b, Ilee et al. 2022). A good example of this problem is viscous spreading, a fundamental feature of viscous evolution that causes the gaseous component of disks to expand in radius as they evolve. As MHD evolution does not show a similar behaviour (Zagaria et al., 2022b), it would in principle be a good candidate for disentangling between the two predictions: however, the high sensitivity required to detect it has until now represented a limit. While Class 0 objects are widely accepted to be born small (< 60 au: Maury et al. 2019, also supported by the numerical experiments of, e.g., Lebreuilly et al. 2021) and grow wider in the first 1-2 Myr of evolution (Najita & Bergin, 2018), whether the radius of Class II disks increases or decreases with time is widely debated. Dust continuum radii are observed to be shrinking with time (Hendler et al. 2020, Zagaria et al. 2022b), as an effect of radial drift, while gas observations (Ansdell et al. 2018, Sanchis et al. 2021, Toci et al. 2021, Long et al. 2022) have covered too small of a sample at too low sensitivities to draw firm conclusions. The advent of ALMA Band 1 (Carpenter et al., 2020) and the next-generation VLA (ngVLA, Tobin et al. 2018) in the near future will allow to perform surveys of protoplanetary disks at unprecedentedly long wavelengths, which will play a crucial role in determining the leading evolutionary mechanism. At the same time, finding novel approaches to tackle this problem is crucial to obtain significant results.

In this Letter, we suggest a new method to distinguish between the two models from the population perspective: through a joint theoretical and population synthesis approach, we investigate the time evolution of disks in the disk mass - accretion rate plane, proving it to be a good approach for our goal. This work is structured as follows: in Section 4.2 we describe the evolutionary prescriptions that we adopt and we discuss their numerical implementation. In Section 4.3 we present our results and we compare them with the

observations. Finally, in Section 4.4 we discuss the implications of these results and draw our conclusions.

4.2 Theoretical model

4.2.1 Secular evolution

The simulations presented in this work have been carried out using the 1D Python population synthesis code `Diskpop`. For a detailed description of the code, as well as its public release, we refer to our upcoming paper (Somigliana et al. in prep; earlier implementations of the code, its basic assumptions and features have been described in Rosotti et al. 2019a, Rosotti et al. 2019b, Toci et al. 2021, Somigliana et al. 2022). The viscous and MHD evolution are implemented following Lynden-Bell & Pringle (1974) and Tabone et al. (2022a) respectively. In this section we briefly present both models, referring to the original papers for a deeper discussion.

In the viscous case, we solve the classic evolution equation

$$\frac{\partial \Sigma}{\partial t} = \frac{3}{R}\frac{\partial}{\partial R}\left(R^{1/2}\frac{\partial}{\partial R}(\alpha_{\rm SS} c_s H \Sigma R^{1/2})\right); \tag{4.1}$$

following the prescription by Shakura & Sunyaev (1973), the viscosity ν is modelled as $\alpha_{\rm SS} c_s H$, where $\alpha_{\rm SS}$ is a dimensionless parameter, c_s is the sound speed, and H is the height of the disk. Furthermore, assuming the viscosity to be a power-law of the disk radius for ease of solving the equation, $\nu = \nu_c (R/R_c)^{\gamma}$ (where $\nu_c = \nu(R = R_c)$ and R_c is a scale radius), the analytical solution by Lynden-Bell & Pringle (1974) holds.

In the MHD case instead (Tabone et al., 2022a), the evolution equation is given by

$$\begin{aligned}\frac{\partial \Sigma}{\partial t} = &\frac{3}{R}\frac{\partial}{\partial R}\left(R^{1/2}\frac{\partial}{\partial R}(\alpha_{\rm SS} c_s H \Sigma R^{1/2})\right) \\ &+\frac{3}{2R}\frac{\partial}{\partial R}\left(\frac{\alpha_{\rm DW}\Sigma {c_s}^2}{\Omega}\right) - \frac{3\alpha_{\rm DW}\Sigma {c_s}^2}{4(\lambda-1)R^2\Omega},\end{aligned} \tag{4.2}$$

where Ω is the keplerian orbital frequency, λ is the magnetic lever arm parameter, and $\alpha_{\rm DW}$ is a magnetic equivalent of $\alpha_{\rm SS}$. Equation (4.2) is a generalisation of Equation (4.1) if the gas surface density evolves not only because of the viscous torque (first term on the RHS) but also because of the effects of MHD disk winds, which extract angular momentum and induce a mass loss (second and third term on the RHS respectively). Assuming that both λ and $\alpha_{\rm DW}$ are constant across the disk, and that $\alpha_{\rm DW} \propto {\Sigma_c}^{-\omega}$ (where $\Sigma_c = \Sigma(R = R_c)$), Equation (4.2) can be solved analytically (see Tabone et al. 2022a).

4.2.2 Isochrones

Isochrones are defined as the curves described by a population of objects of the same age in a given plane. In the case of protoplanetary disks, isochrones in the $M_{\rm d} - \dot{M}$ plane have been the focus of recent studies (Lodato et al. 2017, Somigliana et al. 2020). For viscously evolving disks (Lodato et al., 2017), the isochrone reads

$$\dot{M} = \frac{M_{\rm d}}{2(2-\gamma)t}\left[1 - \left(\frac{M_{\rm d}}{M_0}\right)^{(2-2\gamma)}\right]; \tag{4.3}$$

the only free parameter in Equation (4.3) is the initial disk mass M_0, which only sets the starting point of the isochrone. Nonetheless, at late stages (when $M_{\rm d} \ll M_0$) all disks in a population are bound to reach the same locus on the $M_{\rm d} - \dot{M}$ plane: while this happens at different ages for each disk, depending on its viscous timescale $t_\nu = {R_c}^2/(3(2-\gamma)^2\nu_c)$, a fully evolved population ($t \to +\infty$) will necessarily sit on the theoretical isochrone of the corresponding age.

For MHD disks, the isochrone is defined as (Tabone et al., 2022a)

$$\dot{M} = \frac{1}{\omega(1+f_{\rm M,0})t} M_{\rm d}\left[\left(\frac{M_{\rm d}}{M_0}\right)^{-\omega} - 1\right]; \tag{4.4}$$

Equation (4.4) depends not only on M_0, but also on the equivalent of t_ν in the MHD winds case, the initial accretion timescale $t_{\rm acc,0}$, through $f_{\rm M,0}$ (determined by the disk radius - see Tabone et al. 2022a for details). The interpretation of the isochrones in the two models is therefore different: while the viscous curves for all disks in a population lie on top of each other (except at the early stages, when $M_{\rm d} \sim M_0$), MHD evolution never loses memory of the initial conditions. This is because, depending on whether we fix M_0 or $t_{\rm acc,0}$, we can define two types of isochrones for an MHD population. As a result, disks with a different M_0 will occupy an *area* of the $M_{\rm d} - \dot{M}$ plane, rather than sitting on a single curve, and this will be the case even for evolved populations - which means that it is not possible to use the isochrones to obtain age estimates for disk populations. Based on this argument, we investigate whether the evolution of a population of disks in the $M_{\rm d} - \dot{M}$ plane could carry tangible signatures of the evolutionary model.

4.2.3 Population synthesis

In this work we adopt a population synthesis approach, which consists of generating and evolving a synthetic population of protoplanetary disks via numerical methods. We employ the Python tool `Diskpop`, which we expanded from our previous work (Somigliana et al., 2022) to include MHD disk wind evolution. In this section, we present a brief outline of the

workflow, referring to the upcoming code release for a detailed description of the methods and the implementation.

First, we generate $N \sim 100$ stars, whose masses $M_\star$ follow the Kroupa (2001) initial mass function. We then assemble a Young Stellar Object (YSO) by assigning a disk to each star: to determine the initial mass and radius of said disk, we assume that the initial disk mass and accretion rate scale as power-laws of the stellar mass ($M_\mathrm{d} \propto {M_\star}^{\lambda_\mathrm{m}}$ and $\dot{M} \propto {M_\star}^{\lambda_\mathrm{acc}}$). In our previous work (Somigliana et al., 2022) we have demonstrated how $\lambda_{\mathrm{m},0} \in [0.7, 1.5]$ and $\lambda_{\mathrm{acc},0} \in [1.2, 2.1]$ can reproduce the slopes of observed correlations of disk properties with stellar mass at later ages; we refer to that paper for a detailed discussion. We determine M_d and $\dot{M}$ for each disk drawing from a log-normal distribution, centred in the mean value computed via the power-law correlations and with a width (σ) of choice; R_d is then derived from considerations on $\dot{M}$ (see Somigliana et al. 2022 for details). The other relevant quantities besides $M_\star$, M_d and R_d are fixed in our model: Table 4.1 and 4.2 shows the parameters that we used in the simulations presented in this work, based on the disc evolution studies of Lodato et al. (2017) and Tabone et al. (2022a) for viscosity and MHD winds respectively. While a detailed study of the parameters space is outside of the scope of this work, we have tested two more combinations of parameters (shown by Tabone et al. (2022b) to reproduce the Lupus star-forming region) and we found that our results are independent on the particular combination chosen. Once the population of YSOs is generated, it is evolved following the viscous or MHD prescription via a 1D implementation of the models described in Section 4.2.1. Although `Diskpop` allows to numerically solve the evolution equations, in this work we have used the analytical solutions to Equation (4.1) and (4.2); it is therefore important to note that our results depend on the assumptions needed to obtain such solutions (e.g., the power-law scaling of viscosity with the disk radius).

Model	Distributions	IMF	λ_m, λ_acc	σ_M, σ_R
Viscous	log-normal	Kroupa (2001)	1.5, 2.1	1 dex
MHD				0.65 dex, 0.52 dex

Table 4.1: Parameters used in the viscous and MHD `Diskpop` simulations respectively. σ_M and σ_R are the width of the initial disk mass and radius, respectively. These values were chosen following the work of Lodato et al. (2017).

It is crucial to point out that disk dispersal is an intrinsic feature of MHD winds, but not of viscous evolution. Our code includes an observational effect by considering as dispersed disks with masses lower than $10^{-6} M_\odot$; this simulates a dispersal effect even in the viscous scenario, which would otherwise generate disks with infinite lifetime, that do not match the observed disk fraction (see Appendix 4.5.3). This problem is usually solved in the literature by adding other physical effects to the purely viscous model, such as internal photoevaporation (see e.g. Hollenbach et al. 1994, Clarke et al. 2001, Owen et al. 2011, Picogna et al. 2019, Emsenhuber et al. 2023). In order to account for the statistical effect

Model	H/R at $R = 1$ au	α_{SS}	α_{DW}	ω, λ	$< t_{acc,0} >$
Viscous	0.03	10^{-3}	0	0	0.8 Myr
MHD		0[a]	10^{-3}	0.25, 3	

[a]Although the MHD model of Tabone et al. (2022a) allows both α_{SS} and α_{DW} to be non-zero, Equation (4.2) in the $\omega \neq 0$ case can only be solved analytically if $\alpha_{SS} = 0$.

Table 4.2: Evolutionary parameters used in the viscous and MHD `Diskpop` simulations respectively. These values were chosen following the works of Lodato et al. (2017) and Tabone et al. (2022a).

of reducing our sample throughout the evolution caused by disk dispersal, we performed 100 simulations for both setups described in Table 4.1 and 4.2 and then considered not only the median evolution of the interesting quantities, but also the interval between the 25th and 75th percentile (see Section 4.3).

4.3 Results

In this Section, we show the results of the evolution of viscous and MHD populations of protoplanetary disks in the $M_d - \dot{M}$ plane: in particular, we consider the ratio of the two quantities (hereafter t_{lt}, disk lifetime - see Jones et al. 2012). We first discuss the expected evolution of the distribution of disk lifetimes from an analytical point of view (paragraph 4.3.1), and then we confirm our theoretical results through `Diskpop` simulations (paragraph 4.3.2); finally, we compare our results with the observations (paragraph 4.3.3).

4.3.1 Disk lifetimes distribution

In the traditional viscous picture (Dullemond et al. 2006, Lodato et al. 2017), disks lie on the theoretical isochrone (Equation 4.3) at a given age t if their initial viscous timescale $t_{\nu,0}$ is much shorter than t; as evolution proceeds, more and more disks reach this stage and therefore the population converges around the corresponding isochrone. As a consequence, the spread around the isochrones decreases with time: eventually, once the population is fully self-similar (i.e., its age is larger than all of the viscous timescales), the spread will be vanishingly small and the correlation between M_d and $\dot{M}$ will be perfectly linear. This trend is illustrated in the top panel of Figure 4.1: the solid lines show three theoretical isochrones at different ages, while the dots represent a synthetic population of 100 disks obtained with `Diskpop` evolving in time with the same colour coding. The aforementioned convergence to the theoretical isochrone starts as early as 1 Myr, while at 10 Myr the population is almost fully evolved and closely resembles the theoretical curve. From this argument, we can expect the moments of the distribution of t_{lt} to evolve in the viscous case as follows: (i) the mean value of t_{lt} will converge towards the actual age of the region, (ii) the spread will decrease until $t_\nu < t$ for every disk in the population, (iii) the skewness

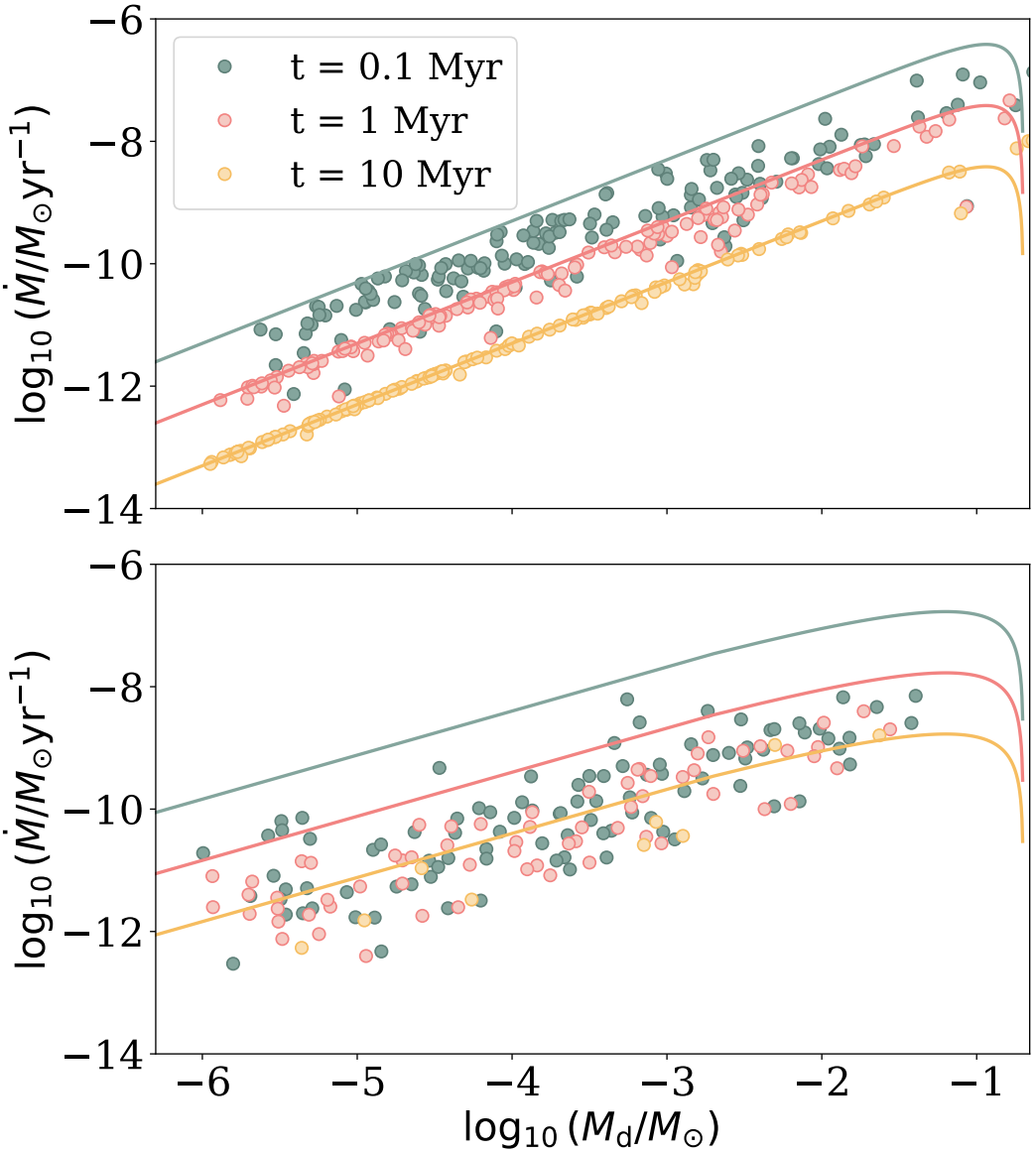

Figure 4.1: Time evolution of a synthetic population of disks, evolved via viscosity (top) or MHD winds (bottom), in the $M_{\rm d} - \dot{M}$ plane. The solid lines show the theoretical isochrones at ages 0.1, 1, and 10 Myr as per the legend, while the disks in the population at each age are represented by dots with the same colour coding. While viscous disks tend to converge to the same isochrone at evolved stages, MHD disks show a larger dispersion.

will increase. For a more detailed discussion on the expected and observed evolution of the skewness, we refer to Appendix 4.5.1.

The bottom panel of Figure 4.1 shows a synthetic population of disks evolved via MHD winds in the $M_{\rm d} - \dot{M}$ plane. As discussed in paragraph 4.2.2, the evolved population does not converge to the same isochrone: the large spread at all ages is such that making a prediction on the time evolution of the distribution of $t_{\rm lt}$ is not as straightforward as for a viscous population. Tabone et al. (2022b) have shown that, assuming an exponential distribution of $t_{\rm acc,0}$ (which is determined fitting the observed disk fraction), the distribution of $t_{\rm lt}$ does not depend on time; however, this result is specific of the exponential distribution. If we consider a different distribution of $t_{\rm acc,0}$, that of $t_{\rm lt}$ for an evolved population may depend on time: this is the case for our choice of a log-normal distribution of $t_{\rm acc,0}$, which can still reproduce both the disk and accretion fraction (see Appendix 4.5.2).

4.3.2 Mean and width

Figure 4.2 shows the time evolution of the mean (top) and width (bottom) of the distributions of $t_{\rm lt}$ for the viscous (blue) and MHD (yellow) models. The lighter shades of both models include an additional observational uncertainty, $\sigma_{\rm obs}$, that we implemented by adding an extra spread on the disk mass and the accretion rate, of 0.1 dex and 0.45 dex respectively (as an estimate of the observational uncertainty, see Manara et al. 2023, Testi et al. 2022). As stated in Section 4.2, we performed 100 runs for each simulation: the solid line represents the median, while the shaded areas around it show the 25th-75th percentile intervals. As the MHD model removes disks more effectively, the sample size decreases more than in the viscous case, making the statistical fluctuations between different simulations larger: this leads the yellow lines to have broader shaded areas.

Considering the mean values of the distributions, adding $\sigma_{\rm obs}$ only slightly shifts the curves for both the viscous and MHD case, resulting in a negligible difference. The two evolutionary models differ at early stages (< 1 Myr), but soon reach a common behavior that makes them indistinguishable within the 25th-75th percentile intervals. On the other hand, the widths of the distribution (bottom panel) significantly differ from one case to the other. The viscous case without additional uncertainty (darker blue) steeply decreases, as expected from viscous theory (Lodato et al., 2017) and discussed in paragraph 4.3.1. This is not the case for the MHD prescription (orange): while the general trend is still decreasing, it is not as steep as the viscous, and ultimately does not tend to zero but rather to an evolved value determined by the initial conditions.

The convolution with observational uncertainty in the viscous case (light blue) significantly shifts the curve up, as well as modifying its shape. The total width of the distribution is the root sum squared of the intrinsic spread ($\sigma_{\rm int}$) and the observational uncertainty ($\sigma_{\rm obs}$), $\sigma_{\rm tot} = \sqrt{{\sigma_{\rm int}}^2 + \sigma_{\rm obs}^2}$. The intrinsic spread $\sigma_{\rm int}$, given by the initial conditions, tends to zero as discussed above: therefore, we expect the final width to tend to

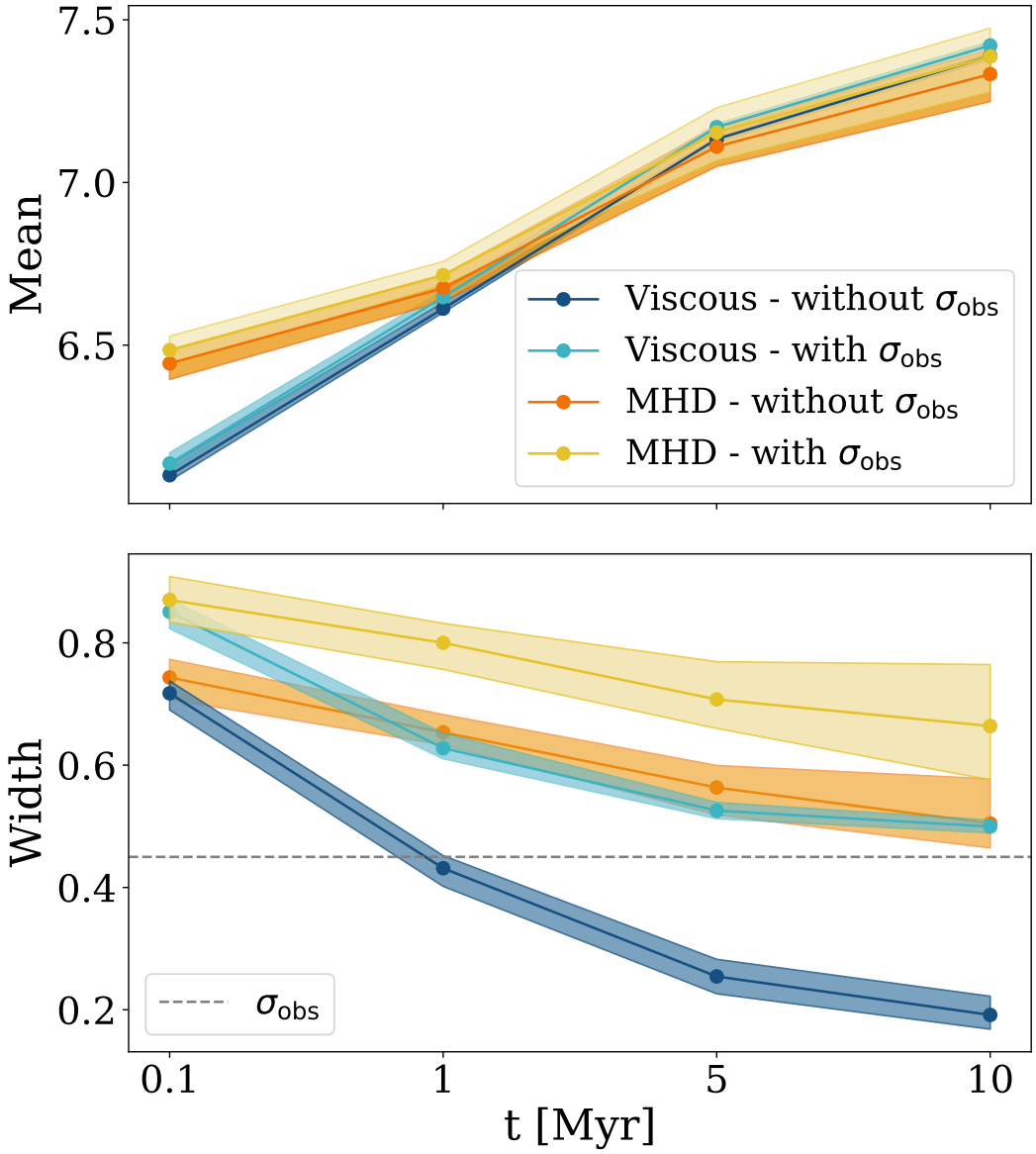

Figure 4.2: Time evolution of the mean (top) and width (bottom) of the distribution of $t_{\rm lt}$ for a synthetic population of protoplanetary disks. The solid lines represent the median values, while the shades cover the interval between the 25th and 75th percentile out of 100 simulations (to account for the statistical effect of disk removal). The blue and yellow lines refer to the viscous and MHD model respectively, with the lighter shades including the observational uncertainty. While the mean value of the distributions is not much affected by the presence of such uncertainty or the choice of the model, the spread shows quite some difference, exhibiting significantly higher values in the MHD than in the viscous case. The dashed line in the bottom panel marks the observational uncertainty.

$\sigma_{\rm obs}$, which is exactly what we recover. This causes the evolved population to have a significantly larger spread than that predicted by theory. On the contrary, despite still being shifted at larger values as an effect of the additional uncertainty, in the MHD case (yellow) the shape of the curve is not dramatically modified. This is because $\sigma_{\rm int}$ is comparable to $\sigma_{\rm obs}$ at all times, which makes this argument strongly dependent on the initial condition: as the total spread is given by $\sqrt{{\sigma_{\rm int}}^2 + {\sigma_{\rm obs}}^2}$, the behaviour of the MHD case will only be significantly different from the viscous case if $\sigma_{\rm int}$ is non negligible with respect to $\sigma_{\rm obs}$. In our previous work (Somigliana et al., 2022) we have shown how initial spreads of 0.65 dex and 0.52 dex for $M_{\rm d}$ and $R_{\rm d}$ respectively are able to reproduce the observed spreads around the correlations with the stellar masses; therefore, we set these values for the MHD simulation, while we choose a bigger spread of 1 dex for the viscous case, as it can better reproduce the observed values (see 4.3.3).

As mentioned in Section 4.2.3, the purely viscous model does not account for disk dispersal. Without exploring the whole parameter space, which is beyond the scope of this Letter, we have run a test model with photoevaporation, assuming the standard model of Owen et al. (2010), with a mass-loss rate of 10^{-10} $\rm M_\odot$ $\rm yr^{-1}$ following the latest constraints (Alexander et al., 2023). The mean and the width of the distribution of $t_{\rm lt}$ increase with respect to the purely viscous case, but the difference is minimal and becomes negligible including the observational uncertainty; therefore, our conclusions are not affected.

4.3.3 Comparison with the observations

In paragraph 4.3.2 we have shown the viscous and MHD predictions for the time evolution of the mean and width of the distribution of $t_{\rm lt}$; in this paragraph, we compare our results with observations of different star-forming regions. We used the table[1] compiled by Manara et al. (2023) for Taurus, Lupus, Chameleon I and Upper Sco, and the data by Testi et al. (2022) for L1688 (to limit the contamination from sub-populations with different ages in the Ophiuchus complex).

Before commenting on the comparison itself, it is important to note that our simulations do not include dust evolution, making our definition of disk mass solely based on the *gas* content of disks; on the other hand, the observed disk masses rely on sub-mm fluxes, tracing the *dust* content instead. As the bulk of disk masses is in the gaseous phase, inferring the total mass from dust observations requires to i) constrain the dust-to-gas ratio in disks and ii) assume optically thin emission; however, as the accuracy of these assumptions is debated, the community is striving towards obtaining more reliable disk mass estimates (see Bergin et al. 2013, McClure et al. 2016 for HD observations; Veronesi et al. 2021 for dynamical measurements; Anderson et al. 2022, Trapman et al. 2022 for a combination of gaseous tracers). The results of the ALMA Large Programs AGE-PRO and DECO will further contribute to this goal; moreover, the advent of the ALMA Band 1 and ngVLA will allow to move to longer wavelengths, where dust emission is less optically

[1]The table is available at http://ppvii.org/chapter/15/.

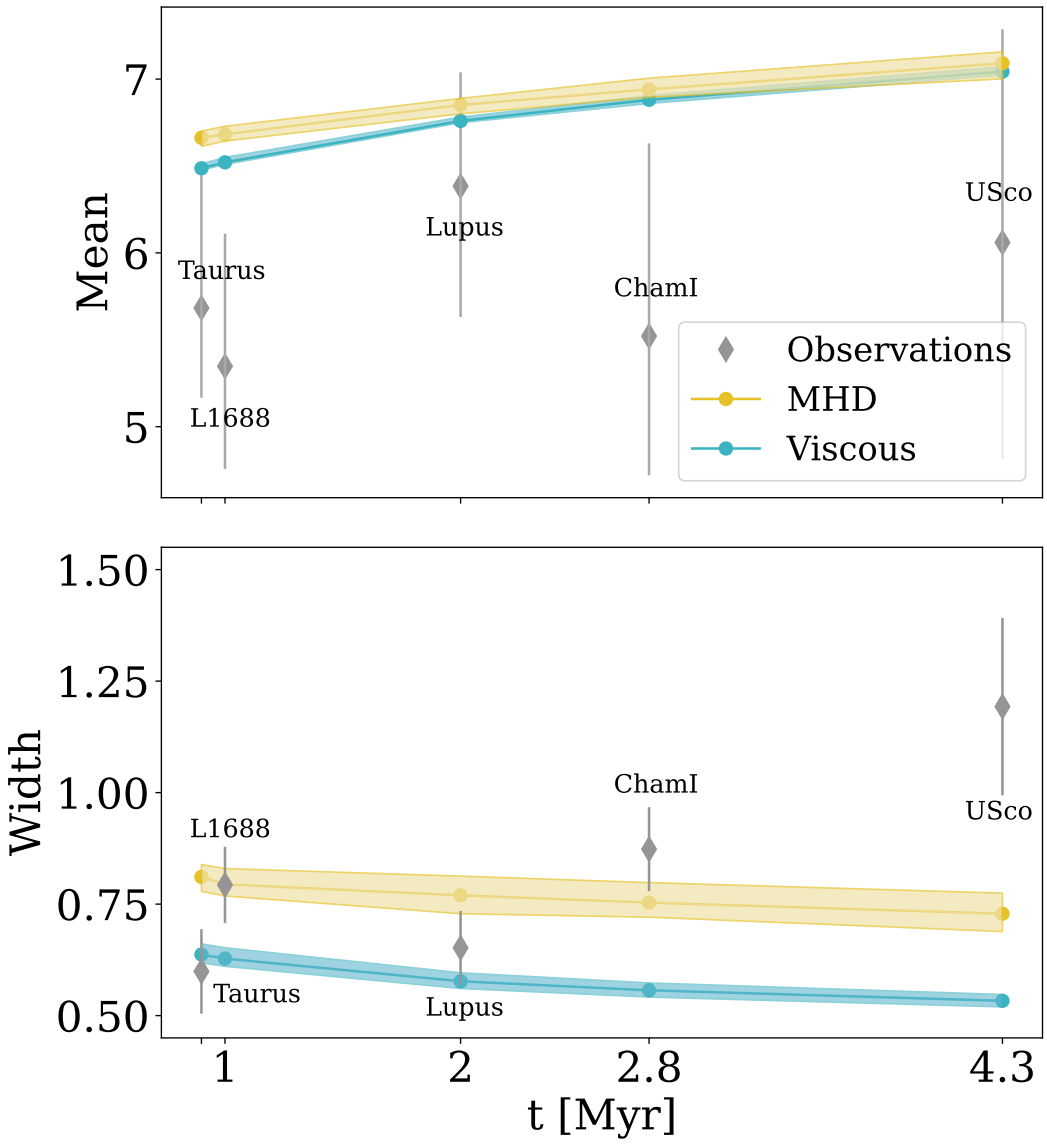

Figure 4.3: Comparison of the evolution of the mean (top) and width (bottom) for the viscous (blue) and MHD (yellow) models, including observational uncertainties, with the observations (grey diamonds). The shaded areas are as in Figure 4.2, while the grey bars represent the interval between the 16th and 84th percentiles (top) and the uncertainty on the width (bottom). While both models overestimate the mean values (see text for details), the evolution of the width of the distribution suggests a better match with the MHD model.

thick (Tazzari et al., 2021). In light of these forthcoming developments, our work can be considered a prediction that will be interpreted to its full potential with the results of this observational effort. The data comparison presented in the following is therefore intended as a state-of-the-art, which we anticipate to revise in the near future.

Figure 4.3 shows the result of our comparison: the mean and width of the distribution are shown in the top and bottom panel respectively, and both include the viscous and MHD (blue and yellow line, as in Figure 4.2 and 4.5) numerical evolution. The grey diamonds represent the observed star-forming regions. None of the two evolutionary mechanisms reproduces the observed mean values, which are systematically lower. A potential reason for this mismatch could be an underestimation of disk masses; a difference of a factor as little as 3 in the observed masses would be sufficient to explain the discrepancy with the models - confirming the need to repeat this comparison with more accurate disk masses estimates. Moreover, Zagaria et al. (2022a) have shown how taking stellar multiplicity into account can explain the high accretors in Upper Sco; we expect this effect to shift the theoretical prediction to lower values of $t_{\rm lt}$ for evolved populations. Dust growth and evolution prescriptions, which were not included in this work, are also likely to play a role as they can better explain the observed disk mass - accretion rate correlation (Sellek et al., 2020a). The width of the distribution, on the other hand, provides more interesting results. The viscous prediction manages to marginally recover observed values at the earliest evolutionary stages, but as such values increase in time, the discrepancy with the viscous expectation grows larger and larger. This result was already anticipated by Manara et al. (2020) (see also Manara et al. 2023). It should be kept in mind that our viscous simulations have a $\sigma_{\rm int}$ of 1 dex for both the disk mass and radius (see Table 4.1 and 4.2); as large as the intrinsic spread can be, the steeply decreasing viscous trend will always evolve the width of the distribution to $\sigma_{\rm obs}$. The MHD simulation instead falls within the error bars of the earliest observed star-forming region, up until ages on $\sim$ 2.5 Myr. There is an increasing discrepancy for more evolved populations, up until around 20% for Upper Sco; however, the oldest populations also represent the less complete samples, and therefore they carry a significant bias that should be kept in mind when comparing with simulations. Moreover, there are caveats to our own simulations, as in the viscous case we neglect disk dispersal mechanisms (such as internal or external photoevaporation, e.g. Malanga et al. in prep.) and only consider a detection threshold in disk masses.

4.4 Discussion and conclusions

In this work, we have investigated how the time evolution of the distribution of a population of disks in the $M_{\rm d} - \dot{M}$ plane is impacted by the evolutionary model, considering the viscous and MHD prescriptions respectively. We have presented a combination of analytical considerations and numerical simulations, performed through the 1D population synthesis code `Diskpop`, in the case of a log-normal distribution of initial accretion timescales (which reproduces both the disk and accretion fraction). We find that, while the mean of the dis-

tribution of $t_{\rm lt} = M_{\rm d}/\dot{M}$ is not significantly impacted by the chosen model, the expected behaviour of the width shows considerable differences depending on the evolutionary prescription; when including the observational biases in the form of additional uncertainty, this distinctive behaviour is maintained.

Our predictions will be exploited to their full potential through a comparison with the results of the current observational effort to obtain direct estimates of disk gas masses; for the time being, we compare our evolutionary trends with the latest available observational data (based on dust observations) in different star-forming regions. We find that the purely viscous case only manages to marginally reproduce the observations at the earliest ages, while the MHD curve resembles them better. Based on these results, we suggest the analysis of these distributions as a viable method to disentangle between the viscous and MHD evolutionary models; our data comparison hints at a better agreement with the MHD model.

Acknowledgments

We thank an anonymous referee for their comments that helped us improving the clarity of the manuscript. This work was partly supported by the Italian Ministero dell'Istruzione, Università e Ricerca through the grant Progetti Premiali 2012-iALMA (CUP C52I13000140001), by the Deutsche Forschungsgemeinschaft (DFG, German Research Foundation) - Ref no. 325594231 FOR 2634/2 TE 1024/2-1, by the DFG Cluster of Excellence Origins (www.origins-cluster.de). This project has received funding from the European Union's Horizon 2020 research and innovation program under the Marie Sklodowska- Curie grant agreement No 823823 (DUSTBUSTERS) and from the European Research Council (ERC) via the ERC Synergy Grant ECOGAL (grant 855130), ERC Starting Grant DiscEvol (grant 101039651) and ERC Starting Grant WANDA (grant 101039452). Views and opinions expressed are however those of the author(s) only and do not necessarily reflect those of the European Union or the European Research Council Executive Agency. Neither the European Union nor the granting authority can be held responsible for them. B.T. acknowledges support from the Programme National 'Physique et Chimie du Milieu Interstellaire' (PCMI) of CNRS/INSU with INC/INP and cofunded by CNES.

4.5 Appendix

4.5.1 Skewness of the distribution

The skewness of a distribution, defined as the third standardized moment, measures the asymmetry of the distribution about its mean. As we mentioned in paragraph 4.3.1, alongside the mean value and the width, in the viscous case we expect also the skewness of the distribution of $t_{\rm lt}$ to evolve in time; in this Appendix we discuss this theoretical expectation and show the results of our numerical simulations.

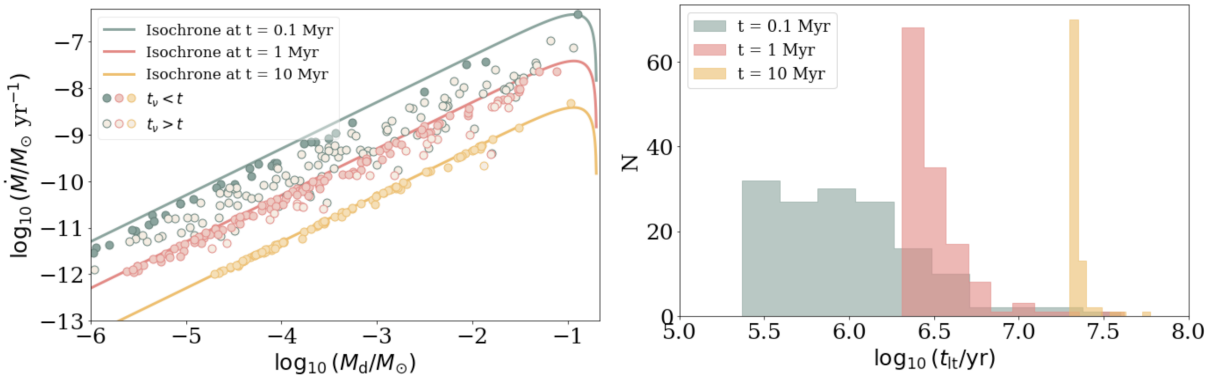

Figure 4.4: Time evolution of a synthetic population of viscous disks in the $M_\mathrm{d} - \dot{M}$ plane (left panel) and corresponding histograms of t_lt (right panel). The color coding is as in Figure 4.1. Full dots represent disks whose initial viscous timescale is shorter than the age of the population, and that can therefore be considered evolved.

The left panel of Figure 4.4 shows a population of viscously evolving disks (dots) at three subsequent ages, as well as the corresponding theoretical isochrones (solid lines). Full dots represent disks whose initial viscous timescale is shorter than the age of the population, which as a whole can therefore be considered evolved: from viscous theory, such disks are expected to have reached the self-similar condition and lie on the analytical isochrone, i.e., to show a linear correlation between the disk mass and the accretion rate. On the other hand, empty dots represent not-yet-evolved disks, which lie below the theoretical isochrone. As the population evolves, more disks satisfy the $t_\nu < t$ condition, as can be visualised by the increasing number of full dots in Figure 4.4; this implies that more disks lie on the theoretical isochrone, bringing the population on the $M_\mathrm{d} - \dot{M}$ plane closer to a line. While this causes the width of the distribution of t_tl to decrease with time, the skewness on the other hand increases - as we show in the right panel of Figure 4.4, which represents the corresponding histograms at all ages. This skewing effect is due to the fact that younger disks, which do not lie on the isochrone yet, have a t_lt *longer* than the actual age of the region, and therefore contribute to positively skew the distribution - while evolved disks, which make up the bulk of the population, cluster close to the mean value. Figure 4.5 shows the evolution of the skewness of a population of disks generated and evolved with `Diskpop` with the same colour coding and shaded areas as Figure 4.1; the left panel represents the case with no observational uncertainty, where the viscous distribution (blue) gets more and more skewed as expected, growing by a factor of 2 between 0.1 and 10 Myr. On the other hand, the MHD distribution (orange) remains symmetrical within the 25th-75th percentile for the whole evolution, resulting in a factor 3 difference from the viscous model for evolved populations. As significant as this theoretical difference is, including the observational biases (right panel) completely smooths it out: the two expected observed behaviours are indistinguishable once convoluted with the additional observational uncertainties.

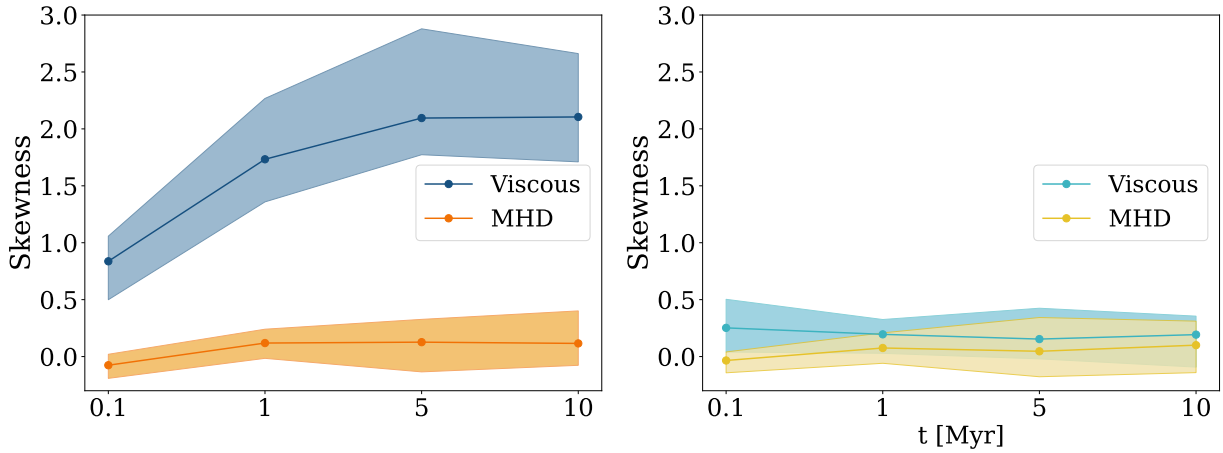

Figure 4.5: Time evolution of the skewness of the distribution of $t_{\rm lt}$ for a synthetic population of protoplanetary disks, with the same colour coding as Figure 4.2. Both panels show the comparison between the viscous and MHD models, without (left) and with (right) the additional observational uncertainty $\sigma_{\rm obs}$. Despite the theoretical predictions of the two models being significantly different (left panel), the convolution with observational biases completely smooths them out (right panel).

In conclusion, while the evolution of the skewness makes an interesting theoretical argument stemming from the different interpretation of isochrones in the two models, it does not provide a reliable method to compare viscosity and MHD from the observational point of view.

4.5.2 Time evolution of the distribution of $t_{\rm lt}$

As $t_{\rm lt}$ depends on $t_{\rm acc,0}$ as $t_{\rm lt} = (1 + f_M)(2t_{\rm acc,0} - \omega t)$, the evolved distribution of $t_{\rm lt}$ is determined by the choice of initial distribution of $t_{\rm acc,0}$: Tabone et al. (2022b) have shown that, choosing an exponential distribution for $t_{\rm acc,0}$, the corresponding distribution of $t_{\rm lt}$ reads

$$\frac{dP}{dt_{\rm lt}} = \frac{1}{\omega\tau(1+f_M)} \exp\left(-\frac{t_{\rm lt}}{(1+f_M)\omega\tau}\right) f_D(t), \tag{4.5}$$

where f_M is defined in Tabone et al. (2022a) and $\tau = 2.5$ Myr to fit the disk fraction, $f_D(t) = \exp(-t/\tau)$. As f_D is only a normalisation factor, (4.5) still have an exponential shape; moreover, it does not depend on time, as well as its mean value. On the other hand, if we pick a log-normal distribution for $t_{\rm acc,0}$, we can still reproduce both the disk and the accretion fraction (see Appendix 4.5.3) but in that case the evolved distribution of $t_{\rm lt}$ becomes

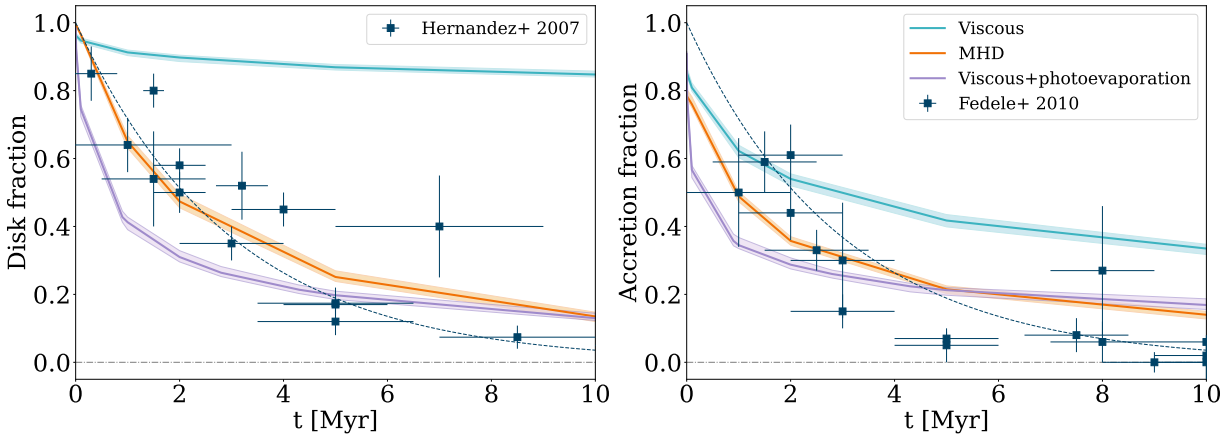

Figure 4.6: Disk and accretion fraction (left and right panel respectively) in our viscous (light blue), MHD (orange) and viscous+photoevaporation (lilac) simulations, compared with data by Hernández et al. (2007) and Fedele et al. (2010) (blue squares). The shaded areas are as in Figure 4.2. The dashed blue lines show the exponential fits to the data. Following the original paper, we define the accretion fraction as the fraction of sources with accretion rate higher than 10^{-11} $M_\odot$/yr. Our choice of a log-normal distribution of initial accretion timescales for the MHD model reproduces both the disk and accretion fraction, as does the exponential distribution chosen by Tabone et al. (2022b). The viscous model does not reproduce any of the fractions due to the lack of a disk dispersal mechanism, while including internal photoevaporation allows to recovered the observed behaviour.

$$\frac{dP}{dt_{\rm lt}} = \frac{1}{\sqrt{2\pi\sigma^2}} \frac{1}{t_{\rm lt} + (1+f_M)\omega t} \exp\left\{-\frac{1}{2\sigma^2}\left[\log\left(\frac{t_{\rm lt}}{2(1+f_M)} + \frac{\omega t}{2}\right) - \mu\right]^2\right\}, \tag{4.6}$$

where μ and σ are the mean value and width of the initial log-normal distribution. Notice that Equation (4.6) is not a log-normal in $t_{\rm lt}$; moreover, it does depend on time, and so does its mean value and spread.

4.5.3 Impact of internal photoevaporation

As mentioned in the main paper, disk dispersal in an intrinsic feature of MHD winds. These models manage to reproduce both the disk and accretion fraction, defined as the fraction of young stars with infrared excess (Hernández et al., 2007) and accreting (i.e., with $\dot{M} > 10^{-11}$ $M_\odot$ yr^{-1} following Fedele et al. 2010) objects respectively, as shown by the orange lines in Figure 4.6. On the other hand, purely viscous models do not account for disk dispersal. This leads to a mismatch between the predicted and observed disk and accretion fraction, represented by the blue lines in Figure 4.6: the disk fraction is almost constant to 1, the little decrease being due to the observational threshold that we

introduced in our simulations (considering dispersed disks with masses lower than 10^{-6} $M_\odot$, see Section 4.2.3), while the accretion fraction does decrease, but not enough to match the observed values. This problem is usually overcome in the literature by including internal photoevaporation, a two-timescale process that introduces a disk dispersal mechanism, allowing to reproduce the observations as shown by the purple lines in Figure 4.6. We ran the test simulation presented in this Appendix using the standard photoevaporative model of Owen et al. (2012), with a mass-loss rate of 10^{-1-} $M_\odot$ yr^{-1}, consistent with the latest constraints (Alexander et al., 2023).

Once internal photoevaporation kicks in, it lowers the accretion rates for a given disc mass, introducing therefore a spread in the $M_d - \dot{M}$ plane (Somigliana et al., 2020); therefore, it could in principle affect the conclusions of this work. However, we have tested that the mean and width of the t_{lt} distribution in the presence of photoevaporation do not significantly deviate from the purely viscous prediction; without observational spread the photoevaporative case lies between the viscous and MHD models, and becomes indistinguishable from the viscosity when the observational spread is included.

5

The evolution of the $M_{\rm d} - M_\star$ and $\dot{M} - M_\star$ correlations traces protoplanetary disc dispersal

Published as
Somigliana et al., 2024, A&A, Volume 689, p. A285

Full authors list:
Alice Somigliana; Leonardo Testi; Giovanni Rosotti; Claudia Toci; Giuseppe Lodato; Rossella Anania; Benoît Tabone; Marco Tazzari; Ralf Klessen; Ugo Lebreuilly; Patrick Hennebelle; Sergio Molinari.

Observational surveys of entire star-forming regions have provided evidence of power-law correlations between the disc properties and the stellar mass, especially the disc mass ($M_{\rm d} \propto {M_\star}^{\lambda_{\rm m}}$) and the accretion rate ($\dot{M} \propto {M_\star}^{\lambda_{\rm acc}}$). Whether the secular disc evolution affects said correlations is still debated: while the purely viscous scenario has been probed, other mechanisms could impact differently. We study the evolution of the slopes $\lambda_{\rm m}$ and $\lambda_{\rm acc}$ in the wind-driven and hybrid case and compare it to the viscous prediction, using a combination of analytical calculations and numerical simulations (performed with the 1D population synthesis code Diskpop, that we also present and release). Assuming $M_{\rm d(0)} \propto {M_\star}^{\lambda_{\rm m,0}}$ and $\dot{M}(0) \propto {M_\star}^{\lambda_{\rm acc,0}}$ as initial conditions, we find that viscous and hybrid accretion preserve the shape of the correlations and evolve their slope; on the other hand, MHD winds change the shape of the correlations, bending them according to the scaling of the accretion timescale with the stellar mass. We also show how a spread in the initial conditions conceals this behaviour. We then analyse the impact of disc dispersal, and find that the currently available sample sizes (~ 30 discs at 5 Myr) introduce stochastic oscillations in the slopes evolution, which dominate over the physical signatures. Increasing the sample size could mitigate this issue: ~ 140 discs at 5 Myr, corresponding to the complete Upper Sco sample, would give small enough error bars to use the evolution of the slopes as a proxy for the driving mechanism of disc evolution. Finally, we discuss how the observational claim of steepening slopes necessarily leads to an initially steeper $M_{\rm d} - M_\star$ correlation with respect to $\dot{M} - M_\star$.

5.1 Introduction

The secular evolution of protoplanetary discs is deeply intertwined with both the planet formation process (Morbidelli et al., 2012) and the accretion onto the central protostar (Hartmann et al., 1998). Planetesimals, the building blocks of planets, form and evolve within the disc following the dynamics of either the gaseous or solid component, depending on their relative size and their coupling (or lack thereof) with the gas particles; on the other hand, the protostar is fed by the disc itself, through the accretion of material that loses angular momentum and drifts inwards. The ideal ground to explore the connection between protoplanetary discs and their host stars is provided by large surveys of entire star-forming regions, targeting the properties of both discs and protostars; the last decade has seen a significant observational effort in the direction of these population-level studies, also thanks to the advent of facilities such as the Atacama Large Millimeter Array (ALMA) (see the PPVII reviews by Manara et al. 2023; Miotello et al. 2023).

Disc masses and accretion rates are arguably the most studied integrated disc properties. Accretion rates are inferred from the spectra of the central stars, which show an excess emission (especially prominent in the UV) when accretion is taking place; surveys performed across different star-forming regions (Muzerolle et al., 2003; Natta et al., 2004; Mohanty et al., 2005; Dullemond et al., 2006; Herczeg & Hillenbrand, 2008; Rigliaco et al., 2011; Manara et al., 2012; Alcalá et al., 2014; Manara et al., 2016a; Alcalá et al., 2017; Manara et al., 2017b; Venuti et al., 2019b; Manara et al., 2020) agree on the presence of a power-law correlation between the accretion rate and the stellar mass, $\dot{M} \propto {M_\star}^{\lambda_{\rm acc,obs}}$ (following the notation of Somigliana et al. 2022). On the other hand, disc masses have traditionally been determined from observations of the sub-millimetre continuum emission of the solid component of discs; due to the large number of assumptions involved in converting fluxes into total disc masses (see Miotello et al. 2023), one of the current main goals of the protoplanetary disc community is the accurate determination of total disc masses - both from dynamical constraints (Veronesi et al., 2021; Lodato et al., 2023) and direct measurements of the total gas content (e.g. Bergin et al. 2013; Anderson et al. 2022; Trapman et al. 2022). Despite the systematic uncertainties involved in their determination, dust-based disc masses also seem to show a power-law correlation with the stellar mass, $M_{\rm d} \propto {M_\star}^{\lambda_{\rm m,obs}}$, across different star-forming regions (Ansdell et al., 2016, 2017; Barenfeld et al., 2016; Pascucci et al., 2016; Testi et al., 2016, 2022; Sanchis et al., 2020).

The existence of the disc mass-stellar mass and accretion rate-stellar mass correlations is now generally accepted; however, there is no consensus on the physical reason behind their establishment and their evolution with time. While the $\dot{M} - M_\star$ correlation appears to have a roughly constant slope[1] of $\lambda_{\rm acc,obs} \approx 1.8 \pm 0.2$ (as first suggested by Muzerolle et al. 2003 and supported by many of the following works mentioned above), the $M_{\rm d} - M_\star$ correlations is claimed to be steepening with time (Ansdell et al., 2017), from the lowest

[1]Throughout this work, we use *slope* as a synonym for the power-law index, referring to the correlations in the logarithmic plane.

$\lambda_{\rm m,obs}(t \sim 1\ {\rm Myr}) = 1.7 \pm 0.2$ (Taurus) to the highest $\lambda_{\rm m,obs}(t \sim 5\ {\rm Myr}) = 2.4 \pm 0.4$ (Upper Sco). Whether these correlations reflect the initial conditions of disc populations, or are rather a product of the secular evolution, is still under debate. Both possibilities have been discussed for the $\dot{M} - M_\star$ correlation: Alexander & Armitage (2006) assumed it to hold as an initial condition, favouring the correlation to be present in young populations, whereas Dullemond et al. (2006) derived it from a simple model of disc formation from a rotating collapsing core, which provided an explanation for evolved disc populations. At the same time, the claimed increase in the slope of $M_{\rm d} - M_\star$ does suggest an evolutionary trend; Somigliana et al. (2022) have found that, assuming power-law correlations between both $M_{\rm d}$ and $\dot{M}$ and the stellar mass as initial conditions, secular evolution can indeed alter the slopes of the correlations themselves (see Section 5.3 for details). However, their analysis was limited to the standard viscous evolution paradigm, whereas the driving mechanism of accretion is far from being constrained (see Manara et al. 2023 for a review).

The traditional viscous accretion model prescribes a macroscopic viscosity as the cause of redistribution of angular momentum within the disc (Lynden-Bell & Pringle, 1974; Pringle, 1981). In this scenario, while part of the material loses angular momentum and moves radially closer to the star, other material gains the same amount of angular momentum and moves further away, increasing the disc size. The viscous paradigm can explain many key features of disc evolution, but it cannot account for disc dispersal - as determined from the observational evidence of an exponentially decreasing fraction of both disc-bearing (Hernández et al., 2007) and accreting (Fedele et al., 2010) sources in star-forming regions with time; furthermore, the low levels of turbulence detected in discs (Pinte et al., 2016; Flaherty et al., 2018; Rosotti, 2023) appear incompatible with the observed evolution. While the discrepancy in the disc and accretion fraction can be mended considering mechanisms such as internal or external photoevaporation (Alexander et al., 2014; Winter et al., 2018), which effectively clear discs on timescales comparable with the observed decline, the tension between the expected and observed amount of turbulence does not appear to have been solved yet. On the other hand, the magneto-hydrodynamic (MHD) disc winds' scenario offers a promising alternative. Pioneering work (Blandford & Payne, 1982; Ferreira, 1997) supported by recent numerical simulations (e.g. Béthune et al. 2017) demonstrated that MHD winds launched from the disc surface have the net effect of removing angular momentum as a consequence of the extraction of material; MHD wind-driven accretion can even lead to disc dispersal (Armitage et al., 2013; Tabone et al., 2022b). Following disc evolution at a population level in numerical simulations remains out of reach; however, 3D core-collapse simulations have shown how non-ideal magneto-hydrodynamics and ambipolar diffusion play a fundamental role in shaping the resulting population of early-type young stellar objects (Lebreuilly et al., 2021, 2024). While some 3D studies of isolated disc formation have attempted to bridge the gap between Class 0/I and Class II stages (Machida & Hosokawa, 2013; Hennebelle et al., 2020; Xu & Kunz, 2021a,b; Machida & Basu, 2024; Mauxion et al., 2024), the high numerical cost of the simulations for 3D population synthesis does not allow one to follow the evolution of the discs up to very evolved stages where they can be considered isolated from the surrounding

environment. MHD wind-driven disc populations can however be modelled in 1D using simple prescriptions as proposed by Suzuki et al. (2016) or Tabone et al. (2022a). Detecting characteristic signatures of either of the two evolutionary prescriptions is a compelling issue (Long et al., 2022; Alexander et al., 2023; Somigliana et al., 2023; Trapman et al., 2023; Coleman et al., 2024).

In the context of the evolution of the correlations between the disc properties and the stellar mass, while the purely viscous scenario has been extensively studied by Somigliana et al. (2022), the wind-driven paradigm remains unexplored; with this paper, we address this deficiency and investigate the impact of MHD wind-driven evolution on the $M_{\rm d} - M_\star$ and $\dot{M} - M_\star$ correlations, with a particular focus on their time evolution. We also extend the work of Somigliana et al. (2022) by including internal photoevaporation to the viscous framework. We employ numerical simulations of populations of protoplanetary discs, performed with the population synthesis code `Diskpop`, which we also introduce and release to the community.

The paper is structured as follows: in Section 5.2, we present `Diskpop` and describe its main features, set up and solution algorithm; in Section 5.3, we discuss the time evolution of the $M_{\rm d} - M_\star$ and $\dot{M} - M_\star$ correlations in three evolutionary scenarios from the theoretical perspective; in Section 5.4, we show the impact of a spread in the initial conditions and dispersal mechanisms on the evolution of the slopes, and we present the numerical results obtained from realistic disc population synthesis; in Section 5.5 we interpret the implications of our findings in the context of the observational determination of the slopes, and finally in Section 5.6 we draw the conclusions of this work.

5.2 Numerical methods: `Diskpop`

In this Section we present the 1D population synthesis code `Diskpop`[2]. We describe the master equation for the secular evolution of discs (Section 5.2.1), the initial conditions to generate a synthetic population (Section 5.2.2), the solution algorithm (Section 5.2.3), and the user interface and output (Section 5.2.4). For a more detailed description, we refer to the code documentation; for a validation of the code, see Appendix 5.7.3.

[2] `Diskpop` and the output analysis library `popcorn` can be installed via the Python Package Index, `pip install diskpop` and `pip install popcorn_diskpop`. The full documentation and tutorials are available at https://alicesomigliana.github.io/diskpop-docs/index.html. If you use `Diskpop` in your work, please cite this paper (Somigliana et al. 2024).

5.2.1 Master equation

The master equation of protoplanetary disc evolution,

$$\frac{\partial \Sigma}{\partial t} = \frac{3}{r}\frac{\partial}{\partial r}\left[\frac{1}{\Omega r}\frac{\partial}{\partial r}\left(r^2 \alpha_{\rm SS} \Sigma {c_s}^2\right)\right] + \frac{3}{2r}\frac{\partial}{\partial r}\left[\frac{\alpha_{\rm DW}\Sigma {c_s}^2}{\Omega}\right] - \frac{3\alpha_{\rm DW}\Sigma {c_s}^2}{4(\lambda-1)r^2\Omega} - \dot{\Sigma}_{\rm photo}, \tag{5.1}$$

describes the time evolution of the gas surface density in the most general framework, where Σ is the gas surface density, Ω the Keplerian orbital frequency, $\alpha_{\rm SS}$ the Shakura & Sunyaev (1973) α parameter, $\alpha_{\rm DW}$ the MHD equivalent of $\alpha_{\rm SS}$ (Tabone et al., 2022a), c_s the sound speed, and λ the magnetic lever arm parameter, which quantifies the ratio of extracted to initial specific angular momentum. The four terms on the right hand side (RHS) refer to (i) the viscous torque, whose strength is parameterised by $\alpha_{\rm SS}$, (ii) the wind-driven accretion, which corresponds to an advection term, parameterised by $\alpha_{\rm DW}$, (iii) mass loss due to MHD disc winds, parameterised by λ and (iv) mass loss due to other physical phenomena (in our case, we consider internal and external photoevaporation). Depending on the values of the specific parameters, Equation (5.1) can describe a purely viscous ($\alpha_{\rm DW} = 0$), purely MHD wind-driven ($\alpha_{\rm SS} = 0$) or hybrid ($\alpha_{\rm SS}, \alpha_{\rm DW} \neq 0$) evolution, with ($\dot{\Sigma}_{\rm photo} \neq 0$) or without ($\dot{\Sigma}_{\rm photo} = 0$) the influence of photoevaporation. In the following, we briefly describe the various evolutionary scenarios and the available analytical solutions.

Viscously evolving discs. In the case of purely viscous evolution, the MHD winds parameter $\alpha_{\rm DW}$ is set to zero. If we also neglect the influence of photoevaporation, Equation (5.1) reduces to the first term on the RHS and its solution depends on the functional form of the effective viscosity, parameterised as $\nu = \alpha_{\rm SS} c_s H$ (where H is the vertical height of the disc). A popular analytical solution for viscous discs is the Lynden-Bell & Pringle (1974) self-similar solution, which assumes viscosity to scale as a power-law of the radius ($\nu \propto R^{\gamma}$).

MHD winds-driven evolution. There are two classes of analytical solutions to Equation (5.1) in the MHD wind-driven scenario, associated with a specific prescription of $\alpha_{\rm DW}$ (Tabone et al., 2022a). We briefly describe their key features, and refer to the original paper for their derivation and an in-depth discussion.

1. The simplest class of solutions (so-called *hybrid solutions*), which highlight the main features of wind-driven accretion in comparison to the viscous model, assume a constant $\alpha_{\rm DW}$ with time; these solutions depend on the value of $\psi \equiv \alpha_{\rm DW}/\alpha_{\rm SS}$, which quantifies the relative strength of the radial and vertical torque.

2. Another class of solutions, which describe the unknown evolution of the magnetic field strength, assume a varying $\alpha_{\rm DW}$ with time. To obtain these, Tabone et al. (2022a) parameterised $\alpha_{\rm DW}(t) \propto \Sigma_{\rm c}(t)^{-\omega}$, with $\Sigma_{\rm c} = M_{\rm d}(t)/2\pi {R_c}^2(t)$ (where R_c is a

characteristic radius) and ω as a free parameter, and neglect the radial transport of angular momentum ($\alpha_{\rm SS} = 0$).

Photoevaporation. The generic $\dot{\Sigma}_{\rm photo}$ term in Equation (5.1) allows to account for photoevaporative processes, both internal and external. The exact form of $\dot{\Sigma}_{\rm photo}$ depends on the specific model considered; therefore, the availability (or lack thereof) of analytical solutions needs to be considered case by case.

`Diskpop` allows populations of discs to be evolved analytically. In particular, as of this release, it includes implementations of the Lynden-Bell & Pringle (1974) self-similar solution and all the analytical solution proposed by Tabone et al. (2022a). In the cases where Equation (5.1) cannot be solved analytically, the code relies on the solution algorithm described in Section 5.2.3.

5.2.2 Initial conditions and parameters

Every `Diskpop` simulation begins with the generation of a synthetic population of Young Stellar Objects (YSOs). Each YSO constitutes of a star and a disc, whose key initial parameters (stellar mass, disc mass, accretion rate, disc radius, evolutionary parameters $\alpha_{\rm SS}$, $\alpha_{\rm DW}$, λ, ω...) can be set by the user. In the following, we describe the standard case where we consider the stellar masses to be distributed according to an Initial Mass Function (IMF) and correlating with the disc mass and radius, and briefly mention the other possible choices; for a deeper discussion, we refer to the `Diskpop` documentation.

`Diskpop` assembles YSOs by determining their parameters as follows:

1. **Stellar mass $M_\star$:** determined following the Kroupa (2001) IMF. Other possible choices are a constant mass for all the stars in the population, or a set of custom stellar masses.

2. **Initial disc mass $M_{\rm d}$, accretion rate $\dot{M}$:** determined from log-normal distributions of given width and mean value. In the standard case, `Diskpop` considers an initial power-law correlation between the initial $M_{\rm d}$ and $\dot{M}$ and the stellar mass (see Section 5.3.1 for a detailed discussion), where the normalisation at 1 $M_\odot$, the slope and the scatter around the power-laws are free parameters. If the correlations with the stellar mass are neglected, the user sets the mean value and spread of the distributions.

3. **Accretion parameters ($\alpha_{\rm SS}$, $\alpha_{\rm DW}$, λ, ω):** global properties of the whole population, given as input from the user. By setting the parameters controlling accretion, `Diskpop` determines the disc radius $R_{\rm d}$ and accretion timescale $t_{\rm acc}$ - which are instead disc-specific and linked to the disc mass and accretion rate.

4. **Internal photoevaporation parameters ($\dot{M}_{\rm wind}$, L_X):** the total photoevaporative mass-loss rate, $\dot{M}_{\rm wind}$, can either be set by the user or computed from the stellar X

luminosity L_X as (Owen et al., 2012)

$$\dot{M}_{\rm wind} = 6.25 \times 10^{-9} \times \left(\frac{M_\star}{M_\odot}\right)^{-0.068} \left(\frac{L_X}{10^{30}{\rm ergs}^{-1}}\right)^{1.14} M_\odot {\rm yr}^{-1}.$$

The surface mass-loss profile $\dot{\Sigma}_{\rm photo}$ (Equation B2 in Owen et al. 2012) is then scaled so that $\int 2\pi R \dot{\Sigma}_{\rm photo} {\rm dR}$ is equal to $\dot{M}_{\rm wind}$. As for $M_{\rm d}$ and $\dot{M}$, $\dot{M}_{\rm wind}$ (or equivalently L_X) is extracted from a log-normal distribution whose mean is determined assuming power-law correlations with the stellar mass, while the normalisation at 1 $M_\odot$, the slope and the width of the distribution are free parameters.

5. **External photoevaporation parameters (FUV):** FUV flux experienced by each disc, in units of G_0[3]. This parameter can be set to any value accessible in the FRIEDv2 grid of mass loss rate (Haworth et al., 2023), spanning from 1 to 10^5 G_0.

5.2.3 Solution algorithm

After generating the initial population of YSOs as described above, `Diskpop` proceeds to evolve it by integrating the master equation (5.1). Our solution algorithm employs an operator splitting method: the original equation is separated into different parts over a time step, and the solution to each part is computed separately. Then, all the solutions are combined together to form a solution to the original equation. We split Equation (5.1) into five different pieces, related to viscosity, wind-driven accretion onto the central star, wind-driven mass loss, internal and external photoevaporation respectively. Furthermore, `Diskpop` includes the possibility to trace the dust evolution in the disc, which is split in radial drift and dust diffusion. In the following, we describe the solution algorithm for each process.

1. **Viscous accretion:** the standard viscous solver is based on the freely available code by Booth et al. (2017). We assume a radial temperature profile $T \propto R^{-1/2}$, which results in $c_s \propto R^{-1/4}$ and $H/R \propto R^{1/4}$. We note that this implies $\nu \propto R$ (i.e. $\gamma = 1$), which will be the case from now on. We assume $H/R = 1/30$ at 1 AU and a mean molecular weight of 2.4. We refer to the original paper for details on the algorithm.

2. **Wind-driven accretion:** the second term in Equation (5.1) is effectively an advection term. The general form of the advection equation for a quantity q with velocity v is $\partial_t q(x,t) + v\partial_x q(x,t) = 0$; in the case of wind-driven accretion, the advected quantity is $R\Sigma$, while the advection (inwards) velocity is given by $v_{\rm DW} = (3\alpha_{\rm DW} H c_s)/2R$. We solve the advection equation with an explicit upwind algorithm (used also for dust radial drift).

[3] G_0 stands for the Habing unit (Habing, 1968), the flux integral over the range of wavelengths [912 - 2400] Å weighted by the average value in the solar neighbourhood (1.6×10^{-3} erg s^{-1} cm^{-2}).

3. **Wind-driven mass loss:** the mass loss term (third in Equation 5.1) does not involve any partial derivative, and therefore is simply integrated in time multiplying by the time step.

4. **Internal photoevaporation:** effectively, internal photoevaporation (implemented through the model of Owen et al. 2012) is another mass loss term - therefore, as above, its contribution is computed with a simple multiplication by the time step. Once the accretion rate of the disc drops below the photoevaporative mass loss rate, a gap opens in the disc at the radius of influence of photoevaporation: in the model of Owen et al. (2012), the prescription changes depending on the radial location in the disc, with respect to the gap itself. Later, the gap continues to widen; when it eventually becomes larger than the disc, we stop the evolution and consider the disc as dispersed.

5. **External photoevaporation:** for a given stellar mass and FUV flux experienced by the disc, the mass loss rate arising from external photoevaporation is obtained, at each radial position, from a bi-linear interpolation of the FRIEDv2 grid (Haworth et al., 2023) using the disc surface density at each radial cell. The outside-in depletion of material is implemented following the numerical approach of Sellek et al. (2020a): we define the *truncation* radius, R_t, as the position in the disc corresponding to the maximum photoevaporation rate (which is related to the optically thin to thick transition of the wind), and we remove material from each grid cell at $R > R_\mathrm{t}$ weighting on the total mass outside this radius. The mass loss attributed to the cell i can be written as:
$$\dot{M}_{\mathrm{ext},i} = \dot{M}_\mathrm{tot} \frac{M_i}{M(R > R_\mathrm{t})}, \tag{5.2}$$
where M_i is the mass contained in the cell i, and $\dot{M}_\mathrm{tot}$ is the total mass loss rate outside the truncation radius.

6. **Dust evolution**[4]: based on the two populations model by Birnstiel et al. (2012) and the implementation of Booth et al. (2017). We consider the dust grain distribution to be described by two representative sizes, a constant monomer size and a time-dependent larger size, which can grow up to the limit imposed by the fragmentation and radial drift barriers. We evolve the dust fraction of both sizes following Laibe & Price (2014), and also include a diffusive term: the diffusion comes from the coupling with the turbulent gas, which has the effect of mixing the dust grains, counteracting gradients in concentration (Birnstiel et al., 2010). The dust-gas relative velocities are computed following Tanaka et al. (2005) and include feedback on the gas component. We refer to Booth et al. (2017) for details on the numerical implementation. Dust evolution is included in the release of `Diskpop`, however the scientific results presented in this work are based on gas simulations only.

[4]As the dust evolution module was forked from Richard Booth's repository, users of `Diskpop` who wish to use dust in their work ought to cite Booth et al. (2017) together with this paper.

The separate pieces of Equation (5.1) must be solved over the same time step to be joined in a coherent solution. We calculate the time step for each process imposing the Courant-Friedrichs-Lewy (CFL) condition. The CFL condition reads $\Delta t = C\min(\Delta x/v)$ and ensures that, within one time step Δt, the material moving at velocity v does not flow further than one grid spacing Δx. The Courant number C must be positive and smaller than 1, with $C = 1$ corresponding to the maximum allowed timestep to keep the algorithm stable. In our implementation, we pick $C = 0.5$. We use zero gradients boundary conditions, setting the value of the first and last cell in our grid to that of the second and second to last. We solve the equation on a radial grid of 10^3 points with power-law spacing and exponent 1/2, extending from 3×10^{-3} au to 10^4 au. From the physical point of view, this choice corresponds to assuming boundary layer accretion (see e.g. Popham et al. 1993; Kley & Lin 1996) - however the difference from magnetic truncation accretion is negligible beyond $\sim 10^{-3}$ au.

After each process has been solved separately, all the pieces are put back together to compute the new surface density, from which the integrated disc quantities are then calculated. As each disc evolves independently of the others in the population, the solver can easily be run in parallel.

5.2.4 User interface and output

The user interface of `Diskpop` is a .json parameters file that includes all the user-dependent parameters. Aside from the number of objects in the population and the evolutionary mechanism, the user can set the chosen IMF (either Kroupa 2001, single stellar mass, or custom input file), the distributions to draw the disc parameters from (single value, flat, normal, log-normal), as well as the normalisation, slope and spread of the correlations, the times at which snapshots are generated, and the initial dust-to-gas ratio. Furthermore, the user can determine a limit disc mass: this is to be intended as a threshold below which the disc would not be detectable anymore, and is therefore considered dispersed in the simulation as well. When a disc is dispersed, the corresponding YSO turns into a Class III object consisting of the central star only.

The output of `Diskpop` is a .hdf5 file containing the properties of both the disc and the star at all chosen time steps for each YSO in the population: this includes the stellar mass, luminosity, temperature, disc mass, accretion rate, accretion timescale, gas and dust surface density, disc radius, dust grain sizes. The output can be easily read and analysed with the dedicated library `popcorn`, released with the code. For a more in-depth description of the parameters, the user interface and the output, we refer to the `Diskpop` documentation.

5.3 The time evolution of the correlations between disc properties and stellar mass under different accretion drivers: Analytical considerations

Parameter	Description
λ	Magnetic lever arm parameter
ψ	Wind-to-turbulent α ratio
ω	Power-law index of $\alpha_{\rm DW}$ with $\Sigma_{\rm c}$
ξ	Mass ejection index
$f_{\rm M,0}$	Initial mass ejection-to-accretion ratio
$\lambda_{\rm m}$	Power-law index of $M_{\rm d}$ with $M_\star$ (Eq. 5.3)
$\lambda_{\rm acc}$	Power-law index of $\dot{M}$ with $M_\star$ (Eq. 5.3)
ζ	Power-law index of $R_{\rm d}$ with $M_\star$ (Eq. 5.3)
β	Power-law index of H/R with $M_\star$
μ	Power-law index of $t_{\rm acc}$ with $M_\star$
δ	$\lambda_{\rm m} - \lambda_{\rm acc}$

Table 5.1: Summary and description of the parameters used throughout the paper. The top block refers to the MHD parameters defined in Tabone et al. (2022a), while the bottom block shows the slopes of the correlations between the disc properties and the stellar mass.

The existence of power-law correlations between the main integrated disc properties - namely the disc mass and stellar accretion rate - and the stellar mass is supported by various surveys across a number of different star-forming regions (e.g. on $M_{\rm d} - M_\star$: Ansdell et al. 2016; Barenfeld et al. 2016; Pascucci et al. 2016; Testi et al. 2016; on $\dot{M} - M_\star$: Muzerolle et al. 2003; Natta et al. 2004; Mohanty et al. 2005; Alcalá et al. 2014; Manara et al. 2016a; Alcalá et al. 2017; Manara et al. 2017b; Venuti et al. 2019b; Manara et al. 2020; Testi et al. 2022). However, whether the establishment and subsequent evolution of said correlations is a product of the secular evolution of discs, or rather an imprint of the initial conditions, remains unclear. Somigliana et al. (2022) explored a combination of both possibilities, assuming the correlations to hold as initial conditions and investigating the impact of purely viscous evolution; we briefly recall their main theoretical results (Section 5.3.1) and extend their analysis to the hybrid (Section 5.3.2) and purely wind-driven (Section 5.3.3) models from the theoretical perspective. We note that the results presented in this work are based on gas simulations.

Following Somigliana et al. (2022), we assume power-law correlations between the disc properties and the stellar mass to hold as *initial conditions*. We focus on the disc mass $M_{\rm d}$, the stellar accretion rate $\dot{M}$ and the disc radius $R_{\rm d}$, and label the slopes of their correlations with the stellar mass $\lambda_{\rm m}$, $\lambda_{\rm acc}$, and ζ respectively. The initial correlations are

set as follows:

$$\begin{cases} M_{\rm d}(0) \propto {M_\star}^{\lambda_{\rm m,0}}, \\ \dot{M}(0) \propto {M_\star}^{\lambda_{\rm acc,0}}, \\ R_{\rm d}(0) \propto {M_\star}^{\zeta_0}. \end{cases} \tag{5.3}$$

To analyse the impact of secular evolution on this set of initial conditions, we analytically determine the evolved expressions for $M_{\rm d}(t)$, $\dot{M}(t)$ and $R_{\rm d}(t)$ in the three different scenarios. Table 5.1 summarises the parameters introduced in this Section.

5.3.1 Purely viscous model

The full calculations for the purely viscous case can be found in Somigliana et al. (2022). Here, we briefly remind the main assumptions and results, and we refer to the original paper for a detailed discussion.

As mentioned in Section 5.2.1, assuming a power-law scaling of viscosity with the disc radius ($\nu \propto R^\gamma$) allows the viscous evolution equation to be solved analytically, recovering the so-called self-similar solution (Lynden-Bell & Pringle, 1974). In this case, the disc mass and accretion rate read

$$M_{\rm d}(t) = M_{\rm d,0} \left(1 + \frac{t}{t_\nu}\right)^{1-\eta}, \tag{5.4}$$

$$\dot{M}(t) = (\eta - 1)\frac{M_{\rm d,0}}{t_\nu} \left(1 + \frac{t}{t_\nu}\right)^{-\eta}, \tag{5.5}$$

where $\eta = (5/2 - \gamma)/(2 - \gamma)$ and the viscous timescale $t_\nu = {R_c}^2/[3(2-\gamma)^2\nu(R = R_c)]$ at the characteristic radius R_c. Because $\dot{M}_0 \propto M_{\rm d,0}/t_{\nu,0}$, a power-law scaling of $M_{\rm d,0}$ and $\dot{M}_0$ with the stellar mass implies the viscous timescale $t_{\nu,0}$ to scale as a power-law with the stellar mass as well, which we define as $t_{\nu,0} \propto {M_\star}^{\mu_0}$; furthermore, this scaling corresponds to the difference between the scaling of the disc mass with the stellar mass and of the accretion rate with the stellar mass. Defining $\delta_0 = \lambda_{\rm m,0} - \lambda_{\rm acc,0}$, in this case $\mu_0 = \delta_0$[5]; therefore, the scaling of $t_{\nu,0}$ with the stellar mass is determined by the relative values of $\lambda_{\rm m,0}$ and $\lambda_{\rm acc,0}$. The main results of Somigliana et al. (2022) are that (i) viscous evolution maintains the power-law shape of the correlations between the stellar mass and the disc parameters, however (ii) the slope of said correlations may evolve with time, depending on the initial conditions. This is because in a purely viscous framework, the $M_{\rm d} - \dot{M}$ correlation is bound to reach a linear correlation with slope unity (Lodato et al., 2017;

[5]The definition of δ_0 might seem redundant at this stage, but it will become important in the following discussion.

Rosotti et al., 2017), which implies the two quantities to have the same dependence on the stellar mass, as $M_{\rm d}/\dot{M} \propto {M_\star}^{\lambda_{\rm m}-\lambda_{\rm acc}}$. Therefore, $\lambda_{\rm m}$ and $\lambda_{\rm acc}$ must eventually reach the same value, determined by the initial conditions as

$$\lambda_{\rm m,evo} = \lambda_{\rm acc,evo} = \frac{3\lambda_{\rm m,0} - \lambda_{\rm acc,0}}{2}. \tag{5.6}$$

Depending on the sign of $\delta_0 = \lambda_{\rm m,0} - \lambda_{\rm acc,0}$, the initial slopes can either

- *steepen*, that is, $\lambda_{\rm m,evo} > \lambda_{\rm m,0}$, if $\delta_0 > 0$ (implying also $\lambda_{\rm acc,evo} > \lambda_{\rm acc,0}$);
- *flatten*, that is, $\lambda_{\rm m,evo} < \lambda_{\rm m,0}$, if $\delta_0 < 0$ (implying also $\lambda_{\rm acc,evo} < \lambda_{\rm acc,0}$);
- *remain constant*, that is, $\lambda_{\rm m,evo} = \lambda_{\rm m,0}$, if $\delta_0 = 0$ (implying also $\lambda_{\rm acc,evo} = \lambda_{\rm acc,0}$).

Because in the viscous case $\delta_0 = \mu_0$, where we note again that μ_0 is the slope of the correlation between the viscous timescale and the stellar mass ($t_{\nu,0} \propto {M_\star}^{\mu_0}$), we can also interpret these scenarios from the viscous timescale perspective. If $\mu_0 > 0$, meaning that the viscous timescale increases with the stellar mass, discs around less massive stars will have shorter viscous timescales, which leads to a faster evolution, compared to discs around more massive stars, which will in turn have longer viscous timescales. This uneven evolution across the stellar mass spectrum leads to a steepening of the linear correlation, as is visualised by Somigliana et al. (2022) in Figure 1. The same reasoning, but with an opposite or constant trend, applies to the other two scenarios.

5.3.2 Hybrid model - $\omega = 0$

In the hybrid viscous and MHD winds model, the general analytical solution by Tabone et al. (2022a) gives

$$M_{\rm d}(t) = M_0 \left(1 + \frac{t}{(1+\psi)t_{\rm acc,0}}\right)^{-(\psi+2\xi+1)/2}, \tag{5.7}$$

$$\dot{M}(t) = \dot{M}_0 \left(1 + \frac{t}{(1+\psi)t_{\rm acc,0}}\right)^{-(\psi+4\xi+3)/2}, \tag{5.8}$$

where $\dot{M}_0$ is defined as

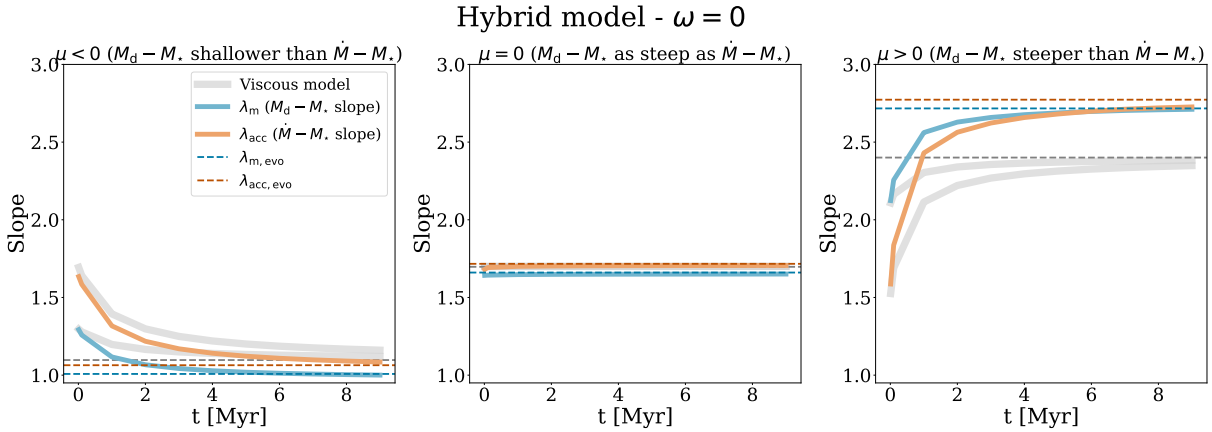

Figure 5.1: Time evolution of the slopes of the $M_\mathrm{d} - M_\star$ and $\dot{M} - M_\star$ correlations, λ_m and λ_acc (blue and orange solid line, respectively) in the hybrid scenario with $\alpha_\mathrm{SS} = \alpha_\mathrm{DW} = 10^{-3}$ ($\psi = 1$), $\lambda = 3$, $\beta = 0.5$, resulting in $\xi = 0.11$. The dashed lines represent the expected evolved value of both slopes, as in Equation (5.12). For comparison, we include the viscous evolution as well, represented by grey solid (actual evolution) and dashed (expected evolved value) lines (see Somigliana et al. 2022 for a detailed discussion). The three panels show different values of μ_0, slope of the $t_\mathrm{acc,0} - M_\star$ correlation, which is directly linked to the difference between $\lambda_\mathrm{m,0}$ and $\lambda_\mathrm{acc,0}$ (see text for details): we expect the slopes to (i) decrease if $\mu_0 < 0$ (left panel), (ii) remain constant if $\mu_0 = 0$ (central panel), and (iii) increase if $\mu_0 > 0$ (right panel). Contrary to the viscous case, the slopes are not expected to reach the same value anymore, but rather settle to a constant difference of $-\xi/2$. This difference is always negative, meaning that the evolved $\dot{M} - M_\star$ correlation is always steeper than that of $M_\mathrm{d} - M_\star$ (explaining the lines crossing in the right panel).

$$\dot{M}_0 = \frac{\psi + 1 + 2\xi}{\psi + 1} \frac{M_0}{2t_\mathrm{acc,0}} \frac{1}{(1 + f_{\mathrm{M}_0})}; \tag{5.9}$$

in this notation, $\psi = \alpha_\mathrm{DW}/\alpha_\mathrm{SS}$ represents the relative strength of MHD winds and viscosity,

$$\xi = \frac{1}{4}(\psi + 1)\left[\sqrt{1 + \frac{4\psi}{(\lambda - 1)(\psi + 1)^2}} - 1\right]$$

is the mass ejection index quantifying the local mass loss rate to the local accretion rate, and $f_\mathrm{M,0} = (R_{c,0}/R_{in})^\xi - 1$ the dimensionless mass ejection-to-accretion ratio (with R_{in} initial disc radius). If we neglect the MHD-driven mass loss ($\psi \ll 1$ and $\xi \ll 1$, which correspond to $f_\mathrm{M,0} \ll 1$ as well), Equations (5.7) and (5.8) reduce to the viscous case; on the other hand, if mass loss is included, it depends on the radial extent of the disc through $f_\mathrm{M,0} + 1$ - which has an impact on the initial accretion rate (Equation 5.9). Because the accretion timescale t_acc is a generalisation of t_ν in the MHD winds framework, the dependence of the

two timescales on the stellar mass is exactly equivalent, and we keep the same notation as above: $t_{\rm acc} \propto M_\star{}^{\mu}$. However, as mentioned above $\dot{M}_0$ depends on the stellar mass not only through M_0 and $t_{\rm acc,0}$ as in the viscous case, but also through $f_{\rm M,0}+1$. As $f_{\rm M,0}+1 \propto R_{c,0}{}^{\xi}$, and $R_{c,0} \propto M_\star{}^{\zeta_0}$, the additional dependence will have a slope of $\zeta_0\xi$. Therefore, in the MHD winds scenario we can link δ_0 with μ_0 as $\delta_0 = \mu_0 + \zeta_0\xi$. The practical meaning of this difference is that, while in the viscous scenario the difference in slope between the two correlations depends only on the scaling of the viscous timescale with the stellar mass, in the hybrid scenario it depends also on the scaling between the disc radius and the stellar mass. It is important to note that ξ is a small number, typically of the order of ~ 0.1, therefore the difference between the viscous and hybrid case is not particularly prominent. For evolved populations, the disc mass and accretion rate read (Tabone et al., 2022a)

$$M_{\rm d}(t \gg t_{\rm acc}) \sim M_0 \left(\frac{t}{t_{\rm acc,0}}\right)^{-(\psi+2\xi+1)/2}, \tag{5.10}$$

$$\dot{M}(t \gg t_{\rm acc}) \sim \dot{M}_0 \left(\frac{t}{t_{\rm acc,0}}\right)^{-(\psi+4\xi+3)/2}; \tag{5.11}$$

this brings the evolved slopes $\lambda_{\rm m,evo}$ and $\lambda_{\rm acc,evo}$ to

$$\begin{aligned} \lambda_{\rm m,evo} &= \lambda_{\rm m,0} + \frac{1}{2}\mu_0(\psi + 2\xi + 1), \\ \lambda_{\rm acc,evo} &= \lambda_{\rm acc,0} + \frac{1}{2}\mu_0(\psi + 4\xi + 3), \end{aligned} \tag{5.12}$$

which reduces to Equation (5.6) in the viscous case ($\psi \ll 1$, $\xi \ll 1$). Similarly to viscosity, a hybrid secular evolution maintains the power-law shape of the correlation; moreover, Equation (5.12) provides a theoretical prediction for the evolved slopes: they can steepen, flatten or remain the same as the initial conditions, depending on the involved parameters. As the terms in parentheses in Equation (5.12) are sums of positive values, the sign of the evolved slopes depends on the sign of μ_0 as in the viscous case. However, there is a difference from the viscous case: as in the hybrid scenario μ_0 and δ_0 do not coincide anymore, a constraint on the value of μ_0 is translated into a constraint on $\delta_0 - \zeta_0\xi$. In particular, the slopes will increase if $\delta_0 > \zeta_0\xi$ (corresponding to $\mu_0 > 0$), whereas if $\delta_0 < \zeta_0\xi$ (corresponding to $\mu_0 < 0$), the slopes will decrease; and finally, if $\delta_0 = \zeta_0\xi$ (corresponding to $\mu_0 = 0$) the slopes will remain constant in time. Another difference from the viscous scenario is that $\lambda_{\rm m,evo}$ and $\lambda_{\rm acc,evo}$ are not expected to reach the same value anymore. The limit difference is given by $\delta_{\rm evo} = \lambda_{\rm m,evo} - \lambda_{\rm acc,evo}$: substituting the values from Equation (5.12) one finds $\delta_{\rm evo} = \delta_0 - \mu_0(\xi + 1)$, which can be further reduced to $\delta_{\rm evo} = \xi(2\beta + \frac{1}{2})$ by using the definition of μ_0 as the slope of the $t_{\rm acc,0} - M_\star$ correlation. In this expression,

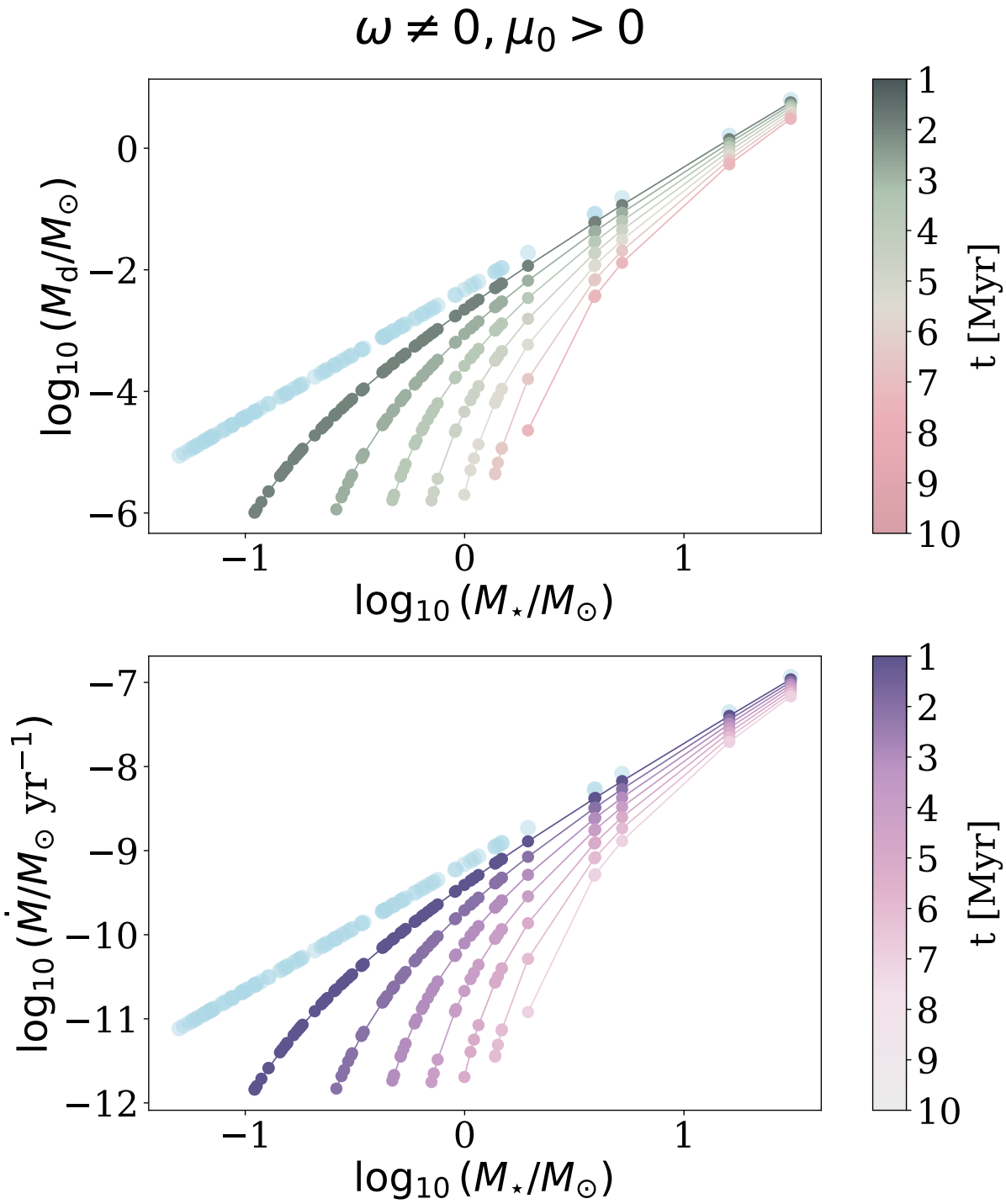

Figure 5.2: Time evolution of $M_d - M_\star$ (left) and $\dot{M} - M_\star$ (right) in the pure wind model ($\omega \neq 0$). This plot is obtained with disc population synthesis modelling, without any spread in the initial conditions. Each dot represents a disc in the population at different ages as shown in the colour bar. The initial power-law correlation, shown in light blue, is lost as early as ~ 1 Myr (corresponding to $\sim 2 < t_{acc,0} >$ with these parameters) due to a downward bending corresponding to lower stellar masses. In this simulation, we have used $N = 100$ discs, $\alpha_{DW} = 10^{-3}$, $\lambda = 3$, $\omega = 0.25$, $\lambda_{m,0} = 2.1$, $\lambda_{acc,0} = 1.5$. The set of MHD parameters is based on Tabone et al. 2022a.

β is the slope of the correlation between the disc aspect ratio and the stellar mass, which comes from definition of the accretion timescale; with a standard $\beta = -1/2$ (a reasonable approximation of the value derived by radiative transfer simulation, see e.g. Sinclair et al. 2020), we obtain $\delta_{\rm evo} = -\xi/2$. As ξ is positive by definition, in the hybrid scenario $\delta_{\rm evo}$ is always negative, meaning that in an evolved population, the correlation between the accretion rate and the stellar mass will necessarily be steeper than that between the disc mass and the stellar mass. However, we stress once more that ξ is a small number and therefore the predicted difference is also small. Figure 5.1 shows the evolution of the slopes from `Diskpop` simulations (with no spread in the initial conditions) for the hybrid model (coloured) compared with the viscous case (grey), which matches the theoretical expectations discussed above. The list of parameters used in the simulations is available in Table 5.4.

Summarising, both the hybrid and viscous secular evolution preserve the power-law shape of the correlations between the disc properties and the stellar mass. The main difference is that the hybrid model does not predict the slopes of the $M_{\rm d} - M_\star$ and $\dot{M} - M_\star$ correlations to reach the same limit value (unlike the viscous case). The predicted difference in the evolved slopes is given by $\delta_{\rm evo} = -\xi/2$ (of the order of 0.1). The current observational uncertainties on $\delta_{\rm evo}$ range from 0.4 to 0.8 (Testi et al. 2022, see Table 5.3), 4 to 8 times larger than the predicted difference, making it not observable at this stage.

5.3.3 Pure wind - $\omega \neq 0$

The solution to the pure wind model (i.e. time-dependent $\alpha_{\rm DW}$ through $\alpha_{\rm DW}(t) \propto \Sigma_{\rm c}(t)^{-\omega}$) by Tabone et al. (2022a) gives

$$M_{\rm d}(t) = M_0 \left(1 - \frac{\omega}{2t_{\rm acc,0}} t\right)^{1/\omega}, \tag{5.13}$$

$$\dot{M}(t) = \frac{M_0}{2t_{\rm acc,0}(1 + f_{\rm M,0})} \left(1 - \frac{\omega}{2t_{\rm acc,0}} t\right)^{-1+1/\omega}; \tag{5.14}$$

in this case, the functional form of Equation (5.13) and (5.14) does not allow us to derive a simple analytical expression for $M_{\rm d}(t \gg t_{\rm acc})$ and $\dot{M}(t \gg t_{\rm acc})$. Therefore, to explore the evolution of the correlations in the pure wind case, we fully rely on `Diskpop` simulations. In order to account for the impact of secular evolution only, we input perfect correlations between the disc properties and the stellar mass - that is, we do not include any spread in the initial conditions. Figure 5.2 shows the time evolution of $M_{\rm d}$ (left panel) and $\dot{M}$ (right panel) as a function of the stellar mass, from younger (darker) to older (lighter) populations. The input power-law correlation (light blue) corresponds to a line in the logarithmic plane; however, as early as $\sim$ 1 Myr (corresponding to $\sim 2 <$ $t_{\rm acc,0}$ $>$ for this simulation), the input correlation starts to bend downwards at lower stellar masses.

This behaviour reveals a significantly different trend from the viscous and hybrid model: in the pure wind scenario, the initial power-law shape of the correlations is not preserved by the secular evolution, but rather broken. In Figure 5.2, the faster evolution of discs around lower mass stars is the consequence of a positive μ_0, implying a positive correlation between the stellar mass and the accretion timescale; a negative correlation between $M_\star$ and $t_{\rm acc,0}$ (i.e. a negative μ_0) would lead to faster evolution of discs around higher mass stars, causing the correlation to bend towards the other end of the stellar mass spectrum (see Figure 5.6). Another parameter that might impact the evolution of the correlation is the dispersal timescale, $t_{\rm disp}$; in the wind-driven case, $t_{\rm disp} \propto t_{\rm acc}$, therefore $t_{\rm disp}$ does not introduce any further dependence on the stellar mass.

5.4 Population synthesis

In Section 5.3 we have discussed analytical trends, and presented simulations with no spread to analyse the effect of secular disc evolution alone on the evolution of the slopes. In order to test our theoretical predictions against observational data, we need to account for both a spread in the initial conditions and disc dispersal mechanisms. In this Section, we discuss the impact of both factors on the $M_{\rm d} - M_\star$ and $\dot{M} - M_\star$ slopes and run realistic population synthesis simulations, to determine whether the model-dependent evolutionary features described in Section 5.3 would be observable with the currently available data.

5.4.1 Effects of a spread in the initial conditions

The introduction of an observationally motivated spread in the initial conditions is crucial to produce realistic population synthesis model. In the purely viscous case, Somigliana et al. (2022) have shown how the spread does not significantly impact the evolution of either the $M_{\rm d} - M_\star$ or $\dot{M} - M_\star$ correlations; the shape of the curves (grey in Figure 5.1) is unaffected, except for their starting point, and the statistical fluctuation - determined as the interval between the 25th and 75th percentile out of 100 realisations of numerical simulations with the same initial conditions - is of the order ~ 0.1 for both slopes. This is a factor two less than the smallest observational uncertainty, and therefore does not produce a detectable difference in the predicted results.

Following Somigliana et al. (2022), we set $\sigma_{M_{\rm d}}(0) = 0.65$ dex and $\sigma_R(0) = 0.52$ dex (determined from Ansdell et al. 2017 and Testi et al. 2022) for the log-normal distributions of $M_{\rm d}(0)$ and $R_{\rm d}(0)$ in the hybrid scenario (with $\alpha_{\rm SS} = \alpha_{\rm DW} = 10^{-3}$ hence $\psi = 1$, $\lambda = 3$, $\omega = 0$). We find that, just as in the purely viscous case, a spread in the initial conditions only shifts the starting point of the curves (coloured in Figure 5.1) and does not have any significant effect on the shape of the evolution of the slopes (see Figure 5-6-7 in Somigliana et al. 2022). The statistical fluctuation for both slopes is again of the order of 0.1, and therefore below the observational error and not impacting our predictions.

On the other hand, wind-driven models with increasing $\alpha_{\rm DW}$ in time and a spread in

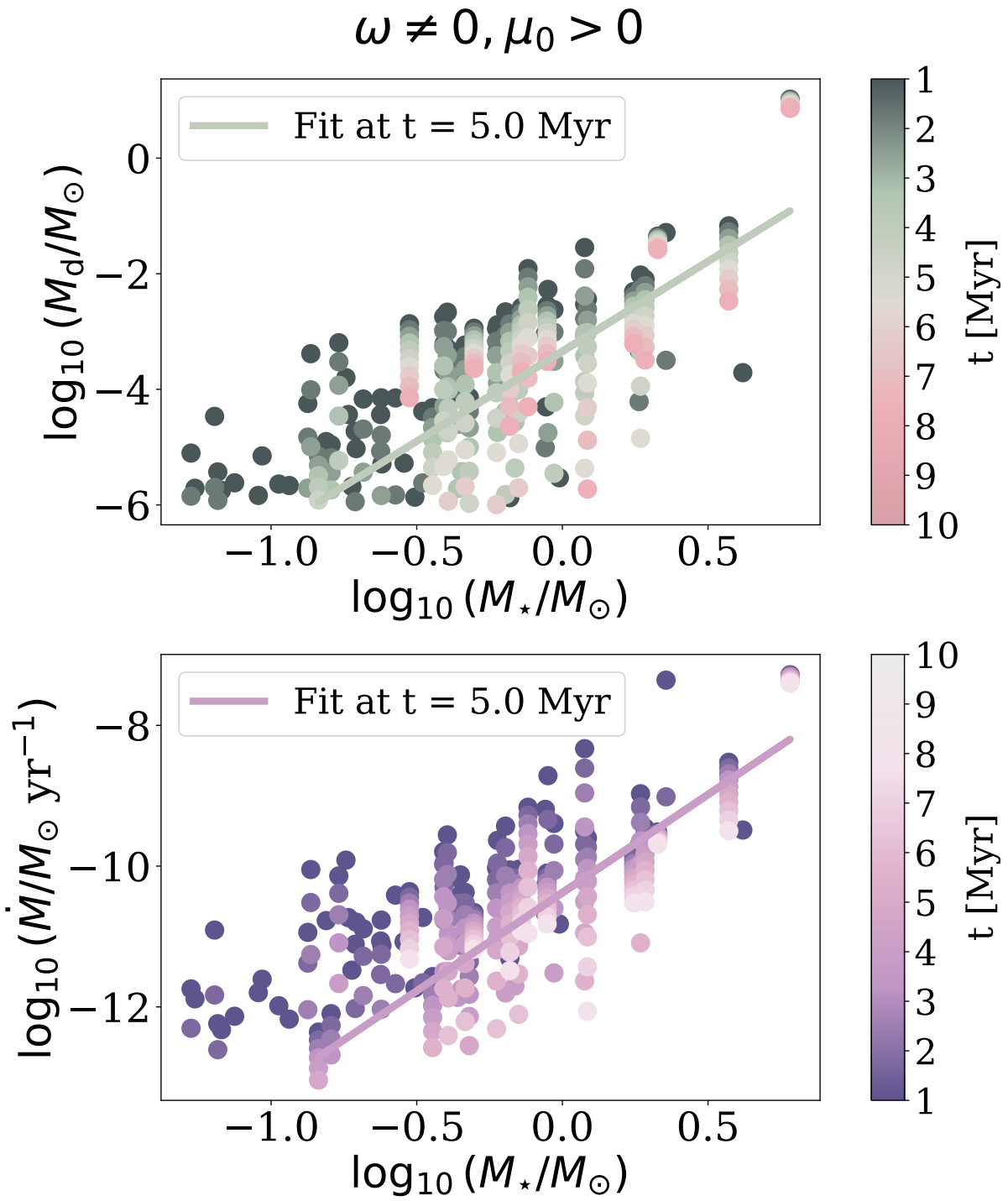

Figure 5.3: Same as Figure 5.2 but with the addition of a spread in the initial correlations between the disc properties and the stellar mass ($\sigma_{M_{\rm d}}(0) = 0.65$ dex, $\sigma_{R_{\rm d}}(0) = 0.52$ dex). Despite the linear correlation being readily broken in theory (see Section 5.3.3), the scatter introduced by the spread in the initial conditions simulates the correlation also at more evolved ages. As an example, we show the fitted line at 5 Myr (the age of the oldest observed population) in both panels ($\log_{10}(M_{\rm d}/M_\odot) = 3.1\log_{10}(M_\star/M_\odot) - 3.3$, $\log_{10}(\dot{M}/M_\odot {\rm yr}^{-1}) = 2.5\log_{10}(M_\star/M_\odot) - 10.4$).

the initial conditions (Figure 5.3) behave quite differently from the theoretical expectation discussed in Section 5.3.3. As the spread introduces a stochastic component, the discs will have higher or lower masses and accretion rates with equal probability; the practical result for the initial correlations is that the bending towards lower stellar masses (approximately $\log_{10}(M_\star/M_\odot) < 0.5$ in Figure 5.2) is lost to the stochastic displacement of the discs in the $M_\mathrm{d} - M_\star$ and $\dot{M} - M_\star$ planes. Actually, the resulting distribution of discs both in the $M_\mathrm{d} - M_\star$ and $\dot{M} - M_\star$ log-log plane does simulate a linear correlation; this implies that, while the stellar mass and the disc properties *should not* exhibit a linear correlation already after a few t_acc, the presence of a spread mimics such correlation, making the wind-driven scenario indistinguishable from the viscous and hybrid ones. The one feature that remains observable, despite the presence of a spread, is the removal of discs around more or less massive stars - depending on the value of μ_0, as discussed in Section 5.3.3; in the simulation shown in Figure 5.3 we have set $\mu_0 > 0$, implying that discs around less massive stars evolve more rapidly and are therefore more readily dispersed, as is visualised by the lack of sources around lower stellar masses at evolved ages.

Summarising, an initial power-law correlation between the disc properties and the stellar mass would keep its power-law shape under wind-driven evolution, similarly to the viscous or hybrid case; however, the interpretation of the observed correlations is different depending on the theoretical framework. While the viscous and hybrid models *preserve* an initially established correlation, making the characteristic evolution of the slopes λ_m and λ_acc a tracer of disc evolution itself, the apparent correlation observed in wind-driven populations is merely a signature of the initial spread, rather than the evolutionary mechanism at play.

5.4.2 Accounting for disc dispersal: Internal photoevaporation

Out of the three theoretical scenarios discussed so far, wind-driven evolution is the only one that manages to reproduce the disc and accretion fraction (as measured by Hernández et al. 2007 and Fedele et al. 2010 respectively) - and therefore, the only one whose predictions can reasonably be compared with observations. Traditionally, the problem of disc dispersal in viscous populations is addressed by including internal photoevaporation (see e.g. Hollenbach et al. 1994; Clarke et al. 2001; Alexander et al. 2006a,c): in this Section, we discuss the impact of internal photoevaporation on the previously described expectations for the evolution of the slopes in the purely viscous scenario. As the lack of analytical solutions to the general equation (5.1) does not allow for analytical arguments, we base the following discussion on physical considerations.

Internal photoevaporation is a threshold process, that kicks in after the accretion rate drops below the photoevaporative mass-loss rate (Clarke et al., 2001). The moment where the effect of photoevaporation becomes non-negligible depends therefore on the initial accretion rate: assuming for simplicity a fixed photoevaporation rate for the whole population, as the accretion rate scales positively with the stellar mass we can expect discs

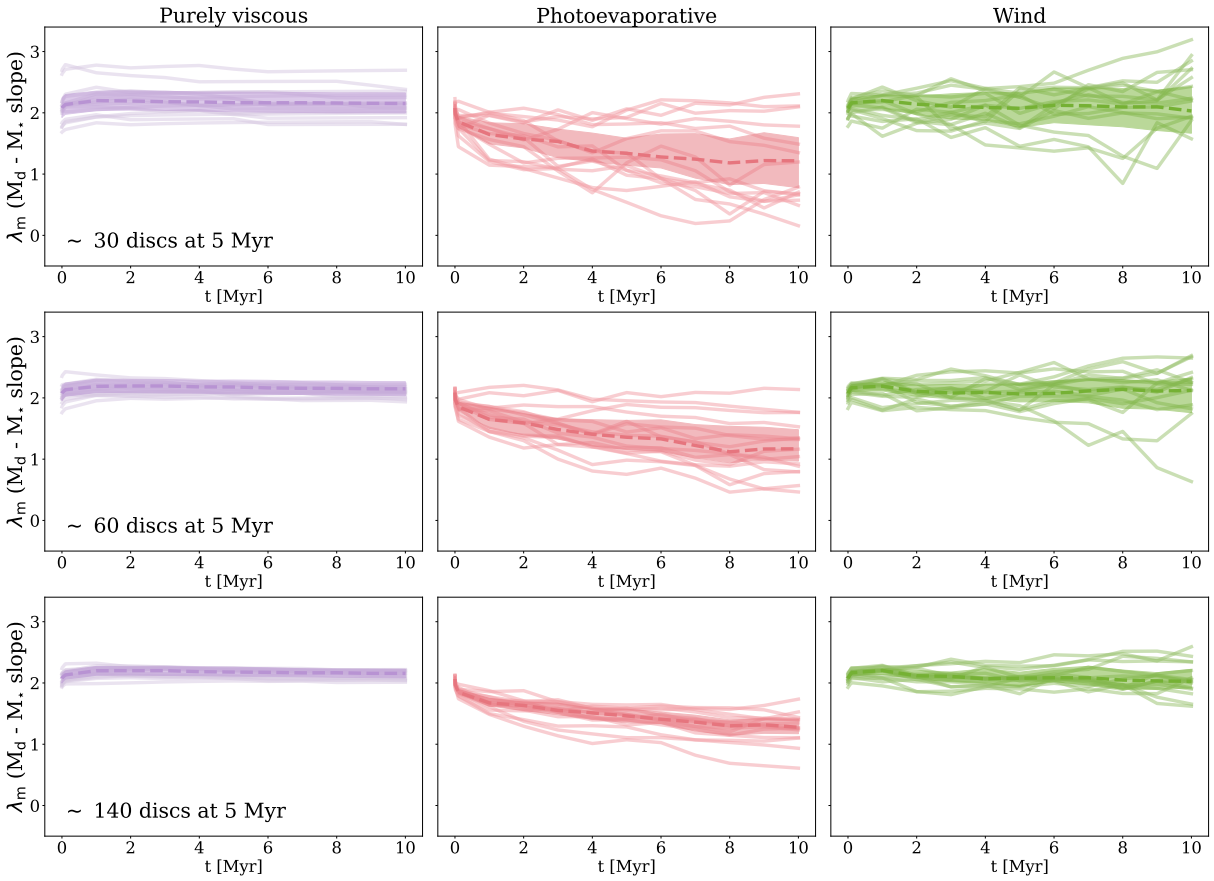

Figure 5.4: Time evolution of the slope of the $M_{\rm d} - M_\star$ correlation for 15 statistical realisations in the purely viscous (left, $\alpha_{\rm SS} = 10^{-3}$), photoevaporative (centre, $\dot{M}_w = 4 \times 10^{-10} {\rm M}_\odot/{\rm yr}$, $\alpha_{\rm SS} = 10^{-3}$), and wind-driven (right, $\omega = 0.25$, $\lambda = 3$, $\alpha_{\rm DW} = 10^{-3}$) model. The dashed lines show the median evolution, while the shaded area represents the interval between the 25th and the 75th percentiles. The three rows show different sample sizes, increasing from top to bottom. The initial size of each population was chosen to obtain a certain number of discs at 5 Myr (the age of the oldest observed population, Upper Sco) with the different disc fractions. In the top row, we match the current size of the Upper Sco sample($\sim$ 30 objects, Testi et al. 2022) with both accretion rate and disc mass measurements; the middle row shows double the current sample size ($\sim$ 60 objects), while the bottom row assumes a complete sample ($\sim$ 140 objects). While the viscous model produces a remarkably similar evolution for all simulations, the latter two show stochastic oscillations from one realisation to another, suggesting that disc dispersal impacts the observed slope more than the evolutionary model does - at least with the currently available sample sizes; increasing the number of sources significantly mitigates the oscillations. The slope of the $\dot{M} - M_\star$ correlation behaves the same way.

around lower mass stars to show the effects of photoevaporation earlier. Moreover, given that the disc mass also scales positively with the stellar mass, said sources correspond to the less massive ones in the population. From these considerations, we can expect discs with lower initial mass to be the first ones to be affected by photoevaporation, causing a steepening of the $M_{\rm d} - M_\star$ and $\dot{M} - M_\star$ correlations. However, photoevaporation also disperses discs: removing sources from the population may alter the expected behaviour, hence the need to perform numerical simulations to understand the evolution of the correlations for a population of discs undergoing internal photoevaporation. Our simulations remove discs either because the photoevaporative gap becomes too large, or because the disc mass or accretion rate fall below a certain detectability threshold. As we mentioned above, the dispersal timescale $t_{\rm disp}$ might also play a role, if it has a different scaling with the stellar mass with respect to the accretion timescale (t_ν in the viscous case). Our numerical implementation of internal photoevaporation follows Owen et al. (2010), and we assume a mass-loss rate of 4×10^{-10} M$_\odot$ yr^{-1} - which allows us to reproduce the observed disc fraction for the set of parameters of our simulation - for all discs in the population; therefore, no further $M_\star$ dependence is introduced, and the $t_\nu - M_\star$ scaling is the only one that matters. We stress that a stellar mass-dependent photoevaporative rate *is* expected (Picogna et al., 2021): we explore the influence of such dependence on disc observables in an upcoming work (Malanga et al. in prep.). We discuss the results of our `Diskpop` simulations in the following Section.

5.4.3 What the slopes are tracing

Figure 5.4 shows the time evolution of the $M_{\rm d} - M_\star$ slope for 15 realisations with the same initial conditions for the viscous plus photoevaporative (central panel) and wind-driven (right panel) models, both reproducing the observed disc and accretion fractions, compared to the purely viscous scenario (left panel). The initial number of discs in the populations was determined to recover a certain number of objects at 5 Myr (increasing from top to bottom), and varies in the different simulations, as the decline (or lack thereof) of the disc fraction is model-dependent (see Figure 6 of Somigliana et al. 2023).

The number of objects in the simulation displayed in the first row was set to obtain $\sim$ 30 discs at 5 Myr, corresponding to the currently available sample size in Upper Sco, the oldest observed star-forming region. In the left panel, we see how the evolution of the slope in the purely viscous model is not significantly affected by a spread in the initial conditions: the single realisations resemble each other remarkably well, the only difference being the starting point of the curve (as found by Somigliana et al. 2022). On the other hand, the photoevaporative and wind-driven models have a dissimilar behaviour: each realisation can deviate substantially from the others, as we can particularly notice by the location, amplitude and direction of the bumps. The key difference between these models and the purely viscous case is disc dispersal: the stochastic nature of the slope evolution suggests that it does not trace the underlying secular disc evolution, as in the viscous scenario, but rather carry the signatures of disc dispersal itself - making it impossible to use the

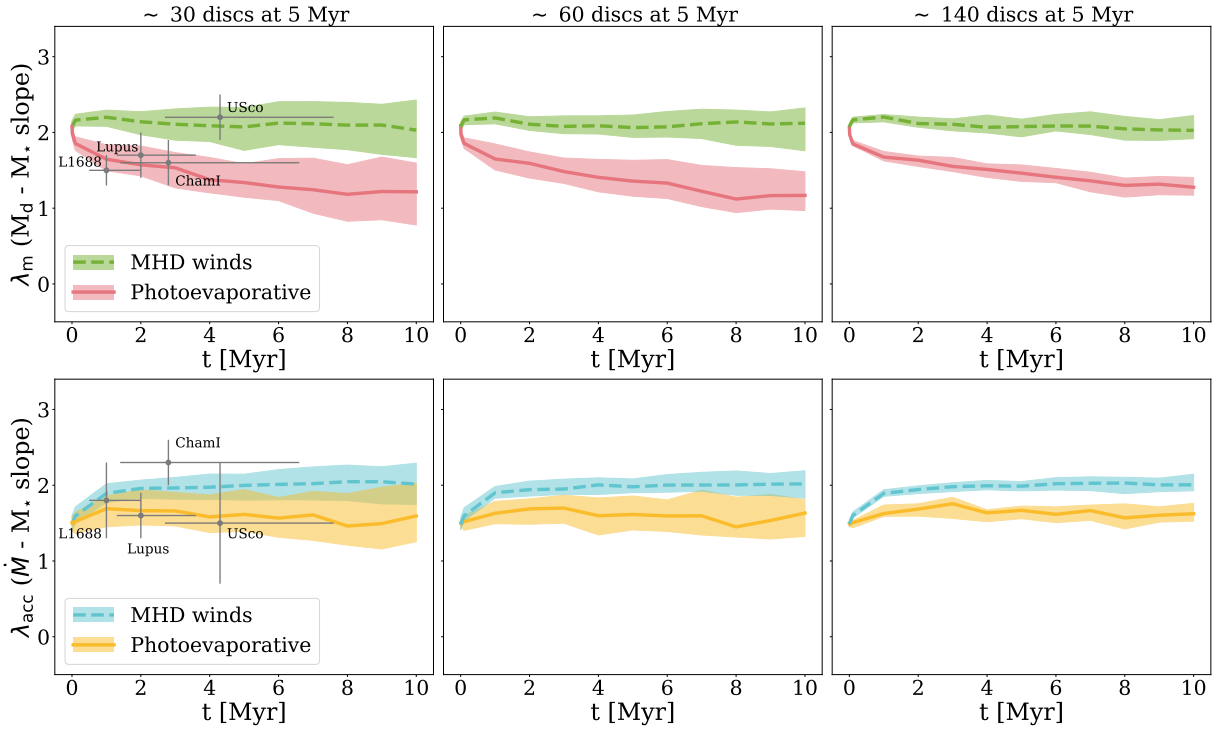

Figure 5.5: Comparison of the time evolution of λ_m (top) and λ_{acc} (bottom) between the viscous+photoevaporative and wind-driven case including measured slopes from four star-forming regions. To account for statistical fluctuations, each simulation combines 100 realisations of the same initial conditions: the lines show the median evolution, while the shaded area represent the interval between the 25th and 75th percentiles. The simulations in the three columns differ for the initial number of discs, determined to obtain a specific sample size at 5 Myr - currently available sample (left), double the currently available sample (centre) and the complete sample (right). Observed slopes from Testi et al. (2022).

evolution of the slopes as a proxy for accretion mechanisms. There are two main factor that play a role in this context:

1. **Initial conditions and spread in the correlations.** The exact evolution of the slopes will depend on the initial conditions, both of the disc mass-stellar mass correlations themselves and of the population-wide parameters. Furthermore, the removal of discs from the population would not impact the results of the fitting procedure only if there was perfect correlations between the disc parameters and the stellar mass; with a spread in the initial correlations, on the other hand, the results may differ depending on *which* discs in the population are dispersed;

2. **Small number statistics.** Depending on the initial number of objects, disc removal can lead to small samples - so small that it might lead to low number statistics issues. This is the case for the top row of Figure 5.4, where the number of objects at 10 Myr is of the order of 10 or lower.

In this work, we have used one specific set of parameters (summarised in Table 5.4), determined following Somigliana et al. (2022) (viscous model) and Tabone et al. (2022a) (hybrid and wind-driven), and we leave a deeper exploration of the parameters space to a future work. While the exact shape of the slope evolution, and therefore the accretion model signature, might depend on the initial conditions, the top panel of Figure 5.4 shows that with the current sample sizes the noise dominates over the physical evolution. However, the currently available sample of the oldest star-forming region (Upper Sco) with both disc masses (derived from the millimetre flux, Barenfeld et al. 2016) and accretion rate (Manara et al., 2020) estimates is highly incomplete; it is therefore worth investigating whether a higher level of completeness would help reducing the entity of the oscillations, allowing to disentangle between the different evolutionary models.

The central and bottom rows of Figure 5.4 show how a larger sample would impact the oscillations of the slope evolution. The simulations in the middle row are performed imposing a double sample size at 5 Myr with respect to the current one ($\sim$ 60 discs), while in the bottom row we assume to have the complete Upper Sco sample, totalling $\sim$ 140 discs (Carpenter et al. in prep.). We remind that we focus on Upper Sco as the oldest observed star-forming region, which makes it the most affected by disc dispersal.

As expected, statistical significance increases with a larger sample, leading to a decreased impact of the oscillations on the global slope evolution; with the complete sample, in particular, we can reduce the spread in the evolution by a factor of $\sim$ 2 compared to the current available data. This argument confirms the importance of larger sample sizes in discriminating between the viscous and wind-driven models, as already suggested by Alexander et al. (2023) in the context of the accretion rates distribution.

As we mentioned in Section 5.4.2, our simulations consider discs as dispersed if their masses or accretion rates fall below the imposed detectability threshold of 10^{-12} $M_\odot$ yr^{-1}.

We have also included a threshold in accretion rates in post-processing to account for non-accreting objects. From the observational point of view, this latter selection depends on both the instrumental sensitivity and the definition of disc itself: how Class II objects are defined, and in turn how Class III sources are removed from the observed samples, impacts the resulting slope. Summarising, with the current sample sizes, the evolution of the slopes is significantly more affected by disc dispersal than it is by secular evolution; therefore, at the state of the art, it cannot be used as a proxy to disentangle between the different evolutionary models. Increasing the sample size would allow the effect of low number statistics to be reduced, potentially allowing the different evolution of the slopes under the two evolutionary mechanisms to be observed; we further discuss this possibility in the following Section.

5.5 The observational relevance of the slopes

Observed star-forming regions have both a spread in the initial conditions in addition to some disc dispersal mechanism (be it photoevaporation or MHD winds); as we discussed in Section 5.4.3, with the current sample sizes, the statistical significance of the observationally determined slopes is undermined and their evolution traces disc dispersal, rather than the accretion mechanism. In this Section, we perform a statistical analysis of our simulated slopes and compare them with the currently available measurements; furthermore, we show the relevance of measuring the slopes despite these limitations and discuss the conditions under which they allow us to put constraints on disc evolution.

5.5.1 Comparison of different evolutionary models

Figure 5.5 shows the comparison of the evolution of the slopes between the viscous + photoevaporative (solid line) and wind-driven (dashed line) models for both the $M_{\rm d} - M_\star$ and $\dot{M} - M_\star$ correlations (top and bottom row, respectively), including the measured slopes in four star-forming regions from Testi et al. (2022) as grey dots. As we mentioned above, both models lead to disc dispersal consistently with the observed disc and accretion fraction (shown in Figure 6 of Somigliana et al. 2023); the three columns show simulations performed with a different initial number of discs, increasing from left to right, to obtain a different sample size at 5 Myr according to the predicted decline of observed discs. As in Figure 5.4, the number of objects at 5 Myr is $\sim$ 30, $\sim$ 60 and $\sim$ 140 from left to right, increasing from the currently available measurements in Upper Sco to the virtually complete sample. To estimate the effect of statistical fluctuations, given by the spread in the initial conditions, we ran 100 simulations for each set up: the solid and dashed lines represent the median evolution, while the intervals between the 25th and 75th percentile are visualised by the shaded areas. The growing shaded area, particularly visible with smaller sample sizes, is representative of the decreasing amount of sources on which the fit is performed: with the current sample size (left column), that leads to $\sim$ 30 discs at 5 Myr, we end up with a 1σ deviation from the median value of $\sim 0.5 - 0.6$. Larger sample

$$\mu_0 = \delta_0 - \zeta_0 \xi$$

ξ	μ_0	$t_{\rm acc,0} - M_\star$	ζ_0	$R_{\rm d} - M_\star$	δ_0	$M_{\rm d} - M\star$ (a) and $\dot{M} - M\star$ (b)	$\Rightarrow$
0	< 0	$t_{\rm acc,0} \downarrow$ $M_\star \uparrow$		any	< 0	(a) shallower than (b)	$=$
	0	$t_{\rm acc,0} \leftrightarrow$ $M_\star \uparrow$		any	0	(a) as steep as (b)	$=$
	> 0	$t_{\rm acc,0} \uparrow$ $M_\star \uparrow$		any	> 0	(a) steeper than (b)	$=$
(0, 1)	< 0	$t_{\rm acc,0} \downarrow M_\star \uparrow$	≤ 0	$R_{\rm d} \downarrow\leftrightarrow$ $M_\star \uparrow$	≤ 0	(a) shallower or as steep as (b)	$=$
			> 0	$R_{\rm d} \uparrow M_\star \uparrow$	$(-\infty, \zeta_0\xi)$	(a) shallower or steeper than (b)[a]	$\neq$
	0	$t_{\rm acc,0} \leftrightarrow M_\star \uparrow$	≤ 0	$R_{\rm d} \downarrow\leftrightarrow$ $M_\star \uparrow$	≤ 0	(a) shallower or as steep as (b)	$\circ$
			> 0	$R_{\rm d} \uparrow M_\star \uparrow$	≥ 0	(a) steeper or as steep as (b)	$=$
	> 0	$t_{\rm acc,0} \uparrow M_\star \uparrow$	≤ 0	$R_{\rm d} \downarrow\leftrightarrow$ $M_\star \uparrow$	$(\zeta_0\xi, +\infty)$	(a) shallower or steeper than (b)[b]	$\circ$
			> 0	$R_{\rm d} \uparrow M_\star \uparrow$	$(\zeta_0\xi, +\infty)$	(a) steeper than (b)	$=$

$$\delta_{\rm evo} = \xi(\zeta_0 - \mu_0), \quad \xi \neq 0$$

$\delta_{\rm evo}$	$M_{\rm d} - M\star$ (a) and $\dot{M} - M\star$ (b)
< 0	(a) shallower than (b)
0	(a) as steep as (b)
> 0	(a) steeper than (b)

[a] $\zeta_0\xi$ is positive, therefore δ_0 can either be negative (implying (a) shallower than (b)) or positive (implying (a) steeper than (b)).
[b] $\zeta_0\xi$ is negative, therefore the same argument as in *a* holds.

Table 5.2: Summary of the different possible theoretical scenarios described in Section 5.3 to visualise the relative signs of the parameters at play. From left to right in the top table, the columns show (i) ξ, a proxy for the evolutionary model (viscous if $\xi = 0$, hybrid or wind-driven otherwise); (ii) μ_0, the slope of the $t_{\rm acc,0} - M_\star$ correlation and its implication on the correlation itself; (iii) ζ_0, the slope of the $R_{\rm d} - M_\star$ correlation, and its implication on the correlation itself; (iv) $\delta_0 = \lambda_{\rm m,0} - \lambda_{\rm acc,0}$, the difference between the initial slopes of the $M_{\rm d} - M_\star$ and $\dot{M} - M_\star$ correlations and its implication on their relative steepness. The final column summarises whether the signs of μ_0 and δ_0 are *necessarily the same* ($=$), *necessarily opposite* ($\neq$) or *can be either* ($\circ$). When discussing the implications on correlations, up(down)wards arrows represent an in(de)crease of the parameters, while horizontal arrows describes the lack of correlation. The different cell colours are purely meant to guide the eye. The top table links the initial conditions, while the bottom table summarises the implications of the evolved difference in the slopes.

sizes significantly reduce the scatter, leading to $\sigma \sim 0.4$ with a double sample and $\sigma \sim 0.2$ for the complete sample, reducing the current one by a factor 3. As mentioned in Section 5.4.2, with the currently available number of objects the dominant role in the evolution of the slopes is played by disc dispersal, which makes it difficult to trace the imprint of the secular evolution. The expected Upper Sco complete sample (right column) allows for a better separation between the two models - particularly for the $M_{\rm d} - M_\star$ correlation: the expected slope in the two scenarios differs by ~ 0.5, while the typical uncertainty of the currently measured slopes is between 0.2 and 0.3. Larger sample sizes would further decrease this uncertainty, allowing us to discriminate between the two models based on the slope evolution.

The observed slopes (from Testi et al. 2022) are only included in the left column of Figure 5.5 as they refer to the current sample size. The main source of uncertainty in the current measurements is given by Upper Sco, mainly due to the incomplete sample; moreover, it is worth pointing out that external photoevaporation is likely to play a significant role in this region (Anania et al. in prep.). This comparison is meant as a first glance of the parameters space of the observed slopes, and we anticipate a proper exploration of the initial conditions once the full sample will be available. In the following Section, we discuss the other constraints that we can put on disc evolution, besides identifying the driving accretion mechanism.

5.5.2 What the slopes are *really* tracing

Despite not allowing to conclusively discriminate between different evolutionary scenarios with the current sample sizes, the slopes of the $M_{\rm d} - M_\star$ and $\dot{M} - M_\star$ correlations can still help with constraining other properties from the theoretical considerations presented in Section 5.3, which we summarise in Table 5.2. If we *assume* an evolutionary model to begin with, and we can estimate (directly or indirectly) either μ_0 or δ_0, we can constrain the other parameter. When discussing the observational determination of what we have so far referred to as *initial conditions*, it is important to clarify the meaning of *initial*. `Diskpop` deals with and evolves Class II, potentially Class III, objects; hence, the initial conditions we input refer to the beginning of the Class II phase, where the protostellar collapse is over and the disc is already formed. From the observational point of view, this means that we expect δ_0 and μ_0 to refer to young Class II objects - around, or younger than, approximately 1 Myr. Earlier phases like the Class 0 and I need a dedicated study, as the accretion of the protostellar envelope is expected to play a prominent role in those stages.

In the following, we discuss the constraints we can put in both directions and comment on their feasibility based on the currently available estimates of μ_0 and δ_0.

Constraining δ_0 from μ_0

Ansdell et al. (2017) claimed $\lambda_{\rm m}$ to be increasing with time. As shown by Somigliana et al.

(2022) and discussed in Section 5.3, increasing slopes imply that discs around less massive stars evolve faster than those around more massive stars; this can be interpreted in terms of increasing accretion timescale with stellar mass, which corresponds to $\mu_0 > 0$ (with $t_{\rm acc,0} \propto {M_\star}^{\mu_0}$). In this section we discuss the implications of the increasing slope scenario on the initial conditions, $\lambda_{\rm m,0}$ and $\lambda_{\rm acc,0}$.

The top panel of Table 5.2 shows the relation between μ_0 and δ_0 in the different evolutionary models. As $\mu_0 = \delta_0 - \zeta_0\xi$, in the viscous case (corresponding to $\xi = 0$) we have $\mu_0 = \delta_0$ as mentioned in Section 5.3. This means that, to recover the suggested increasing slopes scenario, δ_0 necessarily needs to be positive - regardless of the value of any other parameters: this translates to the initial $M_{\rm d} - M_\star$ correlation being steeper than $\dot{M} - M_\star$. In the hybrid and wind-driven case, instead, the implication is less straightforward as a positive μ_0 can lead to opposite signs of δ_0: this is determined by the scaling of the disc radius with the stellar mass, which is suggested to be (weakly) positive from observational evidences (e.g. Andrews et al. 2018b). In principle, as $\delta_0 \in (\zeta_0\xi, +\infty)$, the sign of ζ_0 determines whether negative values of δ_0 are possible; however, as ξ is a small number (0.1 in this work), only a limited area of the parameters space would lead to a negative δ_0. Summarising, if we assume increasing slopes ($\mu_0 > 0$) we can constrain the sign of δ_0 regardless of the evolutionary model assumed: in both cases δ_0 needs to be positive, which leads to an initially steeper $M_{\rm d} - M_\star$ than $\dot{M} - M_\star$ correlation.

Constraining μ_0 from $\delta_{\rm evo}$

Instead of assuming increasing slopes, we can start from the currently measured values of $\delta_{\rm evo}$ and estimate δ_0 in the different evolutionary models. In the viscous case, because $\delta_{\rm evo} = 0$, we focus on the value of the single slopes instead: as $\lambda_{\rm m,evo} = \lambda_{\rm acc,evo} = \delta_0/2 + \lambda_{\rm m,0}$, the measured final value of the slopes does not help in constraining δ_0 as it also depends on $\lambda_{\rm m,0}$. In the hybrid case, instead, we have $\delta_{\rm evo} = \xi(\zeta_0 - \mu_0)$, meaning that if we can determine the sign of $\delta_{\rm evo}$ we can constrain that of μ_0 as well. While in principle the sign of ζ_0 influences that of μ_0, as we mentioned above ζ_0 is likely a small number: therefore, effectively, $\delta_{\rm evo}$ and μ_0 have opposite signs for the vast majority of the parameters space.

Assuming that the observed disc populations can be considered evolved enough for the above arguments to hold, we can estimate $\delta_{\rm evo}$ from the most recent and homogeneous measurements available of $\lambda_{\rm m}$ and $\lambda_{\rm acc}$ (Testi et al., 2022). The resulting values of $\delta_{\rm obs}$ (which we label *observed* as opposed to the theoretical expectation, *evolved*), summarised in Table 5.3, are oscillating: out of the four regions L1668, Lupus, Chameleon I and Upper Sco, we find two positive and two negative median values. Moreover, in three cases out of four the uncertainties are so large that $\delta_{\rm obs}$ would be compatible with both a positive and a negative value. The difficulty in assessing the sign of $\delta_{\rm obs}$ from the current measurements of the slopes make constraining μ_0 from $\delta_{\rm evo}$ not trivial. Larger sample sizes would give a better measurement of the slopes and reduce the uncertainty, leading to a more solid determination of the sign of $\delta_{\rm obs}$ - which would possibly allow μ_0 to be constrained.

Summarising, the (admittedly not robust) observational evidence pointing towards increasing accretion timescale with stellar mass allows us to constrain the initial correlations between the stellar mass and disc parameters; regardless of the evolutionary model considered, the initial slope of the $M_{\rm d} - M_\star$ correlation needs to be larger than that of $\dot{M} - M_\star$. The other way around, constraining the slope of the accretion timescale - stellar mass correlation from the difference between $\lambda_{\rm m}$ and $\lambda_{\rm acc}$ at the present time, requires sample sizes larger by at least a factor two.

Region	Median age [Myr]	$\delta_{\rm obs}$
L1668	1	-0.3 ± 0.5
Lupus	2	0.1 ± 0.4
Cha I	2.8	-0.7 ± 0.4
Upper Sco	4.3	0.7 ± 0.8

Table 5.3: Values of δ derived from the currently available measurements. The values of δ are computed from measurements of $\lambda_{\rm m}$ and $\lambda_{\rm acc}$ reported by Testi et al. (2022).

5.6 Conclusions

In this paper, we have investigated the impact of disc evolution models on the correlations between the stellar mass and the disc properties - especially the disc mass and the accretion rate. We have explored the purely viscous, wind-driven, viscous and wind hybrid, and photoevaporative models. Assuming power-law correlations to hold as initial conditions, $M_{\rm d}(0) \propto {M_\star}^{\lambda_{\rm m,0}}$, $\dot{M}(0) \propto {M_\star}^{\lambda_{\rm acc,0}}$, we performed analytical calculations (where possible) and population synthesis simulations for both evolutionary scenarios, and compared them with the purely viscous case discussed in Somigliana et al. (2022). Our main results are the following:

1. The viscous and hybrid models change the slope of the initial correlations as function of the evolutionary time, but preserve their shape. In the wind-driven model, instead, the correlations deviate from the original power-law shape: this is visualised in the logarithmic plane as a bending of the linear correlation (see Figure 5.1). The bending direction is towards the less or more massive stars depending on the scaling of the accretion timescale with the stellar mass (positive and negative correlation respectively).

2. The characteristic behaviour of the slopes in the wind-driven model is concealed by the presence of a spread in the initial conditions, which introduces a scatter in the correlations and makes it no longer possible to detect the bending (Figure 5.2). This leads to a considerably similar evolution of the correlations in the different accretion models.

3. Performing our simulations with evolutionary models that match the disc dispersal timescales (intrinsic in the wind-driven model and including internal photoevaporation in the viscous case), we find that the evolution of the slopes is significantly impacted by the removal of discs from the population (Figure 5.3). Different realisations of the same simulation dramatically differ from one another, and show a stochastic behaviour with large variations (Figure 5.4). This has both a physical (presence of a spread in the initial conditions) and a statistical (low number of objects left after a few Myr of evolution) reason.

4. While a proper exploration of the parameters space, outside of the scope of this work, would be needed to assess the impact of the initial conditions, with the currently available sample sizes the noise dominates over the physical evolution.

5. Increasing the sample size can mitigate the effects of disc dispersal on the evolution of the slope by removing the stochastic effects. We find that, for our parameters choice, the complete sample of Upper Sco ($\sim$ 140 sources) at 5 Myr would reduce the oscillations enough to make the slopes a proxy for the evolutionary model (Figure 5.5).

6. While the currently available sample sizes do not yet allow to distinguish between the different evolutionary models, we can use them to put some constraints on the initial conditions. We find that in all evolutionary scenarios, the observational claim of increasing slopes leads to an initially steeper correlation between the disc mass and the stellar mass than between the accretion rate and the stellar mass. The other possible way, measuring the current slopes and inferring the correlation between the accretion timescale and the stellar mass from them, provides weaker constraints because of the high uncertainties in the current measurements.

7. We have presented and released the 1D Python disc population synthesis code `Diskpop` and its output analysis library `popcorn`.

In this work, we have shown how large enough samples of protoplanetary discs can provide a way of distinguishing between the evolutionary models (with a standard set of parameters) through the observation of the time evolution of the correlations between the disc properties and the stellar mass. We have shown how the stochastic fluctuations seen with the currently available observations could be significantly reduced if we had access to the complete Upper Sco sample, consisting of approximately 140 sources at 5 Myr. We strongly support the observational effort in the direction of obtaining larger amounts of data for evolved star-forming regions, and encourage the exploration of the parameters space beyond the standard case.

Acknowledgements

We thank an anonymous referee for their useful comments that helped us improve the clarity of the manuscript. This work was partly supported by the Italian Ministero dell'Istruzione, Università e Ricerca through the grant Progetti Premiali 2012-iALMA (CUP C52I13000140001), by the Deutsche Forschungsgemeinschaft (DFG, German Research Foundation) - Ref no. 325594231 FOR 2634/2 TE 1024/2-1, by the DFG Cluster of Excellence Origins (www.origins-cluster.de). This project has received funding from the European Union's Horizon 2020 research and innovation program under the Marie Sklodowska- Curie grant agreement No 823823 (DUSTBUSTERS) and from the European Research Council (ERC) via the ERC Synergy Grant ECOGAL (grant 855130) and ERC Starting Grant DiscEvol (grant 101039651). GR acknowledges support from Fondazione Cariplo, grant No. 2022-1217. Views and opinions expressed are however those of the authors only and do not necessarily reflect those of the European Union or the European Research Council Executive Agency. Neither the European Union nor the granting authority can be held responsible for them.

5.7 Appendix

5.7.1 Parameters used throughout the paper

Table 5.4 shows the parameters used throughout the paper. The general simulation parameters refer to the initial correlations (distribution, slopes and spreads), while the following three tables are divided by evolutionary model and display the main parameters for each of them.

General simulation parameters

$\lambda_{\mathrm{m},0}$	2.1
$\lambda_{\mathrm{acc},0}$	1.5
$\sigma_{\mathrm{M_d}}$	0.65 dex
$\sigma_{\mathrm{R_d}}$	0.52 dex
M_{d}, R_{d} distribution	lognormal

Viscous model

α_{SS}	10^{-3}

Photoevaporative model

α_{SS}	10^{-3}
$\dot{M}_w$	4×10^{-10} $\mathrm{M_\odot\ yr^{-1}}$

Wind-driven model

α_{SS}	10^{-3}
α_{DW}	10^{-3}
λ	3
ω	0.25

Table 5.4: Values of the parameters used throughout the paper, unless explicitly stated otherwise.

5.7.2 MHD model with $\mu < 0$

As mentioned in Section 5.3.3, the breaking of the linear correlation between the disc properties and the stellar mass happens towards higher or lower stellar masses depending on the value of μ_0. Figure 5.2 shows the a simulation $\mu_0 > 0$, while in Figure 5.6 we show the opposite case. As μ_0 is linked to δ_0 through $\mu_0 = \delta_0 - \zeta_0\xi$, if $\delta_0 < \zeta_0\xi$ the resulting μ_0 will be negative, leading to a specular bending of the correlation. Given that $\zeta_0\xi$ is a small number (~ 0.1 in our simulation), this generally requires a negative δ_0. The simulation in Figure 5.6 has $\lambda_{\mathrm{m},0} = 1.3$ and $\lambda_{\mathrm{acc},0} = 1.7$, resulting in $\delta_0 = -0.4$.

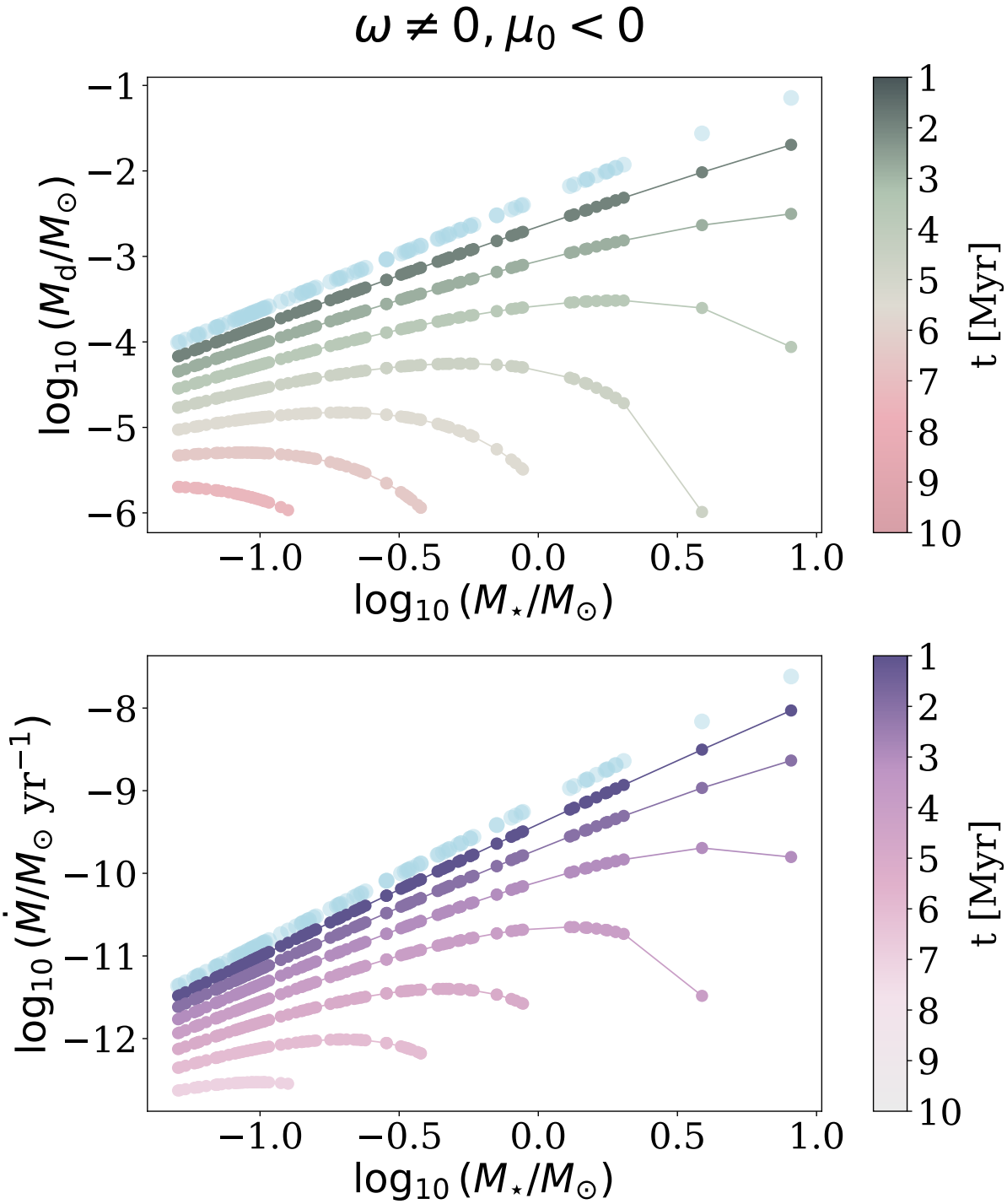

Figure 5.6: Same as Figure 5.2, but with a choice of initial slopes resulting in a negative μ_0 ($\lambda_{m,0} = 1.3, \lambda_{acc,0} = 1.7$). The bending of the linear correlation happens towards larger disc masses, in agreement with the prediction.

5.7.3 Validation of `Diskpop`

Figure 5.7 shows the evolution of the gas surface density as a function of the disc radius in the cases of evolution driven by (i) viscosity, (ii) viscosity and internal photoevaporation, (iii) MHD winds, and (iv) viscosity and external photoevaporation for a single disc simulated with `Diskpop`. The top left panel, corresponding to viscous evolution (i), shows the key feature of viscous spreading: while the global surface density decreases as a consequence of the accretion onto the central star, the radial extent of the disc increases. This is a consequence of the redistribution of angular momentum, that causes part of the disc material to move towards larger radii. The top right panel, where the disc evolves under the combined effect of viscosity and internal photoevaporation (ii), shows the characteristic two-timescales behaviour (Clarke et al., 2001): the evolution is effectively viscous in the earliest stages, as long as the accretion rate is larger than the photoevaporative mass-loss rate; then, photoevaporation opens a cavity within the disc, which gets divided into an inner and an outer disc. The inner disc is less extended and therefore has a shorter viscous timescale, which means it evolves much faster and is quickly completely accreted onto the protostar; the outer disc instead keeps on evolving on timescales comparable to the original one, making photoevaporation a two-timescales process. The bottom left panel shows a disc evolving due to MHD winds (iii): the absolute value of the surface density drops faster than in the viscous model, because of the increase of $\alpha_{\rm DW}$ in time. Furthermore, as angular momentum is removed from the wind (together with material), the disc does not spread but rather shrinks in time, as expected from the theoretical prediction (Tabone et al., 2022a). Finally, the bottom right panel shows the evolution of a disc undergoing external photoevaporation combined with viscosity (iv): the latter dominates at the earliest stages, producing the characteristic features like viscous spreading, while the effect of external photoevaporation is visible at later ages as a truncation of the disc that also halts its spreading. In this case, the disc truncation and the outside-in depletion of disc material is the consequence of the photo-dissociation of gas molecules due to the FUV radiation emitted by massive stars and experienced by the disc. The efficiency of this process depends primarily on the stellar mass and the FUV flux experienced: given a fixed FUV flux, a disc around a lower mass star will lose its material to external winds more easily compared to a disc around a higher mass star, because of the higher gravitational bond of the system. For the same reason, more extended and less massive discs are more prone to external truncation.

Figure 5.8 shows the isochrones in the $\dot{M} - M_{\rm d}$ plane at 0.1, 1 and 10 Myr for the three evolutionary models of viscosity, viscosity and photoevaporation, and MHD winds. Each dot represents a disc in the population, while the solid lines show the analytical prediction (when applicable): in the viscous case, the isochrones read (Lodato et al., 2017)

$$\dot{M} = \frac{M_{\rm d}}{2(2-\gamma)t}\left[1 - \left(\frac{M_{\rm d}}{M_0}\right)^{2(2-\gamma)}\right], \tag{5.15}$$

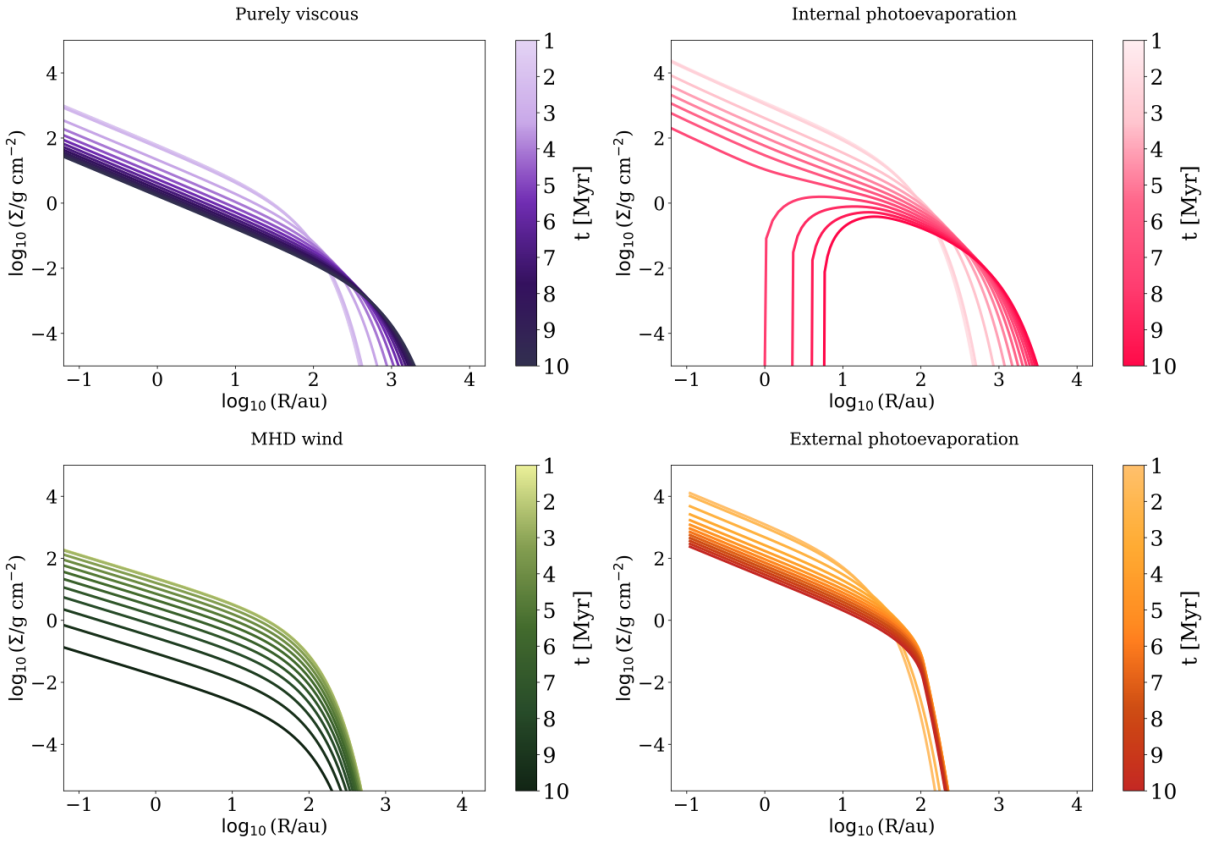

Figure 5.7: Gas surface density as a function of the radius for a disc generated with Diskpop at different times as the colour bar shows. The four models are purely viscous (top left, $\alpha_{\rm SS} = 10^{-3}$), viscous including internal photoevaporation (top right, $\alpha_{\rm SS} = 10^{-3}$, $\dot{M}_{\rm w} = 4 \times 10^{-10}$ M$_\odot$yr^{-1}), wind-driven (bottom left, $\alpha_{\rm DW} = 10^{-3}$, $\lambda = 3$, $\omega = 0.25$) and viscous including external photoevaporation (bottom right, $\alpha_{\rm SS} = 10^{-3}$, FUV = 100 G_0) respectively.

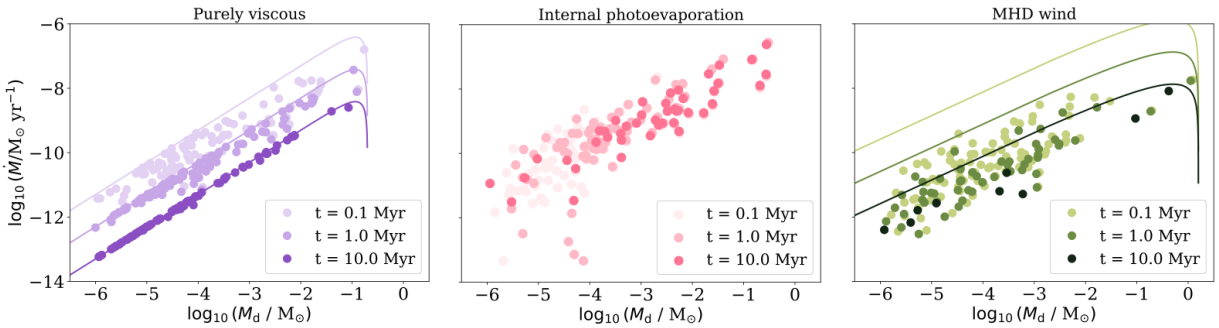

Figure 5.8: Isochrones at 0.1, 1, and 10 Myr for disc populations undergoing viscous, viscous+internal photoevaporation, and wind-driven evolution (left, centre, and right panel, respectively), with the same parameters as Figure 5.7. Each dot represents a disc, while the solid lines show the theoretical isochrones at the corresponding age, where available.

while in the MHD wind-driven scenario (Tabone et al., 2022a)

$$\dot{M} = \frac{1}{\omega(1+f_{\mathrm{M},0})t} M_{\mathrm{d}} \left[\left(\frac{M_{\mathrm{d}}}{M_0} \right)^{-\omega} - 1 \right]. \tag{5.16}$$

The left panel shows the viscous model, where the discs tend more and more towards the theoretical isochrone during their evolution (Lodato et al., 2017); the central panel includes internal photoevaporation, which has the effect of bending the isochrones once the accretion rate becomes comparable to the photoevaporative mass-loss rate (Somigliana et al., 2020); finally, the right panel shows an MHD wind-driven population, where the scatter in the $\dot{M} - M_{\mathrm{d}}$ plane remains significant during the evolution - contrary to the viscous prediction (Somigliana et al., 2023).

6

Conclusions and Outlook

In this Chapter, I summarise the findings and achievements of this thesis and frame them in the context of star and planet formation. I then discuss possible follow-ups of this work and the next challenges that the community is moving towards.

6.1 Summary of this thesis

The broader question that I tackled in this thesis is the angular momentum transport in protoplanetary discs. While the accretion process itself is readily explained in terms of angular momentum, which is either redistributed or lost and that causes material in the disc to drift radially towards the central protostar, the physical process leading to said angular momentum transfer is still debated. The traditional picture assumes a macroscopic, turbulent viscosity responsible for the *redistribution* of angular momentum within the disc; in this framework, part of the material in the disc loses angular momentum and moves to smaller radii, while another portion of material gains angular momentum instead and drifts further away from the protostar, increasing the radial disc size. The virtually infinite lifetime of purely viscous discs, as well as the observational evidence of low turbulence levels - at least, too low to systematically account for the observed accretion levels - have supported the alterative model of magnetohydrodynamic disc winds. In this scenario, vertical magnetic fields anchored in the disc launch winds that *remove* material, with the effect of transporting angular momentum away with it. While the viscous and wind-driven theory would, in principle, have an observable impact on disc evolution, empirically discriminating between the two of them has proven to be more difficult than expected.

The best approach to test evolutionary models is statistical analysis. To make predictions on observables directly affected by the angular momentum transport mechanism, one needs to build a theoretical model and simulate its effect on a large number of objects;

this allows to look for both evolutionary trends and correlations between the observed properties. This method, called population synthesis, gained significant attention in the last decade: the wealth of data available since the advent of ALMA and X-Shooter, capable of measuring the disc masses/sizes and accretion rates respectively, have provided the community with the ideal ground to put evolutionary models to a test. **The aim of this thesis is to advance the understanding of the impact of the angular momentum transport mechanism on observables of disc populations, with the ultimate goal of providing new proxies to constrain the relative importance of viscosity and magnetohydrodynamic winds.**

The use of the population synthesis approach to study protoplanetary discs is still relatively recent; at the beginning of this work, there was no specifically built, freely available software to carry out numerical simulations of disc populations under different physical conditions. A significant portion of this thesis was the development of the population synthesis code `Diskpop`, released in 2024 and freely available for the community. `Diskpop` is built to assemble realistic disc populations, with a variety of possible initial conditions, to then evolve via viscous or wind-driven accretion; it produces evolved synthetic populations whose properties can readily be compared to those of observed discs across different star-forming regions. Furthermore, `Diskpop` allows to account for additional processes, such as internal and external photoevaporation. The development and release of `Diskpop` represents a significant step forward in the field as it enables statistical modelling to complement the results of observational surveys, as well as testing the impact of several physical effects and parameters combinations. Prior to the release, it was already employed in several theoretical works, as well as in the context of the ALMA Large Program AGE-PRO to interpret the evolutionary trends inferred from their results.

I have run `Diskpop` simulations to investigate the impact of the accretion model on the observed correlations between the disc properties and the stellar mass. Assuming the disc mass-stellar mass and accretion rate-stellar mass power-law correlations to hold as initial conditions, I have explored how (i) purely viscous evolution, (ii) a combination of viscosity and internal photoevaporation, and (iii) magnetohydrodynamic winds shape the time evolution of the slopes of the correlations. Where analytical solutions were available, I made theoretical predictions that I later confirmed with `Diskpop`. I found that in the viscous case, the slopes of the two correlations are bound to reach the same evolved value, either increasing, decreasing, or remaining constant over time; this trend is not recovered in the other evolutionary scenarios. I then investigated the observability of this result, finding that - with the current sample sizes - the evolution of the slopes is dominated by disc dispersal. I showed how completing the currently available samples, especially in the older star-forming regions, would significantly reduce the uncertainty and allow to use the evolution of the slopes as an evolutionary proxy.

I have then explored the time evolution of the distribution of disc mass/accretion rate ratio, usually referred to as disc lifetime, under viscosity and wind-driven accretion. My

goal was to assess its suitability as observational diagnostic for disc evolution; I ran `Diskpop` simulations and focused on the mean, width, and skewness of the distribution in both evolutionary models. I found the mean value to be independent on the accretion model, while the width and the skewness showed a different enough evolution to be observed. Once convolving the numerical prediction with the observational uncertainty, however, I found that the otherwise pronounced difference in the skewness of the two models fades away; on the other hand, the width remains model-dependent. I concluded that the evolution of the width of the distribution of disc lifetimes can be used as an evolutionary proxy, and I discussed the impact of the uncertainty on the dust-determined disc masses. These results will be fully exploited in the near future, when the ongoing ALMA Large Programs AGE-PRO and DECO will obtain gas-determined disc masses.

To conclude, in this thesis I have explored the possibility to use novel diagnostics to trace the angular momentum transport mechanism in protoplanetary discs. I have proposed two candidate proxies, the time evolution of (a) the slopes of the disc properties - stellar mass correlations and (b) the width of the distribution of disc lifetimes. To support this scientific goal, I have developed and released the first freely accessible disc population synthesis code.

6.2 Future perspectives

An immediate future perspective of this work is the comparison of the theoretical predictions with the soon-to-be-available observational data, collected by several ongoing programs, to effectively test the evolutionary mechanisms. As technology progresses further and larger and larger amount of data become available to the community, population synthesis models will have a more and more crucial role in the interpretation of the observational evidences; while I have mostly employed it in the context of accretion models so far, `Diskpop` will allow to test the impact of several other physical mechanisms on disc populations. Possible promising applications include (but are not limited to) planet formation, the presence of substructures in the disc, or the chemical composition and evolution.

Most of the results of this thesis are based on the disc properties - stellar mass correlations, in terms of both their shape and time evolution, for Class IIs objects. The power-law correlations have been observed across all nearby star-forming regions, on the whole age spectrum; however, all the observational evidence refers to the same evolutionary stage and does not necessarily inform on the pre-protoplanetary disc regime. Because of this, and because `Diskpop` is conceived to simulate Class II objects, in this work I have assumed the correlations to hold as initial conditions, 'initial conditions' being the beginning of the Class II phase.

A natural development of this work would be to study the *establishment* of such correlations in the broader star formation context. In principle, instead of assuming a set of initial conditions, one could use the results of large scale cloud collapse simulations (see

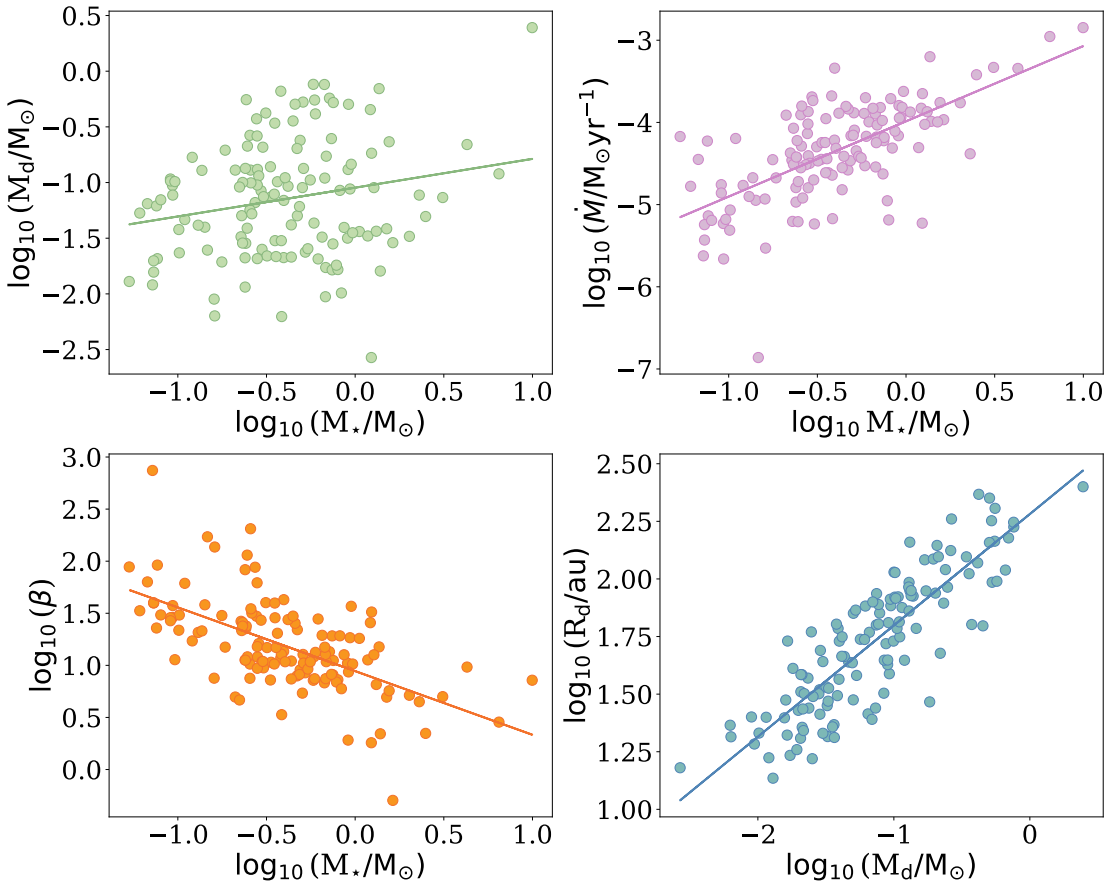

Figure 6.1: Correlations between disc mass and stellar mass (top left), disc mass and accretion rate (top right), plasma β and stellar mass (bottom left) and disc radius and disc mass (bottom right) from the non-ideal magnetohydrodynamic simulation of Lebreuilly et al. (2024).

e.g. Kuffmeier et al. 2017; Bate 2018; Kuffmeier et al. 2019; Lebreuilly et al. 2021). These complex simulations model the three-dimensional collapse of clouds and lead to the formation of self-consistent disc populations, where 'discs' are identified as structures of material around sink particles across the simulation. However, integrating in time up until the start of the Class II phase has an incredible computational cost; the most evolved available simulations so far, performed by Lebreuilly et al. (2024), 'only' reach ages of $\sim 30 - 40$ kyr - one order of magnitude younger than the typical age of the youngest observed star-forming regions ($\sim$ Myr), at a cost of $\sim 3 - 4$ million CPU hours. As further evolving the collapse simulations is not a viable option at the moment, it would be crucial to bridge the evolutionary gap between the resulting Class 0-I objects and the Class IIs simulated with tools like `Diskpop`. Properly addressing this task requires an extensive modelling effort, especially for what concerns the infall of material from the protostellar envelope, and is one of the follow-up works that I will carry on in the immediate future.

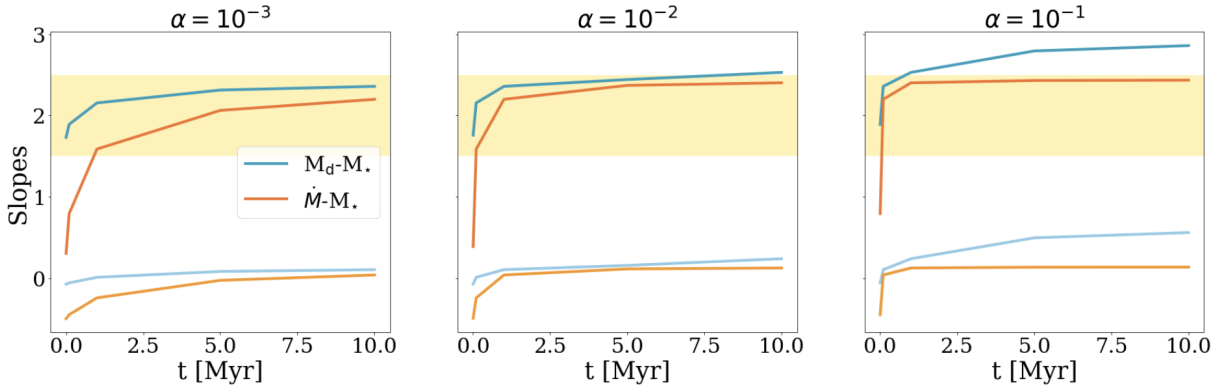

Figure 6.2: Time evolution of the $M_\mathrm{d} - M_\star$ (blue) and $\dot{M} - M_\star$ (orange) correlations for three different values of α_SS ($10^{-3}, 10^{-2}$ and 10^{-1} from left to right) starting from two different initial conditions. The yellow shaded area shows the range of observed slopes for populations of protoplanetary discs.

Keeping this caveat in mind, it is interesting to explore whether the early populations of young stellar objects produced by cloud collapse simulations show the same correlations between the disc properties and the stellar mass as observed in protoplanetary discs. Figure 6.1 shows the populations resulting from the non-ideal multidimensional magnetohydrodynamic simulation of Lebreuilly et al. (2024), sampling each object every 3 kyr. The disc mass - stellar mass correlations (top left panel), that is so pronounced for evolved disc populations, is hardly present: the fitted slope is 0.2, but the spread is large (0.7 dex) and the correlation coefficient is below 0.2, indicating a weak correlation. On the other hand, the the plasma β parameter shows a strong correlation with the stellar mass (bottom left panel); as β is linked to the α_DW parameter, which in turn controls the effectiveness of the accretion via magnetic winds, this suggests a significantly source-dependent accretion as opposed to the standard assumption of constant α_DW across the whole population. Furthermore, the disc radius strongly correlates with the disc mass (bottom right panel) and the accretion rate correlates with the stellar mass (top right panel), although with a slightly larger spread.

Considering the essentially non-existing correlation between the disc mass and the stellar mass at the end of the cloud collapse simulations, it is fair to wonder whether secular disc evolution would lead to its establishment. Figure 6.2 shows the result of preliminary `Diskpop` simulations in the viscous regime with three different α_SS values, spanning from the classic assumption of 10^{-3} to a higher 10^{-1}, more realistic for earlier sources with large disc masses and accretion rates. The different $M_\mathrm{d} - M_\star$ input correlation does not alter the evolutionary behaviour, leading to the same slight increase in time; this means that an initial slope close to zero cannot reach the observed values, highlighted as a yellow shaded region, as a consequence of disc evolution alone. It is however important to keep in mind that these plots are only a preliminary exploration, as (i) this simulation used viscous evolution, (ii) the efficiency of the wind-driven accretion is likely source-dependent, and

(iii) there is an evolutionary gap between the data plotted in Figure 6.1 and 6.2. Still, these results suggest that the observed correlations in protoplanetary discs *need* to be already present at the beginning of Class II phase, as disc evolution can only slightly alter their slope. The numerical implementation of the transition between Class 0-I and Class IIs will need to account for this evidence, and produce the correlations together with the observed values of disc masses, accretion rates, and radii.

Bibliography

Adachi, I., Hayashi, C., & Nakazawa, K. 1976, Progress of Theoretical Physics, 56, 1756

Alcalá, J. M., Manara, C. F., Natta, A., et al. 2017, A&A, 600, A20

Alcalá, J. M., Natta, A., Manara, C. F., et al. 2014, A&A, 561, A2

Alexander, R., Pascucci, I., Andrews, S., Armitage, P., & Cieza, L. 2014, in Protostars and Planets VI, ed. H. Beuther, R. S. Klessen, C. P. Dullemond, & T. Henning, 475–496

Alexander, R., Rosotti, G., Armitage, P. J., et al. 2023, MNRAS, 524, 3948

Alexander, R. D. 2008, MNRAS, 391, L64

Alexander, R. D. & Armitage, P. J. 2006, ApJ, 639, L83

Alexander, R. D. & Armitage, P. J. 2009, ApJ, 704, 989

Alexander, R. D., Clarke, C. J., & Pringle, J. E. 2004, MNRAS, 354, 71

Alexander, R. D., Clarke, C. J., & Pringle, J. E. 2006a, MNRAS, 369, 216

Alexander, R. D., Clarke, C. J., & Pringle, J. E. 2006b, MNRAS, 369, 229

Alexander, R. D., Clarke, C. J., & Pringle, J. E. 2006c, MNRAS, 369, 229

Alibert, Y., Carron, F., Fortier, A., et al. 2013, A&A, 558, A109

ALMA Partnership, Brogan, C. L., Pérez, L. M., et al. 2015, ApJ, 808, L3

Anderson, D. E., Cleeves, L. I., Blake, G. A., et al. 2022, ApJ, 927, 229

Andre, P., Ward-Thompson, D., & Barsony, M. 2000, in Protostars and Planets IV, ed. V. Mannings, A. P. Boss, & S. S. Russell, 59

Andrews, S. M. 2020, ARA&A, 58, 483

Andrews, S. M., Huang, J., Pérez, L. M., et al. 2018a, ApJ, 869, L41

Andrews, S. M., Rosenfeld, K. A., Kraus, A. L., & Wilner, D. J. 2013, ApJ, 771, 129

Andrews, S. M., Terrell, M., Tripathi, A., et al. 2018b, ApJ, 865, 157

Ansdell, M., Haworth, T. J., Williams, J. P., et al. 2020, AJ, 160, 248

Ansdell, M., Williams, J. P., Manara, C. F., et al. 2017, AJ, 153, 240

Ansdell, M., Williams, J. P., Trapman, L., et al. 2018, ApJ, 859, 21

Ansdell, M., Williams, J. P., van der Marel, N., et al. 2016, ApJ, 828, 46

Appelgren, J., Lambrechts, M., & van der Marel, N. 2023, A&A, 673, A139

Armitage, P. J. 2007, arXiv e-prints, astro

Armitage, P. J., Simon, J. B., & Martin, R. G. 2013, ApJ, 778, L14

Aru, M. L., Maucó, K., Manara, C. F., et al. 2024, A&A, 687, A93

Aso, Y., Kwon, W., Ohashi, N., et al. 2023, ApJ, 954, 101

Bacmann, A., André, P., Puget, J. L., et al. 2000, A&A, 361, 555

Bae, J., Hartmann, L., Zhu, Z., & Nelson, R. P. 2014, ApJ, 795, 61

Bae, J., Isella, A., Zhu, Z., et al. 2023, in Astronomical Society of the Pacific Conference Series, Vol. 534, Protostars and Planets VII, ed. S. Inutsuka, Y. Aikawa, T. Muto, K. Tomida, & M. Tamura, 423

Bai, X.-N. 2016, ApJ, 821, 80

Bai, X.-N. 2017, ApJ, 845, 75

Balbus, S. A. 2011, in Physical Processes in Circumstellar Disks around Young Stars, ed. P. J. V. Garcia, 237–282

Balbus, S. A. & Hawley, J. F. 1991, ApJ, 376, 214

Ballabio, G., Alexander, R. D., & Clarke, C. J. 2020a, MNRAS, 496, 2932

Ballabio, G., Alexander, R. D., & Clarke, C. J. 2020b, MNRAS, 496, 2932

Ballering, N. P., Cleeves, L. I., Haworth, T. J., et al. 2023, ApJ, 954, 127

Banzatti, A., Pascucci, I., Edwards, S., et al. 2019, ApJ, 870, 76

Barenfeld, S. A., Carpenter, J. M., Ricci, L., & Isella, A. 2016, ApJ, 827, 142

Barenfeld, S. A., Carpenter, J. M., Sargent, A. I., Isella, A., & Ricci, L. 2017, ApJ, 851, 85

Bary, J. S., Weintraub, D. A., Shukla, S. J., Leisenring, J. M., & Kastner, J. H. 2008, ApJ, 678, 1088

Basri, G. & Batalha, C. 1990, ApJ, 363, 654

Basri, G. & Bertout, C. 1989, ApJ, 341, 340

Bate, M. R. 2018, MNRAS, 475, 5618

Bate, M. R., Bonnell, I. A., & Bromm, V. 2003, in IAU Symposium, Vol. 211, Brown Dwarfs, ed. E. Martín, 27

Beccari, G., Boffin, H. M. J., Jerabkova, T., et al. 2018, MNRAS, 481, L11

Beckwith, S., Sargent, A. I., Scoville, N. Z., et al. 1986, ApJ, 309, 755

Beckwith, S. V. W., Sargent, A. I., Chini, R. S., & Guesten, R. 1990, AJ, 99, 924

Benisty, M., Dominik, C., Follette, K., et al. 2023, in Astronomical Society of the Pacific Conference Series, Vol. 534, Protostars and Planets VII, ed. S. Inutsuka, Y. Aikawa, T. Muto, K. Tomida, & M. Tamura, 605

Benson, P. J. & Myers, P. C. 1989, ApJS, 71, 89

Bergin, E. A., Cleeves, L. I., Gorti, U., et al. 2013, Nature, 493, 644

Bernabò, L. M., Turrini, D., Testi, L., Marzari, F., & Polychroni, D. 2022, ApJ, 927, L22

Bertout, C. 1989, ARA&A, 27, 351

Béthune, W., Lesur, G., & Ferreira, J. 2017, A&A, 600, A75

Birnstiel, T., Dullemond, C. P., & Brauer, F. 2010, A&A, 513, A79

Birnstiel, T., Klahr, H., & Ercolano, B. 2012, A&A, 539, A148

Bitner, M. A., Richter, M. J., Lacy, J. H., et al. 2008, ApJ, 688, 1326

Bjerkeli, P., van der Wiel, M. H. D., Harsono, D., Ramsey, J. P., & Jørgensen, J. K. 2016, Nature, 540, 406

Blandford, R. D. & Payne, D. G. 1982, MNRAS, 199, 883

Bohlin, R. C., Savage, B. D., & Drake, J. F. 1978, ApJ, 224, 132

Booth, A. S., Tabone, B., Ilee, J. D., et al. 2021, ApJS, 257, 16

Booth, R. A., Clarke, C. J., Madhusudhan, N., & Ilee, J. D. 2017, MNRAS, 469, 3994

Brauer, F., Henning, T., & Dullemond, C. P. 2008, A&A, 487, L1

Cacciapuoti, L., Macias, E., Gupta, A., et al. 2024, A&A, 682, A61

Calahan, J. K., Bergin, E., Zhang, K., et al. 2021, ApJ, 908, 8

Calvet, N. & Gullbring, E. 1998, ApJ, 509, 802

Carmona, A., van den Ancker, M. E., Henning, T., et al. 2008, A&A, 477, 839

Carpenter, J., Iono, D., Kemper, F., & Wootten, A. 2020, arXiv e-prints, arXiv:2001.11076

Carrera, D., Johansen, A., & Davies, M. B. 2015, A&A, 579, A43

Cazzoletti, P., Manara, C. F., Baobab Liu, H., et al. 2019, A&A, 626, A11

Chambers, J. 2019, ApJ, 879, 98

Chou, H.-G., Yen, H.-W., Koch, P. M., & Guilloteau, S. 2016, ApJ, 823, 151

Cieza, L. A., Ruíz-Rodríguez, D., Hales, A., et al. 2019, MNRAS, 482, 698

Claes, R. A. B., Manara, C. F., Garcia-Lopez, R., et al. 2022, A&A, 664, L7

Clarke, C. J. & Alexander, R. D. 2016, MNRAS, 460, 3044

Clarke, C. J., Gendrin, A., & Sotomayor, M. 2001, MNRAS, 328, 485

Clarke, C. J. & Pringle, J. E. 2006, MNRAS, 370, L10

Cleeves, L. I., Bergin, E. A., Qi, C., Adams, F. C., & Öberg, K. I. 2015, ApJ, 799, 204

Coleman, G. A. L., Mroueh, J. K., & Haworth, T. J. 2024, MNRAS, 527, 7588

Concha-Ramírez, F., Wilhelm, M. J. C., Portegies Zwart, S., & Haworth, T. J. 2019, MNRAS, 490, 5678

Cox, E. G., Harris, R. J., Looney, L. W., et al. 2017, ApJ, 851, 83

Dahm, S. E. 2008, AJ, 136, 521

Delussu, L., Birnstiel, T., Miotello, A., et al. 2024, A&A, 688, A81

Dipierro, G., Price, D., Laibe, G., et al. 2015, MNRAS, 453, L73

Dittkrist, K. M., Mordasini, C., Klahr, H., Alibert, Y., & Henning, T. 2014, A&A, 567, A121

Dong, R., Zhu, Z., Rafikov, R. R., & Stone, J. M. 2015, ApJ, 809, L5

Dubrulle, B., Morfill, G., & Sterzik, M. 1995, Icarus, 114, 237

Dullemond, C. P., Natta, A., & Testi, L. 2006, ApJ, 645, L69

Dunham, M. M., Allen, L. E., Evans, Neal J., I., et al. 2015, ApJS, 220, 11

Dunham, M. M., Stutz, A. M., Allen, L. E., et al. 2014, in Protostars and Planets VI, ed. H. Beuther, R. S. Klessen, C. P. Dullemond, & T. Henning, 195–218

Eisner, J. A., Arce, H. G., Ballering, N. P., et al. 2018, ApJ, 860, 77

Eisner, J. A., Bally, J. M., Ginsburg, A., & Sheehan, P. D. 2016, ApJ, 826, 16

Emsenhuber, A., Burn, R., Weder, J., et al. 2023, A&A, 673, A78

Ercolano, B., Clarke, C. J., & Hall, A. C. 2011, MNRAS, 410, 671

Ercolano, B., Mayr, D., Owen, J. E., Rosotti, G., & Manara, C. F. 2014, MNRAS, 439, 256

Ercolano, B. & Owen, J. E. 2010, MNRAS, 406, 1553

Ercolano, B., Picogna, G., Monsch, K., Drake, J. J., & Preibisch, T. 2021, MNRAS, 508, 1675

Esplin, T. L. & Luhman, K. L. 2020, AJ, 159, 282

Esplin, T. L. & Luhman, K. L. 2022, AJ, 163, 64

Evans, Neal J., I., Dunham, M. M., Jørgensen, J. K., et al. 2009, ApJS, 181, 321

Fairlamb, J. R., Oudmaijer, R. D., Mendigutía, I., Ilee, J. D., & van den Ancker, M. E. 2015, MNRAS, 453, 976

Fang, M., Pascucci, I., Edwards, S., et al. 2018, ApJ, 868, 28

Favre, C., Cleeves, L. I., Bergin, E. A., Qi, C., & Blake, G. A. 2013, ApJ, 776, L38

Fedele, D., van den Ancker, M. E., Henning, T., Jayawardhana, R., & Oliveira, J. M. 2010, A&A, 510, A72

Ferreira, J. 1997, A&A, 319, 340

Field, G. B., Somerville, W. B., & Dressler, K. 1966, ARA&A, 4, 207

Fiorellino, E., Tychoniec, Ł., Cruz-Sáenz de Miera, F., et al. 2023, ApJ, 944, 135

Flaherty, K., Hughes, A. M., Simon, J. B., et al. 2020, ApJ, 895, 109

Flaherty, K., Hughes, A. M., Simon, J. B., et al. 2024, MNRAS, 532, 363

Flaherty, K. M., Hughes, A. M., Teague, R., et al. 2018, ApJ, 856, 117

Font, A. S., McCarthy, I. G., Johnstone, D., & Ballantyne, D. R. 2004, ApJ, 607, 890

Fortier, A., Alibert, Y., Carron, F., Benz, W., & Dittkrist, K. M. 2013, A&A, 549, A44

Fouchet, L., Alibert, Y., Mordasini, C., & Benz, W. 2012, A&A, 540, A107

Frank, A., Ray, T. P., Cabrit, S., et al. 2014, in Protostars and Planets VI, ed. H. Beuther, R. S. Klessen, C. P. Dullemond, & T. Henning, 451–474

Gaia Collaboration, Prusti, T., de Bruijne, J. H. J., et al. 2016, A&A, 595, A1

Galli, P. A. B., Bouy, H., Olivares, J., et al. 2021, A&A, 654, A122

Galli, P. A. B., Bouy, H., Olivares, J., et al. 2020, A&A, 643, A148

Garufi, A., Podio, L., Codella, C., et al. 2022, A&A, 658, A104

Ginski, C., Facchini, S., Huang, J., et al. 2021, ApJ, 908, L25

Goldsmith, P. F. & Arquilla, R. 1985, in Protostars and Planets II, ed. D. C. Black & M. S. Matthews, 137–149

Goodman, A. A., Benson, P. J., Fuller, G. A., & Myers, P. C. 1993, ApJ, 406, 528

Gorti, U. & Hollenbach, D. 2008, ApJ, 683, 287

Greene, T. P., Wilking, B. A., Andre, P., Young, E. T., & Lada, C. J. 1994, ApJ, 434, 614

Guarcello, M. G., Drake, J. J., Wright, N. J., et al. 2016, arXiv e-prints, arXiv:1605.01773

Gullbring, E., Calvet, N., Muzerolle, J., & Hartmann, L. 2000, ApJ, 544, 927

Gullbring, E., Hartmann, L., Briceño, C., & Calvet, N. 1998, ApJ, 492, 323

Gundlach, B. & Blum, J. 2015, ApJ, 798, 34

Gupta, A., Miotello, A., Manara, C. F., et al. 2023, A&A, 670, L8

Güttler, C., Blum, J., Zsom, A., Ormel, C. W., & Dullemond, C. P. 2010, A&A, 513, A56

Habing, H. J. 1968, Bull. Astron. Inst. Netherlands, 19, 421

Haisch, Karl E., J., Lada, E. A., & Lada, C. J. 2001, ApJ, 553, L153

Hamann, F. 1994, ApJS, 93, 485

Harada, N., Tokuda, K., Yamasaki, H., et al. 2023, ApJ, 945, 63

Harrison, R. E., Looney, L. W., Stephens, I. W., et al. 2021, ApJ, 908, 141

Hartigan, P., Edwards, S., & Ghandour, L. 1995, ApJ, 452, 736

Hartigan, P., Kenyon, S. J., Hartmann, L., et al. 1991, ApJ, 382, 617

Hartmann, L., Calvet, N., Gullbring, E., & D'Alessio, P. 1998, ApJ, 495, 385

Hartmann, L., Herczeg, G., & Calvet, N. 2016, ARA&A, 54, 135

Haworth, T. J., Coleman, G. A. L., Qiao, L., Sellek, A. D., & Askari, K. 2023, MNRAS, 526, 4315

Heigl, S., Hoemann, E., & Burkert, A. 2024, A&A, 686, A246

Hendler, N., Pascucci, I., Pinilla, P., et al. 2020, ApJ, 895, 126

Hennebelle, P., Commerçon, B., Lee, Y.-N., & Charnoz, S. 2020, A&A, 635, A67

Hennebelle, P., Lesur, G., & Fromang, S. 2017, A&A, 599, A86

Henney, W. J. & Arthur, S. J. 1998, AJ, 116, 322

Henney, W. J. & O'Dell, C. R. 1999, AJ, 118, 2350

Henney, W. J., O'Dell, C. R., Meaburn, J., Garrington, S. T., & Lopez, J. A. 2002, ApJ, 566, 315

Herbst, W., Eislöffel, J., Mundt, R., & Scholz, A. 2007, in Protostars and Planets V, ed. B. Reipurth, D. Jewitt, & K. Keil, 297

Herczeg, G. J. & Hillenbrand, L. A. 2008, ApJ, 681, 594

Herczeg, G. J., Kuhn, M. A., Zhou, X., et al. 2019, ApJ, 878, 111

Hernández, J., Hartmann, L., Calvet, N., et al. 2008, ApJ, 686, 1195

Hernández, J., Hartmann, L., Megeath, T., et al. 2007, ApJ, 662, 1067

Heyer, M. H. 1988, ApJ, 324, 311

Hildebrand, R. H. 1983, QJRAS, 24, 267

Hollenbach, D., Johnstone, D., Lizano, S., & Shu, F. 1994, ApJ, 428, 654

Huang, J., Andrews, S. M., Pérez, L. M., et al. 2018, ApJ, 869, L43

Ida, S. & Lin, D. N. C. 2004, ApJ, 604, 388

Ilee, J. D., Walsh, C., Jennings, J., et al. 2022, MNRAS, 515, L23

Ingleby, L., Calvet, N., Herczeg, G., et al. 2013, ApJ, 767, 112

Jin, S., Mordasini, C., Parmentier, V., et al. 2014, ApJ, 795, 65

Johansen, A. & Lambrechts, M. 2017, Annual Review of Earth and Planetary Sciences, 45, 359

Johansen, A., Oishi, J. S., Mac Low, M.-M., et al. 2007, Nature, 448, 1022

Johnstone, D., Hollenbach, D., & Bally, J. 1998, ApJ, 499, 758

Jones, M. G., Pringle, J. E., & Alexander, R. D. 2012, MNRAS, 419, 925

Kalari, V. M., Vink, J. S., Drew, J. E., et al. 2015, MNRAS, 453, 1026

Kido, M., Takakuwa, S., Saigo, K., et al. 2023, ApJ, 953, 190

Kley, W. & Lin, D. N. C. 1996, ApJ, 461, 933

Komaki, A., Nakatani, R., & Yoshida, N. 2021, ApJ, 910, 51

Kratter, K. & Lodato, G. 2016, ARA&A, 54, 271

Kroupa, P. 2001, MNRAS, 322, 231

Kuffmeier, M., Calcutt, H., & Kristensen, L. E. 2019, A&A, 628, A112

Kuffmeier, M., Dullemond, C. P., Reissl, S., & Goicovic, F. G. 2021, A&A, 656, A161

Kuffmeier, M., Frimann, S., Jensen, S. S., & Haugbølle, T. 2018, MNRAS, 475, 2642

Kuffmeier, M., Haugbølle, T., & Nordlund, Å. 2017, ApJ, 846, 7

Kuffmeier, M., Jensen, S. S., & Haugbølle, T. 2023, European Physical Journal Plus, 138, 272

Kurtovic, N. T., Pinilla, P., Long, F., et al. 2021, A&A, 645, A139

Kuznetsova, A., Bae, J., Hartmann, L., & Mac Low, M.-M. 2022, ApJ, 928, 92

Lada, C. J. 1987, in IAU Symposium, Vol. 115, Star Forming Regions, ed. M. Peimbert & J. Jugaku, 1

Lada, C. J. & Wilking, B. A. 1984, ApJ, 287, 610

Laibe, G. & Price, D. J. 2014, MNRAS, 444, 1940

Lebreuilly, U., Hennebelle, P., Colman, T., et al. 2021, ApJ, 917, L10

Lebreuilly, U., Hennebelle, P., Colman, T., et al. 2024, A&A, 682, A30

Lesur, G. 2021, Journal of Plasma Physics, 87, 205870101

Lesur, G., Flock, M., Ercolano, B., et al. 2023, in Astronomical Society of the Pacific Conference Series, Vol. 534, Protostars and Planets VII, ed. S. Inutsuka, Y. Aikawa, T. Muto, K. Tomida, & M. Tamura, 465

Lesur, G., Kunz, M. W., & Fromang, S. 2014, A&A, 566, A56

Liffman, K. 2003, PASA, 20, 337

Liu, B. & Ji, J. 2020, Research in Astronomy and Astrophysics, 20, 164

Liu, S.-F., Jin, S., Li, S., Isella, A., & Li, H. 2018, ApJ, 857, 87

Lodato, G., Rampinelli, L., Viscardi, E., et al. 2023, MNRAS, 518, 4481

Lodato, G., Scardoni, C. E., Manara, C. F., & Testi, L. 2017, MNRAS, 472, 4700

Long, F., Andrews, S. M., Rosotti, G., et al. 2022, ApJ, 931, 6

Long, F., Herczeg, G. J., Harsono, D., et al. 2019, ApJ, 882, 49

Long, F., Pinilla, P., Herczeg, G. J., et al. 2018, ApJ, 869, 17

Longarini, C., Armitage, P. J., Lodato, G., Price, D. J., & Ceppi, S. 2023a, MNRAS, 522, 6217

Longarini, C., Lodato, G., Bertin, G., & Armitage, P. J. 2023b, MNRAS, 519, 2017

Luhman, K. L. 2020, AJ, 160, 186

Luhman, K. L., Allen, P. R., Espaillat, C., Hartmann, L., & Calvet, N. 2010, ApJS, 186, 111

Luhman, K. L. & Esplin, T. L. 2020, AJ, 160, 44

Lynden-Bell, D. & Pringle, J. E. 1974, MNRAS, 168, 603

Machida, M. N. & Basu, S. 2024, arXiv e-prints, arXiv:2405.08271

Machida, M. N. & Hosokawa, T. 2013, MNRAS, 431, 1719

Mamajek, E. E. 2009, in American Institute of Physics Conference Series, Vol. 1158, Exoplanets and Disks: Their Formation and Diversity, ed. T. Usuda, M. Tamura, & M. Ishii, 3–10

Manara, C. F., Ansdell, M., Rosotti, G. P., et al. 2023, in Astronomical Society of the Pacific Conference Series, Vol. 534, Protostars and Planets VII, ed. S. Inutsuka, Y. Aikawa, T. Muto, K. Tomida, & M. Tamura, 539

Manara, C. F., Fedele, D., Herczeg, G. J., & Teixeira, P. S. 2016a, A&A, 585, A136

Manara, C. F., Natta, A., Rosotti, G. P., et al. 2020, A&A, 639, A58

Manara, C. F., Prusti, T., Comeron, F., et al. 2018, A&A, 615, L1

Manara, C. F., Robberto, M., Da Rio, N., et al. 2012, ApJ, 755, 154

Manara, C. F., Rosotti, G., Testi, L., et al. 2016b, A&A, 591, L3

Manara, C. F., Testi, L., Herczeg, G. J., et al. 2017a, A&A, 604, A127

Manara, C. F., Testi, L., Herczeg, G. J., et al. 2017b, A&A, 604, A127

Manara, C. F., Testi, L., Natta, A., et al. 2014, A&A, 568, A18

Mann, R. K., Di Francesco, J., Johnstone, D., et al. 2014, ApJ, 784, 82

Masset, F. S. & Casoli, J. 2010, ApJ, 723, 1393

Maury, A. J., André, P., Testi, L., et al. 2019, A&A, 621, A76

Mauxion, J., Lesur, G., & Maret, S. 2024, arXiv e-prints, arXiv:2403.16753

Mayor, M. & Queloz, D. 1995, Nature, 378, 355

McCaughrean, M. J. & O'Dell, C. R. 1996, AJ, 111, 1977

McClure, M. K., Bergin, E. A., Cleeves, L. I., et al. 2016, ApJ, 831, 167

Mendigutía, I., Calvet, N., Montesinos, B., et al. 2011, A&A, 535, A99

Mignon-Risse, R., González, M., & Commerçon, B. 2021, A&A, 656, A85

Miller, G. E. & Scalo, J. M. 1979, ApJS, 41, 513

Miotello, A., Kamp, I., Birnstiel, T., Cleeves, L. C., & Kataoka, A. 2023, in Astronomical Society of the Pacific Conference Series, Vol. 534, Protostars and Planets VII, ed. S. Inutsuka, Y. Aikawa, T. Muto, K. Tomida, & M. Tamura, 501

Mohanty, S., Jayawardhana, R., & Basri, G. 2005, ApJ, 626, 498

Morbidelli, A., Lunine, J. I., O'Brien, D. P., Raymond, S. N., & Walsh, K. J. 2012, Annual Review of Earth and Planetary Sciences, 40, 251

Mordasini, C., Alibert, Y., & Benz, W. 2009a, A&A, 501, 1139

Mordasini, C., Alibert, Y., Benz, W., & Naef, D. 2009b, A&A, 501, 1161

Mordasini, C., Alibert, Y., Klahr, H., & Henning, T. 2012, A&A, 547, A111

Mordasini, C., Mollière, P., Dittkrist, K. M., Jin, S., & Alibert, Y. 2015, International Journal of Astrobiology, 14, 201

Mulders, G. D., Pascucci, I., Manara, C. F., et al. 2017, ApJ, 847, 31

Murphy, S. J., Lawson, W. A., & Bessell, M. S. 2013, MNRAS, 435, 1325

Muzerolle, J., Hartmann, L., & Calvet, N. 1998, AJ, 116, 2965

Muzerolle, J., Hillenbrand, L., Briceño, C., Calvet, N., & Hartmann, L. 2003, in Brown Dwarfs, Vol. 211, 141

Myers, P. C. & Benson, P. J. 1983, ApJ, 266, 309

Myers, P. C., Fuller, G. A., Goodman, A. A., & Benson, P. J. 1991, ApJ, 376, 561

Najita, J. R. & Bergin, E. A. 2018, ApJ, 864, 168

Nakatani, R., Hosokawa, T., Yoshida, N., Nomura, H., & Kuiper, R. 2018, ApJ, 865, 75

Natta, A., Testi, L., Alcalá, J. M., et al. 2014, A&A, 569, A5

Natta, A., Testi, L., Muzerolle, J., et al. 2004, A&A, 424, 603

Natta, A., Testi, L., & Randich, S. 2006, A&A, 452, 245

Ndugu, N., Bitsch, B., & Lena, L. J. 2024, arXiv e-prints, arXiv:2409.07596

Nelson, R. P., Gressel, O., & Umurhan, O. M. 2013, MNRAS, 435, 2610

Nisini, B., Antoniucci, S., Alcalá, J. M., et al. 2018, A&A, 609, A87

O'Dell, C. R. & Wen, Z. 1994, ApJ, 436, 194

O'Dell, C. R., Wen, Z., & Hu, X. 1993, ApJ, 410, 696

Ormel, C. W. 2017, in Astrophysics and Space Science Library, Vol. 445, Formation, Evolution, and Dynamics of Young Solar Systems, ed. M. Pessah & O. Gressel, 197

Owen, J. E., Clarke, C. J., & Ercolano, B. 2012, MNRAS, 422, 1880

Owen, J. E., Ercolano, B., & Clarke, C. J. 2011, MNRAS, 412, 13

Owen, J. E., Ercolano, B., Clarke, C. J., & Alexand er, R. D. 2010, MNRAS, 401, 1415

Pascucci, I., Cabrit, S., Edwards, S., et al. 2023, in Astronomical Society of the Pacific Conference Series, Vol. 534, Protostars and Planets VII, ed. S. Inutsuka, Y. Aikawa, T. Muto, K. Tomida, & M. Tamura, 567

Pascucci, I., Gorti, U., Hollenbach, D., et al. 2006, ApJ, 651, 1177

Pascucci, I., Herczeg, G., Carr, J. S., & Bruderer, S. 2013, ApJ, 779, 178

Pascucci, I. & Sterzik, M. 2009, ApJ, 702, 724

Pascucci, I., Sterzik, M., Alexander, R. D., et al. 2011, ApJ, 736, 13

Pascucci, I., Testi, L., Herczeg, G. J., et al. 2016, ApJ, 831, 125

Picogna, G., Ercolano, B., & Espaillat, C. C. 2021, MNRAS, 508, 3611

Picogna, G., Ercolano, B., Owen, J. E., & Weber, M. L. 2019, MNRAS, 487, 691

Pineda, J. E., Segura-Cox, D., Caselli, P., et al. 2020, Nature Astronomy, 4, 1158

Pineda, J. E., Zhao, B., Schmiedeke, A., et al. 2019, ApJ, 882, 103

Pinilla, P., Birnstiel, T., Ricci, L., et al. 2012, A&A, 538, A114

Pinilla, P., Pascucci, I., & Marino, S. 2020, A&A, 635, A105

Pinte, C., Dent, W. R. F., Ménard, F., et al. 2016, ApJ, 816, 25

Pinte, C. & Laibe, G. 2014, A&A, 565, A129

Pollack, J. B., Hubickyj, O., Bodenheimer, P., et al. 1996, Icarus, 124, 62

Popham, R., Narayan, R., Hartmann, L., & Kenyon, S. 1993, ApJ, 415, L127

Preibisch, T. 2012, Research in Astronomy and Astrophysics, 12, 1

Pringle, J. E. 1981, ARA&A, 19, 137

Rafikov, R. R. 2017, ApJ, 837, 163

Ribas, Á., Merín, B., Bouy, H., & Maud, L. T. 2014, A&A, 561, A54

Ricci, L., Robberto, M., & Soderblom, D. R. 2008, AJ, 136, 2136

Rigliaco, E., Natta, A., Randich, S., Testi, L., & Biazzo, K. 2011, A&A, 525, A47

Rigliaco, E., Natta, A., Testi, L., et al. 2012, A&A, 548, A56

Rigliaco, E., Pascucci, I., Gorti, U., Edwards, S., & Hollenbach, D. 2013, ApJ, 772, 60

Rosotti, G. P. 2023, New A Rev., 96, 101674

Rosotti, G. P., Booth, R. A., Tazzari, M., et al. 2019a, MNRAS, 486, L63

Rosotti, G. P., Clarke, C. J., Manara, C. F., & Facchini, S. 2017, MNRAS, 468, 1631

Rosotti, G. P., Tazzari, M., Booth, R. A., et al. 2019b, MNRAS, 486, 4829

Rugel, M., Fedele, D., & Herczeg, G. 2018, A&A, 609, A70

Sanchis, E., Testi, L., Natta, A., et al. 2021, A&A, 649, A19

Sanchis, E., Testi, L., Natta, A., et al. 2020, A&A, 633, A114

Sargent, A. I. & Beckwith, S. 1987, ApJ, 323, 294

Schneider, P. C., Günther, H. M., & France, K. 2020, Galaxies, 8, 27

Seifried, D., Banerjee, R., Pudritz, R. E., & Klessen, R. S. 2013, MNRAS, 432, 3320

Sellek, A. D., Booth, R. A., & Clarke, C. J. 2020a, MNRAS, 498, 2845

Sellek, A. D., Booth, R. A., & Clarke, C. J. 2020b, MNRAS, 492, 1279

Sellek, A. D., Clarke, C. J., & Booth, R. A. 2021, MNRAS, 506, 1

Shakura, N. I. & Sunyaev, R. A. 1973, in IAU Symposium, Vol. 55, X- and Gamma-Ray Astronomy, ed. H. Bradt & R. Giacconi, 155

Shu, F. H., Adams, F. C., & Lizano, S. 1987, ARA&A, 25, 23

Shu, F. H., Johnstone, D., & Hollenbach, D. 1993, Icarus, 106, 92

Simon, M. N., Pascucci, I., Edwards, S., et al. 2016, ApJ, 831, 169

Sinclair, C. A., Rosotti, G. P., Juhasz, A., & Clarke, C. J. 2020, MNRAS, 493, 3535

Smith, R. J., Glover, S. C. O., Bonnell, I. A., Clark, P. C., & Klessen, R. S. 2011, MNRAS, 411, 1354

Soderblom, D. R., Hillenbrand, L. A., Jeffries, R. D., Mamajek, E. E., & Naylor, T. 2014, in Protostars and Planets VI, ed. H. Beuther, R. S. Klessen, C. P. Dullemond, & T. Henning, 219

Somigliana, A., Testi, L., Rosotti, G., et al. 2024, A&A, 689, A285

Somigliana, A., Testi, L., Rosotti, G., et al. 2023, ApJ, 954, L13

Somigliana, A., Toci, C., Lodato, G., Rosotti, G., & Manara, C. F. 2020, MNRAS, 492, 1120

Somigliana, A., Toci, C., Rosotti, G., et al. 2022, MNRAS, 514, 5927

Speedie, J., Dong, R., Hall, C., et al. 2024, Nature, 633, 58

Spezzano, S., Caselli, P., Bizzocchi, L., Giuliano, B. M., & Lattanzi, V. 2017, A&A, 606, A82

Stauffer, J., Cody, A. M., Baglin, A., et al. 2014, AJ, 147, 83

Stutz, A. M., Rieke, G. H., Bieging, J. H., et al. 2009, ApJ, 707, 137

Suzuki, T. K., Muto, T., & Inutsuka, S.-i. 2010, ApJ, 718, 1289

Suzuki, T. K., Ogihara, M., Morbidelli, A., Crida, A., & Guillot, T. 2016, A&A, 596, A74

Tabone, B., Cabrit, S., Pineau des Forêts, G., et al. 2020, A&A, 640, A82

Tabone, B., Rosotti, G. P., Cridland, A. J., Armitage, P. J., & Lodato, G. 2022a, MNRAS, 512, 2290

Tabone, B., Rosotti, G. P., Lodato, G., et al. 2022b, MNRAS, 512, L74

Takeuchi, T. & Lin, D. N. C. 2002, ApJ, 581, 1344

Tanaka, H., Himeno, Y., & Ida, S. 2005, ApJ, 625, 414

Tazzari, M., Clarke, C. J., Testi, L., et al. 2021, MNRAS, 506, 2804

Tazzari, M., Testi, L., Natta, A., et al. 2017, A&A, 606, A88

Teague, R., Bae, J., Bergin, E. A., Birnstiel, T., & Foreman-Mackey, D. 2018, ApJ, 860, L12

Terebey, S., Shu, F. H., & Cassen, P. 1984, ApJ, 286, 529

Testi, L., Birnstiel, T., Ricci, L., et al. 2014, in Protostars and Planets VI, ed. H. Beuther, R. S. Klessen, C. P. Dullemond, & T. Henning, 339–361

Testi, L., Natta, A., Manara, C. F., et al. 2022, arXiv e-prints, arXiv:2201.04079

Testi, L., Natta, A., Scholz, A., et al. 2016, A&A, 593, A111

Thi, W. F., van Dishoeck, E. F., Blake, G. A., et al. 2001, ApJ, 561, 1074

Tobin, J., Sheehan, P., Johnstone, D., & Sharma, R. 2018, arXiv e-prints, arXiv:1810.07174

Tobin, J. J., Hartmann, L., Bergin, E., et al. 2012, ApJ, 748, 16

Tobin, J. J., Hartmann, L., Chiang, H.-F., et al. 2013, ApJ, 771, 48

Toci, C., Rosotti, G., Lodato, G., Testi, L., & Trapman, L. 2021, MNRAS, 507, 818

Trapman, L., Facchini, S., Hogerheijde, M. R., van Dishoeck, E. F., & Bruderer, S. 2019, A&A, 629, A79

Trapman, L., Miotello, A., Kama, M., van Dishoeck, E. F., & Bruderer, S. 2017, A&A, 605, A69

Trapman, L., Rosotti, G., Bosman, A. D., Hogerheijde, M. R., & van Dishoeck, E. F. 2020, A&A, 640, A5

Trapman, L., Rosotti, G., Zhang, K., & Tabone, B. 2023, ApJ, 954, 41

Trapman, L., Zhang, K., van't Hoff, M. L. R., Hogerheijde, M. R., & Bergin, E. A. 2022, ApJ, 926, L2

Tripathi, A., Andrews, S. M., Birnstiel, T., & Wilner, D. J. 2017, ApJ, 845, 44

Turrini, D., Marzari, F., Polychroni, D., & Testi, L. 2019, ApJ, 877, 50

Tychoniec, Ł., Tobin, J. J., Karska, A., et al. 2018, ApJS, 238, 19

Valdivia-Mena, M. T., Pineda, J. E., Caselli, P., et al. 2024, A&A, 687, A71

Valdivia-Mena, M. T., Pineda, J. E., Segura-Cox, D. M., et al. 2022, A&A, 667, A12

Valegård, P. G., Ginski, C., Dominik, C., et al. 2022, A&A, 668, A25

Valenti, J. A., Basri, G., & Johns, C. M. 1993, AJ, 106, 2024

van Terwisga, S. E. & Hacar, A. 2023, A&A, 673, L2

Venuti, L., Damiani, F., & Prisinzano, L. 2019a, A&A, 621, A14

Venuti, L., Stelzer, B., Alcalá, J. M., et al. 2019b, A&A, 632, A46

Veronesi, B., Longarini, C., Lodato, G., et al. 2024, A&A, 688, A136

Veronesi, B., Paneque-Carreño, T., Lodato, G., et al. 2021, ApJ, 914, L27

Vlemmings, W. H. T., Lankhaar, B., Cazzoletti, P., et al. 2019, A&A, 624, L7

Walch, S., Naab, T., Whitworth, A., Burkert, A., & Gritschneder, M. 2010, MNRAS, 402, 2253

Wang, L. & Goodman, J. J. 2017, ApJ, 835, 59

Weber, M. L., Ercolano, B., Picogna, G., Hartmann, L., & Rodenkirch, P. J. 2020, MNRAS, 496, 223

Weidenschilling, S. J. 1977, MNRAS, 180, 57

Williams, J. P., Cieza, L., Hales, A., et al. 2019, ApJ, 875, L9

Williams, J. P. & Cieza, L. A. 2011, ARA&A, 49, 67

Winter, A. J., Clarke, C. J., Rosotti, G., et al. 2018, MNRAS, 478, 2700

Winter, A. J., Kruijssen, J. M. D., Longmore, S. N., & Chevance, M. 2020, Nature, 586, 528

Wolcott-Green, J., Haiman, Z., & Bryan, G. L. 2011, MNRAS, 418, 838

Xu, W. & Kunz, M. W. 2021a, MNRAS, 502, 4911

Xu, W. & Kunz, M. W. 2021b, MNRAS, 508, 2142

Yamamoto, T., Kadono, T., & Wada, K. 2014, ApJ, 783, L36

Yang, C.-C., Johansen, A., & Carrera, D. 2017, A&A, 606, A80

Youdin, A. & Johansen, A. 2007, ApJ, 662, 613

Zagaria, F., Clarke, C. J., Rosotti, G. P., & Manara, C. F. 2022a, MNRAS, 512, 3538

Zagaria, F., Rosotti, G. P., Clarke, C. J., & Tabone, B. 2022b, MNRAS, 514, 1088

Zagaria, F., Rosotti, G. P., & Lodato, G. 2021a, MNRAS, 504, 2235

Zagaria, F., Rosotti, G. P., & Lodato, G. 2021b, MNRAS, 507, 2531

Zhang, K., Blake, G. A., & Bergin, E. A. 2015, ApJ, 806, L7

Zormpas, A., Birnstiel, T., Rosotti, G. P., & Andrews, S. M. 2022, A&A, 661, A66

Danksagung

On the very first day I saw ESO, August 30th, 2021, it was raining. Six hours earlier I had left sunny, warm Italy and the comfort of everything I had always known. Later that day, looking at my things spread around the ESO apartment, I felt scared, lost, and lonely. I am amazed at how vividly I remember those feelings, considering how little they lasted. As soon as I finally met Ivanna, Josh, and Rik in person I felt like I had found my people, like maybe it wouldn't be so lonely after all. That night we had dinner together, learnt how to tie shoes a different way, and everything became a bit brighter. Since then, it never stopped getting brighter.

Leonardo, a te devo il primo e più grande ringraziamento. Grazie per aver creduto in me da sempre, per avermi seguita ed insegnato con pazienza e dedizione anche quando gli impegni erano tanti. Grazie per avermi dato la possibilità di seguire la mia strada ed avermici accompagnata, con i tuoi preziosi consigli e la tua curiosità. La passione che hai per questo lavoro traspare in ogni cosa che fai, e io sono onorata di poter dire di aver studiato con te. Mi hai mostrato che è importante avere il coraggio di cambiare, e mi hai dato un esempio che ricorderò sempre.

Giovanni, grazie di tutto quello che hai sempre fatto, e continui a fare, per me - anche quando non sei istituzionalmente tenuto a farlo. Ti sono infinitamente grata di avere sempre trovato tempo da dedicarmi, di tutto quello che mi hai insegnato, di come mi hai supportata tanto nella scienza quanto nelle questioni collaterali. Averti come mentore è un grande privilegio. Carlo, grazie di essere un punto di riferimento a ESO. Grazie di essere sempre disponibile a darmi un'opinione, di spingermi ad essere sempre una ricercatrice migliore e del supporto nei momenti difficili.

To the whole scientific community at ESO: the reason why the environment is so vibrant and lively is the dedicated, passionate people that build it and sustain it with their curiosity and excitement every single day, and being a part of this with all of you has been incredible. I have enjoyed our science coffees, the discussions at Journal Clubs, seminars, JACs and IDs - you have all taught me the importance of interaction, that talking to people *is* being productive, and to always question what we hear and think.

To all the students and postdocs of the SPF group, whom I will deliberately not mention to avoid missing anyone, it has been amazing to discuss science with you in our Monday morning meetings. You are inspiring, smart and brave and I cannot wait to see where your paths will take you. I am sure there will be many chances to catch up at conferences and meetings - we have learned that our world is quite small after all. To the staff members that took the time to interact with us, give us feedback and suggestions: thank you for your presence, your input and the interesting conversations at our Tuesday coffees. Thank you to all the near and far collaborators I have had the pleasure to work with, especially Giuseppe, for always being involved and the support across all my projects (since well before the PhD). Thank you to Benoît, Marco, Rossella, Ugo, and the ECOGAL members for the interesting discussions and the stimulating environment. To the Milan PhDs, thank

you for hosting me every time I passed by and sharing the precious coffee and sweets. To the friends I met at the Dustbusters and Les Houches schools, at EAS and during the visits around Europe, thank you for the fun and the memories.

Nelma, thank you for everything you have done for me, for us. Thank you for being a rock in the sea of new beginnings, for dealing with our big and small issues with patience and empathy, and for standing up for us. The way you care for people is extraordinary and I am so glad I met you.

These years have been filled with old and new endeavours, some quite unexpected. Marta, thank you for making the ESO choir a reality, and thank you to all the people I sang with. Samuel, thank you for leading the arguably best volleyball team that ever played in Garching, and to everyone that joined the trainings and played in Berlin at the Atomiades, it has been such a blast. Thank you to everyone who joined the 'beginner-achievable' ESO hikes, whether that meant a chill walk around Eibsee on a warm summer day or a trudge through the snow. Sk8r souls, thank you for the amazing blade nights skating around Munich. Irene, thank you for dreaming of the crochet & knitting club with me and making it happen, and thank you to everyone that took part in it - it has been such a pleasure to teach you and I am so proud of the crafters you have become. Table football crew, thank you for providing much needed breaks and for making my days much more fun and (just a little) louder.

The blessing and curse of ESO is that, eventually, everyone leaves. Time here is filled with farewells, whether it is for someone who did an internship of just a few months (which, I have learned, is more than enough to build unbreakable bonds) or someone you shared your whole time with. Every time I said a goodbye my heart ached a bit more, but it did because the people I met are awesome. As sad as it might be to see the people you came to love go, knowing the world is filled with friends is an amazing feeling, and watching them walk fearlessly towards their future and build the life we dreamt of makes me grateful to have them in my life. Ivanna, my bestie-bat, how grateful I am to have found you. I am proud of the scientist, and person, I have watched you become and I will always be cheering for you, no matter where life takes us. Ciara, sei un raggio di sole. La tua amicizia è stata uno dei regali più belli del dottorato. Du auch, Tommy, but I won't say anything more before you call an arrrbitro for lack of trash talk. Jenny, ciccina bella, sei speciale e adoro i nostri podcast. Adrien, what a joy to discuss design, hiking, diys, sketches... Lara, sweetie, thank you for being so loving and caring and always open to new adventures together. Giuli, grazie delle chicche su Ostia e l'Infernetto (e di tutto il resto). Elena, prima coinqui della vita, grazie di tutto ma soprattutto del primo disastro con la lavatrice. Sabri, meine liebe, danke für unsere Deutsch-Italienisch Stunden davor, und Abendessen danach. Tine, thank you for brightening the office with your energy, for the brunches and the gossip. Matti, grazie di essere il miglior fratello che avrei potuto desiderare, di avere sempre le parole (e i silenzi) giusti. Ruggero, grazie per tutte le gite in montagna, di avermi accompagnata alla mia prima ferrata e di essere un grande amico. ESO girlies, thank you for the great environment we built together, for lifting each other up and sharing our passions. Andrea, grazie di essere sempre al mio fianco e di supportarmi

in ogni cosa. Sono infinitamente grata alle decisioni, deviazioni e coincidenze che ci hanno portati a (ri)incontrarci qui. Tutto il resto lo sai già.

E infine, a te che stai guardando un insolitamente limpido cielo sopra Milano, dopo mesi a studiare spettroscopia stellare quasi per sbaglio; a te che ti domandi se sarai mai all'altezza di tutti i tuoi grandi sogni; a te che metti in dubbio le tue decisioni e hai paura di sbagliare; a te che ti senti persa nella tua nuova realtà; a tutte voi, e a tutte le altre che siamo state. Ve lo prometto: andrà tutto bene.